UNIVERSITY OF MODENA AND REGGIO EMILIA
DEPARTMENT OF ENGINEERING "ENZO FERRARI"

PhD in
INGEGNERIA INDUSTRIALE E DEL TERRITORIO (D.M.45/2013)

Cycle XXXII

ON THE GYROSCOPIC EFFECTS IN TIME-PERIODIC PARAMETRICALLY EXCITED ROTORS

Candidate: Alessandro De Felice

Tutor: Professor Silvio Sorrentino

PhD School Director: Professor Alberto Muscio

Ai miei Genitori

ABSTRACT

The dynamic analysis of torque-transmitting flexible rotors is a research subject of great interest in mechanics of machines, presently encouraged by a general increasing trend towards high-speed rotating equipment in conjunction with higher power density.

The effects of axial end thrust and twisting moment, representing common loading conditions in engineering applications, have long been investigated restricting the attention to the time-invariant problem. More recently, however, also oscillating load components have been considered, and studied as causes of parametrical excitation in rotor dynamics. The induced effects are potentially destabilizing, making the stability analysis of this specific kind of dynamic systems a problem of both theoretical interest and practical importance, which until now has not been satisfactorily studied in the literature.

In this thesis some novel insights are first provided in the analysis of distributed parameter linearized models of high-speed power transmitting flexible rotors subjected to constant external loads. On this necessary basis, an analysis is then developed aimed at clarifying the gyroscopic effects on the stability of parametrically excited rotors, also highlighting the role played by damping distributions.

As case-study, a balanced shaft is considered, modelled as a spinning Timoshenko beam loaded by oscillating axial end thrust and twisting moment, with possibility of carrying additional inertial elements. After discretization of the equations of motion into a set of coupled ordinary differential Mathieu-Hill equations, stability of Floquet-Lyapunov solutions is studied via eigen- problem formulation, obtained by applying the harmonic balance method. A numerical algorithm is then developed for computing global stability thresholds in presence of both gyroscopic and damping terms, aimed at reducing the computational load. Finally, the influence on stability of the main characteristic parameters of the rotor is analyzed with respect to frequency and amplitude of the external loads on stability charts in the form of Ince-Strutt diagrams.

As a novel result, it is demonstrated that gyroscopic terms produce substantial differences in both critical solutions and stability thresholds: the former are generally non-periodic limited-amplitude functions, and modifications induced on stability thresholds consist of shifts and merging of unstable regions, depending on the separation of natural frequencies into pairs of forward and backward values induced by angular speed.

As a practical result, the developed numerical algorithm provides an effective and efficient tool for tracing stability thresholds, also suitable for application to a more general category of gyroscopic systems, including complex shape rotors in those cases in which properly condensed finite element models would be available. The stability charts thus obtained can then be used as guidelines to provide simple safety limits for the time-varying, periodic loads acting on a rotor.

SINTESI

L’analisi dinamica di rotori flessibili adibiti alla trasmissione di potenza è un soggetto di ricerca di grande interesse nell’ambito della meccanica delle machine, attualmente incoraggiato dal crescente interesse verso applicazioni ad alta velocità di rotazione abbinata a più alte densità di potenza trasmesse.

Gli effetti della spinta assiale e del momento torcente, rappresentanti condizioni di caricamento comuni in ambito ingegneristico, sono stati studiati a lungo concentrando l’attenzione a problemi a carichi costanti. Tuttavia, più di recente, è stato considerato anche il caso di componenti oscillanti, studiate come causa di eccitazione parametrica in abito della dinamica dei rotori. Gli effetti indotti sono potenzialmente destabilizzanti, rendendo l’analisi di stabilità di questa specifica categoria di sistemi dinamici un problema d’importanza sia teorica che pratica, che ad oggi non è stata sufficientemente approfondita in letteratura.

In questa tesi sono inizialmente forniti nuovi approfondimenti riguardo all’analisi di sistemi a parametri distribuiti, linearizzati, rappresentanti rotori flessibili per la trasmissione di potenza ad alta velocità, soggetti a carichi esterni costanti. Sulla base di questa necessaria introduzione, viene condotta un’analisi mirata allo studio degli effetti giroscopici sulla stabilità di rotori eccitati parametricamente, evidenziando inoltre il ruolo delle distribuzioni di smorzamento.

Come caso di studio viene considerato un albero bilanciato, modellato come trave di Timoshenko rotante, caricato agli estremi da spinta assiale e momento torcente oscillanti, con la possibilità di calettamento di elementi inerziali aggiuntivi. A seguito della discretizzazione delle equazioni del moto in un sistema di equazioni differenziali ordinarie, accoppiate, del tipo Mathieu-Hill, la stabilità delle soluzioni di Floquet-Lyapunov viene studiata come problema agli autovalori, ottenuto applicando un metodo di bilancio armonico. Un algoritmo è seguitamente sviluppato per la determinazione delle frontiere di stabilità globali, in concomitanza di effetti giroscopici e dissipativi, mirato alla riduzione del carico computazionale. Infine, viene analizzata l’influenza dei parametri fondamentali del rotore sulle mappe di stabilità, rispetto a frequenza e ampiezza dei carichi, nella forma di diagrammi di Ince-Strutt.

Come nuovo risultato, è stato dimostrato che i termini giroscopici producono deviazioni sostanziali sulle soluzioni critiche e sulle frontiere di stabilità: le prime sono generalmente funzioni limitate nel tempo non periodiche, mentre le mappe di stabilità subiscono spostamenti e fusioni delle regioni di instabilità in ragione della separazione, indotta dalla velocità angolare, delle frequenze naturali del sistema in coppie di valori forward e backward.

Dal punto di vista pratico, l’algoritmo sviluppato fornisce uno strumento efficace ed efficiente per il tracciamento delle frontiere di stabilità, idoneo anche all’utilizzo in categorie di rotori più generali, come rotori di forma complicata, nei casi in cui una condensazione di un modello agli elementi finiti sia disponibile. Le mappe di stabilità così ottenute possono essere utilizzate come linea guida per fornire semplici limiti di sicurezza sulle ampiezze dei carichi oscillanti.

CONTENTS

1 INTRODUCTION

1.1 Motivation and current state of the art

The dynamic analysis of torque-transmitting flexible rotors is a research subject of great interest in mechanics of machines, presently encouraged by a general increasing trend towards high-speed rotating equipment in conjunction with higher power density.

It is a fact that every existing rotor can be understood as a continuous deformable object subjected to the most varied types of force fields. In the boundless field of rotordynamics, stability analysis of flexible rotors represents a topic of paramount importance. The onset of instabilities is generally followed by various categories of issues ranging from anomalous noise and wear to catastrophic failures. While the well-known effects of direct excitation and critical speeds are generally taken into account and carefully studied, the same cannot be stated for parametric excitation-driven resonances and instabilities. However, in a rotor system the probability of matching the conditions for parametric excitation is very high.

A wide range of applications is susceptible to this occurrence, in this case we refer to them as parametrically excited rotor problems. High-speed and high-power-transmitting rotors, commonly used in turbines and compressors for power plant and aeronautical applications, represent a perfect example. Helicopter multi-bladed rotors are often the subject of study in many papers focused on parametric instability. Gear-carrying shafts represent another application in which the presence of a time-varying mesh stiffness can cause parametric resonances. Theoretically every unbalanced rotor and/or subjected to time-varying external force fields can fall into this category under particular circumstances. It is important to recall that parametric instability can occur even in those systems in which non-conservative force fields are not considered; even an ideal Hamiltonian system can give rise to these phenomena.

In addiction to the elusive nature of parametric instabilities, the concept of high-speed rotor does not find a precise definition in the literature. Indeed, the absolute value of the operating angular velocity of a rotor should not be understood as a sufficient indicator to classify the latter as high-speed or low-speed equipment. Many other characteristic parameters of the rotor must be taken into consideration. Intuitively, in the context of this thesis, it is possible to state that a rotor is operating at high-speed if the effects of the latter on the results of modal and stability analysis are not negligible.

In the field of rotordynamics the use of finite element models is nowadays widespread, however distributed parameter formulations still remain of some interest, at least for analytical investigations and validation purposes. Continuous models of spinning shafts have been studied by several researchers who have dealt with many important aspects, highlighting the effects of transverse shear, rotatory inertia, gyroscopic moments and considering the additional contribution of axial end thrust and twisting moment. The gyroscopic effects were studied considering spinning Timoshenko beams [1]. The equilibrium equations for symmetric and asymmetric rotors, without the contribution of axial loads, were derived by Dimentberg [2] adopting the Newtonian formulation and later by Raffa and Vatta [3, 4] with Lagrangian formulation via Hamilton's principle, while the case of eccentric rotation was studied by Filipich and Rosales [5]. Early investigations about the effects of axial end thrust and twisting moment of constant magnitude acting simultaneously on a uniform shaft can be found in the works of Greenhill [6] and Southwell and Gough [7], who first considered the influence of these loads on critical speeds.

The effects of an axial end twisting moment alone on the flexural behavior of a rotating slender shaft was studied according to the Euler-Bernoulli beam model by Colomb and Rosenberg [8], and according to the Timoshenko beam model by Eshleman and Eubanks [9], who focused their analysis on critical speeds without considering natural frequencies. They found that the Euler-Bernoulli model is inaccurate in predicting the critical speeds, and that the latter always decrease with external axial torque. Following the results by Eshleman and Eubanks, the topic was then again considered, among others, by Yim *et al*. [10] and Lee [11]. The equations of motion of a spinning Timoshenko beam subjected to axial end thrust were derived with Lagrangian formulation by Choi *et al*. [12]. An analysis of the effects of combined external axial end thrust and twisting moment was proposed by Willems and Holzer [13] and later by Dubigeon and Michon [14], who adopted the Timoshenko beam model, casting doubts on some results obtained by Eshleman and Eubanks. It should also be remarked that while most authors studied natural frequencies and critical speeds, only a few of them developed a complete modal analysis of a distributed parameter spinning shaft, as for instance Lee *et al*. [15] in the case of a rotating Rayleigh beam.

The effects of axial end thrust and twisting moment, representing common loading conditions in many engineering applications, were deeply investigated in the case of constant magnitude loads. More recently, attention was devoted also to the case of loads with oscillating components, and therefore to stability analysis of parametrically excited rotor systems, a topic of both relevant theoretical interest and practical importance. An oscillating external excitation may give rise to time-varying coefficients in the equations of motion. It is known that, under pertinent conditions, such excitations may lead to parametric resonances, which may eventually cause parametric instabilities [16].

Non-linear time-varying systems represent the most common type of systems for modeling engineering problems. Perturbation theory and numerical continuation techniques are widely used for stability analysis of such systems. However, these methods generally do not allow to obtain clean analytical results about stability. Linear time-varying systems, on the other hand, are easier to deal with and many theoretical results can be found in the literature, as in [17]. Recently, van der Kloet and Neerhoff [18] also proposed a numerical algorithm aimed at diagonalize linear time-varying systems. Linear time-periodic systems represent one of the simplest types of time-varying systems, in which a period of the matrix of coefficients can be univocally identified. Many important mathematicians dealt with this topic, starting from Mathieu [19], who presented his famous equation in 1868 and published an in-depth analysis of a periodic system in 1873 [20]. Few years later, in 1883 [21], Floquet presented his theory and laid the foundations of the modern stability analysis of linear time-periodic systems. In the next hundred years, scientist as Hill [22], Lord Rayleigh [23, 24], Poincaré [25], Lyapunov [26], Meissner [27], Krein

[28-38], Yakubovich [39, 40], Ince [41] and many others provided fundamental theoretical results, leading to the stability analysis of linear time-periodic systems as we know it today.

Floquet theory has been used in many scientific areas, not directly related to rotordynamics. A correct implementation of Bolotin's method [42] and Floquet theory was presented in 2004 by Ruzzene [43] in order to study the stability of periodic stiffened shells. Ahsan, Sadath and Uchida [44] studied the stability of delayed time-periodic differential equations using Galerkin-Arnoldi algorithm to estimate Floquet multipliers. An approximate procedure for the generation of the bifurcation diagram of a softening Duffing oscillator was proposed by Nayfeh and Sanchez [45]. This procedure consists in a combination of second-order perturbation solutions of the system in the neighborhood of its non-linear resonances and Floquet analysis. Floquet multipliers have been involved in stability analysis of periodic orbits of a non-linear gyroscope system in [46]. Also celestial mechanics is a research field in which Floquet theory finds many applications. Among them, an in-depth numerical investigation concerning large scale orbits of particles in irregular asteroid's gravity field can be found in [47], in which Floquet multipliers are computed for bifurcation analysis during orbital continuation.

In the more specific field of rotordynamics, in which both gyroscopic and damping effects can be relevant, the parametric excitation is commonly due periodic components of the external loads which may affect the system's stability. Several studies can be found in the literature on this subject, dealing with stability analysis of rotating shafts [48-59], cylindrical shells [60, 61] under periodic axial forces, high speed mechanisms [62] or on conditions for rotordynamic stability under combined axial forces and torques [63]. In all the above mentioned works, as reported in [64], however, an improper application of Bolotin's method [42] led to wrong conclusions (periodic critical solutions with consequent, apparent destabilizing effects due to gyroscopic terms).

Other contributions, besides [64], are not affected by this error. However, many of them dealt with very simple models as in [65, 66] in which rigid rotors on elastic supports are considered. Jeffcott rotor model was considered in [67-69]. A massless unbalanced shaft on anisotropic bearing, carrying a rigid disc, was studied by Wettergren and Olsson [70], where external and internal damping distributions have been taken into consideration. Other lumped parameters models can be found in the literature, among them, a two degrees of freedom rotor, which was considered in [71] to study the stability of the periodic response and a four degrees of freedom parametric excited rotor in [72, 73]. A study focused on the similarity of the Coleman [74] and Lyapunov-Floquet transformations for modal analysis of a five degrees of freedom three-bladed rotor can be found in [75], while a seven degrees of freedom two-bladed rotor model was adopted in [76]. In the latter two studies, however, no in-depth stability analysis was provided. A more refined model was adopted in [77], in which a stability analysis of an axially loaded spinning Rayleigh beam is presented.

Finite elements method was widely used in combination with Floquet theory for modal and stability analysis of rotor systems. Sundararajan and Noah [78] carried out a stability analysis of the periodic response of a finite elements model of a rotor using Floquet Theory in 1998. More recently, Al-Shudeifat [79] used finite elements for the stability analysis of a parametric excited cracked rotor without considering damping effects. Kirchgäßner [80] used Floquet Theory and finite elements for modal analysis of rotors, without carrying out stability analysis of the latter. A study presenting a Floquet implicit analysis, consisting of a numerical methodology (Arnoldi algorithm [81]) ideally suited in case of very large number of degrees of freedom can be found in [82]. The latter paper, by Bauchau and Nikishkov (2001), follows the line of previous works [83, 84], in which the first attempts at parallel computing in this field of research were born. In 1983, Dugundji and Wendell [85] presented a review on some analysis methods for rotating systems with periodic coefficients: Floquet methods and harmonic balance method, treating them separately.

While many authors dealt with gyroscopic effects in parametrically excited rotor systems (most of them with questionable or incomplete results), few have investigated the role played by damping distributions on stability of such systems. Besides [70], it is worth mentioning Mazzei and Scott [86]. However, in the latter work, poorly approximated stability charts led to incomplete and generally misleading conclusions about how internal damping affects parametric instabilities.

In the above mentioned studies, however, the main focus is not clarifying in general the role played by gyroscopic and damping terms on parametric stability. While the gyroscopic effects in rotordynamics have been deeply studied in the unloaded case [87, 88] and under constant magnitude loads [89], it can be stated that their effects on stability of parametrically excited rotors have not been sufficiently investigated yet.

1.2 Structure and objectives of the thesis

In the present work some novel insights are first provided in the analysis of distributed parameter linearized models of high-speed power transmitting flexible rotors subjected to constant external loads. On this necessary basis, an analysis is then developed aimed at clarifying the gyroscopic effects on the stability of parametrically excited rotors, also highlighting the role played by damping distributions. The next Chapters are structured as follows:

Chapter 2. A brief introduction to Floquet theory is presented, collecting some fundamental results about linear time-periodic systems. Definitions of fundamental and monodromy matrices, Floquet multipliers, characteristic exponents and of elementary divisors along with preliminary considerations about stability are recalled.

Chapter 3. In this Chapter further insights are proposed in the analysis of a distributed parameter model of a high-speed, power transmitting flexible rotor. A homogeneous uniform Timoshenko straight beam with circular section is considered, spinning with constant angular speed about its longitudinal axis on isotropic supports (rigid bearings), and subjected simultaneously to constant end thrust and twisting moment. The equations of motion differ from those derived in [14], and are consistent with those obtained in less general cases [9, 12]. A novel contribution is given in the development of complete modal analysis of the model under study. After clarifying the properties of the operators involved and the relation between eigensolutions obtained for complex and real displacement variables, modal analysis of the rotating shaft is then completed using real displacement variables in both the configuration space and in the state-space, including the derivation of critical loads due to combined effects of axial end thrust and twisting moment. In addition, such analytical developments allow to cast new light on the problem of existence and identification of the second frequency spectrum in the Timoshenko beam theory [90], here reconsidered from a novel perspective. The existence of a second spectrum in the case of non-rotating beams and general boundary conditions has been much debated in the literature [91-93] since it is possible to easily identify the companion natural frequencies constituting the second spectrum only in particular cases. More recently, the existence of a second spectrum in a non-rotating finite–length beam has been demonstrated on the basis of accurate experimental results, at least for free–free boundary conditions [94], and also by considering free waves in beams of infinite length [95]. New evidence of existence of the second spectrum together with a novel definition for its identification are presented, only possible if considering gyroscopic effects, therefore a rotating beam. In parallel, the role of the so–called cut–off Timoshenko beam frequencies [92] is investigated, extending their definition to include the effects of gyroscopic moments and external loads [89, 96, 97].

Chapter 4. A novel contribution is given aimed at clarifying gyroscopic effects on the stability of parametrically excited rotor systems, also considering and analyzing the contextual and not negligible role played by both external (non–rotating) and internal (rotating) damping distributions. As case–study including all features of interest for this analysis, giving rise to a set of coupled differential Mathieu–Hill equations with both gyroscopic and damping terms, a continuous perfectly balanced shaft is considered, modelled as a spinning Timoshenko beam loaded by axial end thrust and twisting moment oscillating at the same period, with possibility of carrying additional inertial elements (like discs or flywheels) mounted at given points on its longitudinal axis. The coupled partial differential equations of motion of the shaft, derived in Chapter 3, are first reduced to a set of coupled ordinary differential Mathieu–Hill equations through Galerkin discretization (exact decoupling into a set of single–degree–of–freedom equations, as for the Rayleigh beam model [77], in this case is not possible).

Stability of solutions is then studied via eigenproblem formulation, obtained by applying the harmonic balance method. Five simplified cases (two Hamiltonian and three non-Hamiltonian) are first analyzed in order to draw theoretical conclusions about the influence of gyroscopic and external damping terms (when they are not both present).

A numerical algorithm is subsequently developed for computing global stability thresholds in presence of both gyroscopic and damping terms. Finally, the influence on stability of the main characteristic parameters of the shaft is analyzed on stability charts (Ince–Strutt diagrams [42]) with respect to frequency and amplitude of the external loads.

From this point onwards, the adopted formulation and numerical algorithms are also suitable for application to a more general category of gyroscopic systems, including complex shape rotors in those cases in which properly condensed finite element models are available.

2 FLOQUET THEORY

2.1 Introduction

On the general solution of linear differential equations with periodic coefficients there is a large collection of results in the literature. Most of them are due to G. Floquet, who formalized, in the second half of the nineteenth century, the basis of the theory that today bears his name. However, modern Floquet Theory results from a subsequent refinement that takes into account contemporary and more recent publications. A. M. Lyapunov and H. Poincaré have laid the foundations of stability analysis of parametric systems and have made great contributions to the evolution of the current Floquet Theory. The most important contributions to the analysis of parametric systems (of which time-varying coefficients systems constitute a subclass), are chronologically listed below.

- 1831 M. Faraday carried out the first studies on parametric systems [98]
- 1873 E. Mathieu presented the first in-depth analysis of a time-periodic system [20]
- 1883 G. Floquet published his theory [21]
- 1886 G. W. Hill published some papers concerning stability analysis of periodic systems in the field of celestial mechanics [22]
- 1887 Lord Rayleigh's studies on second-order systems are published [23, 24]
- 1890 H. Poincaré published important results on 3-body problem [25]
- 1892 A. M. Lyapunov defended his doctoral thesis entitled "*The General Problem of Stability of Motion*" and enriched the meaning of Floquet's results [26]
- 1918 E. Meissner published a paper focused on Hill's equation [27]
- 1950-1965 M. G. Krein brought to light some revolutionary properties of Floquet multipliers, these results constitute the pillars of modern stability theory [28-38]

The list is obviously incomplete and it is not meant to be used as exhaustive bibliography, it is better to interpret it as the core around which the research on parametric systems has been developed. In this chapter some fundamental results of basic Floquet Theory are presented.

However, it is worth mentioning that for a deep understanding of the topics discussed, also considering their vastness, it is advisable to consult directly the original material.

At this stage it is essential to mention the work carried out by V. A. Yakubovich and V. M. Starzhinskii in grouping most of the results of the last two centuries in terms of time-varying linear periodic systems [39, 40]. In the latter, the tools necessary to reach the conclusions contained in this chapter are organized with impeccable logic and clarity. The following Sections are intended to summarize existing definitions, theorems and demostrations widely covered in [39, 40] in order to facilitate the reading of the next Chapters.

2.2 Problem statement

Consider the following equation:

$$\dot{\mathbf{x}}(t) = \mathbf{A}(t)\,\mathbf{x}(t) \tag{2.2.1}$$

Let Eq. (2.2.1) be a system of *n* linear first-order differential equations with integrable, piece-wise-continuous and periodic coefficients and let **A**(*t*) be the $n \times n$ matrix of coefficients. Thus, the matrix **A**(*t*) is a periodic function of time *t*, with real *t* and $t \in (-\infty, \infty)$:

$$\mathbf{A}(t) = \mathbf{A}(t \pm \mathrm{T}), \qquad \forall\, t \text{ and } \mathrm{T} > 0 \tag{2.2.2}$$

where T is a period of **A**(*t*). Without losing in generality, operator + in Eq. (2.2.2) can be chosen. It can be proven [39] that the solution of Eq. (2.2.1), with the initial condition $\mathbf{x}(0) = \mathbf{x}_0(t) = \mathbf{x}_0$, exists and it is unique.

Definition (*fundamental matrix*): Assume that $\mathbf{x}_1(t), \mathbf{x}_2(t), \ldots, \mathbf{x}_n(t)$ are *n* linearly independent solutions of Eq. (2.2.1) and consider a matrix **X**(*t*), called *fundamental matrix* of the system in Eq. (2.2.1), that has solutions $\mathbf{x}_1(t), \mathbf{x}_2(t), \ldots, \mathbf{x}_n(t)$ as columns:

$$\mathbf{X}(t) = \{\; \mathbf{x}_1(t) \quad \mathbf{x}_2(t) \quad \ldots \quad \mathbf{x}_n(t) \;\} \tag{2.2.3}$$

It is easy to notice that **X**(*t*) is non-singular and it is also a solution of Eq. (2.2.1). The problem can be posed in Cauchy form as:

$$\begin{cases} \dot{\mathbf{X}}(t) = \mathbf{A}(t)\,\mathbf{X}(t) \\ \mathbf{X}(t_0) = \mathbf{X}_0 \end{cases} \tag{2.2.4}$$

Definition (*principal fundamental matrix*): if $\mathbf{X}(t_0) = \mathbf{X}_0 = \mathbf{I}$ then **X**(*t*) is called *principal fundamental matrix* of the system in Eq. (2.2.1) or *matrizant* of the system.

2.3 General results

Lemma 1: let **X**(*t*) be a fundamental matrix and let **B** be a non-singular constant matrix. Matrix **Y**(*t*) is introduced, thus:

$$\mathbf{Y}(t) = \mathbf{X}(t)\,\mathbf{B} \tag{2.3.1}$$

It can be shown that also **Y**(*t*) is a fundamental matrix.

Proof: Since **X**(*t*) and **B** are non-singular, also **Y**(*t*) is non-singular:

$$\mathbf{Y}^{-1}(t) = \mathbf{B}^{-1}\,\mathbf{X}^{-1}(t) \tag{2.3.2}$$

Furthermore, $\mathbf{Y}(t)$ is also a solution of Eq. (2.2.1):

$$\dot{\mathbf{Y}}(t) = \dot{\mathbf{X}}(t)\,\mathbf{B} = \mathbf{A}(t)\,\mathbf{X}(t)\,\mathbf{B} = \mathbf{A}(t)\,\mathbf{Y}(t) \quad \Rightarrow \quad \dot{\mathbf{Y}}(t) = \mathbf{A}(t)\,\mathbf{Y}(t) \tag{2.3.3}$$

So $\mathbf{Y}(t)$ is a fundamental matrix. (Q.E.D.)

Definition (*Wronskian*): consider a function $\mathrm{W}(t)$ such that:

$$\mathrm{W}(t) = \det\left[\mathbf{X}(t)\right] \tag{2.3.4}$$

$\mathrm{W}(t)$ is the Wronskian of $\mathbf{X}(t)$. Note that the latter definition is different from the classical one of Wronskian or generalized Wronskian of a vector function.

Lemma 2 *(Abel-Jacobi-Liouville identity)*: take the Wronskian of $\mathbf{X}(t)$ as defined in Eq. (2.3.4), then:

$$\mathrm{W}(t) = \mathrm{W}(t_0)\exp\left[\int_{t_0}^{t} tr\ \left[\mathbf{A}(\tau)\right] d\tau\right] \tag{2.3.5}$$

where t_0 is arbitrary.

Proof: using Leibniz formula for determinants and for the linearity of the determinant with respect to each row, taking derivative with respect to time gives:

$$\frac{d}{dt}\left\{\det\left[\mathbf{X}(t)\right]\right\} = \sum_{j=1}^{n} \det\begin{bmatrix} \mathbf{X}_{1,1} & \mathbf{X}_{1,2} & \cdots & \mathbf{X}_{1,n} \\ \vdots & \vdots & \ddots & \vdots \\ \dot{\mathbf{X}}_{j,1} & \dot{\mathbf{X}}_{j,2} & \cdots & \dot{\mathbf{X}}_{j,n} \\ \vdots & \vdots & \ddots & \vdots \\ \mathbf{X}_{n,1} & \mathbf{X}_{n,2} & \cdots & \mathbf{X}_{n,n} \end{bmatrix} \tag{2.3.6}$$

where the subscript *p,q* in Eq. (2.3.6) indicates the element of position *p,q* of $\mathbf{X}(t)$. Taking into account Eq. (2.2.4), the generic element of $\dot{\mathbf{X}}(t)$ takes the form:

$$\dot{\mathbf{X}}_{j,k} = \sum_{l=1}^{n} \mathbf{A}_{j,l}\,\mathbf{X}_{l,k}\,, \quad l\,,k \in \{1,\dots n\} \tag{2.3.7}$$

where $\mathbf{A}_{j,l}$ represent the *j,l* element of $\mathbf{A}(t)$. For the each *j*-th row Eq. (2.3.7) leads to:

$$\left\{\ \dot{\mathbf{X}}_{j,1} \quad \dot{\mathbf{X}}_{j,2} \quad \dots \quad \dot{\mathbf{X}}_{j,n}\ \right\} = \sum_{l=1}^{n} \mathbf{A}_{j,l}\left\{\ \mathbf{X}_{l,1} \quad \mathbf{X}_{l,2} \quad \dots \quad \mathbf{X}_{l,n}\ \right\} \tag{2.3.8}$$

Now, subtracting from the *j*-th row a linear combination of the other rows as follows:

$$\sum_{l=1}^{n} a_{j,l} \left\{ \mathbf{X}_{l,1} \quad \mathbf{X}_{l,2} \quad \dots \quad \mathbf{X}_{l,n} \right\}, \quad j \neq l \tag{2.3.9}$$

it shows that the determinants in Eq. (2.3.6) do not change, as well as their sum. Moreover, for the linearity of the determinant with respect to each row:

$$\begin{aligned}
\frac{d}{dt}\left\{\det\left[\mathbf{X}(t)\right]\right\} &= \sum_{j=1}^{n} \det \begin{bmatrix} \mathbf{X}_{1,1} & \mathbf{X}_{1,2} & \cdots & \mathbf{X}_{1,n} \\ \vdots & \vdots & \ddots & \vdots \\ \dot{\mathbf{X}}_{j,1} & \dot{\mathbf{X}}_{j,2} & \cdots & \dot{\mathbf{X}}_{j,n} \\ \vdots & \vdots & \ddots & \vdots \\ \mathbf{X}_{n,1} & \mathbf{X}_{n,2} & \cdots & \mathbf{X}_{n,n} \end{bmatrix} = \\
&= \sum_{j=1}^{n} \det \begin{bmatrix} \mathbf{X}_{1,1} & \mathbf{X}_{1,2} & \cdots & \mathbf{X}_{1,n} \\ \vdots & \vdots & \ddots & \vdots \\ \mathbf{A}_{j,j}\, \mathbf{X}_{i,1} & \mathbf{A}_{j,j}\, \mathbf{X}_{i,2} & \cdots & \mathbf{A}_{j,j}\, \mathbf{X}_{i,n} \\ \vdots & \vdots & \ddots & \vdots \\ \mathbf{X}_{n,1} & \mathbf{X}_{n,2} & \cdots & \mathbf{X}_{n,n} \end{bmatrix} = \\
&= \sum_{j=1}^{n} \mathbf{A}_{j,j} \det\left[\mathbf{X}(t)\right]
\end{aligned} \tag{2.3.10}$$

Substituting the expression of Wronskian according to its definition in Eq. (2.3.10) gives:

$$\dot{\mathrm{W}}(t) = \mathrm{W}(t)\, tr\left[\mathbf{A}(t)\right] \tag{2.3.11}$$

The solution of Eq. (2.3.11) coincides with the statement of *Lemma* 2. (Q.E.D.)

Theorem 1: let **A**(t) be as in Eq. (2.2.2). If **X**(*t*) is a fundamental matrix then the following statements are true:

1 $\mathbf{X}(t+\mathrm{T})$ is also a fundamental matrix for the system in Eq. (2.2.1)

2 There exists a constant matrix **B** such that $\mathbf{X}(t+\mathrm{T}) = \mathbf{X}(t)\,\mathbf{B}, \quad \forall\, t$

3 $\det\left[\mathbf{B}\right] = \exp\left[\int_0^{\mathrm{T}} tr\ \left[\mathbf{A}(\tau)\right] d\tau\right]$

Proof of 1: proceed with the following substitution:

$$\mathbf{Y}(t) = \mathbf{X}(t+\mathrm{T}) \tag{2.3.12}$$

then:

$$\dot{\mathbf{Y}}(t) = \dot{\mathbf{X}}(t+\mathrm{T}) = \mathbf{A}(t+\mathrm{T})\,\mathbf{X}(t+\mathrm{T}) = \mathbf{A}(t)\,\mathbf{X}(t+\mathrm{T}) = \mathbf{A}(t)\,\mathbf{Y}(t) \tag{2.3.13}$$

So $\mathbf{Y}(t)$ is a fundamental matrix. (Q.E.D.)

Proof of 2: let's introduce the matrix $\mathbf{B}(t)$ such that:

$$\mathbf{B}(t) = \mathbf{X}^{-1}(t)\,\mathbf{Y}(t) \tag{2.3.14}$$

then:

$$\mathbf{Y}(t) = \mathbf{X}(t)\,\mathbf{X}^{-1}(t)\,\mathbf{Y}(t) = \mathbf{X}(t)\,\mathbf{B}(t) \tag{2.3.15}$$

Moreover $\mathbf{B}_0 = \mathbf{B}(t_0)$ by definition. From *Lemma* 1 it was obtained that:

$$\mathbf{Y}_0(t) = \mathbf{X}(t)\,\mathbf{B}_0 \tag{2.3.16}$$

where $\mathbf{Y}_0(t)$ is a fundamental matrix, ($\mathbf{Y}_0(t_0) = \mathbf{Y}(t_0)$ by definition). Since $\mathbf{Y}_0(t)$ and $\mathbf{Y}(t)$ are both solutions of $\dot{\mathbf{X}}(t) = \mathbf{A}(t)\,\mathbf{X}(t)$ in Eq. (2.2.4), due to the uniqueness of the solution, it must be that:

$$\mathbf{Y}_0(t) = \mathbf{Y}(t), \quad \forall\, t \tag{2.3.17}$$

so, as a result:

$$\mathbf{B}_0 = \mathbf{B}(t), \quad \forall\, t \tag{2.3.18}$$

which means that $\mathbf{B}(t)$ is time-invariant, hence $\mathbf{B}$ is a constant matrix. (Q.E.D.)

Proof of 3: Eq. (2.3.5) of *Lemma* 2 yields:

$$\begin{aligned} \mathrm{W}(t+\mathrm{T}) &= \mathrm{W}(t_0)\exp\left[\int_{t_0}^{t} tr\ \left[\mathbf{A}(\tau)\right] d\tau + \int_{t}^{t+\mathrm{T}} tr\ \left[\mathbf{A}(\tau)\right] d\tau\right] = \\ &= \mathrm{W}(t)\exp\left[\int_{t}^{t+\mathrm{T}} tr\ \left[\mathbf{A}(\tau)\right] d\tau\right] \end{aligned} \tag{2.3.19}$$

For convenience, the function $\int_{t}^{t+\mathrm{T}} tr\ \left[\mathbf{A}(\tau)\right] d\tau$ will be called $\Pi(t)$ from now on. The function $tr\left[\mathbf{A}(t)\right]$ is periodic of period T due to Eq. (2.2.2). For the *Fundamental Theorem of Calculus*, $\Pi(t)$ benefits from the following property:

$$\frac{d}{dt}\left[\Pi(t)\right] = tr\left[\mathbf{A}(t+\mathrm{T})\right] - tr\left[\mathbf{A}(t)\right] = 0 \tag{2.3.20}$$

Hence $\Pi(t)$ is time-invariant. In particular Eq. (2.3.20) yields:

$$\Pi(t) = \Pi(0), \quad \forall t \tag{2.3.21}$$

Substituting Eq. (2.3.21) in Eq. (2.3.19) gives:

$$\mathrm{W}(t+\mathrm{T}) = \mathrm{W}(t) \exp\left[\int_0^{\mathrm{T}} tr \; [\mathbf{A}(\tau)] \, d\tau \right] \tag{2.3.22}$$

It is known from statement 2 of *Theorem* 1 that $\mathbf{X}(t+\mathrm{T}) = \mathbf{X}(t)\,\mathbf{B}$, $\forall t$, so it can be written that:

$$\det[\mathbf{X}(t+\mathrm{T})] = \det[\mathbf{X}(t)] \det[\mathbf{B}] \tag{2.3.23}$$

Substituting Eq. (2.3.4) in Eq. (2.3.23) yields:

$$\mathrm{W}(t+\mathrm{T}) = \mathrm{W}(t) \det[\mathbf{B}] \tag{2.3.24}$$

Finally, replacing Eq. (2.3.24) in Eq. (2.3.22) gives the statement 3 of *Theorem* 1. (Q.E.D.)

2.4 Monodromy matrix, Floquet multipliers and characteristic exponents

Let **B** be a non-singular matrix as in the previous section. From *Theorem* 1 statement 1, 2 and 3, it is true that:

$$\begin{cases} \det[\mathbf{B}] = \exp\left[\int_0^{\mathrm{T}} tr \; [\mathbf{A}(\tau)] \, d\tau \right] \\ \mathbf{B}(t) = \mathbf{X}^{-1}(t)\,\mathbf{Y}(t) = \mathbf{B} \\ \mathbf{Y}(t) = \mathbf{X}(t+\mathrm{T}) \end{cases} \tag{2.4.1}$$

Since **B** is time-invariant it can be evaluated in $t = 0$:

$$\mathbf{B} = \mathbf{X}^{-1}(0)\,\mathbf{X}(\mathrm{T}) \tag{2.4.2}$$

Definition (*monodromy matrix*): consider **B** as in Eq. (2.4.2), if $\mathbf{X}(t)$ is principal, hence if $\mathbf{X}(t)$ is the matrizant of the system in Eq. (2.2.1), *i.e.* $\mathbf{X}(t_0) = \mathbf{X}_0 = \mathbf{I}$ with $t_0 = 0$, Eq. (2.4.2) reduces to:

$$\mathbf{B} = \mathbf{X}(\mathrm{T}) \tag{2.4.3}$$

Such a matrix is called *monodromy matrix*.

Definition (*Floquet multipliers*): let $\eta_1, \eta_2, \ldots, \eta_n$ be the eigenvalues of the monodromy matrix **B** as in Eq. (2.4.3). They are called *characteristic multipliers* or *Floquet multipliers* of the system $\dot{\mathbf{X}}(t) = \mathbf{A}(t)\,\mathbf{X}(t)$.

Definition (*characteristic exponents*): let $\Lambda_1, \Lambda_2, \dots, \Lambda_n$ be *n* scalars that satisfy the following conditions:

$$\eta_1 = e^{\Lambda_1 \mathrm{T}}, \eta_2 = e^{\Lambda_2 \mathrm{T}}, \dots, \eta_n = e^{\Lambda_n \mathrm{T}} \tag{2.4.4}$$

The quantities $\Lambda_1, \Lambda_2, \dots, \Lambda_n$ are called *characteristic exponents* or *Floquet exponents* of the system. Floquet multipliers $\eta_1, \eta_2, \dots, \eta_n$ and characteristic exponents $\Lambda_1, \Lambda_2, \dots, \Lambda_n$ have unique important properties as shown below.
As a corollary of *Theorem* 1 the following identities are satisfied:

$$\det[\mathbf{B}] = \prod_{j=1}^{n} \eta_j = \prod_{j=1}^{n} e^{\Lambda_j \mathrm{T}} = \exp\left[\int_0^{\mathrm{T}} tr\,[\mathbf{A}(\tau)]\,d\tau\right] \tag{2.4.5}$$

and:

$$\sum_{j=1}^{n} \eta_j = \sum_{j=1}^{n} e^{\Lambda_j \mathrm{T}} = tr\,[\mathbf{B}] \tag{2.4.6}$$

Characteristic exponents $\Lambda_1, \Lambda_2, \dots, \Lambda_n$ do not possess the property of uniqueness, indeed considering the generic *j*-th characteristic exponent Λ_j, there is an infinite number of other exponents, obtainable from Λ_j, which correspond to the same multiplier η_j:

$$\eta_j = e^{\Lambda_j \mathrm{T}} \quad \Leftrightarrow \quad \eta_j = e^{\left(\Lambda_j + i\frac{2z\pi}{\mathrm{T}}\right)\mathrm{T}}, \qquad z \in \mathbb{Z} \tag{2.4.7}$$

Where *i* in Eq, (2.4.7) is the imaginary unit. Unlike characteristic exponents, the multipliers are unique and they represent an intrinsic property of the system in Eq. (2.2.1). This means that multipliers do not depend on the choice of the fundamental matrix. Floquet multipliers represent an invariant for the system in Eq. (2.2.1). However, this important property must be proven.

Proof of uniqueness of multipliers: let $\tilde{\mathbf{X}}(t)$ be a fundamental matrix different from $\mathbf{X}(t)$ and $\tilde{\mathbf{B}}$ be the corresponding monodromy matrix. By virtue of *Theorem* 1, statement 2, it has to be:

$$\tilde{\mathbf{X}}(t+\mathrm{T}) = \tilde{\mathbf{X}}(t)\,\tilde{\mathbf{B}} \tag{2.4.8}$$

Since $\tilde{\mathbf{X}}(t)$ and $\mathbf{X}(t)$ are both fundamental matrices and thanks to *Lemma* 1 that states that a non-singular matrix (say $\mathbf{E}$) must exist such that:

$$\tilde{\mathbf{X}}(t) = \mathbf{X}(t)\,\mathbf{E} \tag{2.4.9}$$

then from Eq. (2.4.8):

$$\begin{aligned}\tilde{\mathbf{X}}(t+\mathrm{T}) = \mathbf{X}(t+\mathrm{T})\,\mathbf{E} \quad \Rightarrow \quad & \tilde{\mathbf{X}}(t)\,\tilde{\mathbf{B}} = \mathbf{X}(t)\,\mathbf{B}\,\mathbf{E} \\ & \mathbf{X}(t)\,\mathbf{E}\,\tilde{\mathbf{B}} = \mathbf{X}(t)\,\mathbf{B}\,\mathbf{E} \\ & \mathbf{E}\,\tilde{\mathbf{B}} = \mathbf{B}\,\mathbf{E} \\ & \mathbf{E}\,\tilde{\mathbf{B}}\,\mathbf{E}^{-1} = \mathbf{B}\end{aligned} \tag{2.4.10}$$

Eq. (2.4.10) states that $\tilde{\mathbf{B}}$ and **B** are similar to each other, which means that they share the same eigenvalues. The latter proves that Floquet multipliers do not depend on the choice of fundamental matrix and are therefore unique. (Q.E.D.)

2.5 The Floquet-Lyapunov solution

Theorem 2: let η be a multiplier of Eq. (2.2.1) and Λ be a corresponding characteristic exponent. Then there exists a solution $\mathbf{x}(t)$ of Eq. (2.2.1) that respects these statements:

1 $\mathbf{x}(t+\mathrm{T}) = \eta\,\mathbf{x}(t)$

2 $\exists\,\mathbf{p}(t)$ such that $\mathbf{p}(t+\mathrm{T}) = \mathbf{p}(t)$ and $\mathbf{x}(t) = e^{\Lambda t}\mathbf{p}(t)$

Proof of 1: let **v** be a right eigenvector of the monodromy matrix **B** such that η is the corresponding eigenvalue. Solution $\mathbf{x}(t)$ may be expressed as:

$$\mathbf{x}(t) = \mathbf{X}(t)\,\mathbf{v} \tag{2.5.1}$$

It's easy to notice that Eq. (2.5.1) provides a suitable solution of Eq. (2.2.1). Note that the fact that **v** is an eigenvector of **B** is not a necessary condition to state that $\mathbf{x}(t)$ is a solution of Eq. (2.2.1). Indeed, every vector $\mathbf{v} \in \mathbb{C}^n$, with $\mathbf{v} \neq \mathbf{0}$, is admissible to make $\mathbf{x}(t)$ a solution, this is due the fact that Eq. (2.2.1) is a linear system of differential equations and $\mathbf{X}(t)\,\mathbf{v}$ is a linear combination of linearly independent solutions (superposition principle) by definition of fundamental matrix. If **v** is an eigenvector of **B,** then Eq. (2.5.1) yields:

$$\mathbf{x}(t+\mathrm{T}) = \mathbf{X}(t+\mathrm{T})\,\mathbf{v} = \mathbf{X}(t)\,\mathbf{B}\,\mathbf{v} = \eta\,\mathbf{X}(t)\,\mathbf{v} \tag{2.5.2}$$

Eq. (2.5.2) is true due to the definition of eigenvalues and eigenvectors. Replacing Eq. (2.5.1) in Eq. (2.5.2), statement 1 is obtained. (Q.E.D.)

Proof of 2: if $\mathbf{x}(t) = e^{\Lambda t}\mathbf{p}(t)$, $\mathbf{p}(t)$ can be expressed as:

$$\mathbf{p}(t) = e^{-\Lambda t}\mathbf{x}(t) \tag{2.5.3}$$

Statement 2 is proved if it can be shown that $\mathbf{p}(t)$ is periodic of period T. Due to Eq. (2.5.2), Eq. (2.5.3) can be rewritten as:

$$\mathbf{p}(t+\mathrm{T}) = e^{-\Lambda(t+\mathrm{T})}\mathbf{x}(t+\mathrm{T}) = \eta\, e^{-\Lambda(t+\mathrm{T})}\mathbf{x}(t) = \frac{\eta}{e^{\Lambda \mathrm{T}}}\, e^{-\Lambda t}\mathbf{x}(t) \tag{2.5.4}$$

Recalling the definitions of multiplier and characteristic exponent, Eq. (2.5.4) leads to:

$$\mathbf{p}(t+\mathrm{T}) = e^{-\Lambda t}\mathbf{x}(t) \tag{2.5.5}$$

Direct comparison between Eq. (2.5.5) and Eq. (2.5.3) gives:

$$\mathbf{p}(t) = \mathbf{p}(t+\mathrm{T}) \tag{2.5.6}$$

Hence $\mathbf{p}(t)$ is a periodic function of period T. (Q.E.D.)

Theorem 2 is a variation of *Floquet Theorem*, (or *Floquet-Lyapunov Theorem*), and solution $\mathbf{x}(t) = e^{\Lambda t}\mathbf{p}(t)$ is often referred to as *Floquet-Lyapunov solution*.

2.6 Insights on the properties of the Floquet-Lyapunov solution

Eq. (2.4.7) states that characteristic exponents $\Lambda_1, \Lambda_2, \dots, \Lambda_n$ are not unique, indeed, one can provide a succession of different characteristic exponents for each of them. If Λ is the generic characteristic exponent, let Λ_z be as follows:

$$\Lambda_z = \Lambda + i\,\frac{2z\pi}{\mathrm{T}}, \qquad z \in \mathbb{Z} \tag{2.6.1}$$

Since Λ_z is a characteristic exponent in its turn, the Floquet-Lyapunov solution can take the form:

$$\mathbf{x}(t) = e^{\Lambda_z t}\mathbf{p}(t) \tag{2.6.2}$$

Replacing Eq. (2.6.1) in Eq. (2.6.2) gives:

$$\begin{aligned} \mathbf{x}(t) &= e^{\Lambda_z t}\mathbf{p}(t) = e^{\left(\Lambda + i\frac{2z\pi}{\mathrm{T}}\right)t}\mathbf{p}(t) = \\ &= e^{\Lambda t} e^{i\frac{2z\pi}{\mathrm{T}}t}\mathbf{p}(t) \quad \Rightarrow \quad \mathbf{x}(t) = e^{\Lambda t}\mathbf{f}(t), \quad \mathbf{f}(t) = e^{i\frac{2z\pi}{\mathrm{T}}t}\mathbf{p}(t) \end{aligned} \tag{2.6.3}$$

Solution $\mathbf{x}(t)$ in Eq. (2.6.3) is still a solution of Eq. (2.2.1). The function $e^{i\frac{2z\pi}{\mathrm{T}}t}$ is still periodic, indeed, recalling the Euler formula:

$$e^{i\frac{2z\pi}{\mathrm{T}}t} = \cos\left(\frac{2z\pi}{\mathrm{T}}t\right) + i\sin\left(\frac{2z\pi}{\mathrm{T}}t\right), \qquad z \neq 0 \tag{2.6.4}$$

It is useful, at this point, to recall the necessary and sufficient condition for the sum or the product of periodic functions to be periodic themselves: let *f*(*t*) and g(*t*) be two periodic functions of periods T_1 and T_2 respectively, the sum (or the product) of *f*(*t*) and g(*t*) is still periodic if, and only if, $\mathrm{T}_1/\mathrm{T}_2 \in \mathbb{Q}$, therefore, if $\mathrm{T}_1/\mathrm{T}_2 \neq 1$, the period of the sum (or the product) is equal to $LCM\left(\mathrm{T}_1, \mathrm{T}_2\right)$. It is easy to verify that the function in Eq. (2.6.4) is periodic of period $\mathrm{T}\left|z\right|^{-1}$. If $\left|z\right| \neq 1$, the fact that $\mathbf{f}(t)$ is periodic of period T is assured, because $\mathrm{T} = LCM\left(\mathrm{T}\left|z\right|^{-1}, \mathrm{T}\right)$. In the particular case where $\left|z\right| = 1$, the function $\mathbf{f}(t)$ is still periodic but it is not assured that its period is equal to T. Indeed, the only thing that can be certainly stated is that the period of $\mathbf{f}(t)$, (say $\mathrm{T}^{(f)}$), can take T as maximum value, (so $\mathrm{T}^{(f)} \leq \mathrm{T}$), and that T is an integer multiple of $\mathrm{T}^{(f)}$. The latter means that T is also a period of $\mathbf{f}(t)$. In other words, the non-uniqueness of characteristic exponents does not invalidate the statement 2 of *Theorem* 2.

While $\mathbf{p}(t)$ or $\mathbf{f}(t)$ are periodic, as proven before, nothing can be said about the periodicity of solution $\mathbf{x}(t)$ yet. Remarks on the periodicity of $\mathbf{x}(t)$ can be made by considering the Floquet multipliers instead of characteristic exponents. In order to think about the nature of solution $\mathbf{x}(t)$, let us limit ourselves to the case in which $\mathbf{A}(t)$ is real. *i.e.*:

$$\mathbf{A}(t) \in \mathbb{R}^{n\times n}, \qquad \forall t \tag{2.6.5}$$

Therefore, the monodromy matrix **B** can also be real. Let η be a complex eigenvalue of **B** (multiplier), then the conjugate of η (say η^*) is also a multiplier. Let Λ be a characteristic exponent corresponding to η, then the conjugate of Λ (say Λ^*) due to the logarithmic relation between exponents and multipliers, is still a characteristic exponent, that is:

$$\eta = e^{\Lambda\,\mathrm{T}} \quad \Leftrightarrow \quad \ln\eta = \Lambda\,\mathrm{T}$$

$$\begin{cases} \Lambda = \dfrac{1}{\mathrm{T}}\ln\eta \\ \Lambda^* = \dfrac{1}{\mathrm{T}}\ln\eta^* \end{cases} \tag{2.6.6}$$

Hence, considering the conjugate solution $\mathbf{x}^*(t) = e^{\Lambda^* t}\mathbf{p}^*(t)$, it can be concluded that:

$$\begin{cases} \Lambda = \Lambda_{\Re} + i\,\Lambda_{\Im} \\ \Lambda^* = \Lambda_{\Re} - i\,\Lambda_{\Im} \\ \mathbf{p}(t) = \mathbf{p}_{\Re}(t) + i\,\mathbf{p}_{\Im}(t) \\ \mathbf{p}^*(t) = \mathbf{p}_{\Re}(t) - i\,\mathbf{p}_{\Im}(t) \end{cases} \tag{2.6.7}$$

where subscripts $\Re$ and $\Im$ stand for real and imaginary part respectively. Therefore, according to statement 2 of *Theorem* 2, solution $\mathbf{x}(t)$ and its conjugate $\mathbf{x}^*(t)$ can be rewritten as:

$$\begin{cases} \mathbf{x}(t) = e^{(\Lambda_{\Re}+i\,\Lambda_{\Im})t}\left[\mathbf{p}_{\Re}(t) + i\,\mathbf{p}_{\Im}(t)\right] = \\ \qquad = e^{\Lambda_{\Re}\,t}\left\{\mathbf{p}_{\Re}(t)\cos(\Lambda_{\Im}\,t) - \mathbf{p}_{\Im}(t)\sin(\Lambda_{\Im}\,t) + i\left[\mathbf{p}_{\Im}(t)\cos(\Lambda_{\Im}\,t) + \mathbf{p}_{\Re}(t)\sin(\Lambda_{\Im}\,t)\right]\right\} \\ \mathbf{x}^{*}(t) = e^{(\Lambda_{\Re}-i\,\Lambda_{\Im})t}\left[\mathbf{p}_{\Re}(t) - i\,\mathbf{p}_{\Im}(t)\right] = \\ \qquad = e^{\Lambda_{\Re}\,t}\left\{\mathbf{p}_{\Re}(t)\cos(\Lambda_{\Im}\,t) - \mathbf{p}_{\Im}(t)\sin(\Lambda_{\Im}\,t) - i\left[\mathbf{p}_{\Im}(t)\cos(\Lambda_{\Im}\,t) + \mathbf{p}_{\Re}(t)\sin(\Lambda_{\Im}\,t)\right]\right\} \end{cases} \tag{2.6.8}$$

The solutions in Eq. (2.6.8) are linearly independent, however, in order to obtain a real solution, the superposition principle can be taken into account, *e.g.*:

$$\hat{\mathbf{x}}(t) = \mathbf{x}(t) + \mathbf{x}^{*}(t) = 2e^{\Lambda_{\Re}\,t}\left[\mathbf{p}_{\Re}(t)\cos(\Lambda_{\Im}\,t) - \mathbf{p}_{\Im}(t)\sin(\Lambda_{\Im}\,t)\right] \tag{2.6.9}$$

where $\hat{\mathbf{x}}(t)$ is a possible linear combination of the solutions in Eq. (2.6.8). Alternatively, even the real and imaginary parts of $\mathbf{x}(t)$ can be separately taken as independent solutions. It is clear, according to Eq. (2.6.8) and Eq. (2.6.9), that, in general, the Floquet-Lyapunov solution is non-periodic even if Λ is purely imaginary. More specifically, the necessary and sufficient condition for the sum or the product of periodic functions to be periodic themselves is not automatically satisfied. Indeed, nothing can be said, *a priori*, about the period of $\cos(\Lambda_{\Im}\,t)$, or $\sin(\Lambda_{\Im}\,t)$.

2.7 The structure of solutions of systems with periodic coefficients

Let $\mathbf{\Lambda}$ be a matrix such that:

$$\mathbf{\Lambda} = \frac{1}{\mathrm{T}}\ln\left[\mathbf{X}(\mathrm{T})\right] = \frac{1}{\mathrm{T}}\ln\left[\mathbf{B}\right] \tag{2.7.1}$$

The eigenvalue of $\mathbf{\Lambda}$ are, by definition, the characteristic exponents. Now consider a non-singular matrix **S** such that:

$$\mathbf{Q} = \mathbf{S}^{-1}\mathbf{\Lambda}\,\mathbf{S} \tag{2.7.2}$$

in which **Q** is the Jordan canonical form of $\mathbf{\Lambda}$. Taking into account the generic elementary Jordan block $\mathbf{Q}_k\left(\Lambda_k\right)$ relative to the root Λ_k of the characteristic polynomial of $\mathbf{\Lambda}$:

$$\begin{cases} \mathbf{\Lambda}\,\mathbf{F}_k = \mathbf{F}_k\mathbf{Q}_k\left(\Lambda_k\right), \quad k = 1, \ldots, \mathcal{S} \\ \mathbf{F}_k = \left\{\ \mathbf{f}_1^{(k)} \quad \mathbf{f}_2^{(k)} \quad \ldots \quad \mathbf{f}_{m_k}^{(k)}\ \right\} \end{cases} \tag{2.7.3}$$

where $\mathcal{S}$ is the number of simple cyclic subspaces (relative to $\mathbf{\Lambda}$) in which the whole complex vector-space splits, while $\mathbf{F}_k$ is a rectangular $n \times m_k$ matrix, whose columns form a basis (these vectors are linearly independent) for the *k*-th subspace of dimension m_k. The $m_k \times m_k$ cell $\mathbf{Q}_k\left(\Lambda_k\right)$ takes the form:

$$\mathbf{Q}_k\left(\Lambda_k\right)=\begin{bmatrix} \Lambda_k & 1 & 0 & \cdots & 0 \\ 0 & \Lambda_k & 1 & \cdots & 0 \\ \cdots & \cdots & \cdots & \cdots & \cdots \\ 0 & 0 & 0 & \cdots & 1 \\ 0 & 0 & 0 & \cdots & \Lambda_k \end{bmatrix} \tag{2.7.4}$$

Thus, **S** and **Q** can be expressed as:

$$\begin{cases} \mathbf{S}=\left\{ \mathbf{F}_1 \quad \mathbf{F}_2 \quad \ldots \quad \mathbf{F}_{\mathcal{S}} \right\}= \\ \quad =\left\{ \mathbf{f}_1^{(1)} \quad \mathbf{f}_2^{(1)} \quad \ldots \quad \mathbf{f}_{m_1}^{(1)} \; \mathbf{f}_1^{(2)} \quad \mathbf{f}_2^{(2)} \quad \ldots \quad \mathbf{f}_{m_2}^{(2)} \; \ldots \; \mathbf{f}_1^{(\mathcal{S})} \quad \mathbf{f}_2^{(\mathcal{S})} \quad \ldots \quad \mathbf{f}_{m_{\mathcal{S}}}^{(\mathcal{S})} \right\} \\ \mathbf{Q}=diag\left[\mathbf{Q}_1\left(\Lambda_1\right),\mathbf{Q}_2\left(\Lambda_2\right),\ldots\mathbf{Q}_{\mathcal{S}}\left(\Lambda_{\mathcal{S}}\right)\right] \end{cases} \tag{2.7.5}$$

Definition (*elementary divisor*): for each elementary Jordan block as in Eq. (2.7.4), it can be written that:

$$\det\left[\Lambda\,\mathbf{I}_{m_k}-\mathbf{Q}_k\left(\Lambda_k\right)\right]=\left(\Lambda-\Lambda_k\right)^{m_k} \tag{2.7.6}$$

Hence, since **Q** is the direct sum of the cells $\mathbf{Q}_k\left(\Lambda_k\right)$, as in Eq. (2.7.4), it can be stated that:

$$\det\left[\Lambda\,\mathbf{I}-\mathbf{\Lambda}\right]=\prod_{k=1}^{\mathcal{S}}\left(\Lambda-\Lambda_k\right)^{m_k} \tag{2.7.7}$$

The quantities $\left(\Lambda-\Lambda_k\right)^{m_k}$ are the *elementary divisors* of $\mathbf{\Lambda}$, whose number is $\mathcal{S}$, exactly the number of cyclic subspaces. Some Λ_k in Eq. (2.7.7) can coincide, thus to each root of the characteristic equation $\det\left[\mathbf{\Lambda}-\Lambda\,\mathbf{I}\right]=0$ may correspond several elementary divisors. The sum of the exponents of the elementary divisors corresponding to the same root, is equal to the algebraic multiplicity of the root. While, the number of blocks related to the same root, is equal to the geometric multiplicity of the root. If, for the *k*-th divisor, $m_k=1$, then the divisor is said to be *simple*. Notice that a multiple root can have simple elementary divisors and if all the elementary divisors are simple, *i.e.*:

$$\begin{cases} \mathcal{S}=n \\ m_1=m_2=\ldots=m_{\mathcal{S}}=1 \end{cases} \tag{2.7.8}$$

then **Q** is diagonal and the algebraic and geometric multiplicities coincide.

All the definitions and the passages given in the present section can be retraced considering the multipliers instead of characteristic exponents.
The definition of elementary divisors is of paramount importance in order to accurately describe the structure of solutions of system in Eq. (2.2.1), indeed, taking into account the elementary divisors, it can be stated that the fundamental set of solutions splits in $\mathcal{S}$ groups of the form:

$$\begin{cases} \mathbf{x}_1^{(k)}(t) = e^{\Lambda_k t}\mathbf{p}_1^{(k)}(t) \\ \mathbf{x}_2^{(k)}(t) = e^{\Lambda_k t}\left[t\,\mathbf{p}_1^{(k)}(t) + \mathbf{p}_2^{(k)}(t)\right] \\ \vdots \\ \mathbf{x}_{m_k}^{(k)}(t) = e^{\Lambda_k t}\left[\dfrac{t^{m_k-1}}{(m_k-1)!}\mathbf{p}_1^{(k)}(t) + \dfrac{t^{m_k-2}}{(m_k-2)!}\mathbf{p}_2^{(k)}(t) + \ldots + \mathbf{p}_{m_k}^{(k)}(t)\right] \end{cases}, \quad \begin{cases} k = 1, \ldots, \mathcal{S} \\ \displaystyle\sum_{k=1}^{\mathcal{S}} m_k = n \end{cases} \tag{2.7.9}$$

If all the elementary divisors associated to Λ_k are simple, then all the groups of solutions that correspond to Λ_k reduce to groups made of only one solution, which has the form of the Floquet-Lyapunov solution.

2.8 Preliminary considerations on the stability of the solution

As said in the previous sections, Floquet multipliers are an intrinsic property of the system in Eq. (2.2.1). In particular, the knowledge of Floquet multipliers returns all the information regarding the stability of the solution. As stated in Eq. (2.6.5), let the matrix of the coefficients be real, as well as **B**. So, Floquet multipliers are complex or real valued, and if they are complex, they also occur in conjugate pairs. The multipliers must fall into one of the following cases:

$$\begin{cases} |\eta| < 1 \\ |\eta| = 1 \\ |\eta| > 1 \end{cases} \tag{2.8.1}$$

Case $|\eta| < 1$:

$$|\eta| < 1 \quad \Leftrightarrow \quad \left|e^{\Lambda \mathrm{T}}\right| < 1 \tag{2.8.2}$$

Since $\mathrm{T} \in \mathbb{R}$, it can be stated that:

$$\left|e^{\Lambda \mathrm{T}}\right| = e^{\Lambda_{\Re} \mathrm{T}} < 1 \tag{2.8.3}$$

where, as said before, $\Lambda_{\Re} = \Re(\Lambda)$, therefore, recalling that it was assumed that T is positive, Eq. (2.8.3) yields:

$$|\eta| < 1 \quad \Leftrightarrow \quad \Lambda_{\Re} < 0 \tag{2.8.4}$$

which means that solution $\mathbf{x}(t)$ is asymptotically stable. In other terms, if η, in the Argand-Gauss plane, lies within the unit circle centered in the origin of the axes, then $\mathbf{x}(t)$ is asymptotically stable.

Case $|\eta| = 1$:

$$|\eta| = 1 \quad \Leftrightarrow \quad e^{\Lambda_{\Re}\,\mathrm{T}} = 1 \quad \Leftrightarrow \quad \Lambda_{\Re} = 0 \tag{2.8.5}$$

hence, in this case, η lies on the unit circle centered in the origin and the solution is bounded (merely stable or simply stable) if all the elementary divisors of Λ are simple, or unstable (amplitude grows as powers) if there is at least one multiple elementary divisor associated to Λ.

Case $|\eta| > 1$:

$$|\eta| > 1 \quad \Leftrightarrow \quad e^{\Lambda_{\Re}\,\mathrm{T}} > 1 \quad \Leftrightarrow \quad \Lambda_{\Re} > 0 \tag{2.8.6}$$

Finally, if $|\eta| > 1$, η lies outside the unit circle and the solution is unstable.
It is also possible for a multiplier to be purely real. In the case of real multipliers, the relations contained in Eq. (2.8.4), Eq. (2.8.5) and Eq. (2.8.6) remain valid. It is important to highlight the following special case:

$$\eta \in \mathbb{R}, \quad |\eta| = 1 \quad \Rightarrow \quad \begin{cases} \eta = 1 \\ \eta = -1 \end{cases} \tag{2.8.7}$$

Special case $\eta = 1$:

$$\begin{cases} \eta = 1 \quad \Leftrightarrow \quad e^{\Lambda\,\mathrm{T}} = 1 \quad \Leftrightarrow \quad \Lambda\,\mathrm{T} = 0 \\ \mathrm{T} \neq 0 \quad \Rightarrow \quad \Lambda = 0 \quad \Leftrightarrow \quad \mathbf{x}(t) = \mathbf{p}(t) \end{cases} \tag{2.8.8}$$

Hence, if $\eta = 1$ then $\mathbf{x}(t)$ is bounded and periodic of period T.

Special case $\eta = -1$:

$$\begin{cases} \eta = -1 \quad \Leftrightarrow \quad e^{\Lambda\,\mathrm{T}} = -1 \quad \Leftrightarrow \quad \Lambda\,\mathrm{T} = \pm\, i\pi \\ \mathrm{T} \neq 0 \quad \Rightarrow \quad \Lambda = \pm\dfrac{i\pi}{\mathrm{T}} \quad \Leftrightarrow \quad \mathbf{x}(t) = e^{\pm\frac{i\pi}{\mathrm{T}}\mathrm{t}}\,\mathbf{p}(t) \end{cases} \tag{2.8.9}$$

In this special case $\mathbf{x}(t)$ is bounded and periodic of period 2T, because the necessary and sufficient condition for the the product of periodic functions to be periodic itself is satisfied and $2\mathrm{T} = LCM\left(\mathrm{T}, 2\mathrm{T}\right)$. The special cases in Eq. (2.8.8) and Eq. (2.8.9) can be generalized to complex multipliers that lie on the unit circle ($|\eta| = 1$). As it was proven in Eq. (2.8.5), unitary

moduli in Floquet multipliers means purely imaginary characteristic exponents, so the set of bounded solutions is the union of periodic and quasi-periodic solutions and the set of periodic solutions is dense in that of bounded solutions, like $\mathbb{Q}$ is dense in $\mathbb{R}$.
The previous results are summarized in Table 2.1 and Fig. 2.1

Table 2.1 Floquet multipliers-stability relation

η	Λ	$\mathbf{x}(t)$
$\lvert\eta\rvert < 1$	$\Lambda_{\Re} < 0$	Asymptotically stable
$\lvert\eta\rvert = 1$ with simple divisors	$\Lambda_{\Re} = 0$	Bounded
$\lvert\eta\rvert = 1$ with multiple divisors	$\Lambda_{\Re} = 0$	Unstable
$\lvert\eta\rvert > 1$	$\Lambda_{\Re} > 0$	Unstable

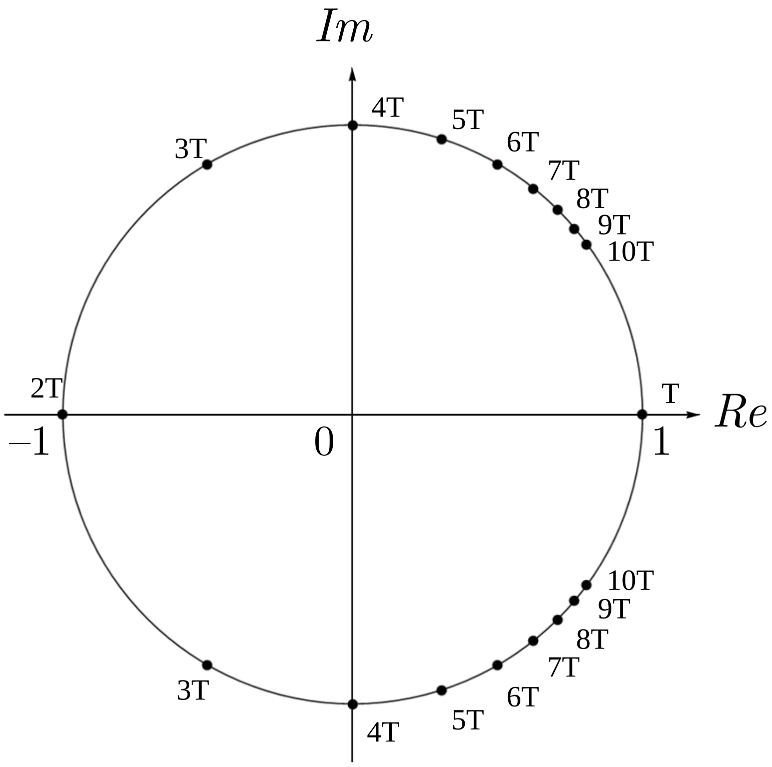

Figure 2.1: Floquet multipliers corresponding to some periodic solutions.

3 ROTATING SHAFTS UNDER COMBINED CONSTANT AXIAL AND TORSIONAL LOADS

3.1 Introduction

In this Chapter further insights are proposed in the analysis of a distributed parameter model of a high-speed, power transmitting flexible rotor. A homogeneous uniform Timoshenko straight beam with circular section is considered, spinning with constant angular speed about its longitudinal axis on isotropic supports (rigid bearings), and subjected simultaneously to constant end thrust and twisting moment. A novel contribution is given in the development of complete modal analysis of the model under study. After clarifying the properties of the operators involved and the relation between eigensolutions obtained for complex and real displacement variables, modal analysis of the rotating shaft is then completed using real displacement variables in both the configuration space and in the state-space, including the derivation of critical loads due to combined effects of axial end thrust and twisting moment. In addition, such analytical developments allow to cast new light on the problem of existence and identification of the second frequency spectrum in the Timoshenko beam theory [90], here reconsidered from a novel perspective.

New evidence of existence of the second spectrum together with a novel definition for its identification are presented, only possible if considering gyroscopic effects, therefore a rotating beam. In parallel, the role of the so-called cut-off Timoshenko beam frequencies [92] is investigated, extending their definition to include the effects of gyroscopic moments and external loads.

3.2 Model description and nomenclature

The model is characterized by the following parameters:

$$\begin{aligned}
&A = \pi r^2 = \text{cross-sectional area } [\mathrm{m}^2] \\
&l = \text{length of the shaft } [\mathrm{m}] \\
&E = \text{Young's modulus } [\mathrm{N/m}^2] \\
&G = \text{shear elasticity modulus } [\mathrm{N/m}^2] \\
&I_y = I_z = J = \text{moment of inertia of the cross-section } [\mathrm{m}^4] \\
&I_x = 2J = \text{polar moment of inertia of the cross-section } [\mathrm{m}^4] \\
&\kappa = \text{transverse shear factor} \\
&N = \text{axial end thrust } [\mathrm{N}] \\
&T = \text{axial end twisting moment } [\mathrm{Nm}] \\
&\nu = \text{Poisson's ratio} \\
&\rho = \text{density } [\mathrm{Kg/m}^3] \\
&\omega = \text{rotating angular speed } [\mathrm{rad/s}]
\end{aligned} \tag{3.2.1}$$

The external loads N (positive if tensile) and T (positive if counterclockwise) are assumed constant with respect to time. Isotropic supports are considered, making the whole model axisymmetric. Hence it can be represented in a non-rotating coordinate system as shown in Fig. 3.1. Additional nomenclature includes:

$$\begin{aligned}
&u, v, w = \text{displacements in the } x, y, z \text{ directions, respectively [m]}\\
&\mathrm{w} = v + iw = \text{complex displacement [m]}\\
&\vartheta_x, \vartheta_y, \vartheta_z = \text{angular displacements about the } x, y, z \text{ axes, respectively [rad]}\\
&\theta = \vartheta_y + i\vartheta_z = \text{complex angular displacement [rad]}
\end{aligned} \tag{3.2.2}$$

In next sections a simplified notation for partial derivatives is adopted, dots denoting differentiation with respect to time as in Chapter 2 and roman numbers denoting differentiation with respect to the spatial coordinate x.

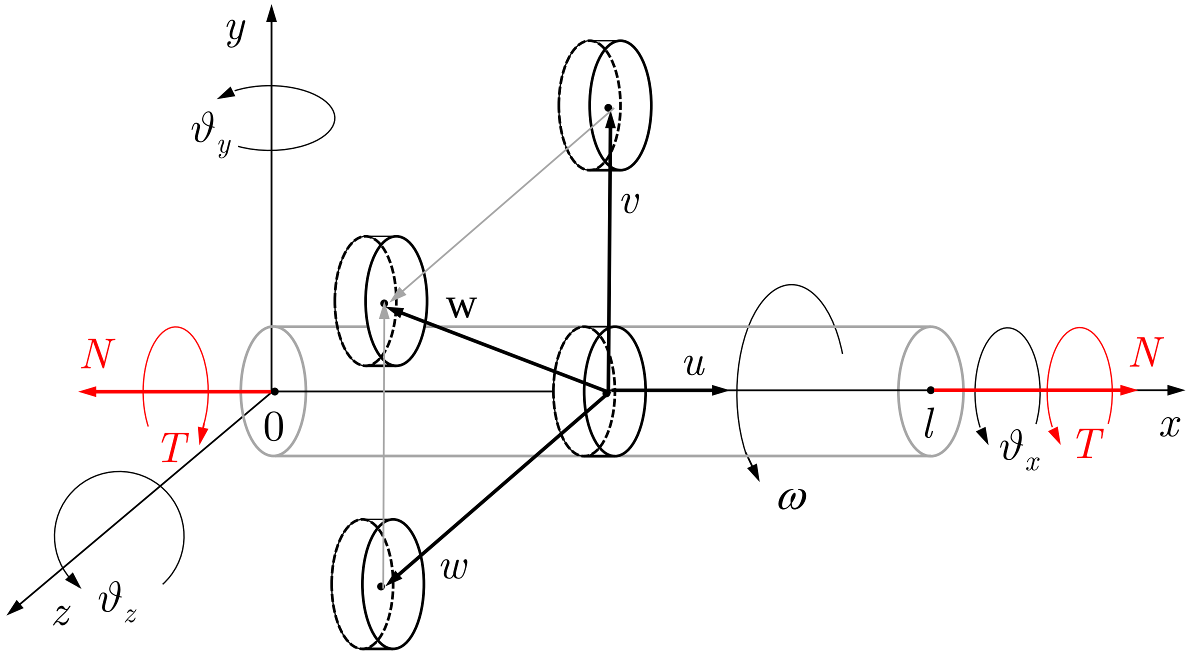

Figure 3.1: Schematic representation of displacements

3.3 Newtonian formulation of the equations of motion

The linear equations of motion of the loaded rotating shaft are obtained with Newtonian formulation, referring to the nomenclature introduced in Section 3.2 and to the equilibrium schemes for a section of infinitesimal length dx reported in Fig. 3.2 to 3.6.

The x-direction translational and rotational well-known equations of motion are decoupled:

$$\begin{cases} F_x + [H(x) - H(x-l)]N = EAu^{\mathrm{I}} \\ F_x^{\mathrm{I}} = \rho A \ddot{u} \end{cases} \tag{3.3.1}$$

And:

$$\begin{cases} M_x + [H(x) - H(x-l)]T = 2GJ\vartheta_x^{\mathrm{I}} \\ M_x^{\mathrm{I}} = 2\rho J \ddot{\vartheta}_x \end{cases} \tag{3.3.2}$$

where $H(\cdot)$ represents the Heaviside unit step distribution. The equation of motion describing the flexural behavior in the x-y plane can be written starting from the expression of the shear angle γ_z (caused by the shear force F_y) in terms of ϑ_z, v^{I} and of the shear angle β_z (caused by the external action N), according to the schemes reported in Fig. 3.2 and 3.3, right side:

$$\begin{cases} \vartheta_z + \gamma_z + \beta_z = v^{\mathrm{I}} \\ \gamma_z = \dfrac{F_y}{\kappa GA} \\ \beta_z = -\dfrac{N\vartheta_z}{\kappa GA} \end{cases} \quad \Rightarrow \quad \vartheta_z = \frac{1}{\psi}\left(v^{\mathrm{I}} - \frac{F_y}{\kappa GA} \right), \quad \psi = 1 - \frac{N}{\kappa GA} \tag{3.3.3}$$

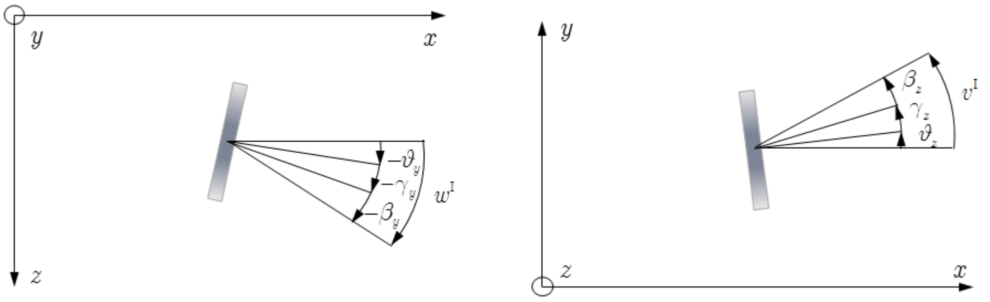

Figure 3.2: Shear deformation scheme

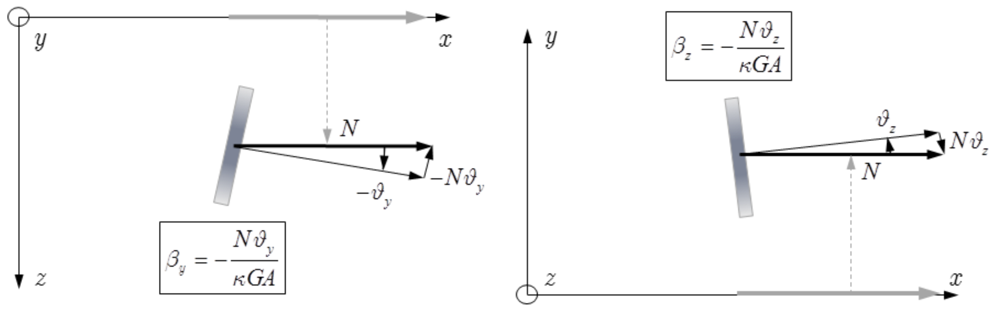

Figure 3.3: Axial thrust N

The constitutive equation for F_y given by Eq. (3.3.3) together with the y-direction translational dynamic equilibrium (Fig. 3.4, right side) yield the following differential link between ϑ_z and v:

$$\begin{cases} F_y = \kappa G A (v^{\mathrm{I}} - \psi \vartheta_z) \\ F_y^{\mathrm{I}} = \rho A \ddot{v} \end{cases} \quad \Rightarrow \quad \vartheta_z^{\mathrm{I}} = \frac{1}{\psi}\left(v^{\mathrm{II}} - \frac{\rho}{\kappa G} \ddot{v} \right) \tag{3.3.4}$$

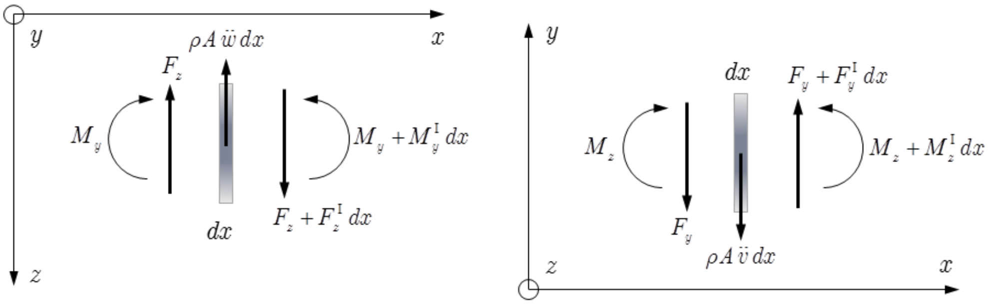

Figure 3.4: Euler-Bernoulli model

Taking into account the effects of *N* and *T* in the constitutive equation for the bending moment M_z (Fig. 3.3 and 3.6, right side) together with the rotational dynamic equilibrium in the x-y plane (Fig. 3.4 and 3.5, right side) gives:

$$\begin{cases} M_z + T\vartheta_y + N\,v = EJ\vartheta_z^{\mathrm{I}} \\ M_z^{\mathrm{I}} + F_y = \rho J \ddot{\vartheta}_z - 2\rho J \omega \dot{\vartheta}_y \end{cases} \quad \Rightarrow \quad EJ\vartheta_z^{\mathrm{II}} - T\vartheta_y^{\mathrm{I}} - N\,v^{\mathrm{I}} + F_y = \rho J \ddot{\vartheta}_z - 2\rho J \omega \dot{\vartheta}_y \tag{3.3.5}$$

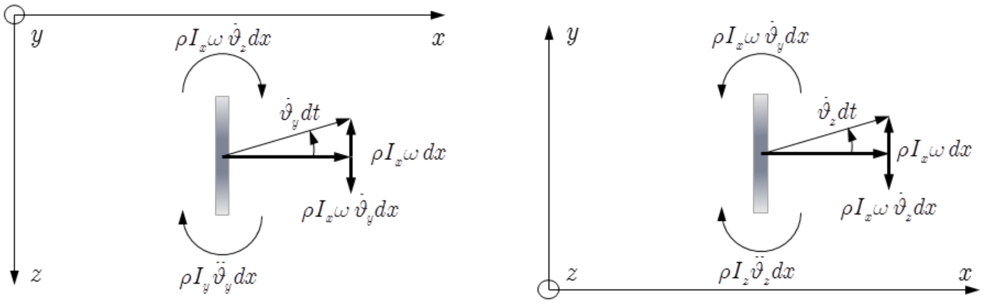

Figure 3.5: Rayleigh model (additional inertial effects only)

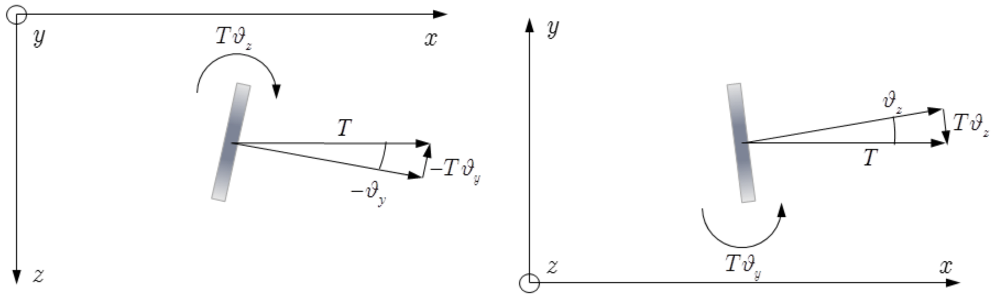

Figure 3.6: Axial twisting moment T

Finally, differentiating Eq. (3.3.4) and introducing the expression of F_y given by Eq. (3.3.4) leads to the equation of motion in the form:

$$EJ\vartheta_z^{\mathrm{III}} - T\vartheta_y^{\mathrm{II}} - N v^{\mathrm{II}} + \rho A\ddot{v} - \rho J\ddot{\vartheta}_z^{\mathrm{I}} + 2\rho J\omega\dot{\vartheta}_y^{\mathrm{I}} = 0 \tag{3.3.6}$$

The equation of motion describing the flexural behaviour in the x-z plane can be written following the same steps, paying attention to sign conventions (Fig. 3.4 to 3.6, left side):

$$EJ\vartheta_y^{\mathrm{III}} + T\vartheta_z^{\mathrm{II}} + N w^{\mathrm{II}} - \rho A\ddot{w} - \rho J\ddot{\vartheta}_y^{\mathrm{I}} - 2\rho J\omega\dot{\vartheta}_z^{\mathrm{I}} = 0 \tag{3.3.7}$$

The flexural degrees of freedom in the x-y and x-z planes are coupled due to both gyroscopic and axial twisting moments. Distributed external loads along the x coordinate could be considered introducing non-homogeneous terms in Eq. (3.3.6) and (3.3.7) [11].

3.4 Lagrangian formulation of the equations of motion

The same linear equations of motion of the loaded rotating shaft are obtained by applying Hamilton's principle to a Lagrangian density function $\mathcal{L} = \mathcal{T} - \mathcal{V} + \mathcal{W}$, written in terms of kinetic energy density $\mathcal{T}$, potential energy density $\mathcal{V}$ and associating a work density $\mathcal{W}$ to the external loads, which are not derivable from a potential.
Referring to the nomenclature introduced in Section 3.2, the kinetic energy density is derived first, along an alternative method with respect to standard formulations.

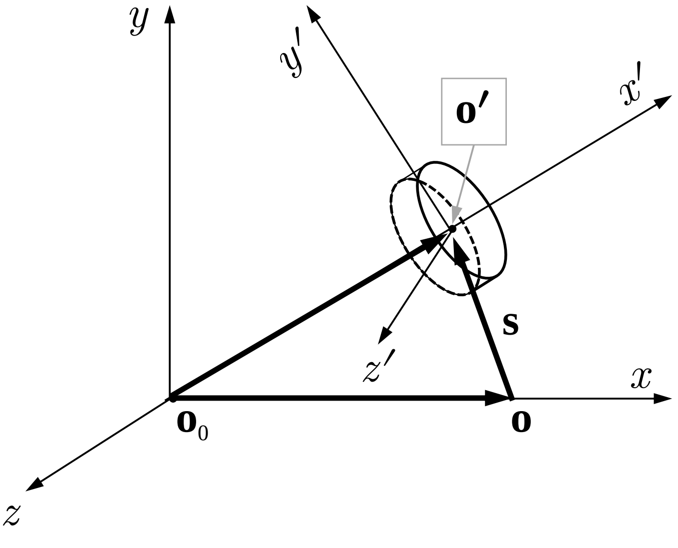

Figure 3.7: Reference systems (fixed and floating) for a cross-section of infinitesimal length dx

A cross-section of infinitesimal length dx is considered, as represented in Fig. 3.7 with two coordinate systems, inertial (x,y,z) and floating (x',y',z'). The velocity of the center of gravity $(\mathbf{o}')$ of the cross-section is given by:

$$\mathbf{o}' = \mathbf{o} + \mathbf{s}, \quad \dot{\mathbf{o}}' = \dot{\mathbf{s}} = \left\{\dot{u}, \dot{v}, \dot{w}\right\}^{\mathrm{T}} \tag{3.4.1}$$

The absolute angular velocity of the cross-section $\boldsymbol{\omega}$, represented in the floating coordinate system, is the sum of a component $\boldsymbol{\omega}_0$ given by the rotating angular speed of the shaft, plus a relative component $\boldsymbol{\omega}_r$, according to:

$$\begin{cases} \boldsymbol{\omega} = \boldsymbol{\omega}_0 + \boldsymbol{\omega}_r \\ \boldsymbol{\omega}_0 = \{\omega, 0, 0\}^{\mathrm{T}} \\ \tilde{\boldsymbol{\omega}}_r = \mathbf{R}^{\mathrm{T}}\,\dot{\mathbf{R}} \end{cases} \tag{3.4.2}$$

where $\tilde{\boldsymbol{\omega}}_r$ is written in skew-symmetric matrix form and $\mathbf{R}$ is its associate rotation matrix. Since the first-order approximation of $\mathbf{R}$ would lead to an incomplete expression of the kinetic energy (lacking of gyroscopic terms), a second-order approximation for small rotations is required. Therefore, the first-order approximation $\mathbf{R}^{(1)}$ is expanded by addition of (small) second-order terms, say ε:

$$\mathbf{R}^{(1)} = \begin{bmatrix} 1 & -\vartheta_z & \vartheta_y \\ \vartheta_z & 1 & -\vartheta_x \\ -\vartheta_y & \vartheta_x & 1 \end{bmatrix} \quad \Rightarrow \quad \mathbf{R}^{(2)} = \begin{bmatrix} 1-\varepsilon_{11} & -\vartheta_z + \varepsilon_{12} & \vartheta_y + \varepsilon_{13} \\ \vartheta_z + \varepsilon_{21} & 1-\varepsilon_{22} & -\vartheta_x + \varepsilon_{23} \\ -\vartheta_y + \varepsilon_{31} & \vartheta_x + \varepsilon_{32} & 1-\varepsilon_{33} \end{bmatrix} \tag{3.4.3}$$

As an alternative method to Taylor expansions of trigonometric terms due to selected (arbitrary) sequences of basic rotations (leading to non-univocal results, as discussed in [3]), here the ε terms are simply determined by requiring that: *i*) the second-order approximation $\mathbf{R}^{(2)}$ must respect the properties of a rotation matrix; *ii*) among all possible choices, the selected $\mathbf{R}^{(2)}$ is the closest to $\mathbf{R}^{(1)}$ (and therefore it is univocally determined). Imposing unit norm to all the columns of $\mathbf{R}^{(2)}$ in Eq. (3.4.3), and neglecting all terms of order higher than two, yields:

$$\begin{cases} \varepsilon_{11} = \dfrac{1}{2}(\vartheta_y^2 + \vartheta_z^2) \\ \varepsilon_{22} = \dfrac{1}{2}(\vartheta_x^2 + \vartheta_z^2) \\ \varepsilon_{33} = \dfrac{1}{2}(\vartheta_x^2 + \vartheta_y^2) \end{cases} \tag{3.4.4}$$

Introducing the expressions given by Eq. (3.4.4) into $\mathbf{R}^{(2)}$, then imposing the linear independency of all its columns, and neglecting again all terms of order higher than two, three further equations are written in the unknowns ε_{hk}, admitting an infinite set of solutions. For satisfying the request of minimal variations with respect to $\mathbf{R}^{(1)}$, equal values $\varepsilon_{hk} = \varepsilon_{kh}$ are selected, yielding:

$$\begin{cases} \varepsilon_{21} = \varepsilon_{21} = \dfrac{1}{2}\vartheta_x\vartheta_y \\ \varepsilon_{31} = \varepsilon_{13} = \dfrac{1}{2}\vartheta_x\vartheta_z \\ \varepsilon_{32} = \varepsilon_{23} = \dfrac{1}{2}\vartheta_y\vartheta_z \end{cases} \tag{3.4.5}$$

Hence the resulting second-order rotation matrix $\mathbf{R}^{(2)}$ takes the form:

$$\mathbf{R}=\begin{bmatrix} 1-\dfrac{1}{2}(\vartheta_y{}^2+\vartheta_z{}^2) & -\vartheta_z+\dfrac{1}{2}\vartheta_x\vartheta_y & \vartheta_y+\dfrac{1}{2}\vartheta_x\vartheta_z \\ \vartheta_z+\dfrac{1}{2}\vartheta_x\vartheta_y & 1-\dfrac{1}{2}(\vartheta_x{}^2+\vartheta_z{}^2) & -\vartheta_x+\dfrac{1}{2}\vartheta_y\vartheta_z \\ -\vartheta_y+\dfrac{1}{2}\vartheta_x\vartheta_z & \vartheta_x+\dfrac{1}{2}\vartheta_y\vartheta_z & 1-\dfrac{1}{2}(\vartheta_x{}^2+\vartheta_y{}^2) \end{bmatrix} \tag{3.4.6}$$

As pointed in *i*), **R** must respect all the properties of a rotation matrix. It only remain to check that the determinant of **R** is equal to 1:

$$\det\left[\mathbf{R}\right]=1+\frac{1}{4}\left(\vartheta_x{}^4+\vartheta_y{}^4+\vartheta_z{}^4\right)+\frac{1}{2}(\vartheta_x{}^2\vartheta_y{}^2+\vartheta_x{}^2\vartheta_z{}^2+\vartheta_y{}^2\vartheta_z{}^2) \tag{3.4.7}$$

Eq. (3.4.7) shows that $\det\left[\mathbf{R}\right]$ is unitary to less than terms of fourth-order. It means that **R** satisfies *i*) up to the second-order approximation.

Recalling Eq. (3.4.1) and (3.4.2), the kinetic energy density $\mathcal{T}$ of a cross-section of infinitesimal length dx can then be written as:

$$\mathcal{T}=\frac{1}{2}\rho(A\dot{\mathbf{s}}^{\mathrm{T}}\dot{\mathbf{s}}+\boldsymbol{\omega}^{\mathrm{T}}\mathbf{J}\,\boldsymbol{\omega}) \tag{3.4.8}$$

where **J** is the cross-section tensor of inertia, consisting of a constant diagonal matrix with elements $\mathbf{J}_{11} = 2J$ and $\mathbf{J}_{22} = \mathbf{J}_{33} = J$. Developing the calculations, and truncating the result to second-order terms, yields the approximate expression of the kinetic energy density as:

$$\mathcal{T}=\frac{1}{2}\rho\left[A(\dot{u}^2+\dot{v}^2+\dot{w}^2)+J(2\dot{\vartheta}_x^2+\dot{\vartheta}_y^2+\dot{\vartheta}_z^2)+2J\omega^2+4J\omega\dot{\vartheta}_x+2J\omega(\vartheta_z\dot{\vartheta}_y-\vartheta_y\dot{\vartheta}_z)\right] \tag{3.4.9}$$

According to [3, 12, 77] the potential energy density reads:

$$\mathcal{V}=\frac{1}{2}\left\{EA(u^{\mathrm{I}})^2+EJ\left[(\vartheta_y^{\mathrm{I}})^2+(\vartheta_z^{\mathrm{I}})^2\right]+\kappa GA\left[(-w^{\mathrm{I}}-\vartheta_y)^2+(v^{\mathrm{I}}-\vartheta_z)^2\right]+2JG(\vartheta_x^{\mathrm{I}})^2\right\} \tag{3.4.10}$$

The inclusion of external loads N and T in the rotating Timoshenko beam model is debated in the literature, leading to different forms of the equations of motion [9, 12, 14, 77]. Here the following expression of the work density is adopted:

$$\begin{aligned}\mathcal{W} = {} & \frac{1}{2}\left\{T(\vartheta_y\vartheta_z^{\mathrm{I}} - \vartheta_y^{\mathrm{I}}\vartheta_z) - N\left[(v^{\mathrm{I}})^2 - (v^{\mathrm{I}} - \vartheta_z)^2 + (w^{\mathrm{I}})^2 - (-w^{\mathrm{I}} - \vartheta_y)^2\right]\right\} + \\ & + [\delta(x-l) - \delta(x)][Nu + T\vartheta_x]\end{aligned} \tag{3.4.11}$$

where $\delta(\cdot)$ represents the Dirac distribution. In Eq. (3.4.11), the first term (related to T) can be immediately obtained referring to the schemes reported in Fig. 3.6, noticing that its expression is not unique (due to symmetry), in the sense that it could be written in a more general form as:

$$\mathcal{W}_T = T(c_1\vartheta_y\vartheta_z^{\mathrm{I}} - c_2\vartheta_y^{\mathrm{I}}\vartheta_z), \quad c_1 \in [0,1], \quad c_2 = 1 - c_1 \tag{3.4.12}$$

leading in any case to the same equations of motion. Similar remarks also apply to the gyroscopic terms in the kinetic energy density, Eq. (3.4.9), as explained in detail in [3]. The second term in Eq. (3.4.11) (related to N) is derived according with [12] taking into account the axial geometric shortening of the shaft, which ensures consistency with the Timoshenko beam model. Introducing Eq. (3.4.9) to (3.4.11) in Lagrange's equations for a continuous second-order one-dimensional problem:

$$\begin{cases}\dfrac{\partial}{\partial t}\left(\dfrac{\partial \mathcal{L}}{\partial \dot{q}_t}\right) + \dfrac{\partial}{\partial x}\left(\dfrac{\partial \mathcal{L}}{\partial q_t^{\mathrm{I}}}\right) - \dfrac{\partial \mathcal{L}}{\partial q_t} = 0 \\ \mathbf{q}_t = \left\{u, v, w, \vartheta_x, \vartheta_y, \vartheta_z\right\}^{\mathrm{T}}\end{cases} \tag{3.4.13}$$

yields the following six equations of motion:

$$\begin{cases}\rho A\ddot{u} - EAu^{\mathrm{II}} - [\delta(x-l) - \delta(x)]N = 0 \\ \rho A\ddot{v} - \kappa GA(v^{\mathrm{II}} - \vartheta_z^{\mathrm{I}}) - N\vartheta_z^{\mathrm{I}} = 0 \\ \rho A\ddot{w} - \kappa GA(w^{\mathrm{II}} + \vartheta_y^{\mathrm{I}}) + N\vartheta_y^{\mathrm{I}} = 0 \\ 2\rho J\ddot{\vartheta}_x - 2GJ\vartheta_x^{\mathrm{II}} - [\delta(x-l) - \delta(x)]T = 0 \\ \rho J\ddot{\vartheta}_y + 2\rho J\omega\dot{\vartheta}_z + \kappa GA(w^{\mathrm{I}} + \vartheta_y) - EJ\vartheta_y^{\mathrm{II}} - T\vartheta_z^{\mathrm{I}} - N(w^{\mathrm{I}} + \vartheta_y) = 0 \\ \rho J\ddot{\vartheta}_z - 2\rho J\omega\dot{\vartheta}_y - \kappa GA(v^{\mathrm{I}} - \vartheta_z) - EJ\vartheta_z^{\mathrm{II}} + T\vartheta_y^{\mathrm{I}} + N(v^{\mathrm{I}} - \vartheta_z) = 0\end{cases} \tag{3.4.14}$$

The first and fourth of Eq. (3.4.14) are decoupled, representing the x-direction translational and rotational dynamic equilibrium equations respectively. The other four equations, representing the flexural dynamic equilibrium of the shaft, are rewritten in a more compact form introducing the parameter ψ, defined as a function of N in Eq. (3.3.3):

$$\begin{cases} \rho A\ddot{v} - \kappa GA(v^{\mathrm{II}} - \psi\vartheta_z^{\mathrm{I}}) = 0 \\ \rho A\ddot{w} - \kappa GA(w^{\mathrm{II}} + \psi\vartheta_y^{\mathrm{I}}) = 0 \\ \rho J\ddot{\vartheta}_y + 2\rho J\omega\dot{\vartheta}_z + \kappa GA\psi(w^{\mathrm{I}} + \vartheta_y) - EJ\vartheta_y^{\mathrm{II}} - T\vartheta_z^{\mathrm{I}} = 0 \\ \rho J\ddot{\vartheta}_z - 2\rho J\omega\dot{\vartheta}_y - \kappa GA\psi(v^{\mathrm{I}} - \vartheta_z) - EJ\vartheta_z^{\mathrm{II}} + T\vartheta_y^{\mathrm{I}} = 0 \end{cases} \tag{3.4.15}$$

The first of Eq. (3.4.15) yields the differential link between ϑ_z and v already given in Eq. (3.3.4), while the second one provides the analogous relation between ϑ_y and w. Introducing them into the last two of Eq. (3.4.15) gives the equations of motion in the form of Eq. (3.3.6) and (3.3.7).

3.5 Operator form of the equations of motion

Eq. (3.4.15) can also be expressed in operator form, as a function of a vector **q** defined in the configuration space by the four flexural lagrangian coordinates:

$$\begin{cases} \mathbf{M}\ddot{\mathbf{q}} + \mathbf{G}\dot{\mathbf{q}} + [\boldsymbol{\mathcal{K}}]\mathbf{q} = \mathbf{0} \\ \mathbf{q} = \left\{ v, w, \vartheta_y, \vartheta_z \right\}^{\mathrm{T}} \end{cases} \tag{3.5.1}$$

where **M** and **G** are linear algebraic operators, diagonal and skew-symmetric respectively:

$$\begin{cases} \mathbf{M} = \begin{bmatrix} \rho A & 0 & 0 & 0 \\ 0 & \rho A & 0 & 0 \\ 0 & 0 & \rho J & 0 \\ 0 & 0 & 0 & \rho J \end{bmatrix} \\ \\ \mathbf{G} = \begin{bmatrix} 0 & 0 & 0 & 0 \\ 0 & 0 & 0 & 0 \\ 0 & 0 & 0 & 2\rho J\omega \\ 0 & 0 & -2\rho J\omega & 0 \end{bmatrix} \end{cases} \tag{3.5.2}$$

and $[\boldsymbol{\mathcal{K}}(\cdot)]$ is a linear second order differential operator, non-self-adjoint:

$$\left[\boldsymbol{\mathcal{K}}(\cdot)\right] = \begin{bmatrix} -\kappa GA(\cdot)^{\mathrm{II}} & 0 & 0 & \kappa GA\psi(\cdot)^{\mathrm{I}} \\ 0 & -\kappa GA(\cdot)^{\mathrm{II}} & -\kappa GA\psi(\cdot)^{\mathrm{I}} & 0 \\ 0 & \kappa GA\psi(\cdot)^{\mathrm{I}} & \kappa GA\psi(\cdot) - EJ(\cdot)^{\mathrm{II}} & -T(\cdot)^{\mathrm{I}} \\ -\kappa GA\psi(\cdot)^{\mathrm{I}} & 0 & T(\cdot)^{\mathrm{I}} & \kappa GA\psi(\cdot) - EJ(\cdot)^{\mathrm{II}} \end{bmatrix} \tag{3.5.3}$$

A possible state-space representation of Eq. (3.5.1), as a function of a vector $\mathbf{q}_s$, reads:

$$\begin{cases} \boldsymbol{\mathcal{A}}\dot{\mathbf{q}}_s + [\boldsymbol{\mathcal{B}}]\mathbf{q}_s = \mathbf{0} \\ \mathbf{q}_s = \left\{ \mathbf{q}^{\mathrm{T}}, \dot{\mathbf{q}}^{\mathrm{T}} \right\}^{\mathrm{T}} \end{cases} \tag{3.5.4}$$

with $\boldsymbol{\mathcal{A}}$ and $[\mathcal{B}(\cdot)]$ defined as follow:

$$\begin{cases} \boldsymbol{\mathcal{A}} = \begin{bmatrix} \mathbf{G} & \mathbf{M} \\ -\mathbf{M} & \mathbf{0} \end{bmatrix} \\ [\boldsymbol{\mathcal{B}}(\cdot)] = \begin{bmatrix} [\boldsymbol{\mathcal{K}}(\cdot)] & \mathbf{0} \\ \mathbf{0} & \mathbf{M} \end{bmatrix} \end{cases} \tag{3.5.5}$$

According to Eq. (3.5.4) and (3.5.5), $\boldsymbol{\mathcal{A}}$ is a linear algebraic operator, skew-symmetric, and $[\boldsymbol{\mathcal{B}}(\cdot)]$ is a linear second order differential operator, non-self-adjoint.

Considering two different functions, say $\mathbf{\Phi}_h$ and $\mathbf{\Phi}_k$, the general definition of the adjoint form of an operator $[\boldsymbol{\mathcal{O}}(\cdot)]$, denoted by the tilde symbol, is given by the following inner products [15, 87]:

$$\left\langle \mathbf{\Phi}_h \middle| [\tilde{\boldsymbol{\mathcal{O}}}]\mathbf{\Phi}_k \right\rangle = \left\langle \mathbf{\Phi}_k \middle| [\boldsymbol{\mathcal{O}}]\mathbf{\Phi}_h \right\rangle \tag{3.5.6}$$

Hence the adjoint operators of the matrices **M**, **G**, $\boldsymbol{\mathcal{A}}$ and of the differential operators $[\mathcal{K}(\cdot)]$ and $[\mathcal{B}(\cdot)]$, assuming same boundary conditions at both ends of the shaft, are simply:

$$\begin{cases} \tilde{\mathbf{M}} = \mathbf{M} \\ \tilde{\mathbf{G}} = \mathbf{G}^{\mathrm{T}} \\ \tilde{\boldsymbol{\mathcal{A}}} = \boldsymbol{\mathcal{A}}^{\mathrm{T}} \\ [\tilde{\boldsymbol{\mathcal{K}}}(\cdot)] = [\boldsymbol{\mathcal{K}}(\cdot)]^{\mathrm{T}} \\ [\tilde{\boldsymbol{\mathcal{B}}}(\cdot)] = [\boldsymbol{\mathcal{B}}(\cdot)]^{\mathrm{T}} \end{cases} \tag{3.5.7}$$

due to skew-symmetry (and first-order derivatives in differential operators) of all terms out of their main diagonals.

3.6 Decoupling the equations of motion

The equations of motion are decoupled using both real and complex variables, and then rewritten in non-dimensional form to facilitate the analysis of the effects of each governing parameter. Adopting a complex-variable approach, the general integral is sought by separation of time and space variables, yielding eigenfrequencies, closed-form expressions of the eigenfunctions, and critical speeds. Equation (3.4.15) can be rewritten as two coupled second-order (with respect to both x and t) partial derivative equations with complex coefficients and complex variables w and θ. This can be done by suitably combining the four equations in Eq. (3.4.15):

$$\begin{cases} \rho A\ddot{v} - \kappa GA(v^{\mathrm{II}} - \psi\vartheta_z^{\mathrm{I}}) + i\left[\rho A\ddot{w} - \kappa GA(w^{\mathrm{II}} + \psi\vartheta_y^{\mathrm{I}})\right] = 0 \\ \rho J\ddot{\vartheta}_y + 2\rho J\omega\dot{\vartheta}_z + \kappa GA\psi(w^{\mathrm{I}} + \vartheta_y) - EJ\vartheta_y^{\mathrm{II}} - T\vartheta_z^{\mathrm{I}} + \\ \qquad + i\left[\rho J\ddot{\vartheta}_z - 2\rho J\omega\dot{\vartheta}_y - \kappa GA\psi(v^{\mathrm{I}} - \vartheta_z) - EJ\vartheta_z^{\mathrm{II}} + T\vartheta_y^{\mathrm{I}}\right] = 0 \end{cases} \tag{3.6.1}$$

Indeed, recalling the definitions of w and θ provided in Section 3.2, Eq. (3.6.1) leads to:

$$\begin{cases} \rho A\ddot{\mathrm{w}} - \kappa GA(\mathrm{w}^{\mathrm{II}} + i\,\psi\theta^{\mathrm{I}}) = 0 \\ \rho J\,\ddot{\theta} - 2i\,\rho J\omega\dot{\theta} - \kappa GA\psi(i\,\mathrm{w}^{\mathrm{I}} - \theta) - EJ\,\theta^{\mathrm{II}} + i\,T\,\theta^{\mathrm{I}} = 0 \end{cases} \tag{3.6.2}$$

Eq. (3.4.15) can also be rewritten as two coupled fourth-order (with respect to both x and t) partial derivative equations with real coefficients and real variables v and w. To do that, one possible way forward is as follows:

$$\begin{cases} \vartheta_z^{\mathrm{I}} = \dfrac{1}{\kappa GA\psi}\left(\kappa GA v^{\mathrm{II}} - \rho A\ddot{v}\right) \\ \vartheta_y^{\mathrm{I}} = \dfrac{1}{\kappa GA\psi}\left(-\kappa GA w^{\mathrm{II}} + \rho A\ddot{w}\right) \\ \rho J\ddot{\vartheta}_y^{\mathrm{I}} + 2\rho J\omega\,\dot{\vartheta}_z^{\mathrm{I}} + \kappa GA\psi(w^{\mathrm{II}} + \vartheta_y^{\mathrm{I}}) - EJ\vartheta_y^{\mathrm{III}} - T\vartheta_z^{\mathrm{II}} = 0 \\ \rho J\ddot{\vartheta}_z^{\mathrm{I}} - 2\rho J\omega\,\dot{\vartheta}_y^{\mathrm{I}} - \kappa GA\psi(v^{\mathrm{II}} - \vartheta_z^{\mathrm{I}}) - EJ\vartheta_z^{\mathrm{III}} + T\vartheta_y^{\mathrm{II}} = 0 \end{cases} \tag{3.6.3}$$

In Eq. (3.6.3) the first two equations are directly derived from the first two of Eq. (3.4.15) and the last two are obtained taking the first derivative with respect to x of all terms in the remaining equations in Eq. (3.4.15). Replacing the expressions of ϑ_z^{I} and ϑ_y^{I} in the third and fourth equations of Eq. (3.6.3), taking first the right derivative with respect to x or t, yields:

$$\begin{cases} EJ\left(v^{\mathrm{IV}} - \dfrac{\rho}{\kappa G}\ddot{v}^{\mathrm{II}}\right) + T\left(w^{\mathrm{III}} - \dfrac{\rho}{\kappa G}\ddot{w}^{\mathrm{I}}\right) - N\psi v^{\mathrm{II}} + \\ \qquad + \rho A\psi\,\ddot{v} - \rho J\left(\ddot{v}^{\mathrm{II}} - \dfrac{\rho}{\kappa G}\ddddot{v}\right) - 2\rho J\omega\left(\dot{w}^{\mathrm{II}} - \dfrac{\rho}{\kappa G}\dddot{w}\right) = 0 \\ EJ\left(w^{\mathrm{IV}} - \dfrac{\rho}{\kappa G}\ddot{w}^{\mathrm{II}}\right) - T\left(v^{\mathrm{III}} - \dfrac{\rho}{\kappa G}\ddot{v}^{\mathrm{I}}\right) - N\psi w^{\mathrm{II}} + \\ \qquad + \rho A\psi\,\ddot{w} - \rho J\left(\ddot{w}^{\mathrm{II}} - \dfrac{\rho}{\kappa G}\ddddot{w}\right) + 2\rho J\omega\left(\dot{v}^{\mathrm{II}} - \dfrac{\rho}{\kappa G}\dddot{v}\right) = 0 \end{cases} \tag{3.6.4}$$

The two coupled fourth-order equations in the real variables ϑ_y and ϑ_z would be exactly the same as Eq. (3.6.4), after substituting ϑ_y with v and ϑ_z with w. Equation (3.6.4) can be in turn decoupled into a single eighth-order (with respect to both x and t) partial derivative equation in a real variable, as shown in Section 3.10. They can also be decoupled into a single fourth-order (with respect to both x and t) partial derivative equation with complex coefficients in a complex variable:

$$\begin{aligned} &EJ\left(\mathrm{w}^{\mathrm{IV}} - \frac{\rho}{\kappa G}\ddot{\mathrm{w}}^{\mathrm{II}}\right) - iT\left(\mathrm{w}^{\mathrm{III}} - \frac{\rho}{\kappa G}\ddot{\mathrm{w}}^{\mathrm{I}}\right) - N\psi\,\mathrm{w}^{\mathrm{II}} + \\ &\qquad + \rho A\psi\,\ddot{\mathrm{w}} - \rho J\left(\ddot{\mathrm{w}}^{\mathrm{II}} - \frac{\rho}{\kappa G}\ddddot{\mathrm{w}}\right) + 2i\rho J\omega\left(\dot{\mathrm{w}}^{\mathrm{II}} - \frac{\rho}{\kappa G}\dddot{\mathrm{w}}\right) = 0 \end{aligned} \tag{3.6.5}$$

The procedure to obtain Eq. (3.6.5) is the same used to reach Eq. (3.6.4). The decoupled fourth-order equation in the complex variable θ would be exactly the same as Eq. (3.6.5), after substituting θ with w. In Eq. (3.6.5) two complex coefficients identify the terms responsible of coupling the flexural behaviour in the x-y and x-z planes. These two coefficients would have opposite signs if adopting the complex variable $\mathrm{w}^* = v - iw$ instead of w, which would be the same as considering a counter-rotating shaft loaded by a clockwise twisting moment T (*i.e.* changing the sign to both ω and T). Notice that Eq. (3.6.5) would retain the same form also in the case of twisting moment T applied tangentially at the ends of the shaft (*i.e.* a follower torque) [11]. It generalizes the expressions given in [9] (effect of T) and in [12] (effect of N). The equation published in [14] is not correct, since the effects of N and T were introduced consistently with the Euler-Bernoulli beam model, rather than with the Timoshenko one. The equation in [14], with the herein adopted notation reads:

$$\begin{cases} EJ\left(\psi^*\mathrm{w}^{\mathrm{IV}} - \dfrac{\rho}{\kappa G}\ddot{\mathrm{w}}^{\mathrm{II}}\right) - iT\psi^*\mathrm{w}^{\mathrm{III}} - N\mathrm{w}^{\mathrm{II}} + \\ \qquad\qquad + \rho A\ddot{\mathrm{w}} - \rho J\left(\psi^*\ddot{\mathrm{w}}^{\mathrm{II}} - \dfrac{\rho}{\kappa G}\ddddot{\mathrm{w}}\right) + 2i\rho J\omega\left(\psi^*\dot{\mathrm{w}}^{\mathrm{II}} - \dfrac{\rho}{\kappa G}\dddot{\mathrm{w}}\right) = 0 \\ \psi^* = 1 + \dfrac{N}{\kappa G A} \end{cases} \tag{3.6.6}$$

3.7 Non-dimensional form of the equations of motion

Considering a dimensionless spatial variable ξ, a dimensionless time τ and a reference frequency parameter $\varOmega$ (which embodies the structural properties of the shaft):

$$\begin{cases} \xi = \dfrac{x}{l} \\ \tau = \varOmega t \\ \varOmega = \dfrac{1}{l^2}\sqrt{\dfrac{EJ}{\rho A}} \end{cases} \tag{3.7.1}$$

and introducing the dimensionless parameters:

$$\begin{cases} \alpha = \sqrt{\dfrac{Al^2}{J}} = \dfrac{2l}{r} \\ \hat{\omega} = \dfrac{\omega}{\varOmega} \\ \sigma = \dfrac{E}{\kappa G} \end{cases} , \quad \begin{cases} \hat{N} = \dfrac{N}{EA} \\ \hat{T} = \dfrac{Tl}{EJ} \end{cases} \tag{3.7.2}$$

where α is the slenderness ratio, then any representation of the equations of motion of the rotating shaft can be rewritten in non-dimensional form, as for instance Eq. (3.6.5):

$$\begin{cases} \left(\mathrm{w}^{\mathrm{IV}} - \dfrac{\sigma}{\alpha^2} \ddot{\mathrm{w}}^{\mathrm{II}} \right) - i\hat{T} \left(\mathrm{w}^{\mathrm{III}} - \dfrac{\sigma}{\alpha^2} \ddot{\mathrm{w}}^{\mathrm{I}} \right) - \hat{N}\alpha^2 \psi \, \mathrm{w}^{\mathrm{II}} + \\ \qquad + \psi \, \ddot{\mathrm{w}} - \dfrac{1}{\alpha^2} \left(\ddot{\mathrm{w}}^{\mathrm{II}} - \dfrac{\sigma}{\alpha^2} \ddddot{\mathrm{w}} \right) + 2i \dfrac{\hat{\omega}}{\alpha^2} \left(\dot{\mathrm{w}}^{\mathrm{II}} - \dfrac{\sigma}{\alpha^2} \dddot{\mathrm{w}} \right) = 0 \\ \psi = 1 - \sigma \hat{N} \end{cases} \tag{3.7.3}$$

In the case of a homogeneous shaft made of isotropic material with circular section, the shear elasticity modulus G and the shear factor κ can be expressed as functions of Young's modulus and Poisson's ratio [99]:

$$\begin{cases} G = \dfrac{E}{2(1+\nu)} \\ \kappa = \dfrac{6(1+\nu)}{7+6\nu} \quad \Rightarrow \quad \sigma = \dfrac{7+6\nu}{3} \end{cases} \tag{3.7.4}$$

hence the dimensionless parameter σ depends on Poisson's ratio only, and within the limits of interest for the present study its variations are of minor importance. As a consequence, the equations of motion of the rotating shaft depend on just four parameters of major interest: slenderness ratio α, dimensionless angular speed $\hat{\omega}$, dimensionless axial end thrust $\hat{N}$ and dimensionless twisting moment $\hat{T}$.

3.8 Differential eigenproblem for complex displacements

The general integral is sought by modal analysis, solving a differential eigenproblem. In this respect, the most convenient form of the equations of motion to deal with is the complex-variable, decoupled fourth-order Eq. (3.7.3). It is rewritten by separating the time and space variables and Laplace transforming with respect to time:

$$\begin{cases} \mathrm{w}(\xi,\tau) = \phi_{\mathrm{w}}(\xi)\,\eta(\tau) \quad \Rightarrow \quad \mathrm{L}(\mathrm{w}) = \phi_{\mathrm{w}}(\xi)\,\eta(s) \\ p_4 \phi_{\mathrm{w}}^{\mathrm{IV}} + p_3 \phi_{\mathrm{w}}^{\mathrm{III}} + p_2 \phi_{\mathrm{w}}^{\mathrm{II}} + p_1 \phi_{\mathrm{w}}^{\mathrm{I}} + p_0 \phi_{\mathrm{w}} = 0 \end{cases} \tag{3.8.1}$$

where the five complex coefficients p read:

$$\begin{cases} p_4 = 1 \\ p_3 = -i\hat{T} \\ p_2 = -\dfrac{1+\sigma}{\alpha^2} s^2 + 2i \dfrac{\hat{\omega}}{\alpha^2} s - \psi \hat{N} \alpha^2 \\ p_1 = i\hat{T} \dfrac{\sigma}{\alpha^2} s^2 \\ p_0 = \dfrac{\sigma}{\alpha^4} s^4 - 2i \dfrac{\sigma\hat{\omega}}{\alpha^4} s^3 + \psi s^2 \end{cases} \tag{3.8.2}$$

Notice that p_2, p_1 and p_0 depend on the eigenvalue s. The general integral of Eq. (3.7.3) can be expressed on the basis of the complex exponential function, yielding a characteristic polynomial equation with complex coefficients for the exponents a:

$$\phi_\mathrm{w}(\xi) = Be^{a\xi}, \quad B, a \in \mathbb{C} \quad \Rightarrow \quad P(a) = \sum_{n=0}^{4} p_n a^n = 0 \tag{3.8.3}$$

Closed-form expressions of the roots of the fourth-order polynomial equation $P(a) = 0$ can be found by adopting either one of the classical solution methods [100] or an advanced symbolic algebra software. The general integral is therefore expressed as a linear combination of four complex exponential functions:

$$\phi_\mathrm{w}(\xi) = \sum_{n=1}^{4} B_n e^{a_n \xi} \tag{3.8.4}$$

and the eigenvalues s can be computed after setting four boundary conditions. Assuming the same conditions at both ends of the shaft, the algebraic eigenproblem related to Eq. (3.8.4) takes the form:

$$\begin{bmatrix} b_1 & b_2 & b_3 & b_4 \\ c_1 & c_2 & c_3 & c_4 \\ b_1 e^{a_1} & b_2 e^{a_2} & b_3 e^{a_3} & b_4 e^{a_4} \\ c_1 e^{a_1} & c_2 e^{a_2} & c_3 e^{a_3} & c_4 e^{a_4} \end{bmatrix} \begin{bmatrix} B_1 \\ B_2 \\ B_3 \\ B_4 \end{bmatrix} = \mathbf{0} \tag{3.8.5}$$

where the first two equations represent the conditions in $\xi = 0$, and the following two the conditions in $\xi = 1$. The complex coefficients b and c depend on the kind of boundary conditions and in the more general case they are explicit functions of both the exponents a and the eigenvalues s. Setting to zero the determinant of the coefficient matrix, (say Δ), in Eq. (3.8.5), yields the characteristic equation for the eigenvalues s:

$$\begin{cases} \Delta = D_{12} D_{34} \left[e^{a_1+a_2} + e^{a_3+a_4} \right] - D_{13} D_{24} \left[e^{a_1+a_3} + e^{a_2+a_4} \right] + D_{14} D_{23} \left[e^{a_1+a_4} + e^{a_2+a_3} \right] = 0 \\ D_{nm} = b_n c_m - b_m c_n \end{cases} \tag{3.8.6}$$

which is a complex function of the complex variable s. However, pure imaginary eigenvalues, *i.e.* $s = i\lambda$, can be numerically computed by using a zero-find routine of a real function g of the real variable λ:

$$g[\Delta(i\lambda)] = 0, \quad \lambda \in (-\infty, +\infty) \tag{3.8.7}$$

The critical speeds $\hat{\omega}_\mathrm{C} = \omega_\mathrm{C} / \Omega$ can be found by following the same procedure, setting $\lambda = \hat{\omega}$ in Eq. (3.8.7) and solving it with respect to $\hat{\omega}$.

The eigenfunctions for the complex angular displacement θ can be obtained from the first of Eq. (3.6.2) in its nondimensional form:

$$\ddot{\mathrm{w}} - \frac{\alpha^2}{\sigma}\mathrm{w}^{\mathrm{II}} - i\,l\,\frac{\alpha^2\psi}{\sigma}\theta^{\mathrm{I}} = 0 \tag{3.8.8}$$

Laplace transforming and considering pure imaginary eigenvalues, Eq. (3.8.8) reads:

$$\lambda^2\phi_w(\xi) + \frac{\alpha^2}{\sigma}\phi_w^{\mathrm{II}}(\xi) + i\,l\,\frac{\alpha^2\psi}{\sigma}\phi_\theta^{\mathrm{I}}(\xi) = 0 \tag{3.8.9}$$

Thus, recalling Eq. (3.8.4), the eigenfunctions $\phi_\theta(\xi)$ can be expressed as:

$$\phi_\theta(\xi) = \frac{i}{l}\sum_{n=1}^{4}\frac{B_n}{\psi a_n}\left(a_n^2 + \frac{\sigma\lambda^2}{\alpha^2}\right)e^{a_n\xi} + h_\lambda \tag{3.8.10}$$

where h_λ is an unknown constant. However, since it is possible to uncoupling the equations of motion in order to obtain a fourth-order equation in the complex variable θ, as discussed in Section 3.6, $\phi_\theta(\xi)$ must be completely determined by a combination of four complex exponential functions:

$$\phi_\theta(\xi) = \sum_{n=1}^{4}\bar{B}_n e^{a_n\xi} \tag{3.8.11}$$

where the four scalars $\bar{B}_n$ could be hypothetically obtained by imposing the boundary condition for complex angular displacement θ, similarly to what was done for w in Eq. (3.8.5). Hence, the constant h_λ can be expressed as a linear combination of the fundamental integrals $\bar{B}_n e^{a_n\xi}$. Considering the superposition principle backwards, the eigenfunctions for the complex angular displacement θ can be expressed as:

$$\begin{cases} \phi_\theta(\xi) = \dfrac{i}{l}\displaystyle\sum_{n=1}^{4} B_n R_n(\lambda)\, e^{a_n\xi} \\ R_n(\lambda) = \dfrac{1}{\psi a_n}\left(a_n^2 + \dfrac{\sigma\lambda^2}{\alpha^2}\right) \end{cases} \tag{3.8.12}$$

The solution of the adjoint problem can be immediately found by considering the adjoint operators in Eq. (3.5.7) and a characteristic polynomial $\tilde{P}(a)$ defined by coefficients $\tilde{p}$, equal to those in Eq. (3.8.2), except for changing the sign to both ω and T, or considering the complex variable $\mathrm{w}^* = v - iw$ instead of w, as noticed in Section 3.6. The eigenvalues are the same as those computed through Eq. (3.8.7), but with opposite signs ($\tilde{\lambda} = -\lambda$), since the characteristic equation in this case would be $g[\Delta(-i\tilde{\lambda})] = 0$.

3.9 Boundary conditions for complex displacements

Isotropic supports are considered, hence the boundary conditions associated to Eq. (3.7.3) can be expressed as functions of the complex variable w alone, due to axial symmetry. In the simplest configurations they read:

Clamped end, case with null rotations and null shear deformations:

$$\begin{cases} v = w = 0 \\ \vartheta_y + \gamma_y + \beta_y = 0, \quad \vartheta_z + \gamma_z + \beta_z = 0 \end{cases} \Rightarrow \begin{cases} \mathrm{w} = 0 \\ \mathrm{w}^{\mathrm{I}} = 0 \end{cases} \tag{3.9.1}$$

Clamped end, case with null rotations only:

$$\begin{cases} v = w = 0 \\ \vartheta_y = \vartheta_z = 0 \end{cases} \Rightarrow \quad \mathrm{w} = 0, \quad \mathrm{w}^{\mathrm{I}} + \frac{\sigma}{\psi\alpha^2}\left[\left(\mathrm{w}^{\mathrm{III}} - \frac{\sigma}{\alpha^2}\ddot{\mathrm{w}}^{\mathrm{I}}\right) - i\hat{T}\,\mathrm{w}^{\mathrm{II}} - \psi\hat{N}\alpha^2\,\mathrm{w}^{\mathrm{I}}\right] = 0 \tag{3.9.2}$$

Simply supported end, case with $T = 0$ or case with tangential T (follower torque) [11]:

$$\begin{cases} v = w = 0 \\ M_y = M_z = 0 \end{cases} \Rightarrow \begin{cases} \mathrm{w} = 0 \\ \mathrm{w}^{\mathrm{II}} = 0 \end{cases} \tag{3.9.3}$$

Simply supported end, case with axial T:

$$\begin{cases} \mathrm{w} = 0 \\ \mathrm{w}^{\mathrm{II}} - i\hat{T}\,\mathrm{w}^{\mathrm{I}} - \dfrac{\sigma}{\psi\alpha^2}\left[i\hat{T}\left(\mathrm{w}^{\mathrm{III}} - \dfrac{\sigma}{\alpha^2}\ddot{\mathrm{w}}^{\mathrm{I}} - i\hat{T}\,\mathrm{w}^{\mathrm{II}} - \psi\hat{N}\alpha^2\,\mathrm{w}^{\mathrm{I}}\right) - \dfrac{1}{\alpha^2}(\ddot{\mathrm{w}}^{\mathrm{II}} - 2i\hat{\omega}\,\dot{\mathrm{w}}^{\mathrm{II}})\right] = 0 \end{cases} \tag{3.9.4}$$

Free end:

$$\begin{cases} M_y = M_z = 0 \\ F_y = F_z = 0 \end{cases} \Rightarrow \begin{cases} \left(\mathrm{w}^{\mathrm{II}} - \dfrac{\sigma}{\alpha^2}\ddot{\mathrm{w}}\right) - i\hat{T}\,\mathrm{w}^{\mathrm{I}} - \psi\hat{N}\alpha^2\,\mathrm{w} = 0 \\ \left(\mathrm{w}^{\mathrm{III}} - \dfrac{\sigma}{\alpha^2}\ddot{\mathrm{w}}^{\mathrm{I}}\right) - i\hat{T}\left(\mathrm{w}^{\mathrm{II}} - \dfrac{\sigma}{\alpha^2}\ddot{\mathrm{w}}\right) + \\ \qquad - \psi\hat{N}\alpha^2\,\mathrm{w}^{\mathrm{I}} - \dfrac{1}{\alpha^2}(\ddot{\mathrm{w}}^{\mathrm{I}} - 2i\hat{\omega}\,\dot{\mathrm{w}}^{\mathrm{I}}) = 0 \end{cases} \tag{3.9.5}$$

Introducing Eq. (3.8.4) into the selected boundary equations gives the expressions of the coefficients *b* and *c* of the characteristic equation (3.8.6). Notice that the second of Eq. (3.9.4) generalizes the expression given in [9] (with opposite sign convention for T), and that in [14] the terms in square brackets are omitted, as a consequence of disregarding the interaction between shear effect and twisting moment in the equations of motion.

3.10 Differential eigenproblem for real displacements

As introduced in Section 3.6 the four second-order equations of motion, Eq. (3.4.15), can also be decoupled into a single eighth-order equation in a real variable, say v. Taking Eq. (3.6.4) in non-dimensional form and performing Laplace transform reads:

$$\begin{cases} v^{\mathrm{IV}} - \dfrac{\sigma s^2}{\alpha^2} v^{\mathrm{II}} + \hat{T}\left(w^{\mathrm{III}} - \dfrac{\sigma s^2}{\alpha^2} w^{\mathrm{I}} \right) + \\ \qquad - \hat{N}\alpha^2 \psi v^{\mathrm{II}} + \psi s^2 v - \dfrac{s^2}{\alpha^2}\left(v^{\mathrm{II}} - \dfrac{\sigma s^2}{\alpha^2} v \right) - 2\hat{\omega}\dfrac{s}{\alpha^2}\left(w^{\mathrm{II}} - \dfrac{\sigma s^2}{\alpha^2} w \right) = 0 \\ w^{\mathrm{IV}} - \dfrac{\sigma s^2}{\alpha^2} w^{\mathrm{II}} - \hat{T}\left(v^{\mathrm{III}} - \dfrac{\sigma s^2}{\alpha^2} v^{\mathrm{I}} \right) + \\ \qquad - \hat{N}\alpha^2 \psi w^{\mathrm{II}} + \psi s^2 w - \dfrac{s^2}{\alpha^2}\left(w^{\mathrm{II}} - \dfrac{\sigma s^2}{\alpha^2} w \right) + 2\hat{\omega}\dfrac{s}{\alpha^2}\left(v^{\mathrm{II}} - \dfrac{\sigma s^2}{\alpha^2} v \right) = 0 \end{cases} \tag{3.10.1}$$

which can be rewritten in a more compact form:

$$\begin{cases} F_v^{\mathrm{II}} + \hat{T} F_w^{\mathrm{I}} - \hat{N}\alpha^2 \psi v^{\mathrm{II}} + \psi s^2 v - \dfrac{s^2}{\alpha^2} F_v - 2\hat{\omega}\dfrac{s}{\alpha^2} F_w = 0 \\ F_w^{\mathrm{II}} - \hat{T} F_v^{\mathrm{I}} - \hat{N}\alpha^2 \psi w^{\mathrm{II}} + \psi s^2 w - \dfrac{s^2}{\alpha^2} F_w + 2\hat{\omega}\dfrac{s}{\alpha^2} F_v = 0 \end{cases} \tag{3.10.2}$$

where the following substitutions have been introduced:

$$\begin{cases} F_v = v^{\mathrm{II}} - \dfrac{\sigma s^2}{\alpha^2} v \\ F_w = w^{\mathrm{II}} - \dfrac{\sigma s^2}{\alpha^2} w \end{cases} \tag{3.10.3}$$

In Eq. (3.10.2) the v- and w-dependent terms can be re-arranged as:

$$\begin{cases} F_w^{\mathrm{I}} = 2\dfrac{\hat{\omega}}{\hat{T}}\dfrac{s}{\alpha^2} F_w + A_v \\ F_w^{\mathrm{II}} = \hat{N}\alpha^2 \psi w^{\mathrm{II}} - \psi s^2 w + \dfrac{s^2}{\alpha^2} F_w + B_v \\ A_v = \dfrac{1}{\hat{T}}\left(-F_v^{\mathrm{II}} + \hat{N}\alpha^2 \psi v^{\mathrm{II}} - \psi s^2 v + \dfrac{s^2}{\alpha^2} F_v \right) \\ B_v = \hat{T} F_v^{\mathrm{I}} - 2\hat{\omega}\dfrac{s}{\alpha^2} F_v \end{cases} \tag{3.10.4}$$

Taking the first derivative with respect to ξ of the first of Eq. (3.10.2):

$$\begin{cases} \hat{T} F_w^{\mathrm{II}} - 2\hat{\omega} \dfrac{s}{\alpha^2} F_w^{\mathrm{I}} + C_v = 0 \\ C_v = -\hat{T} A_v^{\mathrm{I}} \end{cases} \tag{3.10.5}$$

and introducing Eq. (3.10.4) yields w^{II} as a function of w and v :

$$\begin{cases} w^{\mathrm{II}} = -\dfrac{1}{\beta_2}(\beta_1 w + D_v) \\ D_v = C_v + \hat{T} B_v - 2\hat{\omega} \dfrac{s}{\alpha^2} A_v \\ \beta_1 = -\hat{T}\psi s^2 - \hat{T}\sigma \dfrac{s^4}{\alpha^4} + 4\sigma \dfrac{\hat{\omega}^2}{\hat{T}} \dfrac{s^4}{\alpha^6} \\ \beta_2 = \hat{T}\hat{N}\alpha^2\psi + \hat{T} \dfrac{s^2}{\alpha^2} - 4\dfrac{\hat{\omega}^2}{\hat{T}} \dfrac{s^2}{\alpha^4} \end{cases} \tag{3.10.6}$$

Recalling the definition of F_w in Eq. (3.10.3), then Eq. (3.10.6) gives immediately:

$$\begin{cases} F_w = -\beta_3 w + E_v \\ E_v = -\dfrac{D_v}{\beta_2} \\ \beta_3 = \dfrac{\sigma s^2}{\alpha^2} + \dfrac{\beta_1}{\beta_2} \end{cases} \tag{3.10.7}$$

Taking the second derivative with respect to ξ of Eq. (3.10.7):

$$F_w^{\mathrm{II}} = E_v^{\mathrm{II}} - \beta_3 w^{\mathrm{II}} \tag{3.10.8}$$

and introducing the expressions of F_w and of its second derivative given by Eq. (3.10.4) and (3.10.7), as well as that of w^{II} given by Eq. (3.10.6), yields w as a function of v :

$$\begin{cases} w = \dfrac{G_v}{\beta_4} \\ G_v = B_v - \dfrac{1}{\beta_2}(\hat{N}\alpha^2\psi + \beta_3) D_v - E_v^{\mathrm{II}} + \dfrac{s^2}{\alpha^2} E_v \\ \beta_4 = \hat{N}\alpha^2\psi \dfrac{\beta_1}{\beta_2} + \psi s^2 + \left(\dfrac{s^2}{\alpha^2} + \dfrac{\beta_1}{\beta_2} \right) \beta_3 \end{cases} \tag{3.10.9}$$

Finally, the w-independent expressions of F_w and of its first derivative, obtained from Eq. (3.10.7) and (3.10.9):

$$\begin{cases} F_w = E_v - \dfrac{\beta_3}{\beta_4} G_v \\ F_w^{\mathrm{I}} = E_v^{\mathrm{I}} - \dfrac{\beta_3}{\beta_4} G_v^{\mathrm{I}} \end{cases} \tag{3.10.10}$$

are introduced in the first of Eq. (3.10.2) yielding an eighth-order equation in the real variable v:

$$F_v^{\mathrm{II}} + \hat{T}\left(E_v^{\mathrm{I}} - \frac{\beta_3}{\beta_4} G_v^{\mathrm{I}} \right) - \hat{N}\alpha^2 \psi v^{\mathrm{II}} + \psi s^2 v - \frac{s^2}{\alpha^2} F_v - 2\hat{\omega}\frac{s^2}{\alpha^2}\left(E_v - \frac{\beta_3}{\beta_4} G_v \right) = 0 \tag{3.10.11}$$

After substituting the expressions of F_v, E_v and G_v, the resulting coefficients are:

$$\begin{cases} q_8 = 1 \\ q_7 = 0 \\ q_6 = -\dfrac{2(1+\sigma)}{\alpha^2} s^2 + \hat{T}^2 - 2\hat{N}\alpha^2\psi \\ q_5 = -\dfrac{4\hat{T}\hat{\omega}}{\alpha^2} s \\ q_4 = \dfrac{1+\sigma(4+\sigma)}{\alpha^4} s^4 + \left[2\psi\left[1+\hat{N}(1+\sigma)\right] - \dfrac{2\sigma\hat{T}^2}{\alpha^2} + \dfrac{4\hat{\omega}^2}{\alpha^4} \right] s^2 + \hat{N}^2\alpha^4\psi^2 \\ q_3 = \dfrac{8\sigma\hat{T}\hat{\omega}}{\alpha^4} s^3 \\ q_2 = -\dfrac{2\sigma(1+\sigma)}{\alpha^6} s^6 + \left[\dfrac{\sigma^2\hat{T}^2}{\alpha^4} - \dfrac{2\psi\left[1+\sigma(1+\hat{N})\right]}{\alpha^2} - \dfrac{8\sigma\hat{\omega}^2}{\alpha^6} \right] s^4 - 2\hat{N}\alpha^2\psi^2 s^2 \\ q_1 = -\dfrac{4\sigma^2\hat{T}\hat{\omega}}{\alpha^6} s^5 \\ q_0 = \dfrac{\sigma^2}{\alpha^8} s^8 + \left(\dfrac{2\sigma\psi}{\alpha^4} + \dfrac{4\sigma^2\hat{\omega}^2}{\alpha^8} \right) s^6 + \psi^2 s^4 \end{cases} \tag{3.10.12}$$

Simplifying Eq. (3.10.11) as done in Eq. (3.8.1) yields:

$$q_8\phi^{\mathrm{VIII}} + q_7\phi^{\mathrm{VII}} + q_6\phi^{\mathrm{VI}} + q_5\phi^{\mathrm{V}} + q_4\phi^{\mathrm{IV}} + q_3\phi^{\mathrm{III}} + q_2\phi^{\mathrm{II}} + q_1\phi^{\mathrm{I}} + q_0\phi = 0 \tag{3.10.13}$$

whose general integral can be represented on the basis of the complex exponential function, yielding a characteristic polynomial equation with complex coefficients for the exponents a:

$$\phi(\xi) = Ce^{a\xi}, \quad C, a \in \mathbb{C} \quad \Rightarrow \quad Q(a) = \sum_{n=0}^{8} q_n a^n = 0 \tag{3.10.14}$$

The eighth-grade polynomial $Q(a)$ factorizes into the two fourth-grade polynomials $P(a)$ and $\tilde{P}(a)$, then the coefficients q, Eq. (3.10.12), can also be expressed as functions of the coefficients p and $\tilde{p}$ in the form of a convolution sum:

$$Q(a)=P(a)\tilde{P}(a) \quad\Rightarrow\quad q_n=\sum_{m=0}^{n} p_m \tilde{p}_{n-m} \quad \text{with} \quad p_n=\tilde{p}_n=0 \quad \text{for} \quad n>4 \tag{3.10.15}$$

The same characteristic equation $Q(a)=0$ could be obtained directly from Eq. (3.4.15), assuming as a basis the complex exponential function in the following vector representation:

$$\begin{cases} \boldsymbol{\phi}(\xi)=\boldsymbol{\phi}_0\, e^{a\xi} \\ \boldsymbol{\phi}_0=\left\{ C_v \quad C_w \quad C_{\vartheta_y} \quad C_{\vartheta_z} \right\}^{\mathrm{T}}, \quad C,a\in\mathbb{C} \end{cases} \tag{3.10.16}$$

which, introduced in the Laplace transformed operator form of the equations of motion, Eq. (3.5.1), gives:

$$s^2\,\mathbf{M}\boldsymbol{\phi}+s\,\mathbf{G}\boldsymbol{\phi}+\left[\mathcal{K}\right]\boldsymbol{\phi}=\mathbf{0} \quad\Rightarrow\quad \boldsymbol{\mathcal{D}}(s,a)\boldsymbol{\phi}_0=\mathbf{0} \tag{3.10.17}$$

where:

$$\begin{cases} \boldsymbol{\mathcal{D}}=\begin{bmatrix} \mathrm{d}_1 & 0 & 0 & -\mathrm{d}_4 \\ 0 & \mathrm{d}_1 & \mathrm{d}_4 & 0 \\ 0 & -\mathrm{d}_4 & \mathrm{d}_3 & \mathrm{d}_2 \\ \mathrm{d}_4 & 0 & -\mathrm{d}_2 & \mathrm{d}_3 \end{bmatrix} \\ \mathrm{d}_1=a^2-\dfrac{\sigma s^2}{\alpha^2} \\ \mathrm{d}_2=\dfrac{\sigma}{\alpha^2}\left(\hat{T}a-2\hat{\omega}\dfrac{s}{\alpha^2}\right) \\ \mathrm{d}_3=\dfrac{\sigma}{\alpha^2}\left(a^2-\dfrac{s^2}{\alpha^2}\right)-\psi \\ \mathrm{d}_4=\psi a \end{cases} \tag{3.10.18}$$

Notice that in matrix $\boldsymbol{\mathcal{D}}$, coefficients d_4 are responsible of coupling between displacements and rotations on the same plane, while coefficients d_2 couple displacements and rotations in orthogonal planes. The latter are decoupled only when both $T = 0$ and $\omega = 0$.

The algebraic eigenproblem in Eq. (3.10.17) can be solved by setting to zero the determinant of $\boldsymbol{\mathcal{D}}$:

$$\det[\mathcal{D}] = (d_1 d_3 + d_4^2)^2 + (d_1 d_2)^2 = \\ = \underbrace{\left[(d_1 d_3 + d_4^2) + i(d_1 d_2)\right]}_{P(a)} \underbrace{\left[(d_1 d_3 + d_4^2) - i(d_1 d_2)\right]}_{\tilde{P}(a)} = P(a)\tilde{P}(a) = 0 \tag{3.10.19}$$

which is the same characteristic equation for the eight exponents *a* given by Eq. (3.10.14). Therefore the eigenvalues $s = \pm i\lambda$ associated to the eighth-order problem are all those computed solving $g\,[\Delta(i\lambda)] = 0$, Eq. (3.8.7), plus those computed solving $g\,[\Delta(-i\lambda)] = 0$, *i.e.* the adjoint fourth-order problem as discussed in Section 3.8. If both $T = 0$ and $\omega = 0$ (*i.e.* $d_2 = 0$), then Eq. (3.6.4) are decoupled, and the sets of eigenvalues associated to the two fourth-order problems are coincident, meaning that in this case each eigenvalue has multiplicity 2.

3.11 Expression of the eigenfunctions for real displacements

According to the eigenproblem formulation provided in Section 3.10, the four scalar eigenfunctions for the real displacements v, w, ϑ_y, ϑ_z can be expressed as:

$$\begin{cases} \phi_v(\xi) = \sum_{n=1}^{8} C_{nv}\, e^{a_n \xi} \\ \phi_w(\xi) = \sum_{n=1}^{8} C_{nw}\, e^{a_n \xi} \\ \phi_{\vartheta_y}(\xi) = \sum_{n=1}^{8} C_{n\vartheta_y}\, e^{a_n \xi} \\ \phi_{\vartheta_z}(\xi) = \sum_{n=1}^{8} C_{n\vartheta_z}\, e^{a_n \xi} \end{cases} \tag{3.11.1}$$

Relations among the four amplitude constants C_n as functions of one of them (say C_{nv}) can be found recalling the algebraic eigenproblem in Eq. (3.10.17), along with the definitions in Eq. (3.10.16) and (3.10.18). For any given eigenvalue $s = i\lambda$ and for an exponent $a_n\,(i\lambda)$, two possible expressions for the eigenvector $\boldsymbol{\phi}_{0n}$ can be found:

$$\boldsymbol{\phi}_{0n} = C_{nv}\{1 \quad +i \quad -iR_n \quad R_n\}^{\mathrm{T}} \quad \text{or} \quad \tilde{\boldsymbol{\phi}}_{0n} = C_{nv}\{1 \quad -i \quad +iR_n \quad R_n\}^{\mathrm{T}} \tag{3.11.2}$$

where $R_n = d_1/d_4$ with $s = i\lambda$, according to the definition given in Eq. (3.8.12). The meaning of these two possible solutions is clarified after introducing one of them (say $\boldsymbol{\phi}_{0n}$) in the system Eq. (3.10.17), obtaining:

$$\begin{cases} d_1 - d_4 R_n = 0 \\ i(d_1 - d_4 R_n) = 0 \\ -i(d_4 + d_3 R_n + i\,d_2 R_n) = 0 \\ d_4 + d_3 R_n + i\,d_2 R_n = 0 \end{cases} \quad \Leftrightarrow \quad \underbrace{(d_1 d_3 + d_4^2) + i(d_1 d_2)}_{P(a)} = 0 \tag{3.11.3}$$

where the system is reduced to just two independent equations; introducing the first equation into the fourth one yields the characteristic equation in terms of $P(a)$. Clearly, the other eigenvector in Eq. (3.11.2) would lead to the characteristic equation in terms of $\tilde{P}(a)$, associated to the adjoint problem. As a consequence, the eigenfunctions in Eq. (3.11.1) can be expressed in terms of two sets of amplitude constants, four of them given by $\boldsymbol{\phi}$ and the other four by its adjoint $\tilde{\boldsymbol{\phi}}$.

The relations between real displacement eigenfunctions and complex displacement eigenfunctions can then be found recalling the definitions in Eq. (3.8.4), (3.11.1) and (3.11.2):

$$\begin{aligned} \phi_{\mathrm{W}} &= \sum_{n=1}^{4} B_n\, e^{a_n \xi} = \phi_v + i\,\phi_w = \\ &= \sum_{n=1}^{8} (C_{nv} + i\,C_{nw})\, e^{a_n \xi} = \sum_{n=1}^{8} [C_{nv} + i\,(\pm i\,C_{nv})]\, e^{a_n \xi} = 2\sum_{n=1}^{4} C_{nv}\, e^{a_n \xi} = 2\phi_v \end{aligned} \tag{3.11.4}$$

where four out of eight terms in the sum vanish due to opposite signs in $\boldsymbol{\phi}$ and $\tilde{\boldsymbol{\phi}}$. This result was expected: being ϕ_{W} a linear combination of four complex exponentials, also ϕ_v should result as a linear combination of four complex exponentials. Following the same steps, starting from ϕ_θ for the angular displacement eigenfunctions, the four relations between real displacement eigenfunctions and complex displacement eigenfunctions can be given in the form:

$$\begin{cases} \phi_v = \dfrac{\phi_{\mathrm{W}}}{2} \\ \phi_w = -i\,\dfrac{\phi_{\mathrm{W}}}{2} \\ \phi_{\vartheta_y} = \dfrac{\phi_\theta}{2} \\ \phi_{\vartheta_z} = -i\,\dfrac{\phi_\theta}{2} \end{cases} \tag{3.11.5}$$

Also this result was expected, due to symmetry: the only difference between for instance ϕ_v and ϕ_w is a phase-lag consisting in a $\pi / 2$ delay of ϕ_w with respect to ϕ_v. Notice that for $\kappa \to \infty$, Eq. (3.11.5) together with Eq. (3.8.12) yields a result consistent with the Euler-Bernoulli and Rayleigh models, and with Eq. (3.3.3):

$$\begin{aligned} &\lim_{\kappa\to\infty} R_n = a_n \quad \Rightarrow \quad \lim_{\kappa\to\infty} \phi_\theta = \frac{i}{l}\sum_{n=1}^{4} a_n B_n e^{a_n \xi} \quad \Rightarrow \\ &\qquad \Rightarrow \quad \lim_{\kappa\to\infty} \theta = \frac{i\mathrm{w}^{\mathrm{I}}}{l} \quad \Rightarrow \quad \lim_{\kappa\to\infty} \vartheta_y = -\frac{w^{\mathrm{I}}}{l}, \quad \lim_{\kappa\to\infty} \vartheta_z = \frac{v^{\mathrm{I}}}{l} \end{aligned} \tag{3.11.6}$$

where the dimensional factor at the denominator is related to differentiation with respect to the dimensionless spatial variable ξ.

3.12 Bi-orthogonality relations

The vectors of lagrangian coordinates in the configuration space $\mathbf{q}$ and in the state-space $\mathbf{q}_s$ can be expressed as linear combinations of eigenfunctions $\boldsymbol{\phi}$ and state-space eigenfunctions $\boldsymbol{\Phi}$ respectively, according to:

$$\begin{cases} \mathbf{q} = \sum_{h=1}^{\infty} \boldsymbol{\phi}_h \eta_h \\ \mathbf{q}_s = \sum_{h=1}^{\infty} \boldsymbol{\Phi}_h \eta_h \\ \boldsymbol{\Phi}_h = \begin{Bmatrix} \boldsymbol{\phi}_h \\ s_h \boldsymbol{\phi}_h \end{Bmatrix} \end{cases} \tag{3.12.1}$$

Considering non-dimensional operators, the non-homogeneous state-space representation in the Laplace domain of the second-order differential equations of motion, Eq. (3.4.15), reads:

$$s\hat{\boldsymbol{\mathcal{A}}}\mathbf{q}_s + [\hat{\boldsymbol{\mathcal{B}}}]\mathbf{q}_s = \hat{\mathbf{f}}_s \tag{3.12.2}$$

Since the eigenfunctions and the adjoint eigenfunctions are bi-orthogonal [87], and they can be normalized as:

$$\begin{cases} \left\langle \tilde{\boldsymbol{\Phi}}_h \middle| \hat{\boldsymbol{\mathcal{A}}} \boldsymbol{\Phi}_k \right\rangle = \delta_{hk} \\ \left\langle \tilde{\boldsymbol{\Phi}}_h \middle| [\hat{\boldsymbol{\mathcal{B}}}] \boldsymbol{\Phi}_k \right\rangle = -s_h \delta_{hk} \\ \delta_{hk} = \begin{cases} 1 & \text{if} \quad h = k \\ 0 & \text{if} \quad h \neq k \end{cases} \end{cases} \tag{3.12.3}$$

then multiplying Eq. (3.12.2) by the h^{th} adjoint eigenfunction $\tilde{\boldsymbol{\Phi}}_h$ and integrating over the spatial domain gives:

$$s\left\langle \tilde{\boldsymbol{\Phi}}_h \middle| \hat{\boldsymbol{\mathcal{A}}} \mathbf{q}_s \right\rangle + \left\langle \tilde{\boldsymbol{\Phi}}_h \middle| [\hat{\boldsymbol{\mathcal{B}}}] \mathbf{q}_s \right\rangle = \left\langle \tilde{\boldsymbol{\Phi}}_h \middle| \hat{\mathbf{f}}_s \right\rangle \quad \Leftrightarrow \quad (s - s_h)\eta_h = f_h \tag{3.12.4}$$

and:

$$s_h = i\lambda_h \quad \Leftrightarrow \quad \eta_h = \frac{f_h}{s - i\lambda_h} \tag{3.12.5}$$

where $f_h(s)$ is the h^{th} resulting nondimensional modal force. Transforming Eq. (3.12.5) back to time domain gives the expression of the modal coordinate $\eta_h(\tau)$ as a convolution integral. If $f_h(s) = 1$, then:

$$\eta_h(\tau) = e^{i\lambda_h \tau} \tag{3.12.6}$$

Considering now the real displacements related to a single vibration mode of the shaft, they can be expressed as:

$$\upsilon_h(\xi,\tau) = \phi_{\upsilon h} e^{i\lambda_h \tau} + \phi^*_{\upsilon h} e^{-i\lambda_h \tau} \tag{3.12.7}$$

therefore (dropping the subscript *h*):

$$\begin{cases} \upsilon(\xi,\tau) = \ 2\left[\Re(\phi_\upsilon)\cos(\lambda\tau) \ - \Im(\phi_\upsilon)\sin(\lambda\tau)\right] \\ w(\xi,\tau) = 2\left[\Im(\phi_\upsilon)\cos(\lambda\tau) \ + \Re(\phi_\upsilon)\sin(\lambda\tau)\right] \\ \vartheta_y(\xi,\tau) = -2\left[\Im(\phi_{\vartheta_z})\cos(\lambda\tau) - \Re(\phi_{\vartheta_z})\sin(\lambda\tau)\right] \\ \vartheta_z(\xi,\tau) = +2\left[\Re(\phi_{\vartheta_z})\cos(\lambda\tau) - \Im(\phi_{\vartheta_z})\sin(\lambda\tau)\right] \end{cases} \tag{3.12.8}$$

The modal trajectory of each point of the elastic line of the shaft is always described by a circle of radius $r_{el}(\xi)$:

$$\upsilon^2(\xi,\tau) + w^2(\xi,\tau) = 4\left[\Re^2(\phi_\upsilon) + \Im^2(\phi_\upsilon)\right] = r^2_{el}(\xi) \tag{3.12.9}$$

since the phase-lag between its two components is always ± π / 2. If $\lambda > 0$ (and $\omega > 0$), then the modal elastic line rotates counter-clockwise about the *x* axis, therefore the $\lambda > 0$ frequency values are usually referred to as forward natural frequencies; if $\lambda < 0$ (and $\omega > 0$), then the modal elastic line rotates clockwise, and the $\lambda < 0$ frequency values are usually referred to as backward natural frequencies. In the case $|\hat{\omega}| = |\lambda|$, a critical speed occurs only if $\hat{\omega}\lambda > 0$.

3.13 Critical loads

In static conditions the characteristic equation for the exponents *a*, Eq. (3.8.3) with $\lambda = 0$, gives:

$$\begin{cases} a_{1,2} = 0 \\ a_{3,4} = i\dfrac{\hat{T}}{2} \pm \begin{cases} \sqrt{-\Gamma} & \text{if} \quad \Gamma < 0 \\ i\sqrt{\Gamma} & \text{if} \quad \Gamma > 0 \end{cases} \quad \text{with} \quad \Gamma = \dfrac{\hat{T}^2}{4} - \alpha^2\psi\hat{N} \end{cases} \tag{3.13.1}$$

For $\hat{N} \neq 0$, the w equilibrium equation, and its solution in terms of ϕ_w, take the form:

$$EJ\mathrm{w}^{\mathrm{IV}} - iT\mathrm{w}^{\mathrm{III}} - N\psi\mathrm{w}^{\mathrm{II}} = 0 \quad \Rightarrow \quad \phi_\mathrm{w}(\xi) = B_1 e^{a_1\xi} + B_2 e^{a_2\xi} + B_3\xi + B_4 = 0 \tag{3.13.2}$$

Applying the boundary conditions, considering for instance simply supported ends as in Eq. (3.9.3), yields the following results:

$$\begin{array}{lllll} \Gamma \le 0 & \Rightarrow & B\sinh\sqrt{-\Gamma}=0 & \Rightarrow & B=0 \\ \Gamma > 0 & \Rightarrow & B\sin\sqrt{\Gamma}=0 & \Rightarrow & B=0 \quad \text{or} \quad \sqrt{\Gamma}=n\pi \end{array} \tag{3.13.3}$$

As a consequence, if $\Gamma \leq 0$ the shaft does not bend; if $\Gamma > 0$ the shaft bends at the critical equivalent loads:

$$\Gamma = n^2\pi^2 \tag{3.13.4}$$

which, for $\hat{T}=0$ and $\kappa \to \infty$ (*i.e.* $\sigma = 0$, $\psi = 1$), coincides with the well known expression of the critical buckling loads of the simply supported Euler and Rayleigh beam models [101].

3.14 Natural frequencies

The effects of slenderness ratio α, angular speed $\hat{\omega}$, axial end thrust $\hat{N}$ and twisting moment $\hat{T}$ are studied on natural frequencies and, in the further Sections, on modal shapes and critical speeds of the rotating shaft. Admissible ranges of variation for both $\hat{N}$ and $\hat{T}$ can be set recalling the definition of yield strength σ_{ys} of the homogeneous shaft material, and its link with the maximum value of $\hat{N}$ (*i.e.* $\left|\hat{N}_{\max}\right| = \sigma_{ys}/E$). Hence a reasonable assumption can be $\left|\hat{N}_{\max}\right| < 0.01$. Regarding $\left|\hat{T}_{\max}\right|$, the Tresca criterion yields $\left|\hat{T}_{\max}\right| = \alpha\left|\hat{N}_{\max}\right|/2$. In some figures, however, $\hat{T}$ has been increased up to exceedingly high values, to emphasize its effects and making more readable the plots. Natural frequencies are computed according to the procedure described in Section 3.8, through Eq. (3.8.6) and (3.8.7). In the case $\omega = 0$, the absolute value of $\Delta(i\lambda)$ is a symmetric function of the dimensionless parameter λ. Increasing the modulus of $\hat{T}$ (positive or negative) reduces the modulus of natural frequencies λ, as shown in Fig. 3.8 (left). The same qualitative effect can be observed by increasing the modulus of a negative $\hat{N}$ (compression), and the opposite by raising a positive $\hat{N}$ (traction, Fig. 3.9). In the case $\omega \neq 0$, the former symmetry is lost, and two spectra of natural frequencies are generated by considering $\pm\, i\lambda$. Increasing $\hat{\omega}$ with $\omega > 0$, raises the natural frequencies λ as displayed in Fig. 3.8 (right, with $\hat{N} = 0$ and $\hat{T} = 0$). Increasing the modulus of $\hat{\omega}$ with $\omega < 0$, in the case $\hat{T} = 0$ causes the opposite (symmetric) effect, as explained at the end of section 3.8 (the eigenvalues are the same as those computed through Eq. (3.8.7) with $\omega > 0$, but with opposite signs).

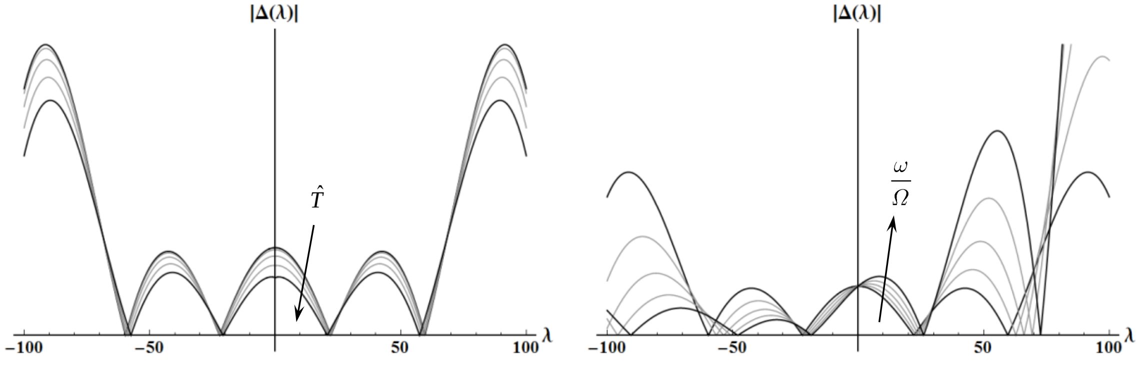

Figure 3.8: Absolute values $|\Delta(\lambda)|$ of the characteristic function ($\alpha = 50$, $\nu = 0.3$, clamped ends with null rotations and shear deformations); left: $\hat{T} > 0$, $\hat{\omega} = 0$, $\hat{N} = 0$; right: $\hat{\omega} > 0$, $\hat{N} = 0$, $\hat{T} = 0$

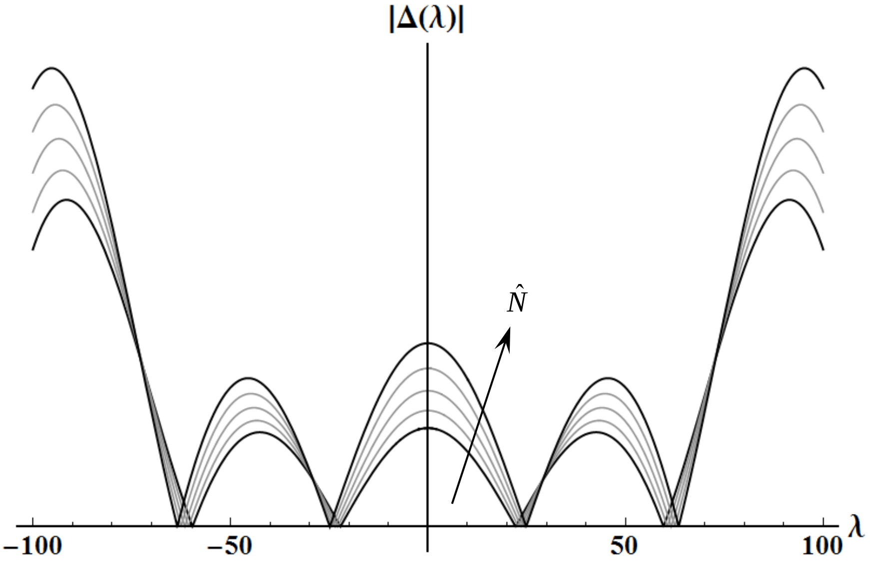

Figure 3.9: Absolute values $|\Delta(\lambda)|$ of the characteristic function ($\alpha = 50$, $\nu = 0.3$, clamped ends with null rotations and shear deformations); $\hat{T} = 0$, $\hat{\omega} = 0$, $\hat{N} > 0$

Table 3.1 First 4 natural frequencies $\lambda\Omega$ [Hz] for a rotating unloaded simply supported shaft

	$\hat{\omega} > 0$				$\hat{\omega} < 0$			
	FEA – number of elements			DPM	FEA – number of elements			DPM
	1	5	10		1	5	10	
1	736.030	652.037	651.882	651.847	726.306	650.833	650.658	650.624
2	3351.66	2561.21	2552.27	2550.21	3330.78	2556.56	2547.73	2545.68
3	–	5652.63	5565.59	5544.83	–	5611.01	5556.45	5535.76
4	–	9931.85	9540.54	9440.12	–	9737.23	9526.28	9426.22

Considering now a simply supported rotating shaft with the following parameters:

$$\rho = 7700\ [\text{Kg/m}^3],\ E = 210\times10^9\ [\text{Pa}],\ \nu = 0.3,\ r = 10\ [\text{mm}],$$
$$l = 250\ [\text{mm}],\ \omega = 1000\ [\text{rad/s}],\ \kappa = 0.8864,\ N = 0,\ T = 0$$

the first 4 positive natural frequencies $\lambda\Omega$ of the two spectra, computed for the distributed parameter model (DPM) according to the method presented in Section 3.8, are reported in Tab. 3.1 ($\alpha = 50$, simply supported shaft) where they are compared with the results of a finite element analysis (FEA) using different numbers of Timoshenko rotating beam elements [96].

Fig. 3.10 shows the absolute values $|\lambda|$ (black continuous lines) of the two couples of eigenvalues related to $n = 1$ (left) and $n = 2$ (right) as functions of $\hat{\omega}$, with $\alpha = 20$, $\nu = 0.3$, $\hat{N} = 0$, $\hat{T} = 0$ and simply supported ends. The asymptotic behavior of the eigenvalues with respect to angular speed will be discussed in Section 3.16.The effects of external loads $\hat{N}$ and $\hat{T}$ on the lower natural frequencies are highlighted in Fig. 3.11, displaying differences [%] on the first (continuous lines) and second (dotted lines) positive natural frequencies λ of the forward spectrum, as functions of $\hat{\omega}$. These differences reduce progressively for increasing natural frequencies, and those due to $\hat{T}$ are so small to be regarded as negligible.

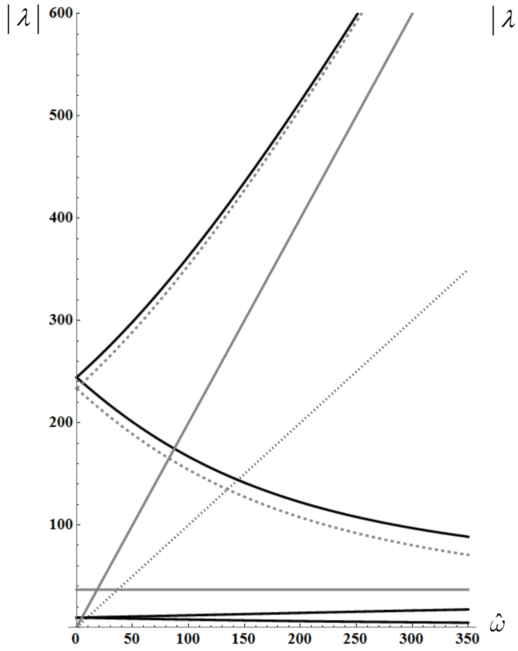

Figure 3.10: Absolute values $|\lambda|$ (black continuous lines) of the two couples of natural frequencies related to $n = 1$ (left) and $n = 2$ (right) as functions of $\hat{\omega}$ ($\alpha = 20$, $\nu = 0.3$, $\hat{N} = 0$, $\hat{T} = 0$, simply supported ends); grey continuous lines identify asymptotes, grey dotted curves identify switch frequencies

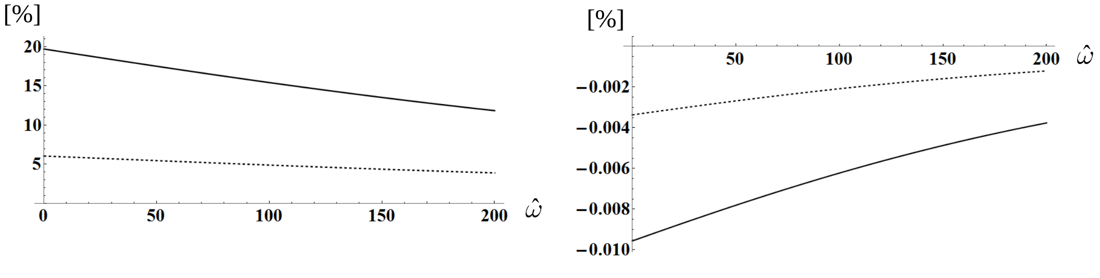

Figure 3.11: Differences due to external loads $\hat{N}$ and $\hat{T}$ on the first (continuous lines) and second (dotted lines) positive natural frequencies λ of the forward spectrum, ($\alpha = 20$, $\nu = 0.3$, simply supported ends); left: effect of the maximum value of $\hat{N} > 0$, differences [%] with respect to the case $\hat{N} = 0$; right: of the maximum value of $\hat{T}$, differences [%] with respect to the case $\hat{T} = 0$

3.15 On the exponents of the characteristic equation

A qualitative analysis of the four exponents *a* in Eq. (3.8.4) highlights some important general aspects of modal shapes, independently from boundary conditions.

The real and imaginary parts of the four roots of *P*(*a*), Eq. (3.8.3), are displayed in 3D plots as functions of a continuous variable λ, representing all possible natural frequencies, as for instance reported in Fig. 3.13 and 3.14 for a rotating shaft with α = 10, $\hat{\omega}$ = 50, $\hat{N}$ = ± 0.005, $\hat{T}$ = 0 and ν = 0.3. In Fig. 3.12 the four roots of *P*(*a*) are displayed for $\hat{N}$ = 0.

If $\hat{T} = 0$, Eq. (3.8.3) is a biquadratic equation, with either two real opposite and two imaginary conjugate roots, or two pairs of imaginary conjugate roots. The diagrams, as in Fig. 3.13 and 3.14, are symmetric with respect to both the λ-$\Re(a)$ and λ-$\Im(a)$ planes. In the case of non-rotating shaft ($\hat{\omega} = 0$) they would be symmetric also with respect to the $\Re(a)$-$\Im(a)$ plane. Therefore the effect of angular speed it that of producing different values of *a* (and therefore of modal shapes) for forward and backward eigenfrequencies. Notice that the asymmetry between forward and backward modal shapes grows with increasing angular speed.

The two non-zero frequency values for which two pairs of real roots *a* become null (and then switch to imaginary conjugate, in the following referred to as switch frequencies) can be found by setting p_0 = 0 in Eq. (3.8.2), yielding:

$$p(\lambda) = \frac{\sigma}{\alpha^4}\lambda^2 - 2\frac{\sigma\hat{\omega}}{\alpha^4}\lambda - \psi = 0 \quad \Rightarrow \quad \begin{cases} \lambda_f = \hat{\omega} + \sqrt{\hat{\omega}^2 + \psi\alpha^4\sigma^{-1}} \\ \lambda_b = \hat{\omega} - \sqrt{\hat{\omega}^2 + \psi\alpha^4\sigma^{-1}} \end{cases} \tag{3.15.1}$$

Inside the interval defined by the two switch frequencies (λ_b , λ_f), the modal shapes can be defined by combinations of hyperbolic and trigonometric functions; outside this range, the modal shapes are represented by trigonometric functions only. At the switch frequencies defined by Eq. (3.15.1) the eigenfunctions take a peculiar form: ϕ_w = 0 (the elastic line does not bend) and ϕ_θ = constant (constant angular displacements along the spatial coordinate ξ).

At zero natural frequency (λ = 0), *i.e.* in static conditions, a null axial thrust ($\hat{N} = 0$) gives four coincident null values for *a* (Fig. 3.12), a traction axial thrust ($\hat{N} > 0$) gives two non-zero opposite real values for *a* (Fig. 3.13), while a compression axial thrust ($\hat{N} < 0$) gives two non-zero pure imaginary conjugate values (Fig. 3.14); in the first and second case the shaft does not bend, in the latter case the shaft bends at critical loads, as discussed in Section 3.13.

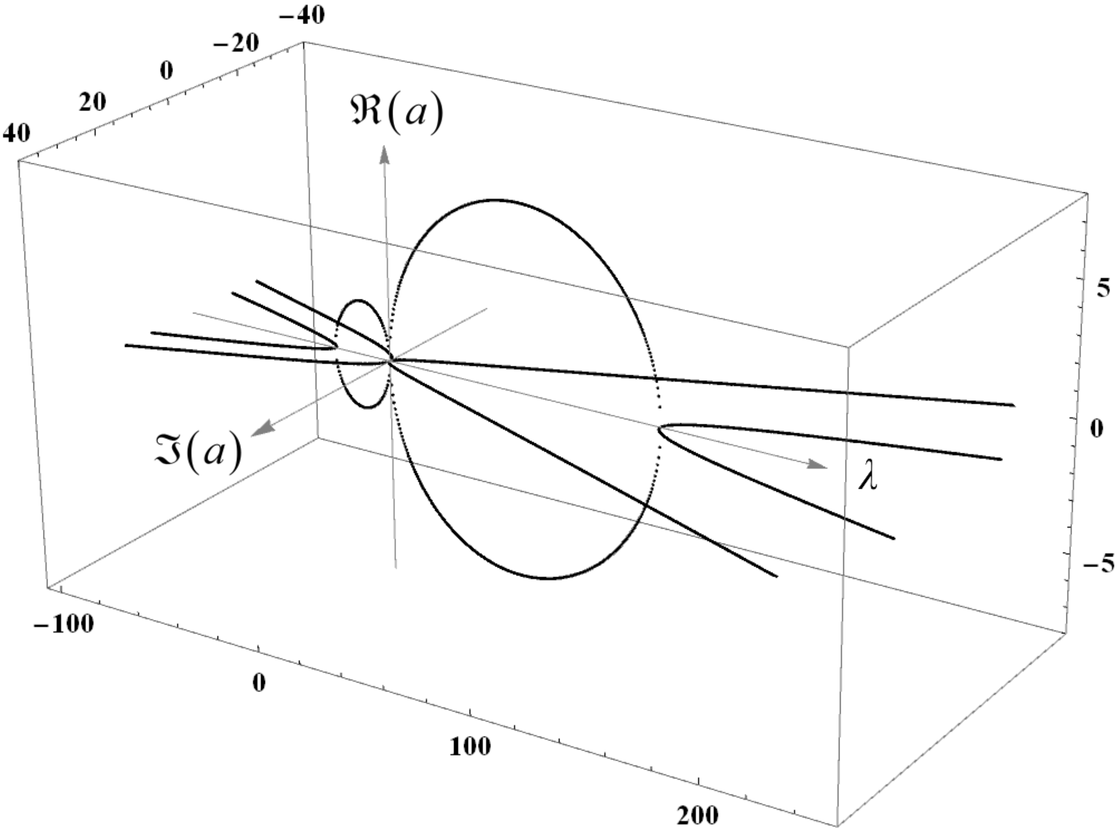

Figure 3.12: The four roots of Eq. (3.8.3), exponents of the modal shapes, as functions of the natural frequencies λ, case with $\hat{N} = 0$ ($\hat{\omega} > 0$, $\hat{T} = 0$)

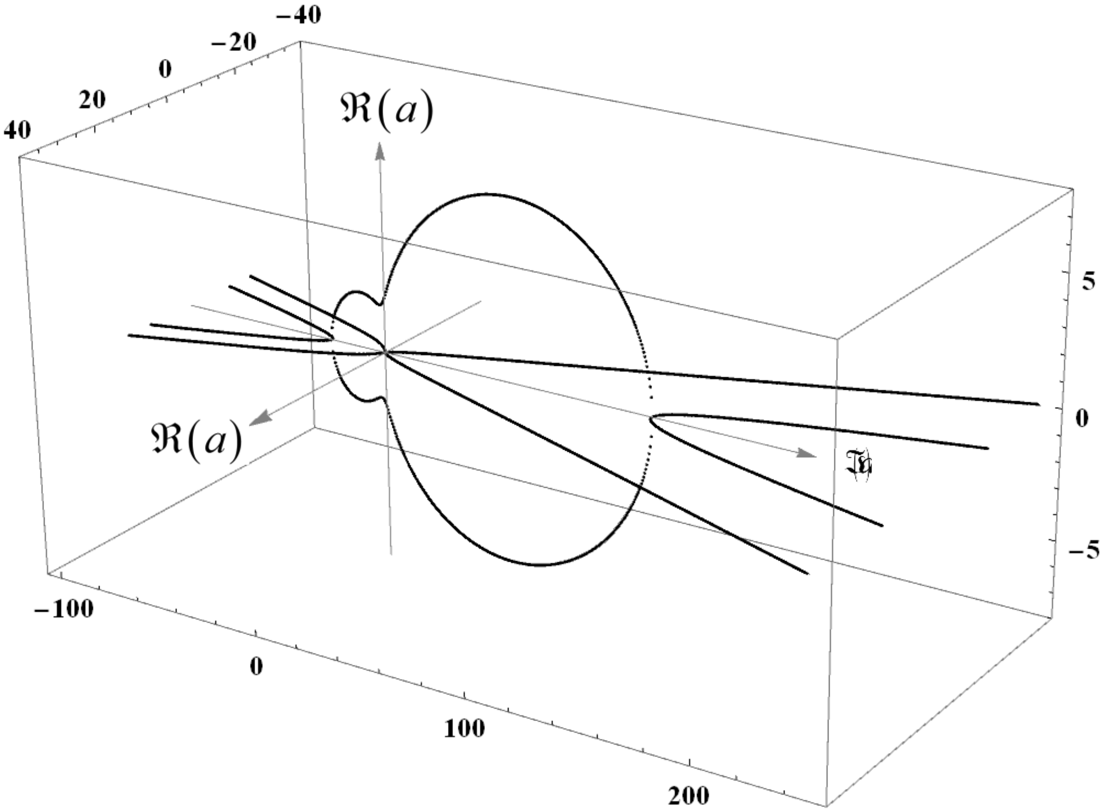

Figure 3.13: The four roots of Eq. (3.8.3), exponents of the modal shapes, as functions of the natural frequencies λ, case with $\hat{N} > 0$ ($\hat{\omega} > 0$, $\hat{T} = 0$)

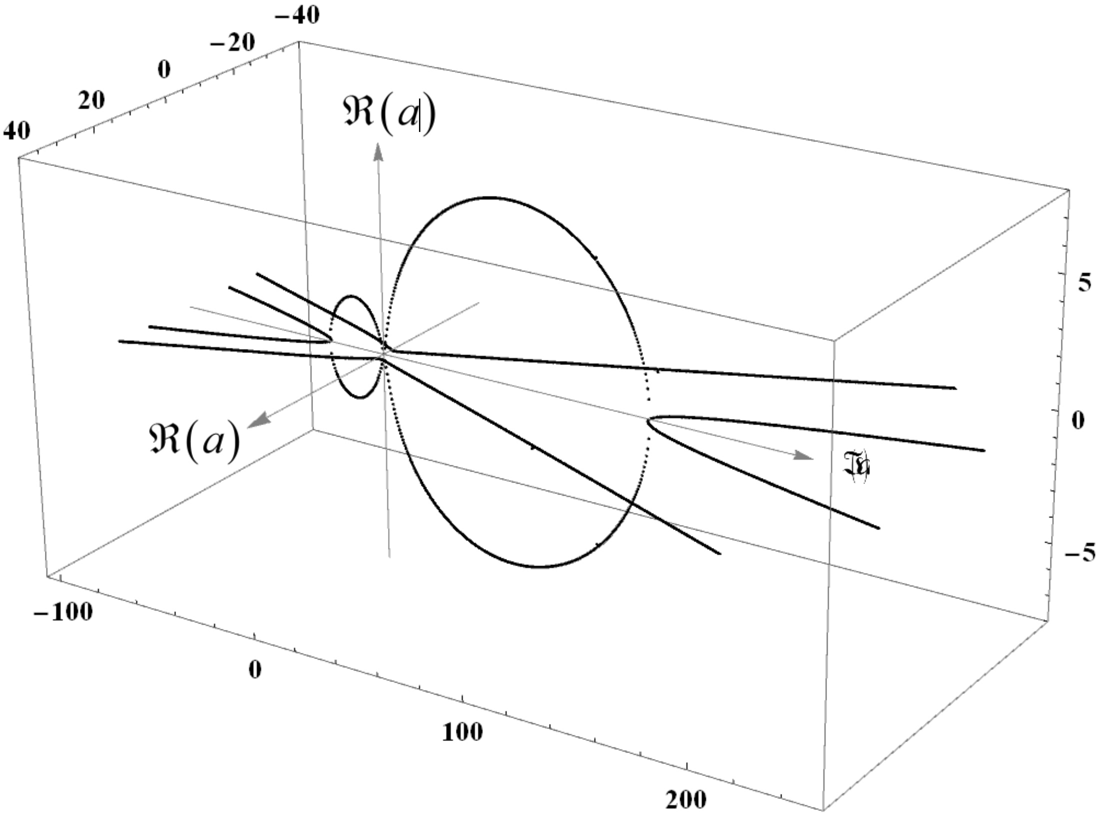

Figure 3.14: The four roots of Eq. (3.8.3), exponents of the modal shapes, as functions of the natural frequencies λ, case with $\hat{N} < 0$ ($\hat{\omega} > 0$, $\hat{T} = 0$)

If a twisting moment acting on the shaft is considered ($\hat{T} \neq 0$), then the only preserved plane of symmetry is the λ-Im (a) plane. Symmetry with respect to the λ-Re (a) plane is lost, as shown in Fig. 3.15 for a rotating shaft with α = 10, $\hat{\omega}$ = 50, $\hat{N}$ = 0, ν = 0.3 and several increasing values of $\hat{T}$ > 0. In Fig. 3.15 (left), to emphasize the effects of $\hat{T}$ on the overall behavior of the roots a in the λ-$\Im(a)$ plane, the twisting moment is increased up to exceedingly high values, the represented map retaining mathematical meaning only. In static conditions (λ = 0), for $\hat{N}$ = 0, $P(a)$ yields a single non-zero imaginary root ($a = i\hat{T}$). In Fig. 3.15 (right), a small portion of the same plot is displayed, around the forward switch frequency values, varying $\hat{T}$ in a realistic range until $|\hat{T}| = |\hat{T}_{\max}| = \alpha |\hat{N}_{\max}| / 2$.

It can be observed that absolute values of switch frequencies are reduced with increasing $|\hat{T}|$, and that inside the whole interval defined by a forward and a backward switch frequency, a pair of exponents a become complex-valued (for realistic values of $\hat{T}$, however, such reduction of switch frequencies, as well as the imaginary parts of complex a, are very slight). The points in which the curves cross the λ-axis are independent from $\hat{T}$, and it can be demonstrated that their frequency values are still given by Eq. (3.15.1). In these points (and not at the actual switch frequencies for $\hat{T} \neq 0$), the modal shapes retain the already described peculiar features (ϕ_w = 0 and ϕ_θ = constant).

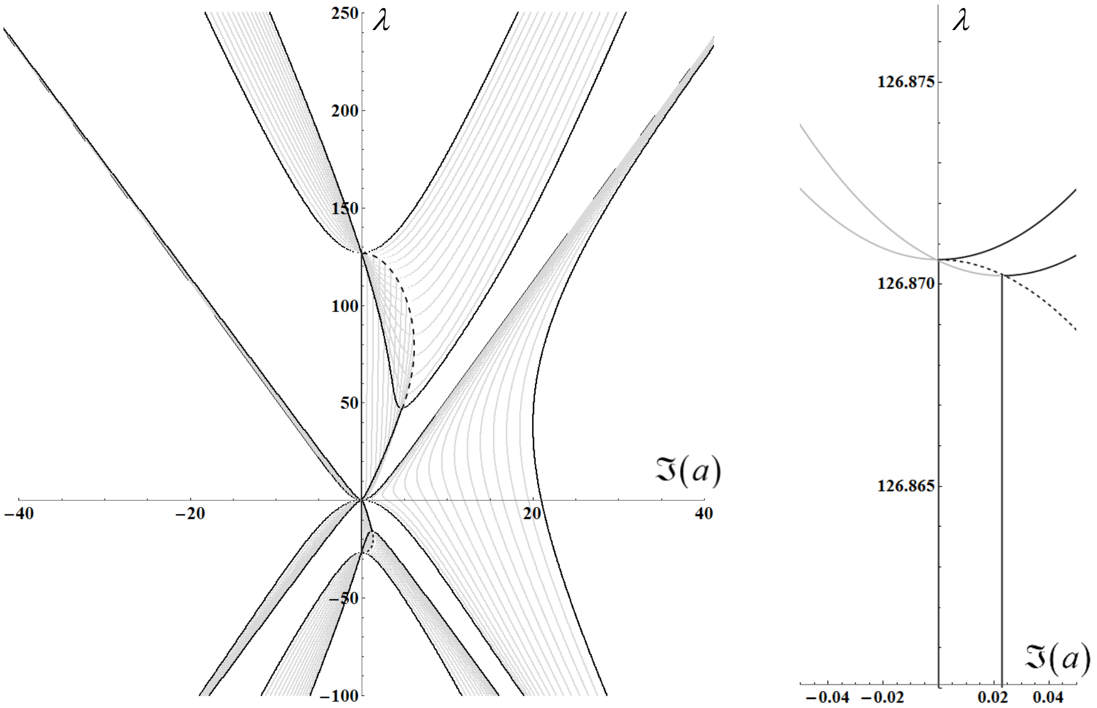

Figure 3.15: The imaginary parts of the four roots of Eq. (3.8.3), exponents of the modal shapes, as functions of the natural frequencies λ; left: overall diagram with several increasing values of $\hat{T} > 0$ ($\hat{\omega} > 0$, $\hat{N} = 0$); right: detail of the position of switch points for realistic values of $\hat{T} > 0$

Regarding the behavior at high frequency, it turns out that in the most general case ($\hat{\omega} \neq 0$, $\hat{N} \neq 0$, $\hat{T} \neq 0$) the pairs of conjugate imaginary roots a are asymptotic to straight lines, given by:

$$\begin{cases} a = \pm i \dfrac{\sqrt{\sigma}}{\alpha} \lambda & \text{always pure imaginary roots} \\ a = \pm \dfrac{i}{\alpha} \lambda & \text{pure imaginary roots beyond the switch frequencies} \end{cases} \tag{3.15.2}$$

which depend strongly on slenderness ratio α and on a lesser extent on Poisson's ratio ν (σ), but they are totally independent from $\hat{\omega}$, $\hat{N}$ and $\hat{T}$. Therefore the effects of rotating speed and external loads are the largest on lower modes, while progressively fading away at increasing frequencies.

3.16 Second spectrum and switch frequencies

The asymptotic behavior of the eigenvalues with respect to angular speed of the rotating shaft ($\omega \rightarrow \infty$, as shown in Fig. 3.10, grey continuous lines), can be studied in a general case.
Considering the equations of motion Eq. (3.4.15), dividing the third and fourth equations by ω and letting $\omega \rightarrow \infty$, then all terms on the third and fourth rows of operators $\mathbf{M}$ and $[\mathcal{K}(\cdot)]$ in Eq. (3.5.2) and (3.5.3), tend to 0. Consequently, if eigenvalues tend to finite values, there are two possible cases: either $\lambda \rightarrow \lambda_\infty$, $\lambda_\infty \neq 0$, in which limit case Eq. (3.4.15) yield:

$$
\begin{aligned}
&\omega \to \infty \quad \Rightarrow \quad \begin{cases} \vartheta_y = 0 \\ \vartheta_z = 0 \end{cases} \quad \Rightarrow \\
&\qquad \Rightarrow \quad \begin{cases} \rho A \ddot{v} - \kappa G A v^{\mathrm{II}} = 0 \\ \rho A \ddot{w} - \kappa G A w^{\mathrm{II}} = 0 \end{cases} \quad \Rightarrow \quad |\lambda_\infty| = \frac{\alpha}{\sqrt{\sigma}} a_{\infty n}, \quad a_{\infty n} = \sqrt{-l^2 \frac{\langle \phi_{v,n}, v^{\mathrm{II}} \rangle}{\langle \phi_{v,n}, v \rangle}}
\end{aligned}
\tag{3.16.1}
$$

or $\lambda \to 0$, in which case Eq. (3.4.15) reduce to Eq. (3.3.4) (null acceleration) and its homologous for w:

$$
\begin{cases} \omega \to \infty \\ \lambda \to 0 \end{cases} \quad \Rightarrow \quad \begin{cases} v^{\mathrm{II}} - \psi \vartheta_z^{\mathrm{I}} = 0 \\ w^{\mathrm{II}} + \psi \vartheta_y^{\mathrm{I}} = 0 \end{cases}
\tag{3.16.2}
$$

If, on the other hand, eigenvalues tend to infinity with angular speed, dividing the third and fourth of Eq. (3.4.15) by ω^2 and letting both $\omega \to \infty$ and $\lambda \to \infty$ gives:

$$
\begin{matrix} \omega \to \infty \\ \lambda \to \infty \end{matrix} \quad \Rightarrow \quad \lambda = k_\infty \omega \quad \text{with} \quad \begin{cases} k_\infty = 2 \quad \text{if} \quad I_x = 2J, \quad I_y = I_z = J \\ k_\infty = \dfrac{I_x}{J} \quad \text{if} \quad I_y = I_z = J \end{cases}
\tag{3.16.3}
$$

which could be obtained directly referring to the equilibrium represented in Fig. 3.5. Therefore the asymptotic behavior of the forward and backward natural frequencies of the rotating shaft can be summarized as:

$$
\omega \to \infty \quad \Rightarrow \quad \begin{cases} \lambda = 0, \quad \text{horizontal asymptote} \\ |\lambda| = \dfrac{\alpha}{\sqrt{\sigma}} a_{\infty n}, \quad \text{horizontal asymptote} \\ \lambda \to \infty, \quad \text{asymptotic to} \quad \lambda = k_\infty \omega \end{cases}
\tag{3.16.4}
$$

where n identifies the mode order. Notice that the horizontal asymptotes in Eq. (3.16.4) correspond to the straight asymptotic lines defined in the first of Eq. (3.15.2), which in the case of finite eigenvalues are reached as $\omega \to \infty$. Notice also that the asymptotic behavior does not depend on the external loads N and T, and that for a shaft with same boundary conditions at both ends, from Eq. (3.16.1) it results simply $a_{\infty n} = n\pi$ as in the case of Fig. 3.10. Each non-zero horizontal asymptote represents a link between two pairs of eigenvalues, one pair at lower frequencies, one pair at higher frequencies. The latter, when $\omega = 0$ and in particular cases of boundary conditions in which the characteristic equation factorizes (as in the case of simply supported ends), can be identified with what is referred to as Timoshenko (beam theory) second spectrum [90]. The existence of such second spectrum in the case of general boundary conditions has been debated in the literature [91, 92], since when $\omega = 0$ it is possible to easily identify the companion natural frequencies constituting the second spectrum only in particular cases, while finite element simulations produced conflicting conclusions [93]. More recently, the existence of a second spectrum in a non-rotating finite-length beam has been demonstrated on the basis of accurate experimental results, at least for free-free boundary conditions [94], and also by considering free waves in beams of infinite length, modelled according to the Timoshenko theory, showing the existence of two distinct frequency branches for any wavenumber [95]. However, when considering a rotating shaft, as $\omega \to \infty$ the existence of non-zero horizontal asymptotes for any boundary conditions suggests a new way for defining and identifying the natural frequencies of the Timoshenko first and second spectra. All first spectrum backward eigenfrequencies tend to 0; all second spectrum forward eigenfrequencies tend to infinity, asymptotic to $\lambda = k_\infty \omega$, while the absolute value of each first spectrum forward eigenfrequency converges to the backward companion one belonging to the second spectrum. Therefore, the first spectrum can be identified by setting $\lambda = k\hat{\omega},\ 0 < k \le k_\infty$ in Eq. (3.8.7) and solving it with respect to $\hat{\omega}$. The solutions identify the curves (or branches) of the first spectrum forward eigenvalues, since those of the second spectrum do not intersect any of the lines $\lambda = k\hat{\omega},\ 0 < k \le k_\infty$, as for example shown in Fig. 3.16. As a consequence, notice also that the whole second spectrum gives no contribution to the forward critical speeds. The problem of identifying the first spectrum frequencies at a given angular speed (eventually at $\omega = 0$) can then be solved by using an iterative procedure (Rayleigh quotient) able to follow each identified branch to the desired value of angular speed.

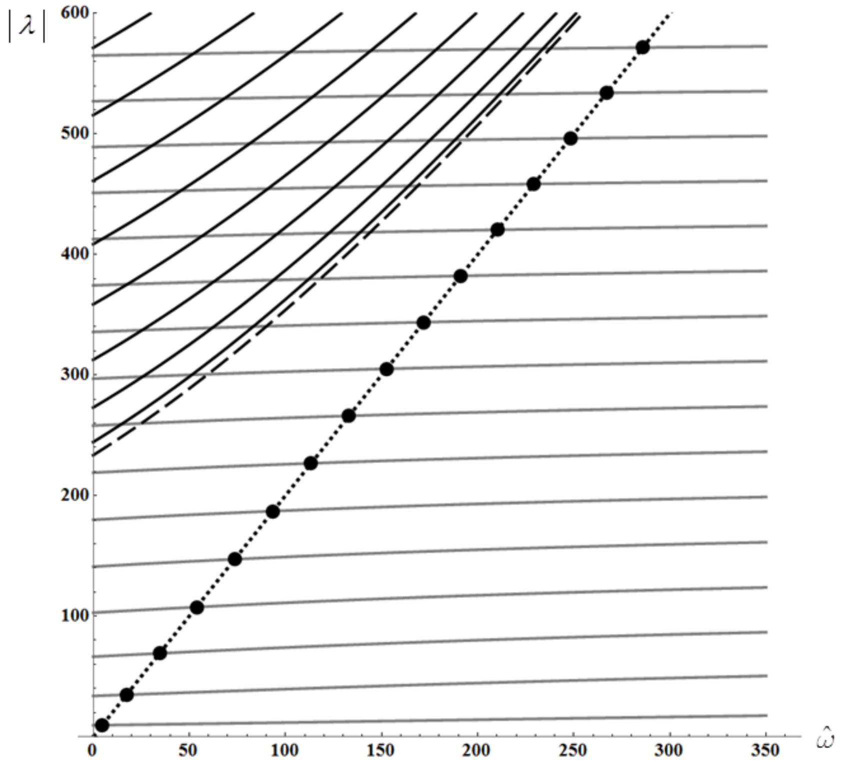

Figure 3.16: Absolute values $|\lambda|$ of forward natural frequencies as functions of $\hat{\omega}$ ($\alpha = 10,\ \sigma = 2.933,\ \hat{N} = \hat{T} = 0$); the dotted line identifies the asymptote $\lambda = 2\omega$, the dashed curve identify the forward switch frequencies

Recalling now the switch frequencies defined in Eq. (3.15.1), in the case of non-rotating unloaded Timoshenko beams they reduce to a unique value $\lambda = \alpha^2 / \sqrt{\sigma}$. This critical value is sometimes referred to as cut-off frequency [92, 93], while Eq. (3.15.1) generalizes its definition to the rotating and axially loaded case; if considering also a twisting moment, for realistic values of $\hat{T}$ Eq. (3.15.1) can be considered a good approximation of the switch frequencies, as shown in Section 3.15, and it still gives the exact frequency values in which no-total-deflection modal shapes occur ($\phi_W = 0$ and ϕ_θ = constant). Clearly, the most influential parameter on the switch frequencies is the slenderness ratio α; however $\hat{\omega}$ can influence significantly λ_f and λ_b at high speed, while the effect of external loads in this case is of minor importance.

Fig. 3.10 shows the two switch frequencies (λ_b, λ_f) as functions of $\hat{\omega}$ (grey dotted curves, case with $\alpha = 20$, $\nu = 0.3$, $\hat{N} = 0$, $\hat{T} = 0$ and simply supported ends). From Eq. (3.15.1) it can be found that as $\omega \rightarrow \infty$ then $\lambda_b \rightarrow 0$ and $\lambda_f \rightarrow +\infty$. It can also be observed that the switch frequency curve is asymptotic to $\lambda = k_\infty \hat{\omega}$ (as shown in Fig. 3.10 and 3.16) and that all the branches of the first spectrum natural frequencies cross the switch frequency curve twice (forward and backward), while those of the second spectrum always lay above it (the switch frequency curve is not a boundary between the two frequency spectra, it is a lower bound for the second frequency spectrum). Therefore, at any given angular speed, all the forward eigenvalues smaller than the switch value (at that angular speed) belong to the first frequency spectrum. Above the switch value the frequencies of the two spectra overlap in some complicated fashion, however they can be identified in general by following the criterion given above. As already noticed in Section 3.15, at the switch frequencies the total deflection angles are zero, consequently the shear angles and the cross-section rotation angles are in counter-phase (equal and opposite if $\psi = 1$), as it can be understood from the expression of the shear angle eigenfunctions ϕ_{γ_z}:

$$\phi_{\gamma_z} = \phi_v^{\mathrm{I}} - \psi \phi_{\vartheta_z} = -\frac{\sigma \lambda^2}{2 l \alpha^2} \sum_{n=1}^{4} \frac{B_n}{a_n} e^{a_n \xi} \tag{3.16.5}$$

obtained from Eq. (3.3.3), (3.8.4), (3.8.12) and Eq. (3.11.5). On the other hand, as $\omega \rightarrow \infty$ at the horizontal asymptotes the cross-section rotation angles become zero, consequently the shear angles and the total deflection angles are in-phase (actually they coincide). Therefore, increasing the angular speed and following a first spectrum forward branch which intersect the switch frequencies curve, changes are observed in phase relations among cross-section rotation, shear angle and total slope. As discussed in the literature, above the cut-off frequencies the results given by the Timoshenko beam theory become progressively less accurate. According to some authors, the whole second spectrum should be disregarded, and considered un-physical [92, 93], in contrast with the results presented in [94, 95]. In any case, it should be noticed that the frequency range of validity of the model under analysis is reduced if considering small values of slenderness ratio α, and this is related to the fact that, beyond certain frequency limits, the assumption of planarity of cross-sections during deformation clearly becomes unrealistic.

3.17 Modal shapes

Modal shapes for the variables in the configuration space are determined through Eq. (3.8.4), (3.8.12), (3.11.5) and (3.12.8). As an example, in Fig. 3.17, 3.18 and in Fig. 3.19 the first three forward modal shapes for the elastic line are displayed, for both simply supported and clamped ends, highlighting the twisting effects of $\hat{T}$ (emphasized by increasing its value up to exceedingly high values, for the sake of readability). While in Fig. 3.20 the whole second modal shape is represented, for the simply supported unloaded rotating shaft. In Fig. 3.17 to 3.19 the continuous black curves represent the elastic line of the beam during motion, while the gray surfaces represent the space domain spanned by the elastic line over a period, consistently with Eq. (3.12.8). Unlike the unloaded case, if $\hat{T} \neq 0$ the elastic line no longer lies in a rotating plane, that is, it can no longer be considered as a plane curve.

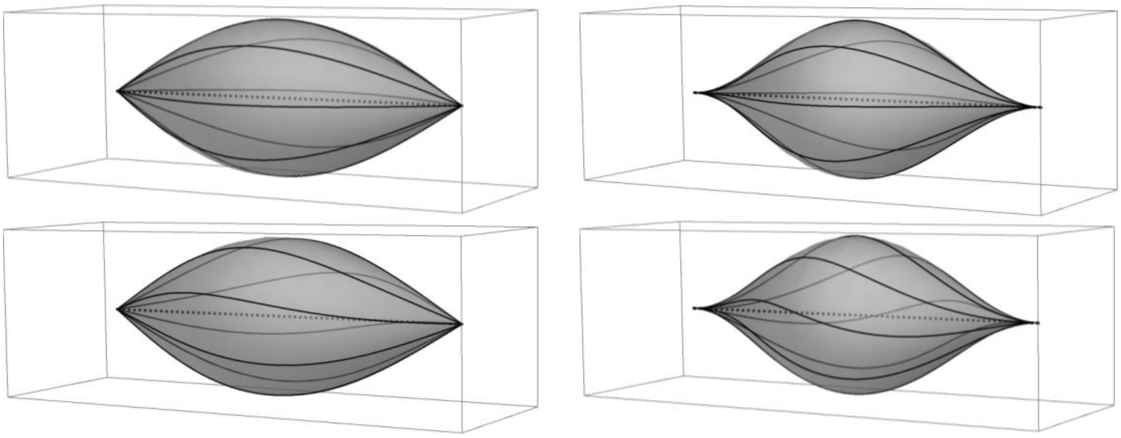

Figure 3.17: First forward modal shape for the elastic line, with α = 50, $\hat{\omega}$ = 10, $\hat{N}$ = 0 and ν = 0.3; left column: simply supported ends, Eq. (3.9.3); right column: clamped ends, Eq. (3.9.1); upper row, $\hat{T}$ = 0; lower row, $\hat{T}$ = 5.

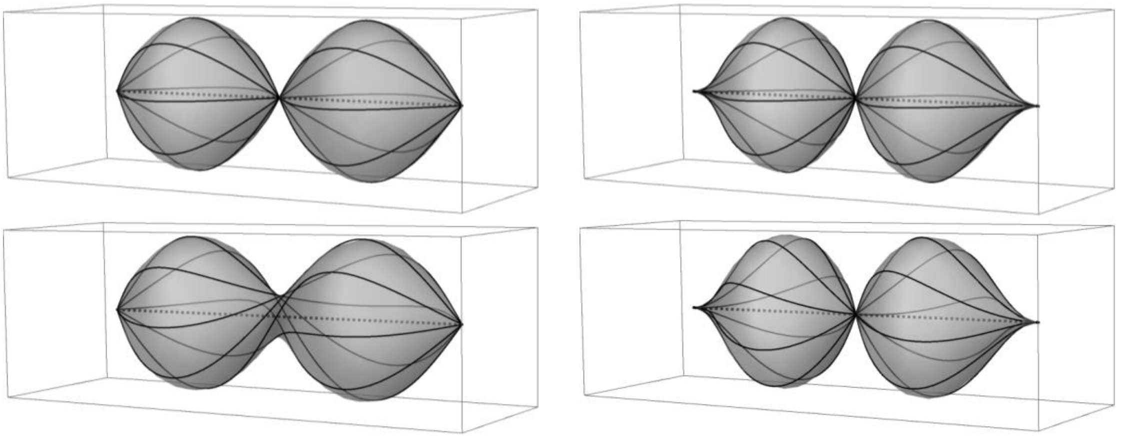

Figure 3.18: Second forward modal shape for the elastic line, with α = 50, $\hat{\omega}$ = 10, $\hat{N}$ = 0 and ν=0.3; left column: simply supported ends, Eq. (3.9.3); right column: clamped ends, Eq. (3.9.1); upper row, $\hat{T}$ = 0; lower row, $\hat{T}$ = 5.

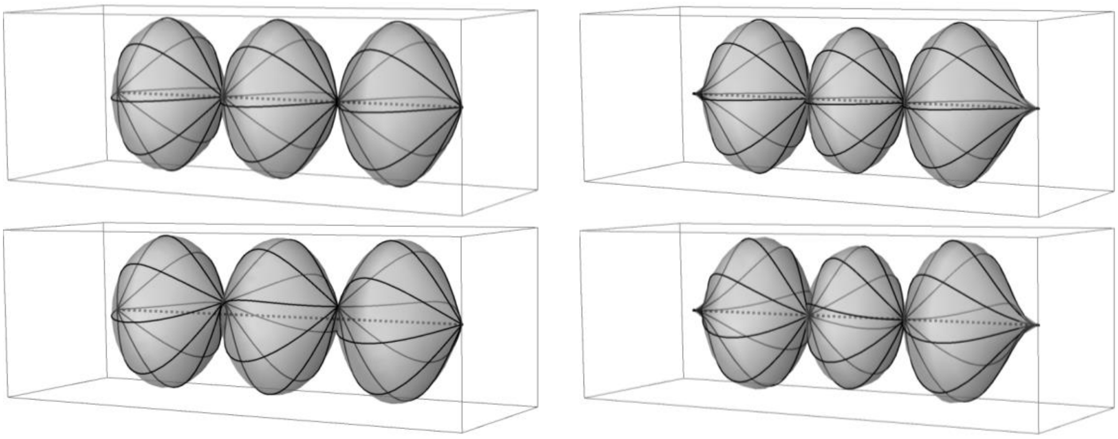

Figure 3.19: Third forward modal shape for the elastic line, with $\alpha = 50$, $\hat{\omega} = 10$, $\hat{N} = 0$ and $\nu = 0.3$; left column: simply supported ends, Eq. (3.9.3); right column: clamped ends, Eq. (3.9.1); upper row, $\hat{T} = 0$; lower row, $\hat{T} = 5$.

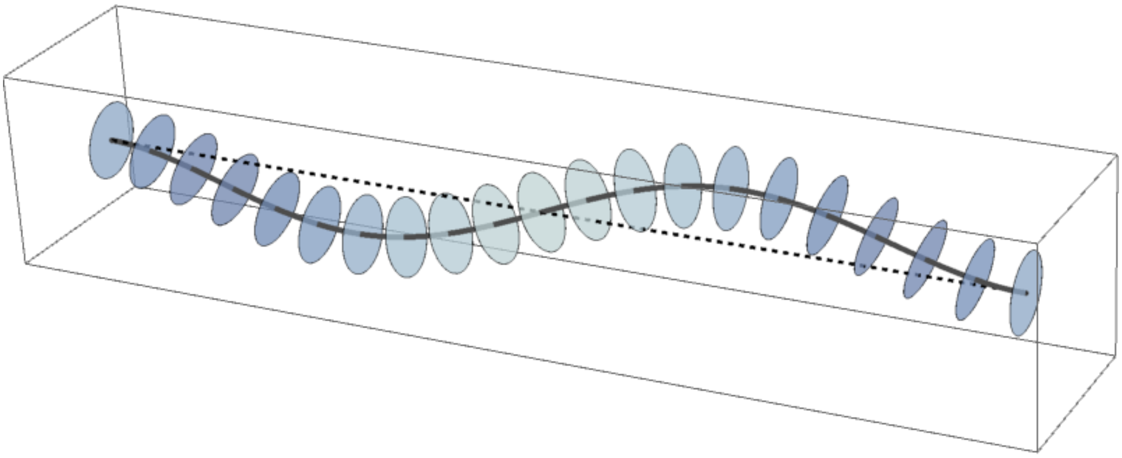

Figure 3.20: Second forward modal shape, with $\alpha = 50$, $\hat{\omega} = 10$, $\hat{N} = 0$, $\hat{T} = 0$ and $\nu = 0.3$.

Taking into account some additional remarks about representation of angular displacements, the instantaneous position of a cross-section of the shaft can be represented in terms of displacement of its center (v,w) and of a versor **n** orthogonal to its surface (planar by assumption), as shown in Fig. 3.21 (left).

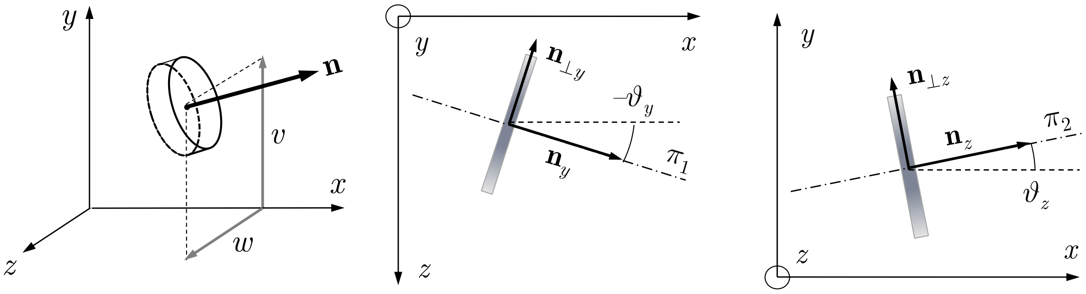

Figure 3.21: Schematic of a cross-section of the shaft in a generic position

The projections of **n** on the *x*-*y* and *x*-*z* orthogonal planes (say $\mathbf{n}_z$ and $\mathbf{n}_y$, respectively) define two other planes, as represented in Fig. 3.21 (right), where π_1 is parallel to $\mathbf{n}_y$ and perpendicular to x-z, while π_2 is parallel to $\mathbf{n}_z$ and perpendicular to x-y. The projections of **n**, along with the parametric representations of the π planes, can be expressed as functions of the angular displacements ϑ_y and ϑ_z:

$$\begin{cases} \dfrac{\mathbf{n}_y}{\left\|\mathbf{n}_y\right\|} = \begin{Bmatrix} \cos\vartheta_y \\ 0 \\ -\sin\vartheta_y \end{Bmatrix}, \quad \mathbf{p}_{\pi_1} = \begin{Bmatrix} n_1\cos\vartheta_y \\ h_1 \\ -n_1\sin\vartheta_y \end{Bmatrix} \\ \dfrac{\mathbf{n}_z}{\left\|\mathbf{n}_z\right\|} = \begin{Bmatrix} \cos\vartheta_z \\ \sin\vartheta_z \\ 0 \end{Bmatrix}, \quad \mathbf{p}_{\pi_2} = \begin{Bmatrix} n_2\cos\vartheta_z \\ n_2\sin\vartheta_z \\ h_2 \end{Bmatrix} \end{cases} \tag{3.17.1}$$

The orthogonal directions with respect to the π planes are identified by:

$$\begin{cases} \mathbf{n}_{\perp y} = \dfrac{\partial \mathbf{p}_{\pi_1}}{\partial h_1} \times \dfrac{\partial \mathbf{p}_{\pi_1}}{\partial n_1} = \begin{Bmatrix} -\sin\vartheta_y \\ 0 \\ -\cos\vartheta_y \end{Bmatrix} \\ \mathbf{n}_{\perp z} = \dfrac{\partial \mathbf{p}_{\pi_2}}{\partial h_2} \times \dfrac{\partial \mathbf{p}_{\pi_2}}{\partial n_2} = \begin{Bmatrix} -\sin\vartheta_z \\ \cos\vartheta_z \\ 0 \end{Bmatrix} \end{cases} \tag{3.17.2}$$

which give a definition of **n** as a function of ϑ_y and ϑ_z:

$$\begin{cases} \mathbf{n} = \dfrac{\mathbf{n}^+}{\left\|\mathbf{n}^+\right\|} \\ \mathbf{n}^+ = \mathbf{n}_{\perp y} \times \mathbf{n}_{\perp z} = \begin{Bmatrix} \cos\vartheta_y \cos\vartheta_z \\ \cos\vartheta_y \sin\vartheta_z \\ -\sin\vartheta_y \cos\vartheta_z \end{Bmatrix} \end{cases} \tag{3.17.3}$$

The expressions in Eq. (3.17.3) provide an unambiguous representation of the cross-section orientation in terms of angular displacements (ϑ_y ,ϑ_z), which in this Section has been adopted for improving the readability of plots. Notice that forward and backward modal shapes are different, as for instance results from Fig. 3.13 to 3.15, due to a lack of symmetry with respect to the $\Re(a)$-$\Im(a)$ plane.

3.18 Critical speeds

Critical speeds are computed according to the procedure described in Section 3.8, through Eq. (3.8.6) and (3.8.7). Campbell 2D diagrams are shown in Fig. 3.10, where straight dotted lines represent the condition $\lambda = \hat{\omega}$. However, the effects of the main governing parameters on critical speeds are better highlighted by the diagrams displayed in Fig. 3.22. There the square root of the first non-dimensional forward critical speed $\sqrt{\hat{\omega}_{C1}}$ of a rotating shaft with $\nu = 0.3$ and clamped ends (null rotations and shear deformations) is represented as a function of the slenderness ratio α, for different values of $\hat{T}$ in combination with $\hat{N} = 0$ (left), $\hat{N} > 0$ (center) and $\hat{N} < 0$ (right). Increasing the modulus of $\hat{T}$ always lowers the critical speeds. If $\hat{N} = 0$, then $\hat{\omega}_{C1}$ shows an asymptotic behaviour towards the first nondimensional natural frequency of a slender beam (dotted line in Fig. 3.22: $\sqrt{\hat{\omega}_{C1}} = 4.730$ [102]), since increasing α the Timoshenko model tends to the Euler-Bernoulli one. The case of traction ($\hat{N} > 0$) produces a stiffening effect on the shaft, raising its critical speeds. The case of compression ($\hat{N} < 0$) causes the opposite effect.

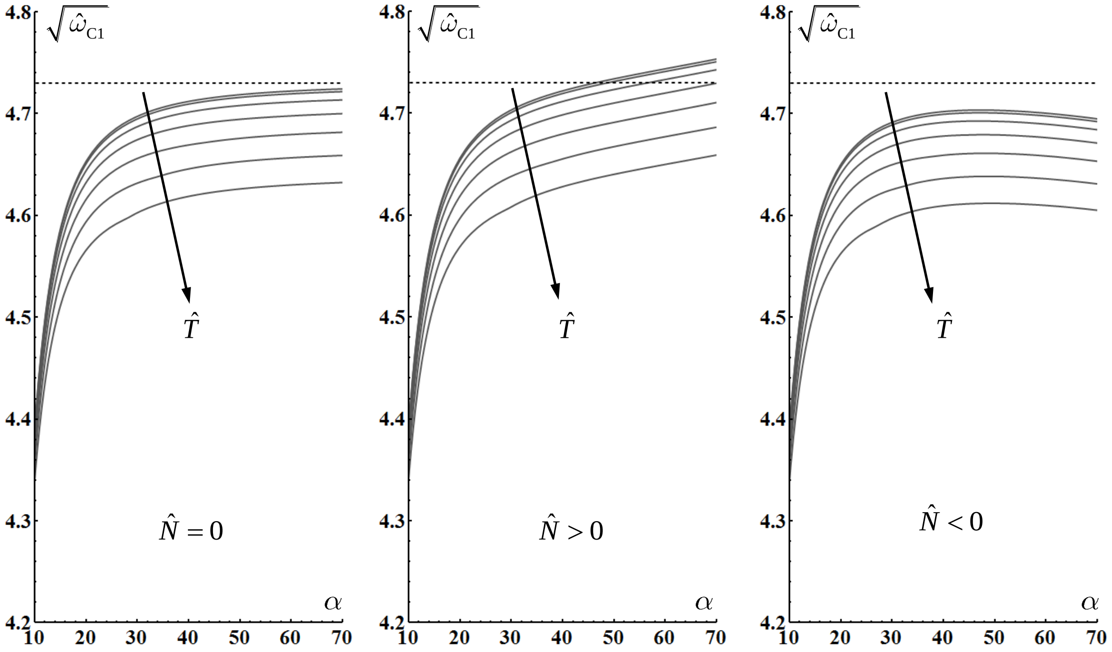

Figure 3.22: First forward critical speed $\sqrt{\hat{\omega}_{C1}}$ as a function of α for different values of $\hat{T}$

Campbell 3D diagrams can also be drawn, highlighting the influence of a third parameter (say β), other than natural frequency λ and rotating angular speed $\hat{\omega}$. The *n*-th non-dimensional critical speed $\hat{\omega}_C$ is represented by a curve obtained by intersection of the surface associated to the *n*-th natural frequency $\lambda = \lambda(\hat{\omega}, \beta)$ with the plane $\lambda = \hat{\omega}$. For instance, the curve representing the first forward critical speed $\hat{\omega}_{C1}$ of a rotating shaft with $\alpha = 50$, $\nu = 0.3$ and clamped ends (null rotations and shear deformations) is displayed in Fig. 3.23 as a function of $\beta = \hat{N}$ with $\hat{T} = 0$ and $\beta = \hat{T}$ with $\hat{N} = 0$ in Fig. 3.24 (where for testing the robustness of computational algorithms and to emphasize the effects of $\hat{T}$, its range of variation has been increased up to unrealistic values).

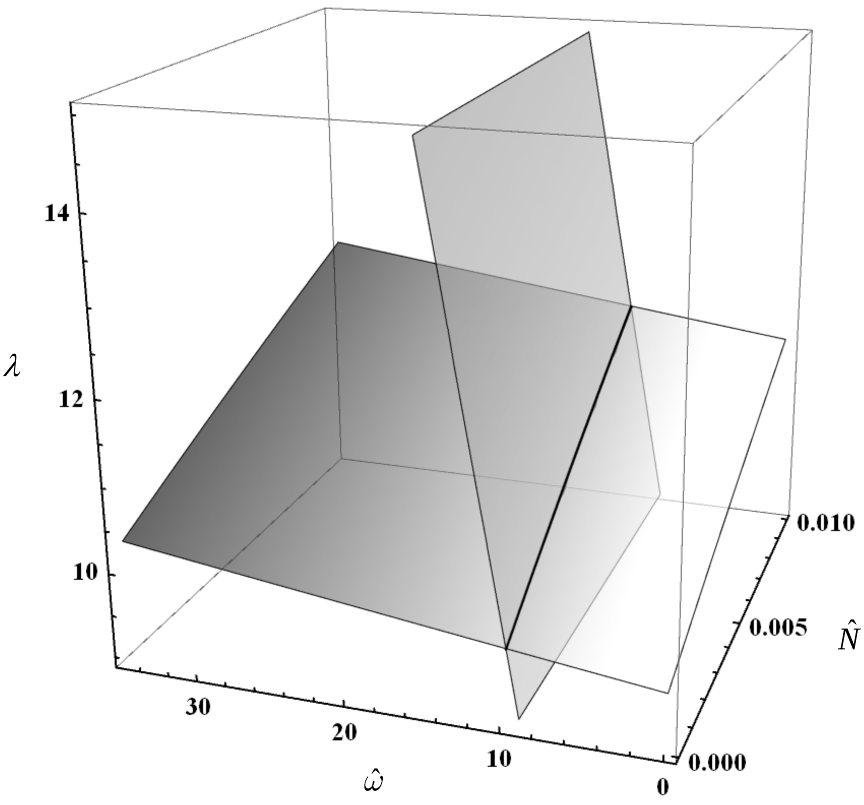

Figure 3.23: Campbell 3D diagrams, first forward critical speed, as a function of $\hat{N}$.

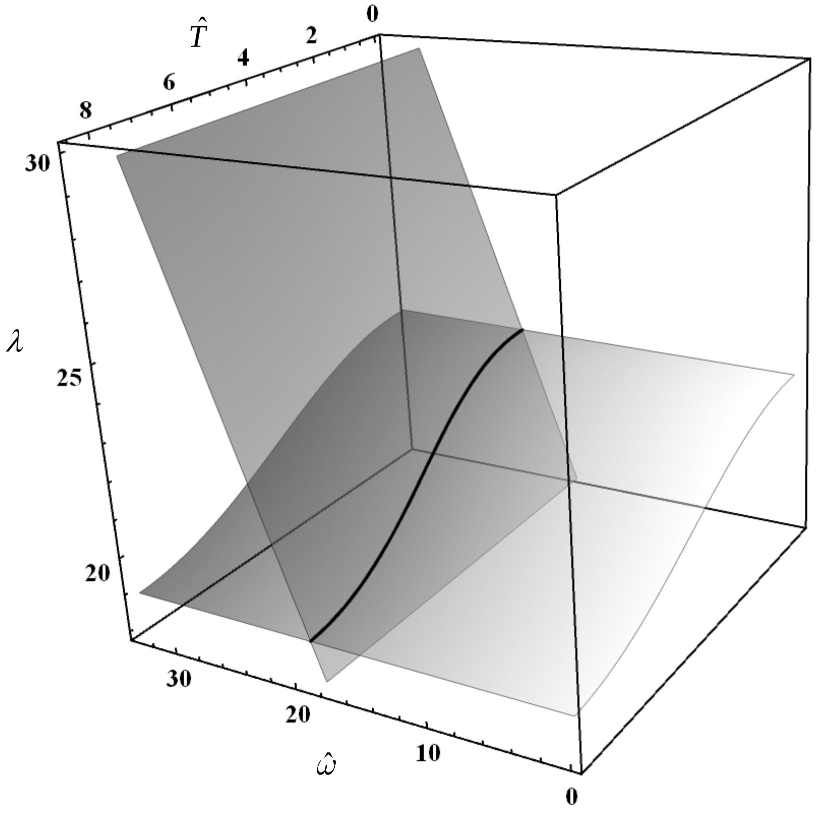

Figure 3.24: Campbell 3D diagrams, first forward critical speed, as a function of $\hat{T}$.

4 STABILITY ANALYSIS OF PARAMETRICALLY EXCITED ROTORS

4.1 Introduction

In this Chapter a novel contribution is given aimed at clarifying gyroscopic effects on the stability of parametrically excited rotor systems, also considering and analyzing the contextual and not negligible role played by both external (non-rotating) and internal (rotating) damping distributions. As study-case including all features of interest for this analysis, giving rise to a set of coupled differential Mathieu-Hill equations with both gyroscopic and damping terms, a continuous perfectly balanced shaft is considered, modelled as a spinning Timoshenko beam loaded by axial end thrust and twisting moment oscillating at the same period. The assumption of different external loads acting at the same frequency does not affect the results presented in this Chapter, indeed the adopted methodology remains valid also in the case of loads acting at different frequencies as long as the resulting system can be considered periodic (see Chapter 2). The coupled partial differential equations of motion of the shaft, derived in Chapter 3, are first reduced to a set of coupled ordinary differential Mathieu-Hill equations through Galerkin discretization (exact decoupling into a set of single-degree-of-freedom equations, as for the Rayleigh beam model [77], in this case is not possible). Stability of solutions is then studied via eigenproblem formulation, obtained by applying the harmonic balance method. Five simplified cases (two Hamiltonian and three non-Hamiltonian) are first analyzed in order to draw theoretical conclusions about the influence of gyroscopic and external damping terms (when they are not both present). A numerical algorithm is subsequently developed for computing global stability thresholds in presence of both gyroscopic and damping terms. Finally, the influence on stability of the main characteristic parameters of the shaft is analyzed on stability charts (Ince-Strutt diagrams [42]) with respect to frequency and amplitude of the external loads.

From this point onwards, the adopted formulation and numerical algorithms are also suitable for application to a more general category of gyroscopic systems, including complex shape rotors in those cases in which properly condensed finite element models are available.

4.2 Description of the study-case and the derivation of the equations of motion

An homogeneous uniform Timoshenko straight beam with circular section is considered, made of isotropic material, rotating at constant angular speed about its longitudinal axis with clamped ends as boundary conditions, with now the possibility of carrying additional inertial elements (like discs or flywheels) mounted at given points on its longitudinal axis, enhancing gyroscopic effects. The choice of boundary conditions that was made is due to the fact that clamped ends is the most common type of constraints in practical applications involving spinning shafts (sufficiently long bearings). The system is simultaneously subjected to axial end thrust and twisting moment, as in Chapter 3, but from now on, both of them assumed to have harmonic time-dependent components oscillating at the same frequency. In Fig. 4.1 a schematic representation of the generic additional inertial element mounted on the shaft is provided.

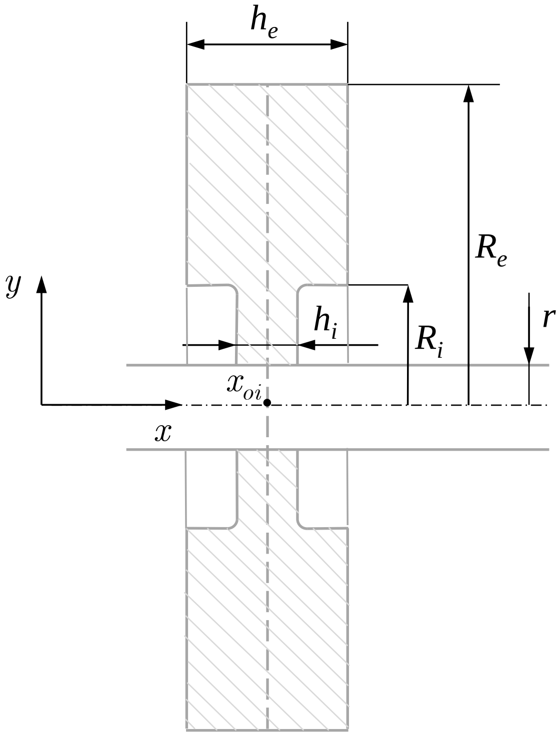

Figure 4.1: Schematic representation of the shaft with additional disc.

Adopting the same notation and nomenclature adopted in Chapter 3, the equations of motion for the system's flexural dynamic behavior, previously described in Eq. (3.4.15), take the form:

$$\begin{cases} \rho A\, f_1 \ddot{v} - \kappa G A (v^{\mathrm{II}} - \vartheta_z^{\mathrm{I}}) - N(t)\,\vartheta_z^{\mathrm{I}} = 0 \\ \rho A\, f_1 \ddot{w} - \kappa G A (w^{\mathrm{II}} + \vartheta_y^{\mathrm{I}}) + N(t)\,\vartheta_y^{\mathrm{I}} = 0 \\ \rho J\, f_2 \ddot{\vartheta}_y + \rho J_0\, f_3 \omega \dot{\vartheta}_z + \left[\kappa G A - N(t)\right](w^{\mathrm{I}} + \vartheta_y) - EJ\vartheta_y^{\mathrm{II}} - T(t)\,\vartheta_z^{\mathrm{I}} = 0 \\ \rho J\, f_2 \ddot{\vartheta}_z - \rho J_0\, f_3 \omega \dot{\vartheta}_y - \left[\kappa G A - N(t)\right](v^{\mathrm{I}} - \vartheta_z) - EJ\vartheta_z^{\mathrm{II}} + T(t)\,\vartheta_y^{\mathrm{I}} = 0 \end{cases} \tag{4.2.1}$$

in which $J_0 = 2\,J$, while:

$$\begin{cases} f_1 = 1 + \sum_i \hat{m}_i\, l\, \delta(x - x_{0i}) \\ f_2 = 1 + \sum_i \hat{J}_{1i}\, l\, \delta(x - x_{0i}) \\ f_3 = 1 + \sum_i \hat{J}_{0i}\, l\, \delta(x - x_{0i}) \\ \mathbf{J}_{di} = \begin{bmatrix} J_{d0i} & 0 & 0 \\ 0 & J_{d1i} & 0 \\ 0 & 0 & J_{d1i} \end{bmatrix} \end{cases} \quad \text{with} \quad \begin{cases} \hat{m}_i = \dfrac{m_{di}}{\rho A l} \\ \hat{J}_{1i} = \dfrac{J_{d1i}}{\rho J l} \\ \hat{J}_{0i} = \dfrac{J_{d0i}}{\rho J_0 l} \end{cases} \tag{4.2.2}$$

where m_{di} is the mass of the *i*-th disc or cylinder mounted on the shaft, $\mathbf{J}_{di}$ is the inertia tensor of the *i*-th disc or cylinder and, as usual, δ(·) represents the Dirac distribution. Notice that Eq, (4.2.1) can be obtained via the procedure described in Section 3.4 considering the additional inertia due to the presence of the rigid bodies. Thus, only the kinetic energy is affected by the presence of discs or cylinders mounted on the shaft. Equation (4.2.1) directly shows the dependence of the load terms on time:

$$\begin{cases} N(t) = N_0 + \Delta N \cos(\omega_\mathrm{L} t) \\ T(t) = T_0 + \Delta T \cos(\omega_\mathrm{L} t) \end{cases} \tag{4.2.3}$$

in which ω_L is the angular frequency of the harmonic component of the external loads. The equations of motion, Eq. (4.2.1), are first cast in full non-dimensional form by recalling Eq. (3.7.1), Eq. (3.7.2) and by introducing the following non-dimensional terms:

$$\begin{cases} \hat{\varOmega} = \dfrac{\omega_\mathrm{L}}{\varOmega} \\ \hat{N}(\tau) = \dfrac{N_0}{EA} + \dfrac{\Delta N}{EA}\cos(\hat{\varOmega}\tau) = \hat{N}_0 + \Delta\hat{N}\cos(\hat{\varOmega}\tau) \\ \hat{T}(\tau) = \dfrac{T_0 l}{EJ} + \dfrac{\Delta T\, l}{EJ}\cos(\hat{\varOmega}\tau) = \hat{T}_0 + \Delta\hat{T}\cos(\hat{\varOmega}\tau) \end{cases} \tag{4.2.4}$$

Notice that $\hat{N}_0$ and $\hat{T}_0$ are defined exactly as $\hat{N}$ and $\hat{T}$ in Chapter 3. Then the mass and gyroscopic operators, both algebraic, already obtained for the spinning beam alone without additional rigid bodies in Section 3.5, take the following matrix form:

$$\begin{cases} \mathbf{M} = \begin{bmatrix} f_1 & 0 & 0 & 0 \\ 0 & f_1 & 0 & 0 \\ 0 & 0 & \dfrac{f_2}{\alpha^2} & 0 \\ 0 & 0 & 0 & \dfrac{f_2}{\alpha^2} \end{bmatrix} \\ \mathbf{G} = \begin{bmatrix} 0 & 0 & 0 & 0 \\ 0 & 0 & 0 & 0 \\ 0 & 0 & 0 & 2\hat{\omega}\dfrac{f_3}{\alpha^2} \\ 0 & 0 & -2\hat{\omega}\dfrac{f_3}{\alpha^2} & 0 \end{bmatrix} \end{cases} \tag{4.2.5}$$

While displacement operator (differential, including stiffness and external load terms) takes the form:

$$[\mathcal{K}(\cdot)]=\begin{bmatrix} -\dfrac{\alpha^2}{\sigma}(\cdot)^{\mathrm{II}} & 0 & 0 & \dfrac{\alpha^2}{\sigma}\psi(\tau)(\cdot)^{\mathrm{I}} \\ 0 & -\dfrac{\alpha^2}{\sigma}(\cdot)^{\mathrm{II}} & -\dfrac{\alpha^2}{\sigma}\psi(\tau)(\cdot)^{\mathrm{I}} & 0 \\ 0 & \dfrac{\alpha^2}{\sigma}\psi(\tau)(\cdot)^{\mathrm{I}} & \dfrac{\alpha^2}{\sigma}\psi(\tau)(\cdot)-(\cdot)^{\mathrm{II}} & -\hat{T}(\tau)(\cdot)^{\mathrm{I}} \\ -\dfrac{\alpha^2}{\sigma}\psi(\tau)(\cdot)^{\mathrm{I}} & 0 & \hat{T}(\tau)(\cdot)^{\mathrm{I}} & \dfrac{\alpha^2}{\sigma}\psi(\tau)(\cdot)-(\cdot)^{\mathrm{II}} \end{bmatrix} \tag{4.2.6}$$

where the quantity $\psi(\tau)$, as the constant parameter ψ introduced in Section 3.3, reads:

$$\psi(\tau)=1-\sigma\hat{N}(\tau) \tag{4.2.7}$$

Notice that the *T*-dependent terms in Eq. (4.2.6) are circulatory terms. Operator $[\mathcal{K}(\cdot)]$ can in turn be expressed as a sum of three operators by splitting the parameter $\psi(\tau)$ in Eq. (4.2.7):

$$[\mathcal{K}(\cdot)]=[\mathcal{K}_0(\cdot)]+[\mathfrak{L}_0(\cdot)]+\Delta L\cos(\hat{\Omega}\tau)[\mathfrak{L}(\cdot)] \tag{4.2.8}$$

in which the quantity ΔL was introduced; in the present analysis ΔL is defined as follows:

$$\begin{cases} \Delta L=\Delta\hat{N} \\ R_{T,N}=\dfrac{\Delta\hat{T}}{\Delta\hat{N}} \quad\Rightarrow\quad \Delta\hat{T}=R_{T,N}\Delta\hat{N}=R_{T,N}\Delta L \end{cases} \tag{4.2.9}$$

where $R_{T,N}$ is a adjustable parameter. Regarding the operators in Eq. (4.2.8), $[\mathcal{K}_0(\cdot)]$ does not depend on external loads, $[\mathfrak{L}_0(\cdot)]$ depends only on the constant components of external loads and $[\mathfrak{L}(\cdot)]$ depends only on the amplitudes of the harmonic components of the latter. The differential operators $[\mathcal{K}_0(\cdot)]$, $[\mathfrak{L}_0(\cdot)]$ and $[\mathfrak{L}(\cdot)]$ are explicitly reported in Eq. (4.2.10).

$$\begin{cases} [\mathcal{K}_0(\cdot)] = \begin{bmatrix} -\dfrac{\alpha^2}{\sigma}(\cdot)^{\mathrm{II}} & 0 & 0 & \dfrac{\alpha^2}{\sigma}(\cdot)^{\mathrm{I}} \\ 0 & -\dfrac{\alpha^2}{\sigma}(\cdot)^{\mathrm{II}} & -\dfrac{\alpha^2}{\sigma}(\cdot)^{\mathrm{I}} & 0 \\ 0 & \dfrac{\alpha^2}{\sigma}(\cdot)^{\mathrm{I}} & \dfrac{\alpha^2}{\sigma}(\cdot)-(\cdot)^{\mathrm{II}} & 0 \\ -\dfrac{\alpha^2}{\sigma}(\cdot)^{\mathrm{I}} & 0 & 0 & \dfrac{\alpha^2}{\sigma}(\cdot)-(\cdot)^{\mathrm{II}} \end{bmatrix} \\ [\mathfrak{L}_0(\cdot)] = \begin{bmatrix} 0 & 0 & 0 & -\alpha^2 \hat{N}_0(\cdot)^{\mathrm{I}} \\ 0 & 0 & \alpha^2 \hat{N}_0(\cdot)^{\mathrm{I}} & 0 \\ 0 & -\alpha^2 \hat{N}_0(\cdot)^{\mathrm{I}} & -\alpha^2 \hat{N}_0(\cdot) & -\hat{T}_0(\cdot)^{\mathrm{I}} \\ \alpha^2 \hat{N}_0(\cdot)^{\mathrm{I}} & 0 & \hat{T}_0(\cdot)^{\mathrm{I}} & -\alpha^2 \hat{N}_0(\cdot) \end{bmatrix} \\ [\mathfrak{L}(\cdot)] = \begin{bmatrix} 0 & 0 & 0 & -\alpha^2(\cdot)^{\mathrm{I}} \\ 0 & 0 & \alpha^2(\cdot)^{\mathrm{I}} & 0 \\ 0 & -\alpha^2(\cdot)^{\mathrm{I}} & -\alpha^2(\cdot) & -R_{T,N}(\cdot)^{\mathrm{I}} \\ \alpha^2(\cdot)^{\mathrm{I}} & 0 & R_{T,N}(\cdot)^{\mathrm{I}} & -\alpha^2(\cdot) \end{bmatrix} \end{cases} \tag{4.2.10}$$

Thus the equations of motion in Eq. (4.2.1) can be expressed in the following non-dimensional operator form:

$$\begin{cases} \mathbf{M}\ddot{\mathbf{q}} + \mathbf{G}\dot{\mathbf{q}} + [\mathcal{K}_0]\mathbf{q} + [\mathfrak{L}_0]\mathbf{q} + \Delta L \cos(\hat{\Omega}\tau)[\mathfrak{L}]\mathbf{q} = \mathbf{0} \\ \mathbf{q} = \{v, w, \vartheta_y, \vartheta_z\}^{\mathrm{T}}, \quad \mathbf{q} = \mathbf{q}(\xi, \tau) \end{cases} \tag{4.2.11}$$

The first of Eq. (4.2.11) represents a system of second-order (with respect to both dimensionless time and space) coupled differential equations, with periodic coefficients. Unlike the system with constant coefficients discussed in Chapter 3, the system in Eq. (4.2.11) does not allow to obtain closed-form solutions in terms of eigenvalues and eigenfunctions. However, stability analysis can be carried out with the help of Floquet Theory after using a discretization technique on spectral basis.

4.3 Discretization of the equations of motion

In order to reduce the system in Eq. (4.2.11) to a system of coupled Mathieu-Hill ordinary differential equations, a suitable discretization technique becomes essential. Since even for the time-independent case the operators remain non-self-adjoint, no technique based on Rayleigh's quotient stationarity principle can be suitable. Thus, Rayleigh's energy method, Rayleigh-Ritz

method, assumed-modes method and all their variants, including those involving the use of comparison functions or quasi-comparison functions, cannot be adopted in order to discretize the system in Eq. (4.2.11). The method of weighted residuals, on the other hand, is suitable for the task, since it works directly with the differential equations and not with the energy density functionals like Rayleigh-Ritz methods. To be precise, the method of weighted residuals corresponds to a group of methods all suited to work with non-self-adjoint differential operators. In the present Section the Galerkin method, which is part of the aforementioned group of methods, is chosen to perform the discretization of the equations of motion.
First of all, a structure for the solution must be assumed. To do so, a single generic linear inseparable partial differential equation is considered and let $X\left(\xi,\tau\right)$ be the unknown function representing its solution. Such a function can be expressed as infinite series as follows:

$$X\left(\xi,\tau\right)=\sum_{i=1}^{\infty}Y_i\left(\xi\right)\,q_i\left(\tau\right) \tag{4.3.1}$$

in which functions $Y_i\left(\xi\right)$ are from a complete infinite set of orthogonal functions over the space domain. To prove that the series converges to the function $X\left(\xi,\tau\right)$ is sufficient to show that functions $q_i\left(\tau\right)$ exist for each *i* and that they depend only on τ. Due to orthogonality properties of the spatial functions it must be:

$$\begin{aligned}
&Y_j\left(\xi\right)\,X\left(\xi,\tau\right)=\sum_{i=1}^{\infty}Y_j\left(\xi\right)\,Y_i\left(\xi\right)\,q_i\left(\tau\right), \quad \Rightarrow\\
&\qquad\Rightarrow\quad \int_0^1 Y_j\left(\xi\right)\,X\left(\xi,\tau\right)d\xi=\int_0^1\left[\sum_{i=1}^{\infty}Y_j\left(\xi\right)\,Y_i\left(\xi\right)\,q_i\left(\tau\right)\right]d\xi \quad \Rightarrow\\
&\qquad\Rightarrow\quad \int_0^1 Y_j\left(\xi\right)\,X\left(\xi,\tau\right)d\xi=q_j\left(\tau\right)\int_0^1\left[Y_j\left(\xi\right)\right]^2 d\xi
\end{aligned} \tag{4.3.2}$$

Hence, replacing the subscript *j* with *i*, functions $q_i\left(\tau\right)$ take the form:

$$\begin{cases}
q_i\left(\tau\right)=s_i\int_0^1 Y_i\left(\xi\right)\,X\left(\xi,\tau\right)d\xi\\
s_i=\left\{\int_0^1\left[Y_i\left(\xi\right)\right]^2 d\xi\right\}^{-1}
\end{cases} \tag{4.3.3}$$

Thus, Eq. (4.3.3) implies that as long as $X\left(\xi,\tau\right)$ and s_i exist, $q_i\left(\tau\right)$ also exists for each *i*. According to the first of Eq. (4.3.3) and to the *Fundamental Theorem of Calculus*, functions $q_i\left(\tau\right)$ depend only on τ. Truncating the series in Eq. (4.3.1) up to a finite number of terms, say N, thus restricting the approximation to a finite-dimensional subspace, Eq. (4.3.1) reads:

$$X\left(\xi,\tau\right)\cong X^{(\mathrm{N})}\left(\xi,\tau\right)=\sum_{i=1}^{\mathrm{N}}Y_i\left(\xi\right)\,q_i\left(\tau\right) \tag{4.3.4}$$

Introducing a quadrature rule and a residual function E_R such that:

$$E_R = \int_0^1 \left[X(\xi,\tau) - \sum_{i=1}^{\mathrm{N}} Y_i(\xi)\, q_i(\tau) \right]^2 d\xi \tag{4.3.5}$$

it is true that, if N is let to tend to infinity, the convergence is guaranteed by the *Completeness Theorem* or *Riesz-Fisher Theorem* [105, 106], in other words $X(\xi,\tau)$ is square integrable if and only if its generalized Fourier series converges and, therefore, the associated Bessel's inequality coincides with the Parseval's identity. Hence, if $X(\xi,\tau)$ is square integrable Eq. (4.3.1) is legitimate and, as a consequence, the residual E_R goes to zero.

By virtue of the simplifying hypothesis of using the same number, say again N, of trial functions to expand the four unknown functions in Eq. (4.2.11), let $\mathbf{q}_d(\tau)$ be a partitioned $4\mathrm{N}\times 1$ vector of unknown weights such that:

$$\mathbf{q}(\xi,\tau) \cong \mathbf{q}^{(\mathrm{N})}(\xi,\tau) = \mathbf{\Gamma}^{\mathrm{T}}(\xi)\, \mathbf{q}_d(\tau) \tag{4.3.6}$$

where $\mathbf{q}^{(\mathrm{N})}(\xi,\tau)$ is the N-th approximate solution and $\mathbf{\Gamma}(\xi)$ is a $4\mathrm{N}\times 4$ matrix such that:

$$\mathbf{\Gamma} = \begin{bmatrix} \mathbf{v} & 0 & 0 & 0 \\ 0 & \mathbf{w} & 0 & 0 \\ 0 & 0 & \boldsymbol{\theta}_y & 0 \\ 0 & 0 & 0 & \boldsymbol{\theta}_z \end{bmatrix} \tag{4.3.7}$$

in which **v**, **w**, $\boldsymbol{\theta}_y$ and $\boldsymbol{\theta}_z$ are N-vectors of trial functions from a complete set:

$$\begin{cases} \mathbf{v} = \left\{ \mathrm{v}_1(\xi), \mathrm{v}_2(\xi), \ldots, \mathrm{v}_{\mathrm{N}}(\xi) \right\}^{\mathrm{T}} \\ \mathbf{w} = \left\{ \mathrm{w}_1(\xi), \mathrm{w}_2(\xi), \ldots, \mathrm{w}_{\mathrm{N}}(\xi) \right\}^{\mathrm{T}} \\ \boldsymbol{\theta}_y = \left\{ \theta_{y1}(\xi), \theta_{y2}(\xi), \ldots, \theta_{y\mathrm{N}}(\xi) \right\}^{\mathrm{T}} \\ \boldsymbol{\theta}_z = \left\{ \theta_{z1}(\xi), \theta_{z2}(\xi), \ldots, \theta_{z\mathrm{N}}(\xi) \right\}^{\mathrm{T}} \end{cases} \tag{4.3.8}$$

It is convenient to choose accurately the sets of trial functions to encourage the convergence of Galerkin method. For this purpose, closed-form expression of eigenfunctions related to the simpler problem (simple shaft with constant loads) have been provided in Chapter 3. Thus, recalling Eq. (3.11.5), Eq. (4.3.8) can be rewritten as:

$$\begin{cases} \mathbf{v} = \left\{ \phi_{v1}(\xi), \phi_{v2}(\xi), \ldots, \phi_{v\mathrm{N}}(\xi) \right\}^{\mathrm{T}} \\ \mathbf{w} = \left\{ \phi_{w1}(\xi), \phi_{w2}(\xi), \ldots, \phi_{w\mathrm{N}}(\xi) \right\}^{\mathrm{T}} \\ \boldsymbol{\theta}_y = \left\{ \phi_{\vartheta_y 1}(\xi), \phi_{\vartheta_y 2}(\xi), \ldots, \phi_{\vartheta_y \mathrm{N}}(\xi) \right\}^{\mathrm{T}} \\ \boldsymbol{\theta}_z = \left\{ \phi_{\vartheta_z 1}(\xi), \phi_{\vartheta_z 2}(\xi), \ldots, \phi_{\vartheta_z \mathrm{N}}(\xi) \right\}^{\mathrm{T}} \end{cases} \tag{4.3.9}$$

Notice that, for some boundary conditions, (Eq. (3.9.1) to Eq. (3.9.5)), the eigenfunctions of the constant coefficient problem remain comparison functions and, therefore, they respect all the boundary conditions even in the case of time-dependent loads. The choice of clamped ends with null shear deformation as in Eq. (3.9.1) is an example.

Replacing Eq. (4.3.9) in Eq. (4.3.7), (4.3.6) and then in Eq. (4.2.11), leads to the following equation:

$$\mathbf{M}\boldsymbol{\Gamma}^{\mathrm{T}}\ddot{\mathbf{q}}_d+\mathbf{G}\boldsymbol{\Gamma}^{\mathrm{T}}\dot{\mathbf{q}}_d+\left\{\left[\mathcal{K}_0\right]\boldsymbol{\Gamma}^{\mathrm{T}}+\left[\mathfrak{L}_0\right]\boldsymbol{\Gamma}^{\mathrm{T}}+\Delta L\cos(\hat{\Omega}\tau)\left[\mathfrak{L}\right]\boldsymbol{\Gamma}^{\mathrm{T}}\right\}\mathbf{q}_d=\mathbf{0} \tag{4.3.10}$$

Multiplying from the left both sides of Eq. (4.3.10) by $\boldsymbol{\Gamma}$ gives:

$$\boldsymbol{\Gamma}\mathbf{M}\boldsymbol{\Gamma}^{\mathrm{T}}\ddot{\mathbf{q}}_d+\boldsymbol{\Gamma}\mathbf{G}\boldsymbol{\Gamma}^{\mathrm{T}}\dot{\mathbf{q}}_d+\boldsymbol{\Gamma}\left\{\left[\mathcal{K}_0\right]\boldsymbol{\Gamma}^{\mathrm{T}}+\left[\mathfrak{L}_0\right]\boldsymbol{\Gamma}^{\mathrm{T}}+\Delta L\cos(\hat{\Omega}\tau)\left[\mathfrak{L}\right]\boldsymbol{\Gamma}^{\mathrm{T}}\right\}\mathbf{q}_d=\mathbf{0} \tag{4.3.11}$$

Integrating Eq. (4.3.11) over the whole dimensionless space-domain leads to:

$$\hat{\mathbf{M}}\ddot{\mathbf{q}}_d+\hat{\mathbf{G}}\dot{\mathbf{q}}_d+\left[\hat{\mathbf{K}}_0+\hat{\mathbf{L}}_0+\Delta L\cos(\hat{\Omega}\tau)\hat{\mathbf{L}}\right]\mathbf{q}_d=\mathbf{0} \tag{4.3.12}$$

in which $\hat{\mathbf{M}}$, $\hat{\mathbf{G}}$, $\hat{\mathbf{K}}_0$, $\hat{\mathbf{L}}_0$ and $\hat{\mathbf{L}}$ are the $4\mathrm{N}\times 4\mathrm{N}$ algebraic operators of the discrete-space system, explicitly:

$$\begin{cases}\hat{\mathbf{M}}=\int_0^1\boldsymbol{\Gamma}\mathbf{M}\boldsymbol{\Gamma}^{\mathrm{T}}d\xi\\ \hat{\mathbf{G}}=\int_0^1\boldsymbol{\Gamma}\mathbf{G}\boldsymbol{\Gamma}^{\mathrm{T}}d\xi\\ \hat{\mathbf{K}}_0=\int_0^1\boldsymbol{\Gamma}\left[\mathcal{K}_0\right]\boldsymbol{\Gamma}^{\mathrm{T}}d\xi\\ \hat{\mathbf{L}}_0=\int_0^1\boldsymbol{\Gamma}\left[\mathfrak{L}_0\right]\boldsymbol{\Gamma}^{\mathrm{T}}d\xi\\ \hat{\mathbf{L}}=\int_0^1\boldsymbol{\Gamma}\left[\mathfrak{L}\right]\boldsymbol{\Gamma}^{\mathrm{T}}d\xi\end{cases} \tag{4.3.13}$$

where $\hat{\mathbf{M}}$ is the mass matrix, $\hat{\mathbf{G}}$ is the gyroscopic matrix, $\hat{\mathbf{K}}_0$ is the stiffness matrix of the unloaded system while $\hat{\mathbf{L}}_0$ and $\hat{\mathbf{L}}$ are the matrices due to external loads. Notice that $\hat{\mathbf{L}}$ is a function of the fixed ratio $R_{T,N}$ defined in Eq. (4.2.9). In addition, a non-rotating (stabilizing) damping distribution is considered, by introducing a damping matrix **D** directly into the discretized equations of motion:

$$\begin{cases}\hat{\mathbf{M}}\ddot{\mathbf{q}}_d+\hat{\mathbf{C}}\dot{\mathbf{q}}_d+\left[\hat{\mathbf{K}}+\Delta L\cos(\hat{\Omega}\tau)\hat{\mathbf{L}}\right]\mathbf{q}_d=\mathbf{0}\\ \hat{\mathbf{C}}=\hat{\mathbf{G}}+\hat{\mathbf{D}}\\ \hat{\mathbf{K}}=\hat{\mathbf{K}}_0+\hat{\mathbf{L}}_0\end{cases} \tag{4.3.14}$$

resulting in a system of coupled Mathieu-Hill ordinary differential equations with both gyroscopic and damping terms. It is convenient for further developments, carried out in the next Sections, to perform specific coordinate transforms that reduce the computational load (also in terms of memory storage) and the possible emergence of ill-conditionings. The simplified problem (without gyroscopic effects, damping effects and without oscillating terms, *i.e.* $\Delta L = 0$) reads:

$$\hat{\mathbf{M}}\ddot{\mathbf{x}} + \hat{\mathbf{K}}\mathbf{x} = \mathbf{0} \tag{4.3.15}$$

First, the right and left modal matrices, say $\mathbf{V}_R$ and $\mathbf{V}_L$ associated to Eq. (4.3.15) are computed. In the present notation $\mathbf{V}_L$ has the left eigenvectors as rows, then the following change of co-ordinates is adopted:

$$\mathbf{q}_d = \mathbf{V}_R\mathbf{y} \tag{4.3.16}$$

Substituting Eq. (4.3.16) in Eq. (4.3.14) and multiplying from the left by $\mathbf{V}_L$ gives:

$$\begin{aligned} &\mathbf{V}_L\hat{\mathbf{M}}\mathbf{V}_R\ddot{\mathbf{y}} + \mathbf{V}_L\hat{\mathbf{C}}\mathbf{V}_R\dot{\mathbf{y}} + \mathbf{V}_L\left[\hat{\mathbf{K}} + \Delta L\cos(\hat{\Omega}\tau)\hat{\mathbf{L}}\right]\mathbf{V}_R\mathbf{y} = \\ &\qquad = \bar{\mathbf{M}}\ddot{\mathbf{y}} + \bar{\mathbf{C}}\dot{\mathbf{y}} + \left[\bar{\mathbf{K}} + \Delta L\cos(\hat{\Omega}\tau)\bar{\mathbf{L}}\right]\mathbf{y} = \mathbf{0} \end{aligned} \tag{4.3.17}$$

in which $\bar{\mathbf{M}}$ and $\bar{\mathbf{K}}$ are diagonal matrices, while $\bar{\mathbf{C}}$ and $\bar{\mathbf{L}}$ are not. It is trivial now to compute the inverse square root of $\bar{\mathbf{M}}$; introducing the next coordinate change:

$$\mathbf{y} = \bar{\mathbf{M}}^{-1/2}\mathbf{u} \tag{4.3.18}$$

replacing it in Eq. (4.3.17) and multiplying from the left again by $\bar{\mathbf{M}}^{-1/2}$ yields:

$$\mathbf{I}\ddot{\mathbf{u}} + \bar{\mathbf{M}}^{-1/2}\bar{\mathbf{C}}\bar{\mathbf{M}}^{-1/2}\dot{\mathbf{u}} + \bar{\mathbf{M}}^{-1/2}\bar{\mathbf{K}}\bar{\mathbf{M}}^{-1/2}\mathbf{u} + \Delta L\cos(\hat{\Omega}\tau)\bar{\mathbf{M}}^{-1/2}\bar{\mathbf{L}}\bar{\mathbf{M}}^{-1/2}\mathbf{u} = \mathbf{0} \tag{4.3.19}$$

More compactly:

$$\begin{cases} \mathbf{I}\ddot{\mathbf{u}} + \bar{\bar{\mathbf{C}}}\dot{\mathbf{u}} + \left[\bar{\bar{\mathbf{K}}} + \Delta L\cos(\hat{\Omega}\tau)\bar{\bar{\mathbf{L}}}\right]\mathbf{u} = \mathbf{0} \\ \bar{\bar{\mathbf{C}}} = \bar{\mathbf{M}}^{-1/2}\bar{\mathbf{C}}\bar{\mathbf{M}}^{-1/2} \\ \bar{\bar{\mathbf{K}}} = \bar{\mathbf{M}}^{-1/2}\bar{\mathbf{K}}\bar{\mathbf{M}}^{-1/2} \\ \bar{\bar{\mathbf{L}}} = \bar{\mathbf{M}}^{-1/2}\bar{\mathbf{L}}\bar{\mathbf{M}}^{-1/2} \end{cases} \tag{4.3.20}$$

where **I** is the $4\mathrm{N} \times 4\mathrm{N}$ identity matrix. Notice that the matrix $\bar{\bar{\mathbf{K}}}$ thus obtained is such that:

$$\bar{\bar{\mathbf{K}}} = diag\left[\omega_1^2, \omega_2^2, \dots, \omega_{4\mathrm{N}}^2\right] \tag{4.3.21}$$

where $\omega_1, \omega_2, \dots, \omega_{4\mathrm{N}}$ are the 4N natural angular frequencies of the auxiliary system in Eq. (4.3.15). Obviously, Eq. (4.3.20) is not the only way to arrange the original system in Eq.

(4.3.14). Other manipulations have been tried resulting to be less efficient in terms of computational stability and memory usage.

4.4 Floquet-Lyapunov solution and harmonic balance method

According to the Floquet-Lyapunov theorem [39], solutions of Eq. (4.3.20) can be expressed in terms of products of an exponential function by a periodic function (of period $\mathrm{T} = 2\pi / \hat{\Omega}$) as seen in Chapter 2:

$$\begin{cases} \mathbf{u}(\tau) = e^{\Lambda_u \tau}\mathbf{p}(\tau) \\ \mathbf{p}(\tau) = \mathbf{p}(\tau \pm z\mathrm{T}), \quad z \in \mathbb{Z} \end{cases} \tag{4.4.1}$$

in which Λ_u is a characteristic exponent. Equation (4.4.1) expanded in Fourier series, reads:

$$\mathbf{u}(\tau) = e^{\Lambda_u \tau}\left\{\frac{1}{2}\mathbf{b}_0 + \sum_{h=1}^{\infty}\left[\mathbf{a}_h \sin(h\hat{\Omega}\tau) + \mathbf{b}_h \cos(h\hat{\Omega}\tau)\right]\right\} \tag{4.4.2}$$

where $\mathbf{b}_0$, $\mathbf{a}_h$ and $\mathbf{b}_h$ are unknown constant 4N-vectors. Taking the first and the second derivatives with respect to τ in Eq. (4.4.2) gives:

$$\begin{cases} \dot{\mathbf{u}}(\tau) = e^{\Lambda_u \tau}\left\{\frac{1}{2}\Lambda_u\mathbf{b}_0 + \sum_{h=1}^{\infty}\left[\left(\Lambda_u\mathbf{a}_h - h\hat{\Omega}\mathbf{b}_h\right)\sin(h\hat{\Omega}\tau) + \left(\Lambda_u\mathbf{b}_h + h\hat{\Omega}\mathbf{a}_h\right)\cos(h\,\hat{\Omega}\tau)\right]\right\} \\ \ddot{\mathbf{u}}(\tau) = e^{\Lambda_u \tau}\left\{\frac{1}{2}\Lambda_u^2\mathbf{b}_0 + \sum_{h=1}^{\infty}\left[\left(\Lambda_u^2 - h^2\hat{\Omega}^2\right)\mathbf{a}_h \sin(h\hat{\Omega}\tau) - 2\Lambda_u h\hat{\Omega}\mathbf{b}_h \sin(h\,\hat{\Omega}\tau)\right] + \right. \\ \qquad\qquad \left. + \sum_{h=1}^{\infty}\left[\left(\Lambda_u^2 - h^2\hat{\Omega}^2\right)\mathbf{b}_h \cos(h\,\hat{\Omega}\tau) + 2\Lambda_u h\hat{\Omega}\mathbf{a}_h \cos(h\hat{\Omega}\tau)\right]\right\} \end{cases} \tag{4.4.3}$$

Replacing Eq. (4.4.2) and Eq. (4.4.3) in Eq. (4.3.14) leads to the following equation of motion:

$$\begin{aligned} &\frac{1}{2}\Lambda_u^2\mathbf{b}_0 + \sum_{h=1}^{\infty}\left[\left(\Lambda_u^2 - h^2\hat{\Omega}^2\right)\mathbf{a}_h \sin(h\hat{\Omega}\tau) - 2\Lambda_u h\hat{\Omega}\mathbf{b}_h \sin(h\,\hat{\Omega}\tau)\right] + \\ &\qquad + \sum_{h=1}^{\infty}\left[\left(\Lambda_u^2 - h^2\hat{\Omega}^2\right)\mathbf{b}_h \cos(h\,\hat{\Omega}\tau) + 2\Lambda_u h\hat{\Omega}\mathbf{a}_h \cos(h\hat{\Omega}\tau)\right] + \\ &\qquad + \bar{\bar{\mathbf{C}}}\left\{\frac{1}{2}\Lambda_u\mathbf{b}_0 + \sum_{h=1}^{\infty}\left[\left(\Lambda_u\mathbf{a}_h - h\hat{\Omega}\mathbf{b}_h\right)\sin(h\hat{\Omega}\tau) + \left(\Lambda_u\mathbf{b}_h + h\hat{\Omega}\mathbf{a}_h\right)\cos(h\,\hat{\Omega}\tau)\right]\right\} + \\ &\qquad + \left[\bar{\bar{\mathbf{K}}} + \Delta L\cos(\hat{\Omega}\,\tau)\bar{\bar{\mathbf{L}}}\right]\left\{\frac{1}{2}\mathbf{b}_0 + \sum_{h=1}^{\infty}\left[\mathbf{a}_h \sin(h\hat{\Omega}\tau) + \mathbf{b}_h \cos(h\hat{\Omega}\tau)\right]\right\} = \mathbf{0} \end{aligned} \tag{4.4.4}$$

Applying the sum and difference formulae to the products of trigonometric functions in Eq. (4.4.4) and dividing both sides by $\hat{\Omega}^2$ yields:

$$
\begin{aligned}
&\frac{1}{2}\left[\Lambda^2\mathbf{I}+\sqrt{\delta}\Lambda\bar{\bar{\mathbf{C}}}+\delta\bar{\bar{\mathbf{K}}}+\varepsilon\cos(\hat{\Omega}\tau)\bar{\bar{\mathbf{L}}}\right]\mathbf{b}_0+\\
&\quad+\sum_{h=1}^{\infty}\left\{\left[\left(\Lambda^2-h^2\right)\mathbf{a}_h-2\Lambda h\,\mathbf{b}_h+\sqrt{\delta}\,\bar{\bar{\mathbf{C}}}\left(\Lambda\mathbf{a}_h-h\mathbf{b}_h\right)+\delta\bar{\bar{\mathbf{K}}}\mathbf{a}_h\right]\sin(h\hat{\Omega}\tau)\right\}+\\
&\quad+\sum_{h=1}^{\infty}\left\{\left[\left(\Lambda^2-h^2\right)\mathbf{b}_h+2\Lambda h\,\mathbf{a}_h+\sqrt{\delta}\,\bar{\bar{\mathbf{C}}}\left(\Lambda\mathbf{b}_h+h\mathbf{a}_h\right)+\delta\bar{\bar{\mathbf{K}}}\mathbf{b}_h\right]\cos(h\hat{\Omega}\tau)\right\}+\\
&\quad+\sum_{h=1}^{\infty}\left\{\frac{1}{2}\varepsilon\bar{\bar{\mathbf{L}}}\mathbf{a}_h\sin\left[\left(h+1\right)\hat{\Omega}\tau\right]\right\}+\sum_{h=1}^{\infty}\left\{\frac{1}{2}\varepsilon\bar{\bar{\mathbf{L}}}\mathbf{a}_h\sin\left[\left(h-1\right)\hat{\Omega}\tau\right]\right\}+\\
&\quad+\sum_{h=1}^{\infty}\left\{\frac{1}{2}\varepsilon\bar{\bar{\mathbf{L}}}\mathbf{b}_h\cos\left[\left(h+1\right)\hat{\Omega}\tau\right]\right\}+\sum_{h=1}^{\infty}\left\{\frac{1}{2}\varepsilon\bar{\bar{\mathbf{L}}}\mathbf{b}_h\cos\left[\left(h-1\right)\hat{\Omega}\tau\right]\right\}=\mathbf{0}
\end{aligned}
\tag{4.4.5}
$$

In Eqs. (4.4.5) a scaled characteristic exponent Λ, a frequency parameter δ and an amplitude parameter ε have been introduced, in analogy with the single degree of freedom dimensionless Mathieu-Hill equation [42], according to:

$$
\begin{cases}
\Lambda=\dfrac{\Lambda_u}{\hat{\Omega}}\\[2ex]
\delta=\dfrac{1}{\hat{\Omega}^2}=\dfrac{\Omega^2}{\omega_{\mathrm{L}}^2}\\[2ex]
\varepsilon=\dfrac{\Delta L}{\hat{\Omega}^2}=\Delta L\,\delta
\end{cases}
\tag{4.4.6}
$$

Notice that dividing the characteristic exponent Λ_u by the real quantity $\hat{\Omega}$, assumed positive, does not change the stability properties of the system, as this does not change the sign of the real part of the characteristic exponent, *i.e.* the Lyapunov exponent:

$$
\begin{cases}
\left\|\delta\mathbf{T}(\tau)\right\|\approx e^{\lambda_L\tau}\left\|\delta\mathbf{T}_0(\tau)\right\|\\
\lambda_L=\Re\left(\Lambda_u\right)=\Re\left(\Lambda\hat{\Omega}\right),\quad \hat{\Omega}>0\quad\Rightarrow\quad \operatorname{sgn}\left[\Re\left(\Lambda_u\right)\right]=\operatorname{sgn}\left[\Re\left(\Lambda\right)\right]=\operatorname{sgn}\left(\lambda_L\right)
\end{cases}
\tag{4.4.7}
$$

Where λ_L indicates a Lyapunov coefficient from the Lyapunov spectrum and the **T** terms represent trajectories in a finite-dimensional phase-space with initial separation $\delta\mathbf{T}_0\left(\tau\right)$. The first of Eq. (4.4.7) shows that the evolution of the separation of infinitesimally close trajectories depends on the real quantity λ_L. In particular, the stability is determined only by the sign of λ_L. The latter can be understood as an alternative interpretation of characteristic exponents presented in Floquet Theory (Chapter 2), and how they relate to Lyapunov exponents.

Truncating the Fourier series to $h=\mathrm{H}$ terms in Eq. (4.4.5) and applying a standard harmonic balance technique, as described in [103] in the case of a single degree of freedom system, *i.e.* collecting all the terms that multiply the different trigonometric functions, yields a set of $4\mathrm{N}\times\left(2\mathrm{H}+1\right)$ homogeneous algebraic equations in the form:

$$\begin{cases}\mathbf{Hc}=\mathbf{0}\\ \mathbf{c}=\left\{\mathbf{b}_0^{\mathrm{T}},\mathbf{b}_1^{\mathrm{T}}\dots\mathbf{b}_{\mathrm{H}}^{\mathrm{T}},\mathbf{a}_1^{\mathrm{T}}\dots\mathbf{a}_{\mathrm{H}}^{\mathrm{T}}\right\}^{\mathrm{T}}\end{cases}\tag{4.4.8}$$

where the algebraic operator **H** has the form of a matrix with $(2\mathrm{H}+1)\times(2\mathrm{H}+1)$ blocks $\mathbf{H}_{\mathrm{i,j}}$ (each of them is a $4\mathrm{N}\times 4\mathrm{N}$ matrix) with five non-zero block diagonals. The main block diagonal is defined as:

$$\begin{cases}\mathbf{H}_{1,1}=\dfrac{1}{2}\left[\Lambda^2\,\mathbf{I}+\Lambda\sqrt{\delta}\,\bar{\bar{\mathbf{C}}}+\delta\bar{\bar{\mathbf{K}}}\right]\\ \mathbf{H}_{1+h,1+h}=\mathbf{H}_{1+H+h,1+H+h}=\left[(\Lambda^2-h^2)\mathbf{I}+\Lambda\sqrt{\delta}\,\bar{\bar{\mathbf{C}}}+\delta\bar{\bar{\mathbf{K}}}\right]\quad\text{for } h=1,\dots,\mathrm{H}\end{cases}\tag{4.4.9}$$

While the remaining non-zero block diagonals read:

$$\begin{cases}\mathbf{H}_{h,1+h}=\mathbf{H}_{1+h,h}=\dfrac{1}{2}\varepsilon\bar{\bar{\mathbf{L}}}\quad\text{for}\quad h=1,\dots,2\mathrm{H}\quad\text{with}\quad h\neq\mathrm{H}+1\\ \mathbf{H}_{1+h,1+H+h}=-\mathbf{H}_{1+H+h,1+h}=h\left[2\Lambda\,\mathbf{I}+\sqrt{\delta}\,\bar{\bar{\mathbf{C}}}\right]\quad\text{for}\quad h=1,\dots,\mathrm{H}\end{cases}\tag{4.4.10}$$

Equation (4.4.8) has non-trivial solutions if $\det[\mathbf{H}]=0$, yielding a quadratic eigenvalue problem for Λ:

$$\begin{cases}\mathbf{H}=\Lambda^2\,\mathbf{H}_2+\Lambda\mathbf{H}_1+\mathbf{H}_0\\ \left(\Lambda^2\,\mathbf{H}_2+\Lambda\mathbf{H}_1+\mathbf{H}_0\right)\mathbf{c}=\mathbf{0}\end{cases}\tag{4.4.11}$$

With a given combination of parameters (in particular: δ, ε), the system is asymptotically or merely stable as long as the real part of all eigenvalues Λ (characteristic exponents of the problem) is non-positive. This is an alternative method with respect to the application of the classical Floquet theory, implying direct evaluation of Floquet multipliers (returning all the information regarding the stability of the solution) as eigenvalues of the monodromy matrix of the system [39, 40], which for the problem under study would carry a higher computational load.

4.5 Choice of parameters for stability analysis

As study-case, a shaft with both clamped ends is considered. According to what was said in Section 4.3 the choice of shape-functions is crucial in order to increase the convergence speed of the Galerkin method. The eigenfunctions of the time-invariant system, Eq. (3.9.1), would be without any doubt, a very good choice. However, it can be noticed that for boundary conditions displayed in Eq. (3.9.2), the eigenfunctions of clamped-clamped Euler-Bernoulli beam are still comparison functions. After several numerical tests it was concluded that using Euler-Bernoulli shape-functions does not considerably reduce the convergence speed, furthermore it allows to avoid the computation of closed-form rotating Timoshenko beam eigenfunctions. It has to be said, however, that using clamped-clamped Euler-Bernoulli eigenfunctions as shape-functions, does not allow the solution to converge respecting the boundary conditions given by Eq. (3.9.1). The latter is due the fact that the Euler-Bernoulli model cannot carry any information concerning shear deformations and, indeed, for an Euler-Bernoulli beam Eq. (3.9.1) and Eq. (3.9.2) coincide. After the latter necessary remarks, the choice of boundary conditions falls on Eq. (3.9.2) with clamped-clamped Euler-Bernoulli eigenfunctions as shape-functions, since it is easier to implement and since this choice does not invalidate the general results, observed in the following Sections, about the roles played by gyroscopic and damping effects on stability charts.

The operator **H** is generated including the first 4 eigenfunctions (N = 4) and the first 19 terms in the Fourier series (H = 18). The model is characterized by the following parameters (see also Eq. (3.7.1) and Eq. (3.7.2)):

$$\begin{aligned} &\mathit{Shaft}: \quad \rho = 7700 \text{ Kg m}^{-3}, \;\; E = 210\times 10^{9} \text{ Pa}, \;\; \nu = 0.3, \;\; \alpha = 80 \\ &\mathit{Load}: \quad R_{T,\mathrm{N}} = 2 \end{aligned} \tag{4.5.1}$$

In the case of null preloads, *i.e.* $\hat{N}_0 = 0$ and $\hat{T}_0 = 0$, the maximum amplitude, say ΔL^{lim}, can be defined as it was $\left|\hat{N}_{\max}\right|$ in Section 3.14, that is $\Delta L^{lim} = 0.01$. Note that the chosen value for $R_{T,\mathrm{N}}$ respects, by a wide margin, the Tresca criterion already adopted in Section 3.14. The maximum admissible value ΔL must be lowered further so as not to allow reaching the first equivalent Euler's critical load and thus avoid buckling effect (see, in the following, Section 4.6 and Fig. 4.3).

4.6 Stability analysis of a simple shaft without gyroscopic and stabilizing damping effects

The spectrum of the monodromy matrix, or the set of Floquet multipliers, as already discussed in Chapter 2, completely characterize the stability behavior of the system in Eq. (4.3.20). The operators of the latter are $4\mathrm{N}\times 4\mathrm{N}$ dimension real matrices, thus it can be rewritten in a state-space form, like Eq. (2.2.1), with the following matrix of coefficients:

$$\mathbf{A}(\tau) = \begin{bmatrix} \mathbf{0} & \mathbf{I} \\ -\left[\bar{\bar{\mathbf{K}}} + \Delta L \cos(\hat{\Omega}\,\tau)\,\bar{\bar{\mathbf{L}}}\right] & -\bar{\bar{\mathbf{C}}} \end{bmatrix} \tag{4.6.1}$$

Equation (4.3.20), in state-space form, after directly replacing Floquet-Lyapunov solution, takes the form of a dynamic eigenvalue problem:

$$\begin{cases} \mathbf{u}_S(\tau) = \left\{\mathbf{u}^{\mathrm{T}}(\tau), \dot{\mathbf{u}}^{\mathrm{T}}(\tau)\right\}^{\mathrm{T}} = e^{\Lambda_u \tau}\mathbf{z}(\tau) \\ \dot{\mathbf{u}}_S(\tau) = \mathbf{A}(\tau)\,\mathbf{u}_S(\tau) \quad \Rightarrow \quad \Lambda_u e^{\Lambda_u \tau}\mathbf{z}(\tau) + e^{\Lambda_u \tau}\dot{\mathbf{z}}(\tau) = \mathbf{A}(\tau)\, e^{\Lambda_u \tau}\mathbf{z}(\tau) \quad \Rightarrow \\ \qquad\qquad\qquad\qquad\quad \Rightarrow \quad \left[\mathbf{A}(\tau) - \Lambda_u \mathbf{I}\right]\mathbf{z}(\tau) = \dot{\mathbf{z}}(\tau) \end{cases} \tag{4.6.2}$$

in which $\mathbf{z}(\tau)$ and Λ_u form a so-called dynamic eigenpair. Notice that in the present case (periodic coefficients), Floquet Theory assures that the dynamic eigenvalue Λ_u is τ-invariant and it assumes the name of characteristic exponent, while the dynamic eigenvector $\mathbf{z}(\tau)$ is a periodic vector-function of the same period of the matrix of coefficients. Matrix $\mathbf{A}(\tau)$ is an $8\mathrm{N}\times 8\mathrm{N}$ dimension real matrix, hence the associated monodromy matrix is, in its turn, a real $8\mathrm{N}\times 8\mathrm{N}$ dimension matrix, thus there are exactly 8N multipliers related to the system in Eq. (4.3.20). Since the monodromy matrix is real, the Floquet multipliers occur in complex conjugate pairs or in pairs of distinct or coincident reals values. Floquet multipliers are τ-invariant quantities. Thus, determining their position (with respect to the unit circle in the Argand-Gauss plane) for each pair $\{\hat{\Omega}, \Delta L\}$ means to know entirely the stability properties of the system, regardless the initial conditions.

The harmonic balance method leads to the system in Eq. (4.4.11), that definitely shift the focus from multipliers to characteristic exponents. Equation (4.4.11) allows to compute directly $8\mathrm{N}(2\mathrm{H}+1)$ characteristic exponents for each pair $\{\delta, \varepsilon\}$, thus for each point of the two-dimensional domain spanned by δ and ε there are 16NH redundant characteristic exponents that, in groups of 2H elements, correspond to the same 8N independent multipliers. Since characteristic exponents are not unique, as shown in Eq. (2.4.7), the redundancy of exponents, given by the quadratic eigenproblem in Eq. (4.4.11), is an expected result. Nevertheless, it is possible to identify the original multipliers as follows:

$$\eta = e^{\left(\Lambda_u \pm i\frac{2z\pi}{\mathrm{T}}\right)\mathrm{T}} = e^{\Lambda_u \mathrm{T}} = e^{\Lambda \hat{\Omega} \mathrm{T}} = e^{2\pi\Lambda}, \qquad z \in \mathbb{Z} \tag{4.6.3}$$

where, as usual, η is a multiplier. Notice that this strategy permits to avoid completely the computation of the monodromy matrix and reduces the stability analysis of a time-periodic system to a computation of eigenvalues. Despite the latter huge advantage, solving a $4\mathrm{N}\times(2\mathrm{H}+1)\times(2\mathrm{H}+1)$ quadratic eigenvalue problem for each $\{\delta, \varepsilon\}$ pair in a chosen technological domain, could turn out to be extremely time consuming when the number of comparison functions N is increased and the number of terms in the Fourier series H is raised to reach a sufficiently good approximation of the dynamic eigenvectors. Replacing a particular value of Λ in the operator **H** allows to write the quadratic eigenvalue problem in Eq. (4.4.11) as a linear one with ε as the eigenvalue, while the role of the eigenvector **c** remains the same. Thus, for each value of δ, it is possible to solve a linear algebraic eigenvalue problem for ε and cover the whole δ-ε domain for a specific Λ (a specific solution). Notice that the eigenvalue ε has a proper physical sense if and only if it is real. It is also possible, as an alternative, to solve a nonlinear eigenproblem for δ at every fixed ε, taking only the real values of the eigenvalue δ as admissible ones.

Under the assumption in which the δ-ε two-dimensional domain can be represented as union of different sub-domains, *i.e.* stability and instability regions, there must be a set of particular solutions for which the system undergoes a transition from stable to unstable behavior. Those solutions are called critical or transition solutions. In the simplest cases, there is a finite set of critical Λ that corresponds to a set of parametric curves in the δ-ε domain, called transition curves, which can be, by definition, stability thresholds due the fact they separate two regions characterized by different stability behavior. In more general cases, every Λ represents a locus of points that forms a set of curves in which no one is a transition curve, hence a set of critical values of Λ cannot be identified. In these general cases stability thresholds are generated by an envelope of families of non-critical curves on which only a certain limited number of points are critical (see, in the following, Sections 4.12, 4.13 and 4.14).

A point in the δ-ε domain belongs to a stability region if every Λ returned by Eq. (4.4.11) has negative real part and thus every multiplier lies within the unit circle. A point in the δ-ε domain belongs to an instability region if Eq. (4.4.11) returns at least one value of Λ with positive real part, thus there is at least one multiplier that lies outside the unit circle. A point belongs to a stability threshold if and only if all the returned values of Λ related to the latter are purely imaginary and there is a non-empty neighborhood of the point that contains at least a $\{\delta,\varepsilon\}$ pair that returns at least one Λ with positive real part and at least one Λ with non-positive real part, excluding the critical point itself. Finally, if all the values of Λ have null real part, all the associated multipliers have simple elementary divisors and there is no neighborhood as in the previous case, then the point belongs to a mere stability (non-asymptotic) region and all the multipliers lie again on the unit circle.

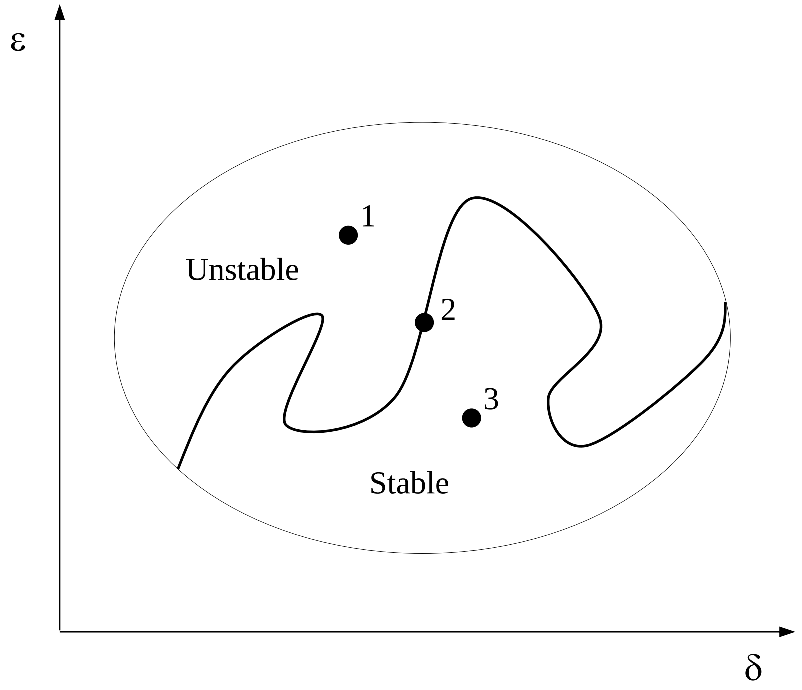

Figure 4.2: Schematic representation of a stability threshold

In Fig 4.2 the topological properties of a stability threshold are summarized: points 1 and 3 lie in different regions (unstable and stable), while point 2 is a critical point and, indeed, it belongs to the stability threshold.

Knowing in advance which values of Λ are critical allows to trace directly the stability thresholds, without proceeding by trial and error scrolling through the various choices of Λ. However, in many general cases, finding a set of critical values of Λ is simply impossible. The present Section focuses on a simple case in which information concerning critical solutions can be extracted from the structure of the eigenproblem in Eq. (4.4.11), leaving the task of dealing with the more general cases in the next Sections.

Equation (4.4.11) can be rewritten, according to Eq. (4.4.9) and (4.4.10), as follows:

$$\begin{cases} \left[\Lambda^2 \mathbf{H}_2 + \Lambda\left(\mathbf{H}_1^{(1)} + \mathbf{H}_1^{(2)}\right) + \mathbf{H}_0^{(1)} + \varepsilon \mathbf{H}_0^{(2)} + \mathbf{H}_0^{(3)}\right]\mathbf{c} = \mathbf{0} \\ \Lambda = \Lambda(\varepsilon) \\ \mathbf{c} = \mathbf{c}(\varepsilon) \end{cases} \tag{4.6.4}$$

in which the dependence on ε of the eigenpair $\{\Lambda, \mathbf{c}\}$ has been made explicit, while the dependence on δ remains implicit. In Eq. (4.6.4) operators $\mathbf{H}_1$ and $\mathbf{H}_0$ have been decomposed in order to highlight their properties. Matrix $\mathbf{H}_1^{(1)}$ is block diagonal depending on no other matrix than $\bar{\bar{\mathbf{C}}}$, $\mathbf{H}_0^{(1)}$ is a block diagonal matrix which is independent from $\bar{\bar{\mathbf{C}}}$ and $\bar{\bar{\mathbf{L}}}$, and thus it depend only on then $\bar{\bar{\mathbf{K}}}$. Matrix $\mathbf{H}_0^{(2)}$ contains only the blocks that are multiplied by ε (in these block only $\bar{\bar{\mathbf{L}}}$ appears) and, as a consequence, $\mathbf{H}_0^{(3)}$ contains only the blocks dependent on $\bar{\bar{\mathbf{C}}}$. Thus, the remaining operator $\mathbf{H}_1^{(2)}$ can be computed as follows:

$$\mathbf{H}_1^{(2)} = \mathbf{H}_1 - \mathbf{H}_1^{(1)} \tag{4.6.5}$$

Depending on the case (damping distribution, gyroscopic terms, etc…), the algebraic operators $\mathbf{H}_1^{(1)}, \mathbf{H}_0^{(1)}, \mathbf{H}_0^{(2)}$ and $\mathbf{H}_0^{(3)}$ can have different properties, while operator $\mathbf{H}_2$ is always a symmetric, positive definite, block diagonal matrix and $\mathbf{H}_1^{(2)}$ is a singular, block skew-symmetric matrix:

$$\begin{cases} [\mathbf{H}_2]^{\mathrm{T}} = \mathbf{H}_2 \\ \left[\mathbf{H}_1^{(2)}\right]^{\mathrm{T}} = -\mathbf{H}_1^{(2)}, \quad \det\left[\mathbf{H}_1^{(2)}\right] = 0 \end{cases} \tag{4.6.6}$$

From now on, operators $\bar{\bar{\mathbf{K}}}$ and $\bar{\bar{\mathbf{L}}}$ will be considered symmetric. If Euler-Bernoulli eigenfunctions are chosen as comparison functions for boundary conditions as in Eq. (3.9.2), then $\bar{\bar{\mathbf{K}}}$ and $\bar{\bar{\mathbf{L}}}$ are symmetric (see Sections 3.9 and 4.5). In more general cases, operators $\bar{\bar{\mathbf{K}}}$ and $\bar{\bar{\mathbf{L}}}$ can be non-symmetric. For these general cases see Section 4.11.

Simplified case 1: no damping, non-rotating shaft (no gyroscopic effects), $\bar{\bar{\mathbf{C}}} = \mathbf{0}$.

The present scenario is the simplest one and it can be summarized as follows:

$$\begin{cases} \mathbf{H}_1^{(1)} = \mathbf{0} \\ \left[\mathbf{H}_0^{(1)}\right]^{\mathrm{T}} = \mathbf{H}_0^{(1)} \\ \left[\mathbf{H}_0^{(2)}\right]^{\mathrm{T}} = \mathbf{H}_0^{(2)} \\ \mathbf{H}_0^{(3)} = \mathbf{0} \end{cases} \tag{4.6.7}$$

Eq. (4.6.4) reads:

$$\begin{aligned}&\left[\Lambda^2\,\mathbf{H}_2+\Lambda\,\mathbf{H}_1^{(2)}+\mathbf{H}_0^{(1)}+\varepsilon\,\mathbf{H}_0^{(2)}\right]\mathbf{c}=\mathbf{0}\quad\Rightarrow\\ &\qquad\Rightarrow\quad\mathbf{c}^*\left[\Lambda^2\,\mathbf{H}_2+\Lambda\,\mathbf{H}_1^{(2)}+\mathbf{H}_0^{(1)}+\varepsilon\,\mathbf{H}_0^{(2)}\right]\mathbf{c}=0\quad\Rightarrow\\ &\qquad\Rightarrow\quad\Lambda^2\,H_2(\varepsilon)+\Lambda\,i\,H_1^{(2)}(\varepsilon)+H_0^{(1)}(\varepsilon)+\varepsilon\,H_0^{(2)}(\varepsilon)=0\end{aligned}\tag{4.6.8}$$

where $\mathbf{c}^*$ is the Hermitian of **c**, thus $H_2(\varepsilon), H_1^{(2)}(\varepsilon), H_0^{(1)}(\varepsilon)$ and $H_0^{(2)}(\varepsilon)$ are real scalar functions of the real variable ε; $H_2(\varepsilon)$ is positive for each value of ε, since $\mathbf{H}_2$ is positive definite. Notice that, according to Eq. (4.6.6), $\mathbf{H}_1^{(2)}$ is always a block skew-symmetric matrix, then the product $\mathbf{c}^*\mathbf{H}_1^{(2)}\mathbf{c}=i\,H_1^{(2)}(\varepsilon)$ is always an imaginary quantity for each ε, or null, since $\mathbf{H}_1^{(2)}$ is also singular. The eigenvector **c**, along with its Hermitian $\mathbf{c}^*$, returns two values of Λ:

$$\Lambda_{1,2}=-i\frac{H_1^{(2)}(\varepsilon)}{2H_2(\varepsilon)}\pm\sqrt{-\left[\frac{H_1^{(2)}(\varepsilon)}{2H_2(\varepsilon)}\right]^2-\frac{H_0^{(1)}(\varepsilon)+\varepsilon\,H_0^{(2)}(\varepsilon)}{H_2(\varepsilon)}}\tag{4.6.9}$$

Requesting that all the Floquet multipliers occur in conjugate pairs, according to the fact that the monodromy matrix is real and excluding the distinct real values case, means that also the characteristic exponents must occur in conjugate pairs. A sufficient condition can be obtained from Eq. (4.6.9):

$$\begin{cases}H_1^{(2)}(\varepsilon)=0,\quad\forall\varepsilon\\ -\left(H_0^{(1)}(\varepsilon)+\varepsilon\,H_0^{(2)}(\varepsilon)\right)<0\end{cases}\tag{4.6.10}$$

If only the set of independent multipliers is considered, due to the uniqueness of the solution, Eq. (4.6.10) is also a necessary condition. In other words, if all the 8N multipliers occur in 4N conjugate pairs then the characteristic exponents are purely imaginary. This means that all the multipliers lie on the unit circle. Due to the symmetry of multipliers with respect to the real axis and since conjugate pairs of multipliers mean purely imaginary characteristic exponents, multipliers can exit the unit circle only on the real axis, giving rise to a pair of distinct real values. Thus, in this simple case, finding a set of critical values of Λ is possible. The critical values of Λ are two, and they correspond to multipliers that lie on both the unit circle and the real axis:

$$\begin{cases}\eta_{cr}^{(1)}=1\quad\Rightarrow\quad e^{2\pi\Lambda_{cr}^{(1)}}=1\quad\Rightarrow\quad\Lambda_{cr}^{(1)}=0\\ \eta_{cr}^{(2)}=-1\quad\Rightarrow\quad e^{2\pi\Lambda_{cr}^{(2)}}=-1\quad\Rightarrow\quad\Lambda_{cr}^{(2)}=\dfrac{1}{2\pi}\ln(-1)=\dfrac{i}{2}\end{cases}\tag{4.6.11}$$

Thus, the critical solutions, according to Section 2.7, are periodic. $\Lambda_{cr}^{(1)}$ corresponds to a single-period critical solution while $\Lambda_{cr}^{(2)}$ corresponds to a double-period solution which is also anti-periodic. The Floquet multipliers related to the *simplified case* 1 can lie only on the unit circle or on the real axis. Furthermore, if the system is stable all the multipliers lie on the unit circle and no asymptotic stability region can exist. Thus, in the present case, stability occurs only in the form of mere or simple stability.

An important observation is the following: in the *simplified case* 1 the nature of critical solutions do not depend on ε, thus further information on multipliers can be extracted directly from the operator **H** imposing a fixed arbitrary value for ε, *e.g.* $\varepsilon = 0$ (unperturbed system), then the components of $\mathbf{b}_0$ are decoupled from those of $\mathbf{b}_1 \ldots \mathbf{b}_{\mathrm{H}}, \mathbf{a}_1 \ldots \mathbf{a}_{\mathrm{H}}$ in Eq. (4.6.4). Hence, according to Eq. (4.4.8), (4.4.9) and Eq. (4.4.10), with $\bar{\bar{\mathbf{C}}} = \mathbf{0}$:

$$\mathbf{H}_{1,1}\mathbf{b}_0 = \mathbf{0} \;\; \Rightarrow \;\; \frac{1}{2}\left(\Lambda^2\,\mathbf{I} + \delta\bar{\bar{\mathbf{K}}}\right)\mathbf{b}_0 = \mathbf{0} \;\; \Rightarrow \;\; \det\left[\Lambda^2\,\mathbf{I} + \delta\bar{\bar{\mathbf{K}}}\right] = 0 \tag{4.6.12}$$

Since $\bar{\bar{\mathbf{K}}}$ is diagonal, as in Eq. (4.3.21), then $\Lambda^2\,\mathbf{I} + \delta\bar{\bar{\mathbf{K}}}$ is diagonal as well. As long as Eq. (4.6.9) returns only imaginary values for Λ, Eq. (4.6.12) is sufficient to claim that the system is stable if and only if all the multipliers lie on the unit circle with the exceptions of the points (+1, 0) and (–1, 0). Like in the single degree of freedom Mathieu equation, it is possible to compute the values for which the transition curves cross the δ-axis. Indeed, the phase of each multiplier on the unit circle, according to Eq. (4.6.3) and Eq. (4.6.12) can be expressed as:

$$\varphi_n = 2\pi\,\omega_n\sqrt{\delta}\,, \quad n = 1,2,\ldots,4\mathrm{N} \tag{4.6.13}$$

When the phase is equal to $k\pi,\; k \in \mathbb{Z}$, multipliers are equal to +1 or –1. The critical values of δ when $\varepsilon = 0$ are:

$$\delta^{crit}_{nk,\varepsilon=0} = \frac{k^2}{4\omega_n^2}, \quad n = 1,2,\ldots,4\mathrm{N}, \quad k = 0,1,2,\ldots \tag{4.6.14}$$

Thus the critical values for Λ are:

$$\Lambda^{crit}_{nk,\varepsilon=0} = \frac{i\,k}{2}, \quad k = 0,1,2,\ldots \tag{4.6.15}$$

These results are consistent with those obtained in Eq. (4.6.11) due to the non uniqueness of characteristic exponents. Replacing the critical values provided in Eq. (4.6.11) in Eq. (4.4.11) and solving a linear eigenproblem for ε (or a non-linear one for δ), returns the stability chart. The global stability chart is displayed in Fig. 4.3, resulting in a superposition of sequences of instability regions, each sequence generated by a different eigenvalue (or better by a different Floquet multiplier; grey: single-period solutions; black: double-period solutions; global stability region in the lower part of the map, given by the complement area with respect to the union of all sequences of instability regions). Oblique lines crossing the whole map represent operation lines, *i.e.* lines $\varepsilon = \Delta L\,\delta$: in this case the black line is drawn at the assumed maximum admissible value ΔL^{lim}, while the red one at a value of ΔL corresponding to the equivalent first Euler's critical load (in which, in the case of null preloads, $\Delta L = \Delta\hat{N}$ and $\Delta\hat{T} = R_{T,N}\Delta\hat{N}$ assume the roles of $\hat{N}$ and $\hat{T}$, respectively, in Section 3.13). The effects of preloads on stability charts will be discussed separately (Section 4.12).

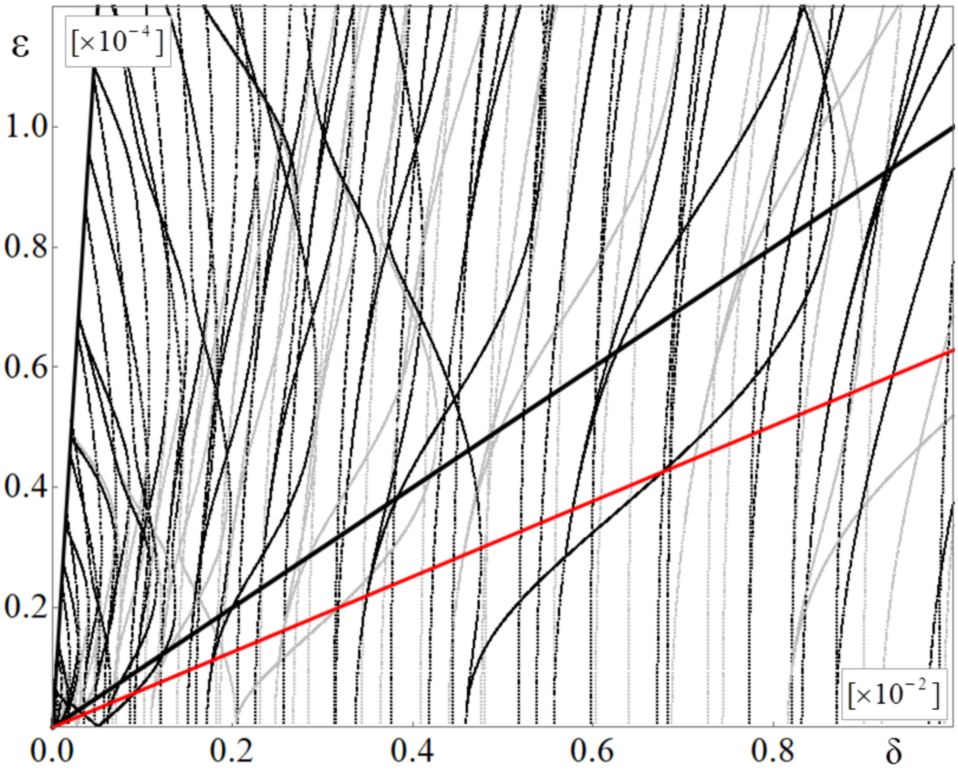

Figure 4.3: Stability chart without gyroscopic and damping terms (with null preloads). Black thick line: limit identified by ΔL^{lim}. Red line: limit related to the equivalent first Euler's critical load

Notice that in Fig. 4.3 (and following ones) the instability regions due to the Timoshenko second frequency spectrum (Section 3.16) are not reported, hidden on purpose (since they would consist of a tangle of curves) behind the blank triangular region on the left side of each stability chart. Clearly, if considering more and more degrees of freedom in the discretized model, the superposition of sequences of instability regions would become so intricate to be virtually unreadable for practical purposes. A difficulty that can be overcome by introducing dissipative effects into the model (which is both realistic and necessary for getting readable stability maps, see from Fig. 4.10 to Fig. 4.14). The effects of damping will be discussed in the next Sections. In order to further clarify further the obtained results, it is necessary to recall some fundamental concepts of the stability theory of Hamiltonian systems. The next Section therefore focuses on those cases, including the *simplified case* 1, in which the equations of motion can be cast in Hamiltonian (canonical) form.

4.7 Behavior of multipliers of Hamiltonian systems under a deformation of the Hamiltonian

The *simplified case* 1 represents, of course, a Hamiltonian system and Eq. (4.3.20) can be cast in canonical form as follows:

$$\mathbf{I}\,\ddot{\mathbf{u}} + \left[\bar{\bar{\mathbf{K}}} + \Delta L\cos(\hat{\Omega}\tau)\,\bar{\bar{\mathbf{L}}}\right]\mathbf{u} = \mathbf{0} \quad \Rightarrow \quad \mathcal{J}\,\dot{\mathbf{u}}_S = \mathcal{H}(\tau)\,\mathbf{u}_S \tag{4.7.1}$$

where $\mathbf{u}_S$ is a state-space vector-function, $\mathcal{J}$ is a non-singular skew-symmetric matrix and $\mathcal{H}(\tau)$ is a symmetric matrix. If $\mathbf{u}_S$ is as in Eq. (4.6.2) then:

$$\begin{cases} \mathcal{J} = \begin{bmatrix} \mathbf{0} & -\mathbf{I} \\ \mathbf{I} & \mathbf{0} \end{bmatrix} \\[2ex] \mathcal{J}^{\mathrm{T}} = \mathcal{J}^{-1} = -\mathcal{J} \quad \Rightarrow \quad \mathcal{J}^{2} = -\mathbf{I}_{8\mathrm{N}} \\[2ex] \mathcal{H}(\tau) = \begin{bmatrix} \bar{\bar{\mathbf{K}}} + \Delta L\cos(\hat{\Omega}\tau)\,\bar{\bar{\mathbf{L}}} & \mathbf{0} \\ \mathbf{0} & \mathbf{I} \end{bmatrix} \\[2ex] \mathbf{A}(\tau) = -\mathcal{J}\,\mathcal{H}(\tau) = \begin{bmatrix} \mathbf{0} & \mathbf{I} \\ -\left[\bar{\bar{\mathbf{K}}} + \Delta L\cos(\hat{\Omega}\tau)\,\bar{\bar{\mathbf{L}}}\right] & \mathbf{0} \end{bmatrix} \end{cases} \tag{4.7.2}$$

The matrix $\mathcal{H}(\tau)$ is the Hamiltonian of the canonical equation $\mathcal{J}\,\dot{\mathbf{u}}_S = \mathcal{H}(\tau)\mathbf{u}_S$ (a canonical equation is also Hamiltonian). A fundamental property of real Hamiltonian (canonical) equations is that their matrizants (principal fundamental matrices, Section 2.2) are symplectic. The eigenvalues of a symplectic matrix are symmetric, in the sense of the inversion, with respect to the unit circle in the Argand-Gauss plane. The last property coincides, when the principal fundamental matrix is evaluated in $\tau = \mathrm{T}$ (monodromy matrix), with the statement of the *Lyapunov-Poincaré Theorem*, that exactly says, from [39]:

The multipliers of a Hamiltonian equation, allowing for their multiplicities and the structure of the elementary divisors, are symmetric (in the sense of the inversion) about the unit circle.

However, following a deformation of the Hamiltonian (induced by varying its parameters), multipliers change their position in the complex plane. After a deformation, Lyapunov-Poincaré theorem still applies if the deformed system is in turn Hamiltonian. Such a perturbation may or may not allow the system to switch from stable to unstable behavior and *vice versa*. In order to find precise criteria to understand the switching mechanism that gives rise to instability, it is convenient to recall further definitions and important results concerning the behavior of multipliers under perturbations of the Hamiltonian.

Definition (*indefinite scalar product*): let $\mathcal{G}$ be a complex non-singular Hermitian matrix and consider two non-zero complex vectors **x** and **y**, the product:

$$\mathbf{y}^{*}\mathcal{G}\,\mathbf{x} = \langle \mathcal{G}\mathbf{x}, \mathbf{y} \rangle = \langle \mathbf{x}, \mathbf{y} \rangle^{(\mathcal{G})} \tag{4.7.3}$$

is called *indefinite scalar product* of vectors **x** and **y**. If $\langle \mathbf{x},\mathbf{y}\rangle^{(\mathcal{G})}=0$, then **x** and **y** are said to be $\mathcal{G}$-orthogonal. Then the product in Eq. (4.7.3) is linear, Hermitian and it has the non-degeneracy property (there is no non-zero vector which is $\mathcal{G}$-orthogonal to every other non-zero vectors). Notice that the product $\langle \mathbf{x},\mathbf{x}\rangle^{(\mathcal{G})}$ can be negative, this is why it is called indefinite.

Definition (*$\mathcal{G}$-adjoint*): let **Z** be a complex matrix of the same dimensions of $\mathcal{G}$, a matrix $\tilde{\mathbf{Z}}$ is *$\mathcal{G}$-adjoint* to **Z** if:

$$\langle \mathbf{Z}\mathbf{x},\mathbf{y}\rangle^{(\mathcal{G})}=\langle \mathbf{x},\tilde{\mathbf{Z}}\mathbf{y}\rangle^{(\mathcal{G})} \tag{4.7.4}$$

Or:

$$\langle \mathbf{Z}\mathbf{x},\mathbf{y}\rangle^{(\mathcal{G})}=\langle \mathcal{G}\mathbf{Z}\mathbf{x},\mathbf{y}\rangle=\langle \mathbf{x},\mathbf{Z}^*\mathcal{G}\mathbf{y}\rangle=\langle \mathcal{G}\mathbf{x},\mathcal{G}^{-1}\mathbf{Z}^*\mathcal{G}\mathbf{y}\rangle=\langle \mathbf{x},\mathcal{G}^{-1}\mathbf{Z}^*\mathcal{G}\mathbf{y}\rangle^{(\mathcal{G})} \tag{4.7.5}$$

Thus:

$$\tilde{\mathbf{Z}}=\mathcal{G}^{-1}\mathbf{Z}^*\mathcal{G} \tag{4.7.6}$$

Definition (*$\mathcal{G}$-unitary*, *$\mathcal{G}$-Hermitian and $\mathcal{G}$-Hamiltonian*): a complex matrix **Z** is said to be *$\mathcal{G}$-unitary* if:

$$\langle \mathbf{Z}\mathbf{x},\mathbf{Z}\mathbf{y}\rangle^{(\mathcal{G})}=\langle \mathbf{x},\mathbf{y}\rangle^{(\mathcal{G})} \quad \Leftrightarrow \quad \tilde{\mathbf{Z}}\mathbf{Z}=\mathbf{I} \quad \Leftrightarrow \quad \mathbf{Z}^*\mathcal{G}\mathbf{Z}=\mathcal{G} \tag{4.7.7}$$

$\mathcal{G}$-Hermitian if:

$$\langle \mathbf{Z}\mathbf{x},\mathbf{y}\rangle^{(\mathcal{G})}=\langle \mathbf{x},\mathbf{Z}\mathbf{y}\rangle^{(\mathcal{G})} \quad \Leftrightarrow \quad \tilde{\mathbf{Z}}=\mathbf{Z} \quad \Leftrightarrow \quad \mathbf{Z}=\mathcal{G}^{-1}\mathcal{H} \quad \text{with} \quad \mathcal{H}^*=\mathcal{H} \tag{4.7.8}$$

$\mathcal{G}$-Hamiltonian (or *$\mathcal{G}$-anti-Hermitian*) if:

$$\langle \mathbf{Z}\mathbf{x},\mathbf{y}\rangle^{(\mathcal{G})}=-\langle \mathbf{x},\mathbf{Z}\mathbf{y}\rangle^{(\mathcal{G})} \quad \Leftrightarrow \quad \tilde{\mathbf{Z}}=-\mathbf{Z} \quad \Leftrightarrow \quad \mathbf{Z}=i\,\mathcal{G}^{-1}\mathcal{H} \quad \text{with} \quad \mathcal{H}^*=\mathcal{H} \tag{4.7.9}$$

Any Hamiltonian equation with complex coefficients can be written in the following form:

$$\begin{cases} i^{-1}\mathcal{G}\,\dot{\mathbf{z}}=\mathcal{H}(\tau)\,\mathbf{z} \\ \mathcal{G}^*=\mathcal{G} \\ \mathcal{H}^*(\tau)=\mathcal{H}(\tau) \end{cases} \quad \Rightarrow \quad \mathbf{A}(\tau)=i\,\mathcal{G}^{-1}\mathcal{H}(\tau) \tag{4.7.10}$$

Hence, the complex matrix of coefficients $\mathbf{A}(\tau)$ of the Hamiltonian equation in Eq. (4.7.10) is, according to Eq. (4.7.9), $\mathcal{G}$-Hamiltonian. Now consider the principal fundamental matrix (matrizant) of the equation $\dot{\mathbf{z}}=\mathbf{A}(\tau)\,\mathbf{z}$, say $\mathbf{X}(\tau)$, as in Chapter 2, and its $\mathcal{G}$-adjoint $\tilde{\mathbf{X}}(\tau)$.

Taking the first derivative with respect to τ of the product $\tilde{\mathbf{X}}(\tau)\,\mathbf{X}(\tau)$ gives (dropping temporarily the dependence on τ for clarity):

$$\begin{aligned}\frac{d}{d\tau}\left[\tilde{\mathbf{X}}\,\mathbf{X}\right] = \tilde{\mathbf{X}}\,\dot{\mathbf{X}} + \dot{\tilde{\mathbf{X}}}\,\mathbf{X} = \tilde{\mathbf{X}}\,\mathbf{A}\,\mathbf{X} + \mathcal{G}^{-1}\mathbf{X}^{*}\mathbf{A}^{*}\mathcal{G}\,\mathbf{X} = \\ = \tilde{\mathbf{X}}\,\mathbf{A}\,\mathbf{X} + \mathcal{G}^{-1}\mathbf{X}^{*}\mathcal{G}\mathcal{G}^{-1}\mathbf{A}^{*}\mathcal{G}\,\mathbf{X} = \\ = \tilde{\mathbf{X}}\,\mathbf{A}\,\mathbf{X} + \tilde{\mathbf{X}}\left(-\mathbf{A}\right)\mathbf{X} = \\ = \tilde{\mathbf{X}}\,\mathbf{A}\,\mathbf{X} - \tilde{\mathbf{X}}\,\mathbf{A}\,\mathbf{X} = \mathbf{0}\end{aligned} \tag{4.7.11}$$

Thus $\tilde{\mathbf{X}}(\tau)\,\mathbf{X}(\tau)$ does not depend on τ, and since $\mathbf{X}(0) = \mathbf{I}$ (by definition of principal fundamental matrix or matrizant, Section 2.2), , it has to be:

$$\tilde{\mathbf{X}}(\tau)\,\mathbf{X}(\tau) = \mathbf{I} \tag{4.7.12}$$

Hence, the principal fundamental matrix of a Hamiltonian system is $\mathcal{G}$-unitary. Equation (4.7.7) leads to:

$$\mathbf{X}^{*}(\tau) = \mathcal{G}\,\mathbf{X}^{-1}(\tau)\,\mathcal{G}^{-1} \tag{4.7.13}$$

If η_X is an eigenvalue of $\mathbf{X}$, then η_X^{*} (the conjugate of η_X) is an eigenvalue of $\mathbf{X}^{*}$ and Eq. (4.7.13) states also that η_X^{-1} is an eigenvalue of $\mathbf{X}^{*}$ by similarity. Consequently if η_X^{*} and η_X^{-1} coincide, also η_X and $\eta_X^{*\,-1}$ coincide. The latter conclusion means that the spectrum of the matrizant of a Hamiltonian system (a $\mathcal{G}$-unitary matrix) is symmetric about the unit circle. Similarly, it can be proven that the spectrum of the matrix of coefficients of a Hamiltonian system (a $\mathcal{G}$-Hamiltonian matrix) is symmetric about the imaginary axis. Considering a particular Hermitian matrix $\mathcal{G} = i\,\mathcal{J}$, in which $\mathcal{J}$ is as in Eq. (4.7.2) , replacing it in Eq. (4.7.10) and considering real coefficients, leads to a canonical equation as in Eq. (4.7.1). Thus, evaluating the matrizant over a period (monodromy matrix) leads exactly to the statement of the Lyapunov-Poincaré theorem. Notice that the matrizant, and so the monodromy matrix of the system in Eq. (4.7.1) are $\left(i\,\mathcal{J}\right)$-unitary matrices. A $\left(i\,\mathcal{J}\right)$-unitary matrix has the following property:

$$\begin{aligned}\mathbf{X}^{*}(\tau) = \left(i\,\mathcal{J}\right)\mathbf{X}^{-1}(\tau)\left(i\,\mathcal{J}\right)^{-1} = \mathcal{J}\,\mathbf{X}^{-1}(\tau)\,\mathcal{J}^{-1} \quad \Rightarrow \\ \Rightarrow \quad \mathbf{X}^{*}(\tau)\,\mathcal{J}\,\mathbf{X}(\tau) = \mathcal{J}\end{aligned} \tag{4.7.14}$$

which is the definition of symplectic matrix.

Definition (*eigenvalues of the first, second and mixed kind*): let **Z** be a $\mathcal{G}$-unitary matrix, and let η_Z be an r-fold eigenvalue of **Z** (eigenvalue with multiplicity r) such that $\left|\eta_Z\right| = 1$, then let $\mathbf{v}_Z$ be an eigenvector of **Z** belonging to the η_Z-eigensubspace; η_Z is said to be an r-fold eigenvalue of the *first kind* if $\left\langle \mathbf{v}_Z\,,\mathbf{v}_Z\right\rangle^{(\mathcal{G})} > 0$ and of the *second kind* if $\left\langle \mathbf{v}_Z\,,\mathbf{v}_Z\right\rangle^{(\mathcal{G})} < 0$. Eigenvalues of the first and second kind are also called *definite*, since the indefinite scalar product returns a value of fixed sign. If an r-fold eigenvalue η_Z lies on the unit circle ($\left|\eta_Z\right| = 1$) and $\left\langle \mathbf{v}_Z\,,\mathbf{v}_Z\right\rangle^{(\mathcal{G})}$ does not return a value of fixed sign on the η_Z-eigensubspace, then there must be a non-zero vector $\mathbf{v}_Z$ in that eigensubspace such that $\langle \mathbf{v}_Z, \mathbf{v}_Z \rangle^{(\mathcal{G})} = 0$, thus η_Z is said to be an r-fold eigenvalue of *mixed kind* or an *indefinite* eigenvalue. When η_Z does not lie on the unit circle, *i.e.* $|\eta_Z| \neq 1$, simpler definitions concerning definite eigenvalues are available: η_Z is an eigenvalue of the first kind if $|\eta_Z| < 1$ and of the second kind if $|\eta_Z| > 1$.

Lemma 1 (*multiple elementary divisors and mixed kind*): Let $\mathbf{Z}$ be a $\mathcal{G}$-unitary matrix with an r-fold eigenvalue on the unit circle η_Z with at least one multiple elementary divisor, then η_Z is of mixed kind, thus there is an eigenvector $\mathbf{v}_Z$ corresponding to η_Z such that $\langle \mathbf{v}_Z, \mathbf{v}_Z \rangle^{(\mathcal{G})} = 0$.

Lemma 2 (*isotropic eigenvectors*): if η_Z is an r-fold eigenvalue of a $\mathcal{G}$-unitary matrix $\mathbf{Z}$ that does not lie on the unit circle, then every eigenvector $\mathbf{v}_Z$ corresponding to η_Z is *isotropic*, *i.e.* $\langle \mathbf{v}_Z, \mathbf{v}_Z \rangle^{(\mathcal{G})} = 0$.

Theorem 1 (*Krein Theorem on perturbation of $\mathcal{G}$-unitary matrices*): Let $\mathbf{Z}_0$ be a $2k \times 2k$ $\mathcal{G}$-unitary matrix with a definite eigenvalue $\eta_Z^{(0)}$ on the unit circle, then:

1 All the elementary divisors of $\eta_Z^{(0)}$ are simple

2 There exist $\mu_1 > 0$ and $\mu_2 > 0$ such that for any $2k \times 2k$ $\mathcal{G}$-unitary matrix $\mathbf{Z}$ for which it is true that:

$$\| \mathbf{Z} - \mathbf{Z}_0 \| < \mu_1$$

all the eigenvalues η_Z of $\mathbf{Z}$ that satisfy $|\eta_Z - \eta_Z^{(0)}| < \mu_2$ lie on the unit circle and all their elementary divisors are simple.

Proof of 1 Proceeding by *reductio ad absurdum,* suppose that $\eta_Z^{(0)}$ has multiple divisors, thus, by *Lemma* 1 there is a vector $\mathbf{v}_Z^{(0)}$ in the $\eta_Z^{(0)}$-eigensubspace for which $\left\langle \mathbf{v}_Z^{(0)}, \mathbf{v}_Z^{(0)} \right\rangle^{(\mathcal{G})} = 0$, but this is impossible due the fact $\eta_Z^{(0)}$ is a definite eigenvalue on the unit circle. (Q.E.D.)

Proof of 2 Consider a sequence of $\mathcal{G}$-unitary matrices that converge to $\mathbf{Z}_0$: $\mathbf{Z}_1, \mathbf{Z}_2, \ldots \to \mathbf{Z}_0$, with eigenvalues $\eta_Z^{(1)}, \eta_Z^{(2)}, \ldots \to \eta_Z^{(0)}$, suppose that the generic matrix $\mathbf{Z}_m$ in the sequence has an eigenvalue $\eta_Z^{(m)}$ that can lie or not on the unit circle, $|\eta_Z^{(m)}| = 1$ or $|\eta_Z^{(m)}| \neq 1$, with multiple elementary divisors and let $\mathbf{v}_Z^{(m)}$ be a normalized corresponding eigenvector, thus for *Lemma* 1 and 2:

$$\begin{cases} \mathbf{Z}_m \mathbf{v}_Z^{(m)} = \eta_Z^{(m)} \mathbf{v}_Z^{(m)} \\ \left\| \mathbf{v}_Z^{(m)} \right\| = 1 \\ \left\langle \mathbf{v}_Z^{(m)}, \mathbf{v}_Z^{(m)} \right\rangle^{(\mathcal{G})} = 0 \end{cases} \tag{4.7.15}$$

It is possible to find a subsequence such that:

$$\left[\mathbf{v}_Z^{(m)}\right]_{m\to\infty} \to \mathbf{v}_Z^{(0)} \quad \Rightarrow \quad \lim_{m\to\infty}\left\|\mathbf{v}_Z^{(m)} - \mathbf{v}_Z^{(0)}\right\| = 0, \quad \begin{cases} \mathbf{Z}_0\mathbf{v}_Z^{(0)} = \eta_Z^{(0)}\mathbf{v}_Z^{(0)} \\ \left\|\mathbf{v}_Z^{(0)}\right\| = 1 \\ \left\langle \mathbf{v}_Z^{(0)}, \mathbf{v}_Z^{(0)} \right\rangle^{(\mathcal{G})} = 0 \end{cases} \tag{4.7.16}$$

Hence $\eta_Z^{(0)}$ is not definite and there are no numbers $\mu_1 > 0$ and $\mu_2 > 0$ for which the neighborhood $\left|\eta_Z - \eta_Z^{(0)}\right| < \mu_2$ contains η_Z on the unit circle with simple elementary divisors. The latter contradiction proves the statement 2 of *Krein Theorem*. (Q.E.D.)

Definition (*strong and weak stability of the Hamiltonian*): let $\mathcal{H}_0(\tau)$ be a Hamiltonian matrix with T-periodic coefficients corresponding to an equation as in Eq. (4.7.10) and let $\mathcal{H}(\tau)$ the Hamiltonian after a deformation such that:

$$\begin{cases} i^{-1}\mathcal{G}\dot{\mathbf{z}} = \mathcal{H}(\tau)\mathbf{z} \\ \mathcal{G}^* = \mathcal{G} \\ \mathcal{H}^*(\tau) = \mathcal{H}(\tau) = \mathcal{H}(\tau + \mathrm{T}) \end{cases}, \quad \int_0^{\mathrm{T}} \left\|\mathcal{H}(\tau) - \mathcal{H}_0(\tau)\right\| d\tau < \mu \tag{4.7.17}$$

where μ is some positive number. If the solutions of the system, whose Hamiltonian is $\mathcal{H}(\tau)$, are bounded for $\tau \in (-\infty, \infty)$ then $\mathcal{H}_0(\tau)$ is called *strongly stable*. If the solutions of the system whose Hamiltonian is $\mathcal{H}_0(\tau)$ are bounded for $\tau \in (-\infty, \infty)$, but it is not strongly stable, then $\mathcal{H}_0(\tau)$ is said to be *weakly stable*, thus there is no μ for which $\mathcal{H}(\tau)$ returns bounded solutions. Assume that a Hamiltonian system is strongly stable, this is equivalent to presume that all the multipliers of the system lie on the unit circle and they are slightly separated from each other. The latter assertion is due the fact that after a small deformation of the Hamiltonian, multipliers cannot leave the unit circle without violating the symmetry (about the circle) if they are displaced. On the other hand, if there is a couple of coincident multipliers on the unit circle, there may be a suitable deformation of the Hamiltonian, because of which, multipliers can leave the unit circle without violating the symmetry. It can be proven that a proper $2k \times 2k$ Hamiltonian system as in Eq. (4.7.17), has exactly k multipliers of the first kind and k multipliers of the second kind. It can also be proven (*Continuity Theorem* [39]), that multipliers of fixed kind depend continuously on the Hamiltonian, thus, a continuous deformation of the Hamiltonian induces a continuous displacement of definite multipliers in the complex plane. Since definite multipliers that have left the unite circle can be classified by the definition of eigenvalues of the first and of the second kind, *i.e.* of the first kind if a multiplier lies within the unit circle and of second kind if it lies outside the unit circle, and since they must respect the symmetry about this circle, multipliers can leave the unit circle, after a meeting, only if they belong to different kinds. Conversely, if two multipliers of the same kind, under a deformation of the Hamiltonian, meet on the unit circle, then they cannot leave the circle without breaking the symmetry. If the system has real coefficients, then multipliers are also symmetric with respect to the real axis, thus, if a meeting occurs on the upper part of the unit circle (positive imaginary parts), then a specular one occurs on the bottom part of the circle (negative imaginary parts), as displayed in Fig. 4.4.

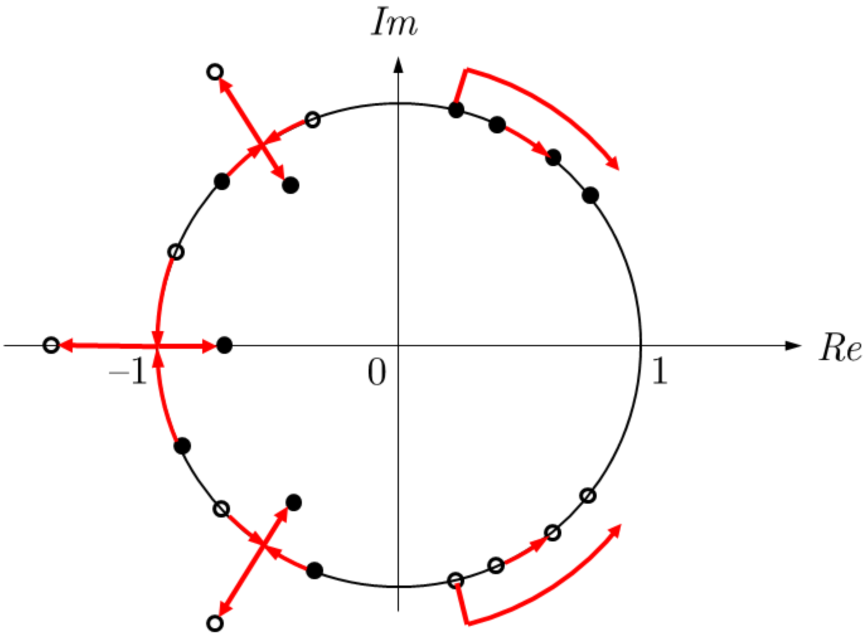

Figure 4.4: Multipliers moving in the complex plane, solid dots represent multipliers of the first kind and empty circles represent multipliers of the second kind

The definitions of eigenvalues of the first, second and mixed kind, along with the *Theorem* 1 and the above observations lead to an important conclusion: if definite multipliers of the same kind meet on the unit circle, then the algebraic multiplicity of the resulting multiple multiplier is equal to its geometric multiplicity and it remains definite with simple elementary divisors. Conversely a meeting of definite multipliers of different kinds gives rise to a discrepancy between multiplicities of the resulting multiple multiplier, thus, a multiplier of mixed kind is formed on the unit circle and, according to *Lemma* 1, it has multiple elementary divisors. It can be shown (Gel'fand-Lidskii theorem, [39]) that a system as in Eq. (4.7.17) with a multiplier of mixed kind, after an arbitrary small deformation of the Hamiltonian, can generate definite multipliers that not lie on the unit circle and such a deformation always exists. Thus, the switching mechanism that brings a Hamiltonian system to instability is a collision of multipliers of different kind on the unit circle. The latter is none other than a revisited form of the more compact statement of the *Krein-Gel'fand-Lidskii strong stability Theorem*:

A Hamiltonian system is strongly stable if and only if its multipliers lie on the unit circle and are definite.

Meetings involving multipliers of different kinds are called *Krein collisions* and they are the origin of *Krein bifurcation*s. Further classifications and nomenclature of those bifurcations, depending on where the collision occurs (and on the context of the analysis), are also available.

4.8 Simple undamped shaft with gyroscopic effects

In the case of spinning shaft without dissipative effects, Eq. (4.3.20) reads:

$$\begin{cases} \mathbf{I}\,\ddot{\mathbf{u}} + \bar{\bar{\mathbf{C}}}\,\dot{\mathbf{u}} + \left[\bar{\bar{\mathbf{K}}} + \Delta L\cos(\hat{\varOmega}\tau)\bar{\bar{\mathbf{L}}}\right]\mathbf{u} = \mathbf{0} \\ \bar{\bar{\mathbf{C}}}^{\mathrm{T}} = -\bar{\bar{\mathbf{C}}} \end{cases} \tag{4.8.1}$$

Thus, $\bar{\bar{\mathbf{C}}}$ is skew-symmetric. Equation (4.8.1) is another particular case and, for simplicity, it will be named:

Simplified case 2: no damping, rotating shaft with gyroscopic effects, $\bar{\bar{\mathbf{C}}}^{\mathrm{T}} = -\bar{\bar{\mathbf{C}}}$.

The present case, like the *simplified case* 1, is Hamiltonian. Hence, it can be cast in canonical form. Consider the following state-space coordinate transformation:

$$\begin{cases} \bar{\mathcal{J}}\,\dot{\mathbf{u}}_S = \bar{\mathcal{H}}(\tau)\mathbf{u}_S \\ \mathbf{u}_S(\tau) = \left\{\mathbf{u}^{\mathrm{T}}(\tau), \dot{\mathbf{u}}^{\mathrm{T}}(\tau)\right\}^{\mathrm{T}} \end{cases} \tag{4.8.2}$$

where $\bar{\mathcal{J}}$ is a non-singular skew-symmetric, and $\bar{\mathcal{H}}(\tau)$ is symmetric:

$$\begin{cases} \bar{\mathcal{J}} = \begin{bmatrix} -\bar{\bar{\mathbf{C}}} & -\mathbf{I} \\ \mathbf{I} & \mathbf{0} \end{bmatrix} \\ \bar{\mathcal{H}}(\tau) = \begin{bmatrix} \bar{\bar{\mathbf{K}}} + \Delta L\cos(\hat{\varOmega}\tau)\bar{\bar{\mathbf{L}}} & \mathbf{0} \\ \mathbf{0} & \mathbf{I} \end{bmatrix} \end{cases} \tag{4.8.3}$$

$\bar{\mathcal{J}}$ respect the following equality:

$$\begin{cases} \bar{\mathcal{J}} = \mathcal{S}^{\mathrm{T}}\mathcal{J}\,\mathcal{S}, \quad \mathcal{J} = \begin{bmatrix} \mathbf{0} & -\mathbf{I} \\ \mathbf{I} & \mathbf{0} \end{bmatrix} \\ \mathcal{S} = \begin{bmatrix} \mathbf{I} & \mathbf{0} \\ \frac{1}{2}\bar{\bar{\mathbf{C}}} & \mathbf{I} \end{bmatrix} \;\Rightarrow\; \mathcal{S}^{\mathrm{T}} = \begin{bmatrix} \mathbf{I} & -\frac{1}{2}\bar{\bar{\mathbf{C}}} \\ \mathbf{0} & \mathbf{I} \end{bmatrix}, \quad \det\left[\mathcal{S}\right] \neq 0 \end{cases} \tag{4.8.4}$$

Hence:

$$\bar{\mathcal{J}}\,\dot{\mathbf{u}}_S = \bar{\mathcal{H}}(\tau)\mathbf{u}_S \quad\Rightarrow\quad \mathcal{S}^{\mathrm{T}}\mathcal{J}\,\mathcal{S}\,\dot{\mathbf{u}}_S = \bar{\mathcal{H}}(\tau)\mathbf{u}_S \tag{4.8.5}$$

Adopting the substitution $\mathbf{z} = \mathcal{S}\mathbf{u}_S \Rightarrow \mathbf{u}_S = \mathcal{S}^{-1}\mathbf{z}$, since $\mathcal{S}$ is non-singular, Eq. (4.8.5) becomes:

$$\mathcal{J}\,\dot{\mathbf{z}} = \mathcal{S}^{-\mathrm{T}}\bar{\mathcal{H}}(\tau)\,\mathcal{S}^{-1}\mathbf{z} \tag{4.8.6}$$

And, finally:

$$\begin{cases} \mathcal{J}\,\dot{\mathbf{z}} = \mathcal{H}(\tau)\,\mathbf{z} \\ \mathbf{z} = \mathcal{S}\,\mathbf{u}_S = \left\{ \mathbf{u}^{\mathrm{T}}, \left(\dfrac{1}{2}\bar{\bar{\mathbf{C}}}\,\mathbf{u} + \dot{\mathbf{u}} \right)^{\mathrm{T}} \right\}^{\mathrm{T}} \\ \\ \mathcal{H}(\tau) = \mathcal{H}^{\mathrm{T}}(\tau) = \begin{bmatrix} \bar{\bar{\mathbf{K}}} + \Delta L \cos(\hat{\Omega}\tau)\,\bar{\bar{\mathbf{L}}} - \dfrac{1}{4}\bar{\bar{\mathbf{C}}}^{2} & \dfrac{1}{2}\bar{\bar{\mathbf{C}}} \\ -\dfrac{1}{2}\bar{\bar{\mathbf{C}}} & \mathbf{I} \end{bmatrix} \end{cases} \tag{4.8.7}$$

The monodromy matrix of the canonical equation in Eq. (4.8.6) is $\left(i\,\mathcal{J}\right)$-unitary, as proven in Section 4.7, then the multipliers of the *simplified case* 2 are symmetric about the unit circle and all the theorems and the definitions given in Section 4.7 apply. In this case, Eq. (4.6.4) reads:

$$\begin{cases} \left[\Lambda^2\,\mathbf{H}_2 + \Lambda\left(\mathbf{H}_1^{(1)} + \mathbf{H}_1^{(2)} \right) + \mathbf{H}_0^{(1)} + \varepsilon\,\mathbf{H}_0^{(2)} + \mathbf{H}_0^{(3)} \right]\mathbf{c} = \mathbf{0} \\ \left[\mathbf{H}_2\right]^{\mathrm{T}} = \mathbf{H}_2 \\ \left[\mathbf{H}_1^{(1)}\right]^{\mathrm{T}} = -\mathbf{H}_1^{(1)} \\ \left[\mathbf{H}_1^{(2)}\right]^{\mathrm{T}} = -\mathbf{H}_1^{(2)}, \quad \det\left[\mathbf{H}_1^{(2)}\right] = 0 \\ \left[\mathbf{H}_0^{(1)}\right]^{\mathrm{T}} = \mathbf{H}_0^{(1)} \\ \left[\mathbf{H}_0^{(2)}\right]^{\mathrm{T}} = \mathbf{H}_0^{(2)} \\ \left[\mathbf{H}_0^{(3)}\right]^{\mathrm{T}} = -\mathbf{H}_0^{(3)}, \quad \det\left[\mathbf{H}_0^{(3)}\right] = 0 \end{cases} \tag{4.8.8}$$

Hence:

$$\begin{aligned} & \left[\Lambda^2\,\mathbf{H}_2 + \Lambda\left(\mathbf{H}_1^{(1)} + \mathbf{H}_1^{(2)} \right) + \mathbf{H}_0^{(1)} + \varepsilon\,\mathbf{H}_0^{(2)} + \mathbf{H}_0^{(3)} \right]\mathbf{c} = \mathbf{0} \quad \Rightarrow \\ & \qquad \Rightarrow \quad \mathbf{c}^{*}\left[\Lambda^2\,\mathbf{H}_2 + \Lambda\left(\mathbf{H}_1^{(1)} + \mathbf{H}_1^{(2)} \right) + \mathbf{H}_0^{(1)} + \varepsilon\,\mathbf{H}_0^{(2)} + \mathbf{H}_0^{(3)} \right]\mathbf{c} = 0 \quad \Rightarrow \\ & \qquad \Rightarrow \quad \Lambda^2\,H_2\left(\varepsilon\right) + \Lambda\left[i\,H_1^{(1)}\left(\varepsilon\right) + i\,H_1^{(2)}\left(\varepsilon\right) \right] + H_0^{(1)}\left(\varepsilon\right) + \varepsilon\,H_0^{(2)}\left(\varepsilon\right) + i\,H_0^{(3)}\left(\varepsilon\right) = 0 \end{aligned} \tag{4.8.9}$$

Thus, since $\mathbf{H}_1^{(1)}$ is in general non-singular (unlike $\mathbf{H}_1^{(2)}$ that is always singular), no further information can be taken from Eq. (4.8.9). This is due the fact that in order to obtain complex conjugate pairs for Λ, one has to consider more that one complex quadratic polynomial equation, like Eq. (4.8.9), at a time. The latter means that, unlike in the *simplified case* 1, the possibility of complex quadruplet has to be taken into consideration.

Recalling the Krein theorem and the Krein-Gel'fand-Lidskii strong stability theorem, if the system is stable, then its multipliers lie on the unit circle and are definite. A complex quadruplet is formed by multipliers that do not lie on the unit circle, and so the system is already unstable due to the symmetry about the unit circle, *i.e.* two of the four multipliers lie outside it. This means that, to form a complex quadruplet, two specular (symmetric with respect the real axis) collisions occur simultaneously involving multipliers of different kinds, in groups of two.

Consider a deformation of the Hamiltonian, because of which the system has four imaginary multipliers (imaginary quadruplet) near to a double collision; the system is still stable, *i.e.* all its multipliers are definite. A further deformation is considered, such that the system has a pair of multiple multipliers of mixed kind. These indefinite multipliers have to be symmetric about the real axis. At this point, Krein-Gel'fand-Lidskii theorem assures that a deformation that brings the system to instability always exists. Hence, when the system is stable, the multipliers are organized into imaginary quadruplets, which, under a deformation of the Hamiltonian, move in different directions on the unit circle, in groups of two definite multipliers of different kinds that move in tandem.

The concept above is displayed in Fig. 4.5, where (left) two pairs of multipliers give rise to a double collision on the unit circle, and (right) the aftermath of the Krein collision is displayed, with the multipliers that do not lie on the circle, arranged in a complex quadruplet. The initial split of multipliers is due to the fact that gyroscopic effects produce a separation of the spectrum of the unperturbed system in forward and backward values (Section 3.12). Due to the continuity theorem, a subsequent deformation of the Hamiltonian cannot cope with this separation, nullifying it. The latter observation, that relates the behavior of multipliers and the modal properties of the unperturbed system, is the reason for which there are no separations between multipliers in the *simplified case* 1: the spectrum of the unperturbed system is not partitioned in forward and backward values (all modes correspond to synchronous motions), thus the complex quadruplet degenerates in a pair of double multipliers of fixed kinds. Hence, critical collisions can only occur on the real axis.

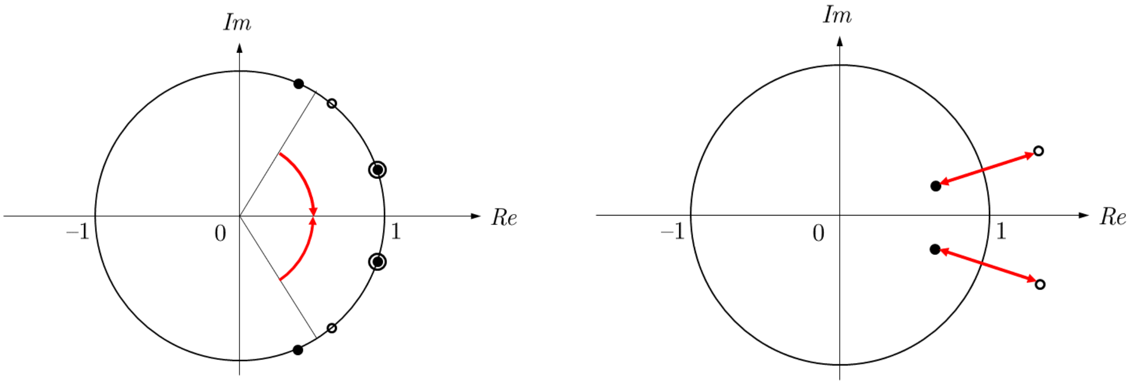

Figure 4.5: An imaginary quadruplet of multipliers (solid and empty dots represent different kinds) collide under a deformation (left) and give rise to a complex quadruplet (right).

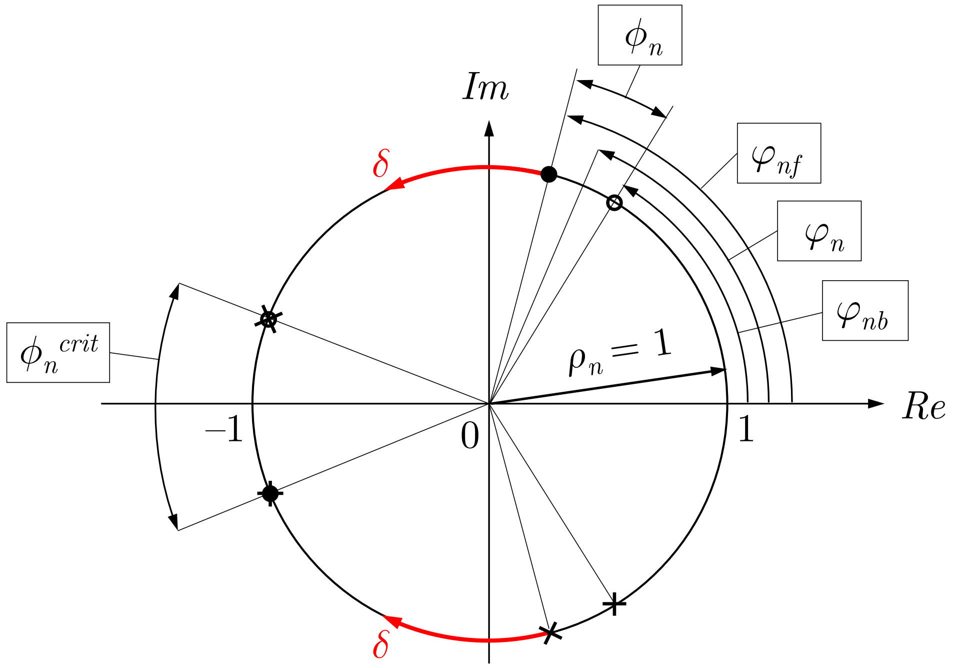

Figure 4.6: An imaginary quadruplet of multipliers moving towards a double collision

As done in the *simplified case* 1, also in the present case it is possible to draw conclusions about the transition solutions. In the presence of gyroscopic effects each pair of coincident values of natural frequency ω_n separate into two distinct values $\omega_{nf} > \omega_{nb}$ (forward and backward values). As a consequence, also the Floquet multipliers for each mode separate into two pairs of counter-rotating multipliers on the unit circle, as represented in Fig. 4.6.

The positions of the Floquet multipliers on the unit circle can be determined as functions of ω_{nf}, ω_{nb} and δ by considering the characteristic equation det $\mathbf{H}_{1,1} = 0$. Therefore, referring to Fig. 4.6, the phase relations found between the forward and backward points are:

$$\begin{cases} \varphi_{nf} = 2\pi\,\omega_{nf}\sqrt{\delta} \\ \varphi_{nb} = 2\pi\,\omega_{nb}\sqrt{\delta} \\ \phi_n = 2\pi\,(\omega_{nf} - \omega_{nb})\sqrt{\delta} \\ \varphi_n = \pi\,(\omega_{nf} + \omega_{nb})\sqrt{\delta} \\ \varphi_{nk}^{crit} = k\pi, \quad k = 0,1,2,\ldots \\ \rho_n = 1 \end{cases} \tag{4.8.10}$$

where ρ_n is the modulus (radius) of each multiplier, ϕ_n is their phase difference, and φ_n is the phase of their intermediate point, which in critical conditions (collisions) must be either 0 or an integer multiple of π. Equating φ_n with $k\,\pi$ in Eq. (4.8.10), yields the critical values of δ at $\varepsilon = 0$, for both the non-gyroscopic and the gyroscopic problems:

$$\begin{cases} \omega_{nf} = \omega_{nb} = \omega_n \quad \Rightarrow \quad \delta^{crit}_{nk,\varepsilon=0} = \dfrac{k^2}{4\omega_n^2} \\ \omega_{nf} \neq \omega_{nb} \neq \omega_n \quad \Rightarrow \quad \delta^{crit}_{nk,\varepsilon=0} = \dfrac{k^2}{(\omega_{nf} + \omega_{nb})^2} \end{cases} \tag{4.8.11}$$

The first of Eq. (4.8.11) coincide with what was obtained in Eq. (4.6.14). For a given eigenvalue of order n, these critical values produce a sequence of k points on the δ axis, from which the related sequence of instability regions originate. On the unit circle, the critical eigenvalues Λ form quadruplets out of the real axis, which can be identified recalling Eq. (4.8.10) and Eq. (4.8.11):

$$\begin{aligned} \Lambda^{crit}_{nk,\varepsilon=0} = \frac{i}{2\pi}\left(\varphi^{crit}_{nk} \pm \frac{1}{2}\phi^{crit}_{nk}\right) = \frac{i}{2}\left[k \pm (\omega_{nf} - \omega_{nb})\sqrt{\delta^{crit}_{nk,\varepsilon=0}}\right] = \\ = \frac{ik}{2}\left[1 \pm \left(\frac{\omega_{nf} - \omega_{nb}}{\omega_{nf} + \omega_{nb}}\right)\right] \end{aligned} \tag{4.8.12}$$

which reduces to $i\,k/2$ in absence of gyroscopic effects. Hence, in the rotating case, the critical solutions are represented by generally non-periodic, limited-amplitude functions. When $\varepsilon > 0$, the critical values Λ^{crit}_{nk} can still be defined following the same scheme, as functions of a δ^{crit}_{nk}, different from $\delta^{crit}_{nk,\varepsilon=0}$ given in Eq. (4.8.11):

$$\Lambda^{crit}_{nk} = \frac{i}{2}\left[k \pm (\omega_{nf} - \omega_{nb})\sqrt{\delta^{crit}_{nk}}\right] \tag{4.8.13}$$

The latter equation provides a function $\Lambda^{crit}_{nk}(\delta)$ which, introduced in the operator **H**, yields a linear eigenproblem in ε, as in the non-rotating case. The difference is that in this case the critical values of Λ depend on the eigenvalue order, hence the solution of such an eigenproblem yields the instability regions related to a single characteristic exponent at a time, as shown in Fig. 4.7 for the critical values of the first characteristic exponent (forcing an unrealistic, exceedingly high value $\hat{\omega} = 300$ for the sake of readability).

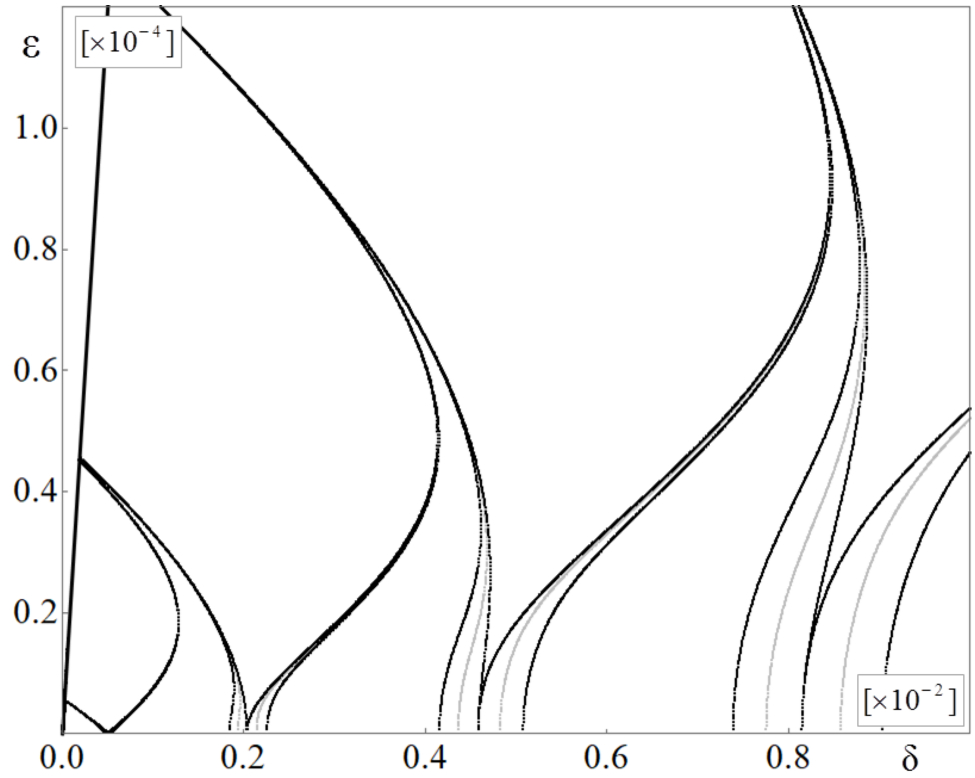

Figure 4.7: Ince-Strutt diagram for the first critical characteristic exponent

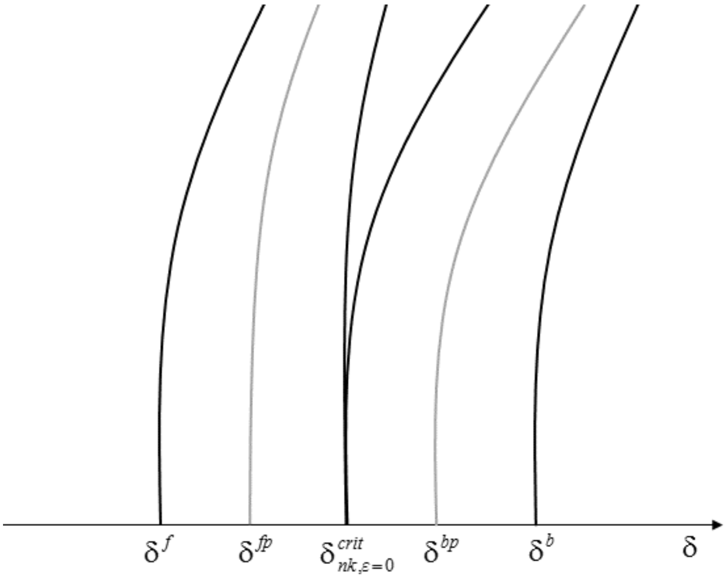

Figure 4.8: Critical values on the δ axis

Notice that the critical values Λ^{crit}_{nk} given by Eq. (4.8.13) not only produce the stability thresholds, but also two other stable solutions for each k, as shown in Fig. 4.7 and Fig. 4.8 (lateral black curves), together with the pairs of periodic solutions at $\Lambda = i\,k/2$ (lateral grey curves; the whole areas between each pair of grey curves were erroneously interpreted as instability regions in several studies, as reported in [64]). These four solutions occur for each k at «false» collision points on the unit circle, *i.e.* points in which two multipliers of the same kind coincide: either (+1, 0) or (–1, 0). On stability charts, they originate on the δ axis at ε = 0 with the following values:

$$\begin{cases} \delta^{f} = \left(\dfrac{\omega_{nb}}{\omega_{nf}}\right)^2 \delta^{crit}_{nk,\varepsilon=0}, \quad \delta^{b} = \left(\dfrac{\omega_{nf}}{\omega_{nb}}\right)^2 \delta^{crit}_{nk,\varepsilon=0} \\ \delta^{crit}_{nk,\varepsilon=0} = \left(\dfrac{k}{\omega_{nf}+\omega_{nb}}\right)^2 \\ \delta^{bp} = \left(\dfrac{k}{2\omega_{nb}}\right)^2, \quad \delta^{fp} = \left(\dfrac{k}{2\omega_{nf}}\right)^2 \end{cases} \Rightarrow \quad \delta^{f} < \delta^{fp} < \delta^{crit}_{nk,\varepsilon=0} < \delta^{bp} < \delta^{b} \tag{4.8.14}$$

Recalling Eq. (4.8.13), it is also clear that for a given mode n two consecutive critical values of Λ coincide at:

$$\delta_{nm} = \frac{1}{4(\omega_{nf} - \omega_{nb})^2} \tag{4.8.15}$$

Therefore a quadruple collision occurs on the unit circle at (0, + i) and (0, – i), and the related two adjacent instability regions merge at a certain value of ε > 0. This is another peculiar feature due to gyroscopic effects, yielding a substantial qualitative difference in the Ince-Strutt diagram.

It can be concluded that critical solutions in the rotating case are given by (generally) non-periodic limited-amplitude functions, and that the modifications induced by gyroscopic effects on global stability charts consist of shifts and merging of unstable regions. The magnitude of these modifications depends on separation of natural frequencies into pairs of forward and backward values (therefore they are expected to be very small for the simple shaft herein considered, without additional inertial elements). More in particular, at ε = 0 the shifts of unstable regions depend on the difference between the natural frequency ω_n and the average value $(\omega_{nf} + \omega_{nb})$ / 2 (not directly on the difference $\omega_{nf} - \omega_{nb}$).

4.9 Simple non-rotating shaft with mass-proportional damping distribution

The present Section focuses on a simple non-Hamiltonian case in which the angular speed of the shaft is set to zero, while an external damping, proportional with respect to the mass distribution, is considered. Thus, Eq. (4.3.14) reads:

$$\hat{\mathbf{M}}\ddot{\mathbf{q}}_d + a\hat{\mathbf{M}}\dot{\mathbf{q}}_d + \left[\hat{\mathbf{K}} + \Delta L \cos(\hat{\Omega}\tau)\hat{\mathbf{L}}\right]\mathbf{q}_d = \mathbf{0} \tag{4.9.1}$$

where *a* is a constant of proportionality. Introducing the changes of coordinates as in Section 4.3, Eq. (4.3.20) becomes:

$$\mathbf{I}\,\ddot{\mathbf{u}} + a\,\mathbf{I}\,\dot{\mathbf{u}} + \left[\bar{\bar{\mathbf{K}}} + \Delta L\cos(\hat{\Omega}\tau)\,\bar{\bar{\mathbf{L}}}\right]\mathbf{u} = \mathbf{0} \tag{4.9.2}$$

With $\bar{\bar{\mathbf{K}}}$ and $\bar{\bar{\mathbf{L}}}$ symmetric, as in the previous cases. The present case will be named as:

Simplified case 3: non-rotating shaft (no gyroscopic effects), mass-proportional damping, $\bar{\bar{\mathbf{C}}} = a\,\mathbf{I}$.

Then, Eq. (4.6.4) reads:

$$\begin{cases} \left[\Lambda^2\,\mathbf{H}_2 + \Lambda\left(a\,\mathbf{H}_2 + \mathbf{H}_1^{(2)}\right) + \mathbf{H}_0^{(1)} + \varepsilon\,\mathbf{H}_0^{(2)} + \mathbf{H}_0^{(3)}\right]\mathbf{c} = \mathbf{0} \\ \left[\mathbf{H}_2\right]^{\mathrm{T}} = \mathbf{H}_2 \\ \left[\mathbf{H}_1^{(2)}\right]^{\mathrm{T}} = -\mathbf{H}_1^{(2)}, \quad \det\left[\mathbf{H}_1^{(2)}\right] = 0 \\ \left[\mathbf{H}_0^{(1)}\right]^{\mathrm{T}} = \mathbf{H}_0^{(1)} \\ \left[\mathbf{H}_0^{(2)}\right]^{\mathrm{T}} = \mathbf{H}_0^{(2)} \\ \left[\mathbf{H}_0^{(3)}\right]^{\mathrm{T}} = -\mathbf{H}_0^{(3)}, \quad \det\left[\mathbf{H}_0^{(3)}\right] = 0 \end{cases} \tag{4.9.3}$$

And:

$$\begin{aligned} &\left[\Lambda^2\,\mathbf{H}_2 + \Lambda\left(a\,\mathbf{H}_2 + \mathbf{H}_1^{(2)}\right) + \mathbf{H}_0^{(1)} + \varepsilon\,\mathbf{H}_0^{(2)} + \mathbf{H}_0^{(3)}\right]\mathbf{c} = \mathbf{0} \\ &\qquad \Rightarrow \quad \mathbf{c}^*\left[\Lambda^2\,\mathbf{H}_2 + \Lambda\left(a\,\mathbf{H}_2 + \mathbf{H}_1^{(2)}\right) + \mathbf{H}_0^{(1)} + \varepsilon\,\mathbf{H}_0^{(2)} + \mathbf{H}_0^{(3)}\right]\mathbf{c} = 0 \quad \Rightarrow \\ &\qquad \Rightarrow \quad \Lambda^2\,H_2(\varepsilon) + \Lambda\left[a\,H_2(\varepsilon) + i\,H_1^{(2)}(\varepsilon)\right] + \\ &\qquad\qquad\qquad + H_0^{(1)}(\varepsilon) + \varepsilon\,H_0^{(2)}(\varepsilon) + i\,H_0^{(3)}(\varepsilon) = 0 \end{aligned} \tag{4.9.4}$$

which returns for each **c**:

$$\Lambda_{1,2} = -\frac{a}{2} - i\,\frac{H_1^{(2)}(\varepsilon)}{2H_2(\varepsilon)} \pm \left[\Psi_R(\varepsilon) + i\,\Psi_I(\varepsilon)\right] \tag{4.9.5}$$

Where $\Psi_R(\varepsilon) + i\,\Psi_I(\varepsilon)$ is the principal value of the square root:

$$\sqrt{\left[\frac{a\,H_2(\varepsilon) + i\,H_1^{(2)}(\varepsilon)}{2H_2(\varepsilon)}\right]^2 - \frac{H_0^{(1)}(\varepsilon) + \varepsilon\,H_0^{(2)}(\varepsilon) + i\,H_0^{(3)}(\varepsilon)}{H_2(\varepsilon)}} \tag{4.9.6}$$

Eq. (4.9.5) returns a conjugate pair if:

$$\begin{cases} H_1^{(2)}(\varepsilon) = 0 \\ \Psi_R(\varepsilon) = 0 \end{cases} \tag{4.9.7}$$

The result does not change if, instead of the principal value of the square root in (4.9.6), one chooses the conjugate value $\Psi_R(\varepsilon) - i\,\Psi_I(\varepsilon)$. Thus, Eq. (4.9.7) is a sufficient condition to obtain conjugate pairs for Λ. Hence, Eq. (4.9.5) reduces to:

$$\Lambda_{1,2} = -\frac{a}{2} \pm i\,\Psi_I(\varepsilon) \tag{4.9.8}$$

Suppose that $\Psi_R(\varepsilon) \neq 0$, then Eq. (4.9.5) gives:

$$\Lambda_{1,2} = -\frac{a}{2} \pm \left[\Psi_R(\varepsilon) + i\,\Psi_I(\varepsilon)\right] \tag{4.9.9}$$

Thus, in order to obtain only pairs of conjugate values for Λ, there must be another eigenvector, say $\hat{\mathbf{c}}$, for which Eq. (4.9.5) returns:

$$\hat{\Lambda}_{1,2} = -\frac{a}{2} \pm \left[\Psi_R(\varepsilon) - i\,\Psi_I(\varepsilon)\right] \tag{4.9.10}$$

Eq. (4.9.9) along with (4.9.10) represent a complex quadruplet of characteristic exponents symmetric with respect to both the real axis and the vertical line $\Re(\Lambda) = -a/2$. Notice that *a* do not depend on ε, so it is possible to reduce the *simplified case* 3 to the *simplified case* 1 with continuity ($a \to 0$) without nullify $\Psi_R(\varepsilon)$. By virtue of the relationship between the behavior of multipliers and the modal properties of the unperturbed system, claiming that a complex quadruplet exists is equivalent to state that the unperturbed system does not have modal synchronous motions. This is in contradiction with the hypothesis of proportional damping and symmetric discretized operators. The limit case occurs when the preloads and the oscillating term of the load do not depend on the twisting moment, thus the equations of motion are completely decoupled with respect to two orthogonal planes (since gyroscopic effects are already neglected) and the pair $\hat{\Lambda}_{1,2}$ cannot be taken into consideration. In other words, Eq. (4.9.7) is also a necessary condition. The same is not true for general non-proportional damping even if the damping matrix is symmetric.

Since the real part of characteristic exponents (if they occur in pairs of conjugate values), does not depend on ε, information can be taken from the following characteristic equation:

$$\begin{aligned} &\begin{cases} \det \mathbf{H} = 0 \\ \varepsilon = 0 \end{cases} \quad \Rightarrow \quad \det \mathbf{H}_{1,1} = 0 \quad \Leftrightarrow \quad \prod_{n=1}^{4\mathrm{N}} \left[\Lambda^2 + 2\zeta_n \omega_n \sqrt{\delta}\,\Lambda + \omega_n^2\,\delta\right] = 0 \quad \Rightarrow \\ &\Rightarrow \quad \rho_n = e^{2\pi \Re(\Lambda_n)} = e^{-2\pi \zeta_n \omega_n \sqrt{\delta}} \end{aligned} \tag{4.9.11}$$

where ζ_n is the *n*-th modal damping factor, Λ_n is the *n*-th root of the characteristic equation and ρ_n is the modulus of the *n*-th multiplier. It is easy to see that:

$$2\zeta_n\omega_n = a \quad \Leftrightarrow \quad \zeta_n = \frac{1}{2}\frac{a}{\omega_n} \quad \Rightarrow \quad \rho_n = e^{-a\pi\sqrt{\delta}} \tag{4.9.12}$$

Hence, ρ_n does not depend on neither ε or *n*, but only on δ. This important result means that all multipliers lie on a circle of radius $e^{-a\pi\sqrt{\delta}}$, when they occur in complex conjugate pairs. With $a > 0$, (proper positive definite damping matrix), multipliers lie on a circle of radius less than 1, thus they all lie within the unit circle. Since multipliers cannot occur in complex quadruplet, they can exit the unit circle if and only if they occur in distinct real values.

It is important to recall that the *simplified case* 3 is not a Hamiltonian system, thus all the theorems and the definition provided in Section 4.7 do not apply. Even the definitions of multipliers of first, second or of mixed kind, as given in Section 4.7, have no meaning in this case, and the monodromy matrix is not symplectic. However, the monodromy matrix of the *simplified case* 3 falls into a known category of matrices: μ*-symplectic* matrices [104].

Definition (μ*-symplectic matrix*): a $2k \times 2k$ real matrix **Z** is called μ*-symplectic* if:

$$\mathbf{Z}^{\mathrm{T}}\mathcal{J}\,\mathbf{Z} = \mu\,\mathcal{J}, \quad 0 \le \mu \le 1 \tag{4.9.13}$$

with $\mathcal{J}$ as in the previous Sections. Such a matrix has the following property:

The eigenvalues of a μ*-symplectic matrix are symmetric, in the sense of the inversion, about a circle in the complex plane, centered in the origin, of radius* $\rho_\mu = \sqrt{\mu}$.

Definition (γ*-Hamiltonian matrix*): a $2k \times 2k$ real matrix **U** is called γ*-Hamiltonian* if:

$$\mathbf{U}^{\mathrm{T}}\mathcal{J} + \mathcal{J}\,\mathbf{U} = -2\gamma\,\mathcal{J}, \quad \gamma \ge 0 \tag{4.9.14}$$

Notice that **U** is γ*-Hamiltonian* if and only if $\mathbf{U} + \gamma\,\mathbf{I}_{2k}$ is Hamiltonian.

Proof: Eq. (4.9.14) can be rewritten as:

$$\left(\mathbf{U} + \gamma\mathbf{I}_{2k}\right)^{\mathrm{T}}\mathcal{J} + \mathcal{J}\left(\mathbf{U} + \gamma\mathbf{I}_{2k}\right) = \mathbf{0} \tag{4.9.15}$$

which is the definition of Hamiltonian matrix. (Q.E.D.)

Definition (γ*-Hamiltonian linear system*): any system of linear ordinary differential equations that can be written in the form:

$$\dot{\mathbf{z}} = \bar{\mathbf{A}}(\tau)\mathbf{z} = \mathcal{J}\left[\mathcal{H}(\tau) + \gamma\,\mathcal{J}\right]\mathbf{z}, \quad \gamma \ge 0, \quad \mathcal{H}^{\mathrm{T}}(\tau) = \mathcal{H}(\tau) \tag{4.9.16}$$

is said to be a γ*-Hamiltonian linear system*. Where $\bar{\mathbf{A}}(\tau)$ is the $2k \times 2k$ matrix of coefficients of the system. It can be proven [104] that the principal fundamental matrix of a γ-Hamiltonian system is μ-symplectic with $\mu = e^{-2\gamma\tau}$. Indeed, let $\mathbf{Z}(\tau)$ be the matrizant of the system in Eq. (4.9.16), thus $\dot{\mathbf{Z}}(\tau) = \bar{\mathbf{A}}(\tau)\mathbf{Z}(\tau)$, hence, (dropping temporarily the dependence on τ for clarity):

$$
\begin{aligned}
\frac{d}{d\tau}\left[\mathbf{Z}^{\mathrm{T}}\mathcal{J}\,\mathbf{Z}\right] = \dot{\mathbf{Z}}^{\mathrm{T}}\mathcal{J}\,\mathbf{Z} + \mathbf{Z}^{\mathrm{T}}\mathcal{J}\,\dot{\mathbf{Z}} = \left(\bar{\mathbf{A}}\,\mathbf{Z}\right)^{\mathrm{T}}\mathcal{J}\,\mathbf{Z} + \mathbf{Z}^{\mathrm{T}}\mathcal{J}\,\bar{\mathbf{A}}\,\mathbf{Z} = \\
&= \mathbf{Z}^{\mathrm{T}}\left[\bar{\mathbf{A}}^{\mathrm{T}}\mathcal{J} + \mathcal{J}\,\bar{\mathbf{A}}\right]\mathbf{Z} = \\
&= \mathbf{Z}^{\mathrm{T}}\left[\mathcal{J}\left(\mathcal{H} + \gamma\,\mathcal{J}\right)^{\mathrm{T}}\mathcal{J} + \mathcal{J}^{2}\left(\mathcal{H} + \gamma\,\mathcal{J}\right)\right]\mathbf{Z} = \\
&= -2\gamma\,\mathbf{Z}^{\mathrm{T}}\mathcal{J}\,\mathbf{Z}
\end{aligned}
\tag{4.9.17}
$$

And, since $\mathbf{Z}^{\mathrm{T}}\left(0\right)\mathcal{J}\,\mathbf{Z}\left(0\right) = \mathbf{I}_{2k}^{\mathrm{T}}\mathcal{J}\,\mathbf{I}_{2k} = \mathcal{J}$, it has to be:

$$
\mathbf{Z}^{\mathrm{T}}\left(\tau\right)\mathcal{J}\,\mathbf{Z}\left(\tau\right) = e^{-2\gamma\tau}\mathcal{J} = \mu\,\mathcal{J}
\tag{4.9.18}
$$

The latter result leads to the next important proposition:

The monodromy matrix of a γ-Hamiltonian system is μ-symplectic with $\mu = e^{-2\gamma\mathrm{T}}$.

Where T, as usual, is the period of the system matrix of coefficients. To demonstrate that the *simplified case* 3 represents a γ-Hamiltonian system, Eq. (4.9.2) can be cast in the following form:

$$
\begin{cases}
\dot{\mathbf{u}}_S = \mathbf{A}(\tau)\,\mathbf{u}_S \\
\mathbf{u}_S\left(\tau\right) = \left\{\mathbf{u}^{\mathrm{T}}\left(\tau\right), \dot{\mathbf{u}}^{\mathrm{T}}\left(\tau\right)\right\}^{\mathrm{T}} \\
\\
\mathbf{A}(\tau) = \begin{bmatrix} \mathbf{0} & \mathbf{I} \\ -\left[\bar{\bar{\mathbf{K}}} + \Delta L\cos(\hat{\Omega}\tau)\,\bar{\bar{\mathbf{L}}}\right] & -a\,\mathbf{I} \end{bmatrix}
\end{cases}
\tag{4.9.19}
$$

Consider an orthogonal matrix $\hat{\mathbf{S}}$ such that:

$$
\begin{cases}
\hat{\mathbf{S}} = \dfrac{\sqrt{2}}{2}\left(\mathbf{I}_{8\mathrm{N}} - \mathcal{J}\right) = \begin{bmatrix} \mathbf{I} & \mathbf{I} \\ -\mathbf{I} & \mathbf{I} \end{bmatrix} \\
\hat{\mathbf{S}}\,\hat{\mathbf{S}}^{\mathrm{T}} = \hat{\mathbf{S}}^{\mathrm{T}}\hat{\mathbf{S}} = \mathbf{I}_{8\mathrm{N}}, \quad \mathcal{J}\,\hat{\mathbf{S}} = \hat{\mathbf{S}}\,\mathcal{J}
\end{cases}
\tag{4.9.20}
$$

Introducing the change of coordinates $\mathbf{u}_S = \hat{\mathbf{S}}\,\mathbf{z}$, Eq. (4.9.19) and Eq. (4.9.20) lead to:

$$
\dot{\mathbf{z}} = \hat{\mathbf{S}}^{\mathrm{T}}\bar{\mathbf{A}}(\tau)\,\hat{\mathbf{S}}\,\mathbf{z}
\tag{4.9.21}
$$

Then:

$$
\dot{\mathbf{z}} = \frac{1}{2}\begin{bmatrix} \left[\bar{\bar{\mathbf{K}}} + \Delta L\cos(\hat{\Omega}\tau)\,\bar{\bar{\mathbf{L}}}\right] - \left(1 + a\right)\mathbf{I} & \left[\bar{\bar{\mathbf{K}}} + \Delta L\cos(\hat{\Omega}\tau)\,\bar{\bar{\mathbf{L}}}\right] + \left(1 + a\right)\mathbf{I} \\ -\left[\bar{\bar{\mathbf{K}}} + \Delta L\cos(\hat{\Omega}\tau)\,\bar{\bar{\mathbf{L}}}\right] - \left(1 - a\right)\mathbf{I} & -\left[\bar{\bar{\mathbf{K}}} + \Delta L\cos(\hat{\Omega}\tau)\,\bar{\bar{\mathbf{L}}}\right] + \left(1 - a\right)\mathbf{I} \end{bmatrix}\mathbf{z}
\tag{4.9.22}
$$

or:

$$\begin{cases} \dot{\mathbf{z}} = \mathcal{J}\left[\mathcal{H}(\tau) + \dfrac{1}{2} a \mathcal{J}\right]\mathbf{z} \\ \\ \mathcal{H}(\tau) = -\dfrac{1}{2}\begin{bmatrix} \left[\bar{\bar{\mathbf{K}}} + \Delta L \cos(\hat{\Omega}\tau)\bar{\bar{\mathbf{L}}}\right] + (1-a)\mathbf{I} & \left[\bar{\bar{\mathbf{K}}} + \Delta L \cos(\hat{\Omega}\tau)\bar{\bar{\mathbf{L}}}\right] - \mathbf{I} \\ \left[\bar{\bar{\mathbf{K}}} + \Delta L \cos(\hat{\Omega}\tau)\bar{\bar{\mathbf{L}}}\right] - \mathbf{I} & \left[\bar{\bar{\mathbf{K}}} + \Delta L \cos(\hat{\Omega}\tau)\bar{\bar{\mathbf{L}}}\right] + (1+a)\mathbf{I} \end{bmatrix} \end{cases} \tag{4.9.23}$$

Since $\mathcal{H}^{\mathrm{T}}(\tau) = \mathcal{H}(\tau)$, the *simplified case* 3 is a γ-Hamiltonian system with $\gamma = a/2$. Hence its monodromy matrix is μ-symplectic with $\mu = e^{-2\gamma\mathrm{T}}$:

$$\rho_{\mu} = \sqrt{\mu} = \left(e^{-2\gamma\mathrm{T}}\right)^{\frac{1}{2}} = e^{-\gamma\mathrm{T}} = e^{-\frac{a}{2}\mathrm{T}} = e^{-\frac{a}{2}\frac{2\pi}{\hat{\Omega}}} = e^{-a\pi\sqrt{\delta}} = \rho_n \tag{4.9.24}$$

Equation (4.9.24) coincides with the result obtained in Eq. (4.9.12).

Since the multipliers do not lie on the unit circle when the system is stable, the switching mechanism that brings the system to instability cannot be defined as in Hamiltonian systems. However, interactions between multipliers can be observed in numerical investigations and collisions occur on the circle of radius $e^{-a\pi\sqrt{\delta}}$, similarly to what happens on the unit circle in the Hamiltonian case. Those collisions cannot be explained with the classical Krein Theory on perturbation of $\mathcal{G}$-unitary matrices. Furthermore, since a precise definition of *kind* of multipliers is missing, from now on a collision that does not take place on the unit circle will be called *generalized Krein collision*. An example is displayed in Fig. 4.9 for the *simplified case* 3 (in which double collision giving rise to a complex quadruplet cannot occur). In Fig. 4.9 a deformation of the γ-Hamiltonian, that involves only ε for a fixed δ, is represented.

Definition (*characteristic circles*): consider a deformation that involves only a variation of the amplitude parameter ε on a closed interval I_{ε}, if the modulus of a multiplier, say η, is invariant with respect to such a deformation, then there exists a circle (with ε-invariant radius) on which the multipliers lies, for all $\varepsilon \in I_{\varepsilon}$. Such a circle is a *characteristic circle* for the multiplier η.

Notice that the radius of a characteristic circle depends on δ. In the present case, the circle of radius $e^{-a\pi\sqrt{\delta}}$ is characteristic for all the multipliers, since the monodromy matrix is μ-symplectic. In the particular case of Hamiltonian system ($a = 0$ in the present case), the characteristic circle coincides with the unit circle. Thus, for a Hamiltonian system the radius of the characteristic circle is also δ-invariant.

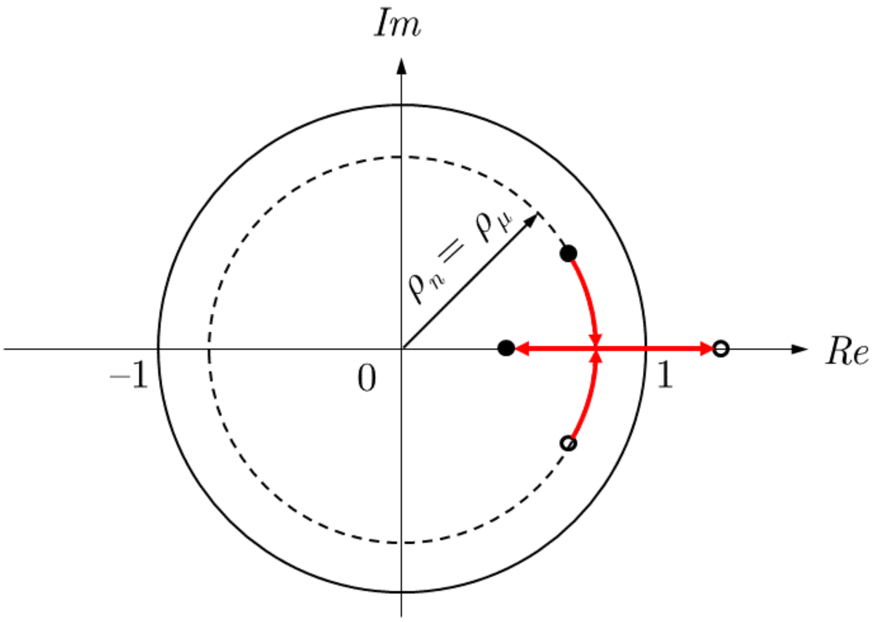

Figure 4.9: Multipliers moving on the characteristic circle and eventually exiting the unit circle

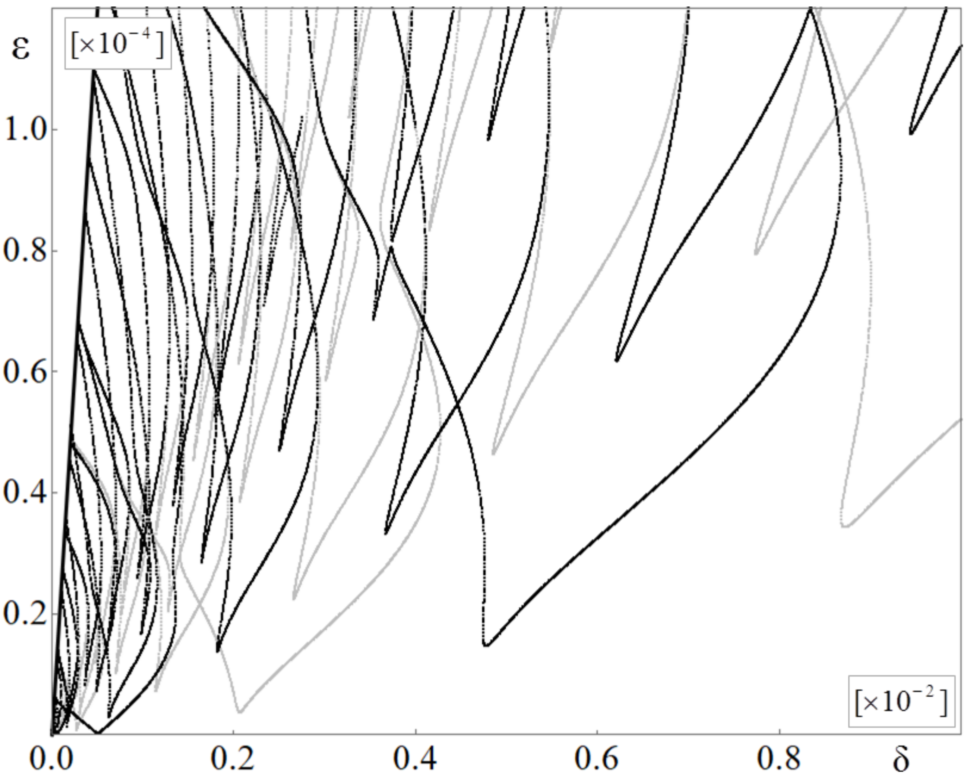

Figure 4.10: Ince-Strutt diagram for the damped case: mass-proportional with $\zeta_0 = 0.01$

In Fig 4.10 a stability chart for the present case is displayed. The chart has been obtained replacing the critical values $\Lambda_{cr}^{(1)} = 0$ (gray curves) and $\Lambda_{cr}^{(2)} = i/2$ (black curves) in the **H** operator, with reference to the parameters reported in Eq. (4.5.1) and null preloads, *i.e.* $\hat{N}_0 = 0$ and

$\hat{T}_0 = 0$, hence $\hat{\mathbf{L}}_0 = \mathbf{0} \Rightarrow \hat{\mathbf{K}} = \hat{\mathbf{K}}_0$ in Eq. (4.3.14). The effects of preloads on stability charts will be discussed separately (Section 4.12). The constant of proportionality adopted to generate Fig. 4.10 is $a = 2\zeta_0\omega_1$, where ω_1 is the first natural angular frequency of the unperturbed system and $\zeta_0 = 0.01$. The damping distribution analyzed in the present Section is characterized by monotonic decreasing modal damping factors ζ_n with respect to natural angular frequencies ω_n. Two main features can be noticed, observing Fig. 4.10. First, in each sequence of instability regions the contractions due to damping (in terms of ε) are larger for increasing δ, as in the well known case of the single degree of freedom damped Mathieu-Hill equation. Second, in a given range of δ, the contraction of instability regions is larger for higher order sequences (or, in other words, the contraction is larger in thinner instability regions). Clearly, this is also a consequence of δ-scaling in the global stability chart. Such behavior is consistent with the fact that the radius of the characteristic circle decreases for increasing positive δ, and that multipliers, related to sequences of different order, move at different rates on the characteristic circle. It can be concluded that a mass-proportional damping distribution is always stabilizing, and that the magnitude of this stabilization can be quantified as a function of *a*, *i.e.* the radius of the characteristic circle. The difference $1-\rho_\mu$ grows monotonically with increasing *a* for every fixed δ.

4.10 Simple non-rotating shaft with stiffness-proportional damping distribution and constant modal damping factors

Equation (4.3.14) without gyroscopic effects, ($\hat{\mathbf{G}} = \mathbf{0}$), and null preloads, ($\hat{\mathbf{L}}_0 = \mathbf{0}$), reads:

$$\hat{\mathbf{M}}\ddot{\mathbf{q}}_d + \hat{\mathbf{D}}\dot{\mathbf{q}}_d + \left[\hat{\mathbf{K}}_0 + \Delta L\cos(\hat{\Omega}\tau)\hat{\mathbf{L}}\right]\mathbf{q}_d = \mathbf{0} \tag{4.10.1}$$

In the present Section two kinds of damping distribution will be considered: stiffness proportional damping distribution and constant modal damping factor distribution. First, consider a constant of proportionality *b* such that:

$$\hat{\mathbf{D}} = b\hat{\mathbf{K}}_0 \tag{4.10.2}$$

Thus, after introducing the coordinate changes as Section 4.3, Eq. (4.3.20) reads:

$$\begin{cases} \mathbf{I}\ddot{\mathbf{u}} + \bar{\bar{\mathbf{C}}}\dot{\mathbf{u}} + \left[\bar{\bar{\mathbf{K}}} + \Delta L\cos(\hat{\Omega}\tau)\bar{\bar{\mathbf{L}}}\right]\mathbf{u} = \mathbf{0} \\ \bar{\bar{\mathbf{C}}} = b\,diag\left[\omega_1^2, \omega_2^2, \dots, \omega_{4\mathrm{N}}^2\right] \\ \bar{\bar{\mathbf{K}}} = \bar{\mathbf{M}}^{-1/2}\,\mathbf{V}_L\hat{\mathbf{K}}_0\mathbf{V}_R\,\bar{\mathbf{M}}^{-1/2} = \bar{\bar{\mathbf{K}}}_0 = diag\left[\omega_1^2, \omega_2^2, \dots, \omega_{4\mathrm{N}}^2\right] \\ \bar{\bar{\mathbf{L}}} = \bar{\mathbf{M}}^{-1/2}\,\bar{\mathbf{L}}\,\bar{\mathbf{M}}^{-1/2} \end{cases} \tag{4.10.3}$$

In which, due to the symmetry of $\hat{\mathbf{K}} = \hat{\mathbf{K}}_0$, it has to be $\mathbf{V}_L = \mathbf{V}_R^{\mathrm{T}}$ and the quantities $\omega_1, \omega_2, \dots, \omega_{4\mathrm{N}}$ are the 4N natural angular frequencies of the auxiliary system $\hat{\mathbf{M}}\ddot{\mathbf{x}} + \hat{\mathbf{K}}_0\mathbf{x} = \mathbf{0}$. The stiffness-proportional damping distribution is characterized by monotonic increasing modal damping factors ζ_n with respect to natural angular frequencies ω_n. The *n*-th modal damping factor takes the form:

$$\zeta_n = \frac{1}{2} b\,\omega_n \tag{4.10.4}$$

The present case will be named:

Simplified case 4: non-rotating shaft (no gyroscopic effects), stiffness-proportional damping, $\bar{\bar{\mathbf{C}}} = b\,diag\left[\omega_1^2, \omega_2^2, \dots, \omega_{4\mathrm{N}}^2\right]$.

Unlike the *simplified case* 3, the present one does not allow to write essential conditions like Eq. (4.9.7) and (4.9.8), *i.e.* the hypothesis of having complex conjugate multipliers does not automatically imply that the real parts of the latter do not depend on ε. However, it is possible to show that the generic conjugate pair of characteristic exponents takes the form:

$$\Lambda_{1,2} = \Upsilon_R\left(\varepsilon\right) \pm i\,\Upsilon_I\left(\varepsilon\right) \tag{4.10.5}$$

Suppose that, for small values of ε, the eigenvector **c** linearly depends on ε. Or, truncating the Taylor expansion up to the first order term:

$$\begin{cases} \mathbf{c}\left(\varepsilon\right) \approx \mathbf{c}_0 + \varepsilon\mathbf{c}_1 \\ \mathbf{c}^*\left(\varepsilon\right) \approx \mathbf{c}_0^* + \varepsilon\mathbf{c}_1^* \end{cases}, \quad \mathbf{c}_1 = \left\{\frac{d}{d\varepsilon}\left[\mathbf{c}\left(\varepsilon\right)\right]\right\}_{\varepsilon=0} \tag{4.10.6}$$

Hence, the function $\Upsilon_R\left(\varepsilon\right)$ takes the form:

$$\begin{aligned} \Upsilon_R\left(\varepsilon\right) &= -\frac{1}{2}\frac{\mathbf{c}^*\mathbf{H}_1^{(1)}\,\mathbf{c}}{\mathbf{c}^*\mathbf{H}_2\,\mathbf{c}} \approx -\frac{1}{2}\frac{\left[\mathbf{c}_0^* + \varepsilon\mathbf{c}_1^*\right]\mathbf{H}_1^{(1)}\left[\mathbf{c}_0 + \varepsilon\mathbf{c}_1\right]}{\left[\mathbf{c}_0^* + \varepsilon\mathbf{c}_1^*\right]\mathbf{H}_2\left[\mathbf{c}_0 + \varepsilon\mathbf{c}_1\right]} = \\ &= -\frac{1}{2}\frac{\mathbf{c}_0^*\,\mathbf{H}_1^{(1)}\,\mathbf{c}_0 + \varepsilon\mathbf{c}_1^*\,\mathbf{H}_1^{(1)}\,\mathbf{c}_0 + \varepsilon\mathbf{c}_0^*\,\mathbf{H}_1^{(1)}\,\mathbf{c}_1 + \varepsilon^2\,\mathbf{c}_1^*\,\mathbf{H}_1^{(1)}\,\mathbf{c}_1}{\mathbf{c}_0^*\,\mathbf{H}_2\,\mathbf{c}_0 + \varepsilon\mathbf{c}_1^*\,\mathbf{H}_2\,\mathbf{c}_0 + \varepsilon\mathbf{c}_0^*\,\mathbf{H}_2\,\mathbf{c}_1 + \varepsilon^2\,\mathbf{c}_1^*\,\mathbf{H}_2\,\mathbf{c}_1} = \\ &= -\frac{1}{2}\frac{\Psi_1^{(1)} + \varepsilon\Psi_1^{(2)} + \varepsilon^2\,\Psi_1^{(3)}}{\Psi_2^{(1)} + \varepsilon\Psi_2^{(2)} + \varepsilon^2\,\Psi_2^{(3)}} \end{aligned} \tag{4.10.7}$$

The real function $\Upsilon_R\left(\varepsilon\right)$ can be, in its turn, expanded through Taylor series as follows:

$$\Upsilon_R\left(\varepsilon\right) = -\frac{1}{2}\frac{\Psi_1^{(1)}}{\Psi_2^{(1)}} + \frac{1}{2}\varepsilon\frac{\Psi_1^{(1)}\,\Psi_2^{(2)} - \Psi_2^{(1)}\,\Psi_1^{(2)}}{\left(\Psi_2^{(1)}\right)^2} + \mathrm{O}\left(\varepsilon^2\right) \tag{4.10.8}$$

in which the terms $\Psi_i^{(j)}$ are generally unknown quantities and they depend on $\mathbf{c}_0$ and $\mathbf{c}_1$. Equation (4.10.8) states that, at least for small values of ε, the real parts of characteristic exponents can be expressed as a sum, in which one term is dominant and it does not depend on ε. The parameter ε is generally very small (as can be noticed from the scale of the stability charts).

Notice that small values of ε does not necessarily mean small load amplitudes (see Eq. (4.2.4), Eq. (4.2.9) and Eq. (4.4.6)). In other words it is possible, as a first approximation, to find the radius of a characteristic circle for each multiplier. Hence, replacing Eq. (4.10.4) in Eq. (4.9.11), gives:

$$\rho_n = e^{2\pi\Re(\Lambda_n)} = e^{-2\pi\zeta_n\omega_n\sqrt{\delta}} = e^{-b\pi\omega_n^2\sqrt{\delta}} \tag{4.10.9}$$

Equivalently:

$$\rho_n = e^{2\pi\Re(\Lambda_n)} = e^{2\pi\left(-\frac{1}{2}\frac{\Psi_1^{(1)}}{\Psi_2^{(1)}}\right)_n} = e^{-\pi\left(\frac{\Psi_1^{(1)}}{\Psi_2^{(1)}}\right)_n} = e^{-b\pi\omega_n^2\sqrt{\delta}} \quad \Rightarrow \quad \left(\frac{\Psi_1^{(1)}}{\Psi_2^{(1)}}\right)_n = b\,\omega_n^2\sqrt{\delta} \tag{4.10.10}$$

The approximation of the real parts of characteristic exponents is justified by several numerical investigations, which showed that the rate of change of the real parts with respect to ε is at least two orders of magnitude smaller than that of the imaginary parts. Thus, when a multiplier moves under a deformation induced by a variation of ε its phase varies, while its module remains practically unchanged. The unperturbed system related to the *simplified case* 4 is diagonal, resulting in a set of decoupled ordinary differential equations, thus no initial separation in multipliers occurs and such a system has only modal synchronous motions. This is the reason why it is possible to write the generic pair of conjugate characteristic exponents as in Eq. (4.10.5). Hence, the multipliers can exit the unit circle if and only if they are real. It can be concluded that, for the *simplified case* 4, critical solutions can be found, again, considering the two critical values $\Lambda_{cr}^{(1)} = 0$ and $\Lambda_{cr}^{(2)} = i/2$.

Practical tip: if, for some reason, wrong values of critical characteristic exponents are replaced in **H**, the resulting stability chart presents easily recognizable anomalies:

1 The eigenvalue problem for ε (or for δ) returns only complex values for some fixed δ (or ε), resulting in partially (or totally) missing transition curves. In some cases the transition curves progressively fade in certain regions (erosion), while they are abruptly interrupted or absent in others (miss). These issues are typically found in proportional damped systems without gyroscopic effects. Furthermore, these phenomena are extremely sensible to the internal accuracy used to solve the eigenproblem, which is not the case when correct critical values of Λ are used.

2 The transition curves are continuous and there are no missing or eroded branches, but they do not give rise to a closed global stability threshold on the δ-axis. The latter happens in undamped systems in the presence of gyroscopic effects.

While point 1 is easy to interpret, point 2 is more delicate. An open global stability threshold on the δ-axis means unstable unperturbed system (exponentially growing amplitude solutions). The latter is obviously a wrong conclusion, since the unperturbed system, without damping terms, has only imaginary eigenvalues (see Section 1.1, wrong results can be found in [48-63]).

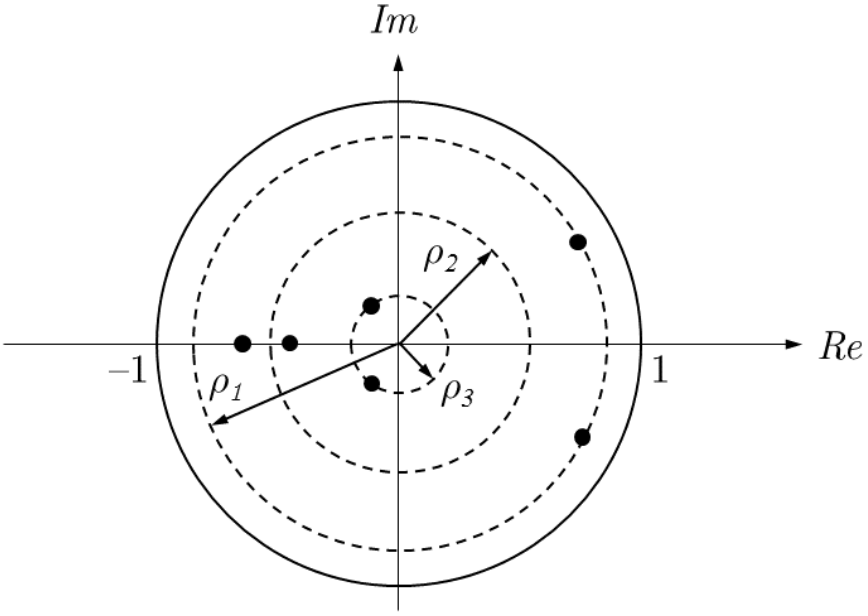

Figure 4.11: Multipliers and their approximated characteristic circles

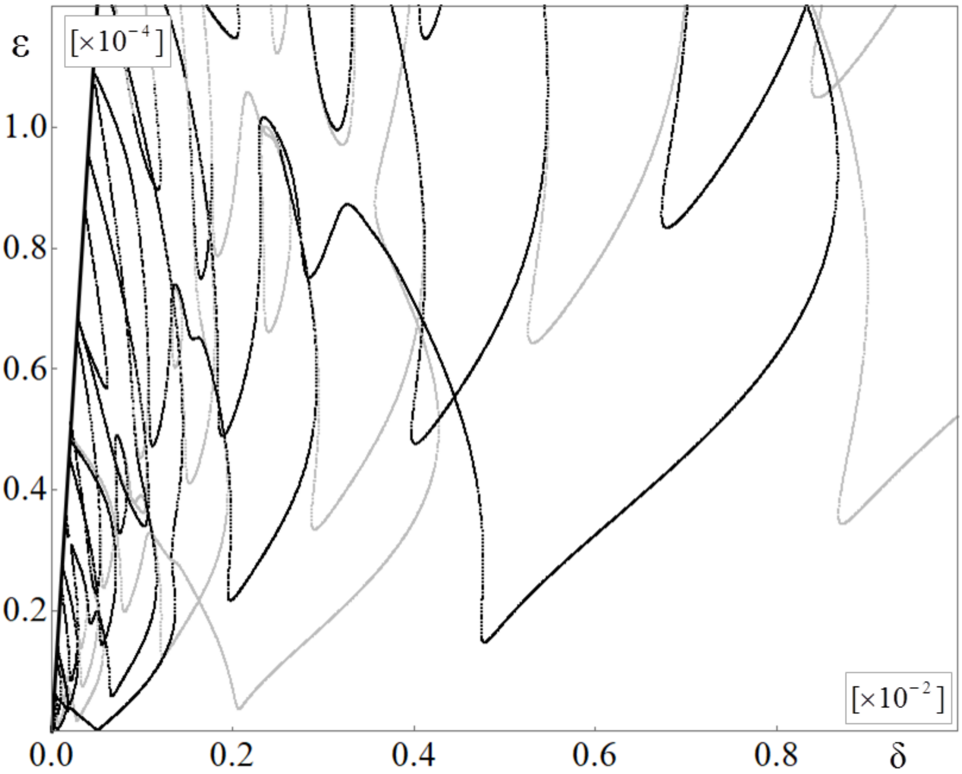

Figure 4.12: Ince-Strutt diagram for the damped case: stiffness-proportional with $\zeta_0 = 0.01$

The first three approximated characteristic circles are displayed in Fig. 4.11. Notice that each dot in Fig. 4.11 represents a multiple (double) multiplier. The radius of the *n*-th characteristic circle, according to Eq. (4.10.9), depends on ω_n^2, thus higher order sequences have smaller characteristic radii. The effect of this feature becomes clear observing the stability chart in Fig. 4.12, where higher order sequences of instability regions are more smooth in the lower part with respect to the lower order sequences. A smaller characteristic radius means a greater margin for stability: in Fig. 4.11 a generalized collision on the real axis (for the sequence of order 2) is displayed, but the difference $1-\rho_2$ is large enough to not allow the system to switch to unstable behavior (saddle-node bifurcation). This is the reason why the transition curves of damped system are contracted. In the *simplified case* 4 this aspect is magnified by the progressive reduction of ρ_n for increasing *n*.

The constant *b*, adopted to generate the stability chart in Fig. 4.12, is $b = 2\zeta_0/\omega_1$, where ω_1 is the first natural angular frequency of the unperturbed system and $\zeta_0 = 0.01$. Thus, the systems, whose stability charts are displayed in Fig. 4.10 and 4.12 (*simplified case* 3 and 4 respectively), are characterized by having the same first modal damping factor.

The last case, that will be discussed in the present Section, is the one related to the constant modal damping factor distribution. Consider a damping matrix such that:

$$\begin{cases} \hat{\mathbf{D}} = \mathbf{V}_L^{-1} \bar{\mathbf{M}}^{1/2}\, \hat{\mathbf{D}}_0\, \bar{\mathbf{M}}^{1/2} \mathbf{V}_R^{-1} \\ \hat{\mathbf{D}}_0 = diag\left[2\zeta_0\,\omega_1,\, 2\zeta_0\,\omega_2,\, \dots,\, 2\zeta_0\,\omega_{4\mathrm{N}}\right] \end{cases} \tag{4.10.11}$$

in which $\mathbf{V}_L = \mathbf{V}_R^{\mathrm{T}}$. Replacing Eq. (4.10.11) in Eq. (4.10.1) returns:

$$\begin{cases} \mathbf{I}\,\ddot{\mathbf{u}} + \bar{\bar{\mathbf{C}}}\,\dot{\mathbf{u}} + \left[\bar{\bar{\mathbf{K}}} + \Delta L \cos(\hat{\Omega}\tau)\,\bar{\bar{\mathbf{L}}}\right]\mathbf{u} = \mathbf{0} \\ \bar{\bar{\mathbf{C}}} = \hat{\mathbf{D}}_0 = diag\left[2\zeta_0\,\omega_1,\, 2\zeta_0\,\omega_2,\, \dots,\, 2\zeta_0\,\omega_{4\mathrm{N}}\right] \\ \bar{\bar{\mathbf{K}}} = \bar{\mathbf{M}}^{-1/2}\, \mathbf{V}_L \hat{\mathbf{K}}_0 \mathbf{V}_R\, \bar{\mathbf{M}}^{-1/2} = \bar{\bar{\mathbf{K}}}_0 = diag\left[\omega_1^2,\, \omega_2^2,\, \dots,\, \omega_{4\mathrm{N}}^2\right] \\ \bar{\bar{\mathbf{L}}} = \bar{\mathbf{M}}^{-1/2}\, \bar{\mathbf{L}}\, \bar{\mathbf{M}}^{-1/2} \end{cases} \tag{4.10.12}$$

Simplified case 5: non-rotating shaft (no gyroscopic effects), constant modal damping factors, $\bar{\bar{\mathbf{C}}} = diag\left[2\zeta_0\,\omega_1,\, 2\zeta_0\,\omega_2,\, \dots,\, 2\zeta_0\,\omega_{4\mathrm{N}}\right]$.

All the consideration made for the *simplified case* 4 remain valid also for the *simplified case* 5. Hence, the *n*-th approximated characteristic radius takes the form:

$$\rho_n = e^{2\pi\Re(\Lambda_n)} = e^{-2\pi\zeta_n\omega_n\sqrt{\delta}} = e^{-2\pi\zeta_0\omega_n\sqrt{\delta}} \tag{4.10.13}$$

The behavior of multipliers of the *simplified case* 5 is analogous to that of the previous case.

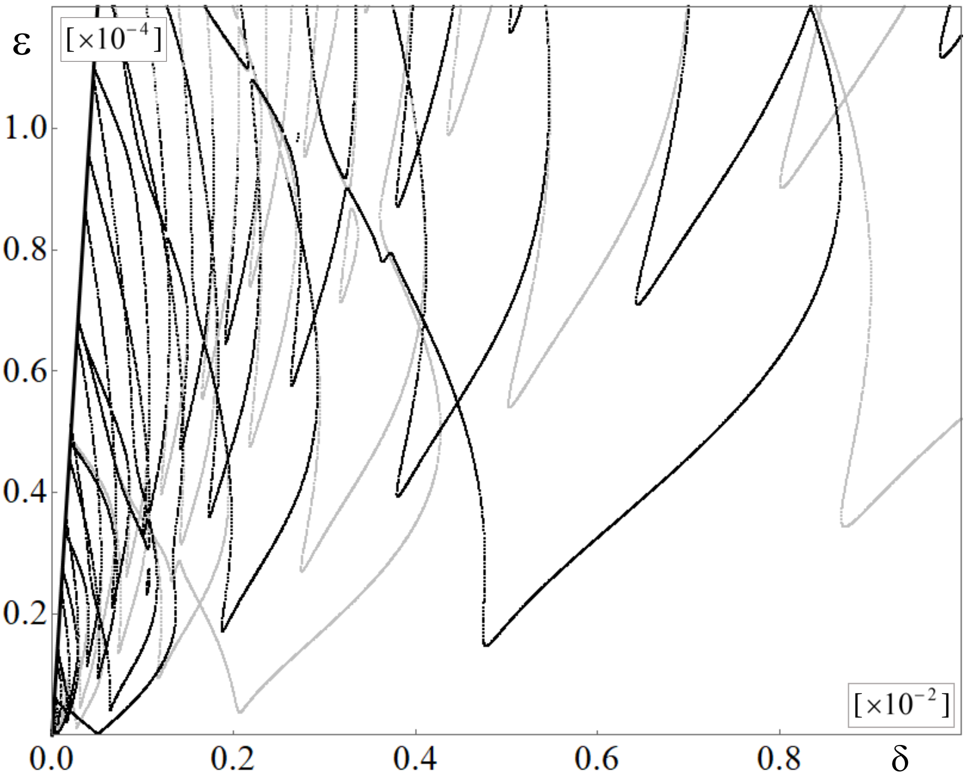

Figure 4.13: Ince-Strutt diagram for the damped case: constant modal damping factors with $\zeta_0 = 0.01$

In Fig. 4.13, the Ince-Strutt diagram for the *simplified case* 5 is displayed. The stability chart is generated adopting $\zeta_0 = 0.01$.

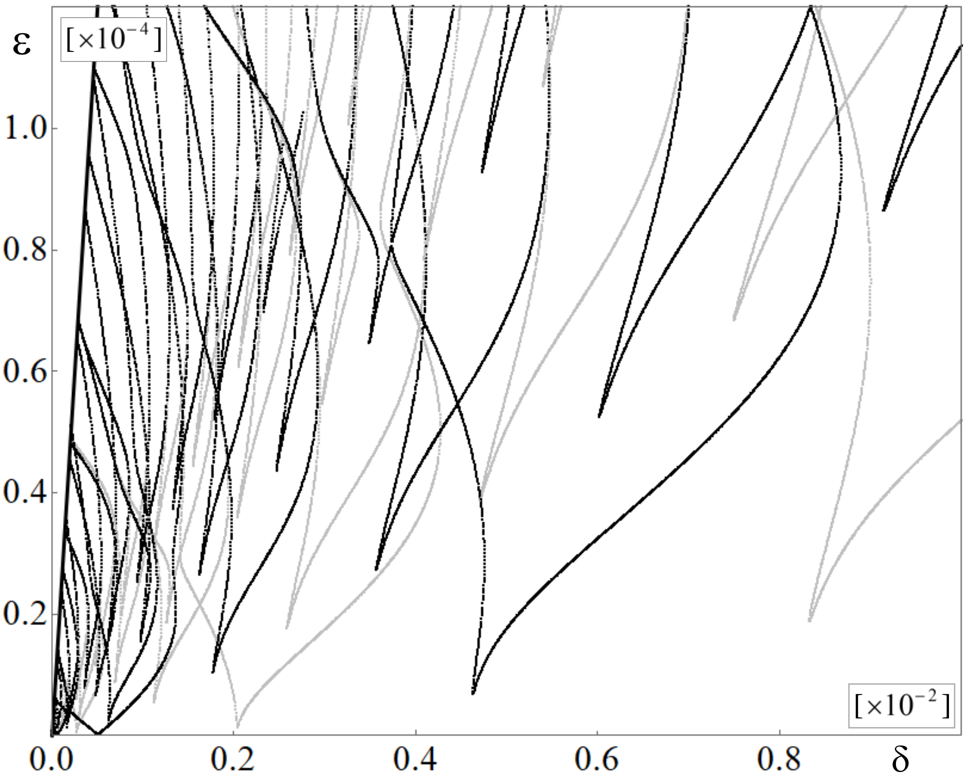

Figure 4.14: Ince-Strutt diagram for the damped case: constant modal damping factors with $\zeta_0 = 0.001$

The effects of external, stabilizing damping distributions have been investigated by considering three different basic models, characterized by: (*simplified case* 3) monotonic decreasing modal damping factors ζ_n with respect to natural angular frequencies ω_n, (*simplified case* 4) monotonic increasing ζ_n with respect to ω_n, (*simplified case* 5) constant ζ_n for all modes. The focus is not studying the influence of a specific, realistic damping distribution, but providing an overview by covering a very broad range of possible monotonic variations of modal damping factors. As simplest choice, viscous-damping models have been adopted, with mass-proportional distribution, stiffness-proportional distribution, and constant modal damping factors. Observing Fig. 4.10, 4.12, 4.13 and Fig. 4.14, it can also be noticed that interactions among instability regions grow with ε, due to coupling of the Mathieu-Hill equations of motion (hence the stability charts are not mere superpositions of scaled single degree of freedom Ince-Strutt diagrams). At low values of ε, however, interactions appear to be negligible.

It can be concluded that stabilizing (proportional) damping distributions produce substantial clearing of high-order eigenvalue contributions to global stability regions in Ince-Strutt diagrams. For even a very small damping amount (as in Fig. 4.14, with a constant modal damping factor $\zeta_0 = 0.001$), global stability thresholds can be computed by considering the lower eigenvalues only (very few, for low modal density systems), in any case with great advantage in terms of reduction of computational load.

4.11 Numerical approach to the general case

In Sections 4.6 to 4.10, five different simplified cases have been discussed (*simplified case* 1 to 5), in which definitive conclusions, about critical values of characteristic exponents, could be drawn. However, as anticipated in Section 4.6, this is not always possible and, in the majority of cases, an analytical treatment on the behavior of multipliers cannot be developed. Nevertheless, Floquet Theory remains valid even in these general cases and, in conjunction with a suitable discretization of the equations of motion (weighted residuals method), Eq. (4.4.11) can still be used to trace the stability charts.

Recalling the definitions of transition curve and stability threshold, it can be concluded that a stability chart (Ince-Strutt diagram) presents several sequences of transition curves, but not all the points, belonging to these curves, also belong to the global stability threshold. As its name suggests, the global stability threshold separates regions characterized by different stability behavior from a global perspective. In other words, while each sequence of transition curves returns information regarding the stability of the related set of multipliers, the global stability threshold returns information regarding the whole system. Figure 4.15, in which the first and second sequences of transition curves (corresponding to two different sets of multipliers) are taken into consideration on a δ-ε domain, gives a schematic representation of this concept.

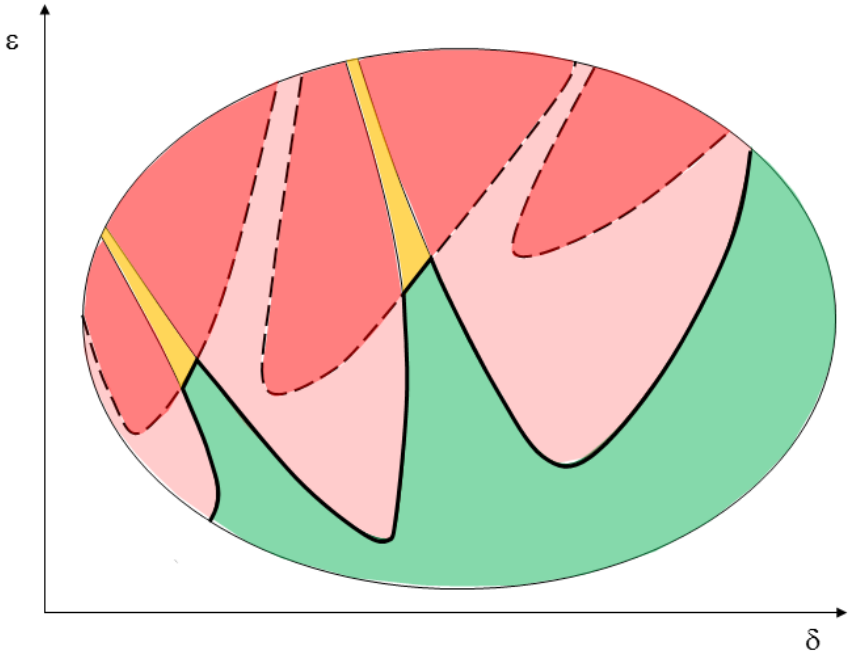

Figure 4.15: Global stability threshold (thick black curve)

Different colors stay for different global stability behavior. Green: all the multipliers related to the two sequences lie within the unit circle (or on the unit circle and are definite). Pink: at least one multiplier related to the first sequence lies outside the unit circle, while all the multipliers of the second sequence are inside the unit circle (or on the unit circle and are definite). Red: at least one multiplier related to the first sequence and at least one of the second lie outside the unit circle. Yellow: at least one multiplier related to the second sequence lies outside the unit circle, while all the multipliers of the first sequence are inside the unit circle (or on the unit circle and are definite). Thus, the system is globally stable if and only if the pair $\{\delta, \varepsilon\}$ belongs to the green region. Finally, in Fig. 4.15, the global stability threshold is represented as a thick black curve.

In the present Section, a numerical algorithm aimed at directly compute the global stability threshold is described.

Conjecture: the global stability threshold of a generic dissipative non-Hamiltonian system is unique.

The above conjecture is surely verified for realistic technological range of δ and ε. In other terms, if there exist a stability sub-region different from the one that includes the δ-axis, it lies in a high ε area of the chart. Furthermore, if other global stability regions exist, their stability thresholds are closed, resulting in a non-simply-connected global stability region (as union of all the global stability sub-regions). Figure 4.16 displays the latter eventuality.

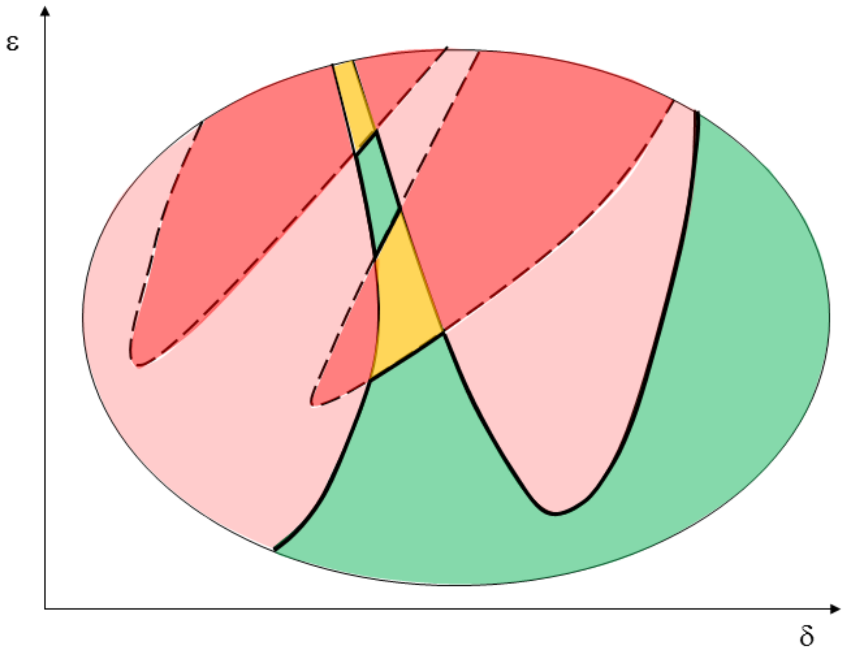

Figure 4.16: Global stability threshold of a non-simply-connected global stability region

However, the stability sub-regions separated from the main one (isolated stability sub-regions) are generally very small and of little interest, from a practical point of view.

Under the assumption of having a single, continuous global stability threshold, the algorithm is able to trace the entire unknown locus, on a fixed δ-ε domain, in a single run. After the initialization, which will be discussed later, each step is focused on evaluating the eigenvalues of the quadratic problem in Eq. (4.4.11), *i.e.* the characteristic exponents, only in few points $\{\delta,\varepsilon\}$ in a neighborhood of the predicted critical point. The output of each step is a point of the stability threshold. The input of the generic step consists in two points of the stability threshold (the outputs of the previous two steps) and the operator **H**, in which only δ, ε and Λ are unknown. Thus, each step is developed in the following phases:

Phase 1. The code takes the last two points of the discretized stability threshold, (output of the previous steps), $\mathbf{P}_{j-1}$ and $\mathbf{P}_j$, and computes the vector $\mathbf{v}_1^{(A)}$ (first attempt), as follows:

$$\begin{cases} \mathbf{v}_1^{(A)} = V\dfrac{\left(\mathbf{P}_j - \mathbf{P}_{j-1}\right)}{\left\|\mathbf{P}_j - \mathbf{P}_{j-1}\right\|} \\ V = \mho\left(\mathbf{P}_j - \mathbf{P}_{j-1}\right) \end{cases} \tag{4.11.1}$$

in which $\mho$ is a real function of the vector $\mathbf{P}_j - \mathbf{P}_{j-1}$.

Thus, the norm V of $\mathbf{v}_1^{(A)}$ is a variable scalar step. It depends on the slope of the stability threshold and it can be tuned through the function $\mho$.

Notice that the stability threshold, generally, is not a single valued function of δ, (nor of ε), thus its slope takes on a broader meaning. A first-attempt critical point is then computed as follows:

$$\mathbf{P}_1^{(A)} = \mathbf{P}_j + \mathbf{v}_1^{(A)} \tag{4.11.2}$$

$\mathbf{P}_1^{(A)}$ would be a critical point if, in a neighborhood of $\mathbf{P}_j$, the stability threshold did not change its slope, in other words, $\mathbf{P}_1^{(A)}$ represents a first order approximation in a neighborhood of $\mathbf{P}_j$. A first check can be performed on $\mathbf{P}_1^{(A)}$ introducing the following operator:

$$\mathcal{M}(\cdot) = \max\left\{\Re\left[\Xi\left(\mathbf{H}\right)\right]\right\}_{\mathbf{H}=\mathbf{H}\left[(\cdot)\right]} \tag{4.11.3}$$

where $\Xi\left(\mathbf{H}\right)$ is the spectrum of a generalized eigenproblem (resulting from Eq. (4.4.11) in a proper state-space). Thus, the operator $\mathcal{M}(\cdot)$ returns the maximum real part of the characteristic exponents Λ, when Eq. (4.4.11) is evaluated for $\{\delta, \varepsilon\} = (\cdot)$. Explicitly, the check on $\mathbf{P}_1^{(A)}$ reads:

$$\left|\mathcal{M}(\mathbf{P}_1^{(A)})\right| = \left|\mathcal{M}(\delta_1^{(A)}, \varepsilon_1^{(A)})\right| \leq u \tag{4.11.4}$$

where u is some adjustable positive real number. The choice of u depends on the precision adopted for the whole computation. If Eq. (4.11.4) is true, then $\mathbf{P}_1^{(A)} = \mathbf{P}_{j+1}$ is appended to the list of critical points that make up the discretized stability threshold and the algorithm restart from the *phase* 1 with an updated list of critical points. If Eq. (4.11.4) is false, then there are only two possibilities:

$$\left|\mathcal{M}(\mathbf{P}_1^{(A)})\right| > u \quad \Rightarrow \quad \mathcal{M}(\mathbf{P}_1^{(A)}) < -u < 0 \ \vee \ \mathcal{M}(\mathbf{P}_1^{(A)}) > u > 0 \tag{4.11.5}$$

Suppose that $\mathcal{M}(\mathbf{P}_1^{(A)}) < -u < 0$, then $\mathbf{P}_1^{(A)}$ lies in the stability region, the maximum real part of Λ is negative and all the multipliers lie within the unit circle. At this stage, the code generates a rotation matrix $\boldsymbol{\mathcal{R}}\left(\hat{\gamma}\right)$ such that:

$$\begin{cases} \mathbf{v}_2^{(A)} = \boldsymbol{\mathcal{R}}\left(\hat{\gamma}\right)\mathbf{v}_1^{(A)} \quad \Rightarrow \quad \mathbf{P}_2^{(A)} = \mathbf{P}_j + \boldsymbol{\mathcal{R}}\left(\hat{\gamma}\right)\mathbf{v}_1^{(A)} = \mathbf{P}_j + \mathbf{v}_2^{(A)} \\ \hat{\gamma} = \dfrac{\pi}{k_1} \end{cases} \tag{4.11.6}$$

where k_1 is a positive integer. The angle $\hat{\gamma}$ is a scalar step which can be tuned through k_1. Matrix $\boldsymbol{\mathcal{R}}\left(\hat{\gamma}\right)$ is such that the resulting vector $\mathbf{v}_2^{(A)}$ forms a positive angle $\hat{\gamma}$ with respect to $\mathbf{v}_1^{(A)}$, (counterclockwise rotation). The new point $\mathbf{P}_2^{(A)}$ is checked through the operator $\mathcal{M}(\cdot)$ as in Eq. (4.11.4) and Eq. (4.11.5). If $\mathbf{P}_2^{(A)}$ lies again in the global stability region, the procedure above is repeated. This sub-routine produce a sequence of points $\mathbf{P}_i^{(A)}$, (each vector $\mathbf{v}_i^{(A)}$ forms

an angle equal to $\hat{\gamma}$ with respect to $\mathbf{v}_{i-1}^{(A)}$), that lie on a circumference centered in $\mathbf{P}_j$, of radius equal to the norm of $\mathbf{P}_i^{(A)}$ – $\mathbf{P}_j$. The latter sub-routine stops when $\left|\mathcal{M}(\mathbf{P}_i^{(A)})\right| \leq u$, or when a point $\mathbf{P}^{(S)} = \mathbf{P}_j + \mathbf{v}^{(S)}$, which returns $\mathcal{M}(\mathbf{P}^{(S)}) > u > 0$, is found.
The procedure described above is methodologically the same, but with $\hat{\gamma} < 0$ (clockwise rotations) if, instead of having a stable starting point $\mathbf{P}_1^{(A)}$, $\mathcal{M}(\mathbf{P}_1^{(A)}) < -u < 0$, one has an unstable starting point, $\mathcal{M}(\mathbf{P}_1^{(A)}) > u > 0$. This is due the fact that the global stability region was supposed to be simply-connected, hence, moving on the stability threshold, starting from a neighborhood of the origin of the axes, with initial tangent vector that has positive component along the increasing δ direction, means having the global stability region always facing right. The *phase* 1 of the generic step is schematized in Fig. 4.17, in the case of stable initial point $\mathbf{P}_1^{(A)}$.

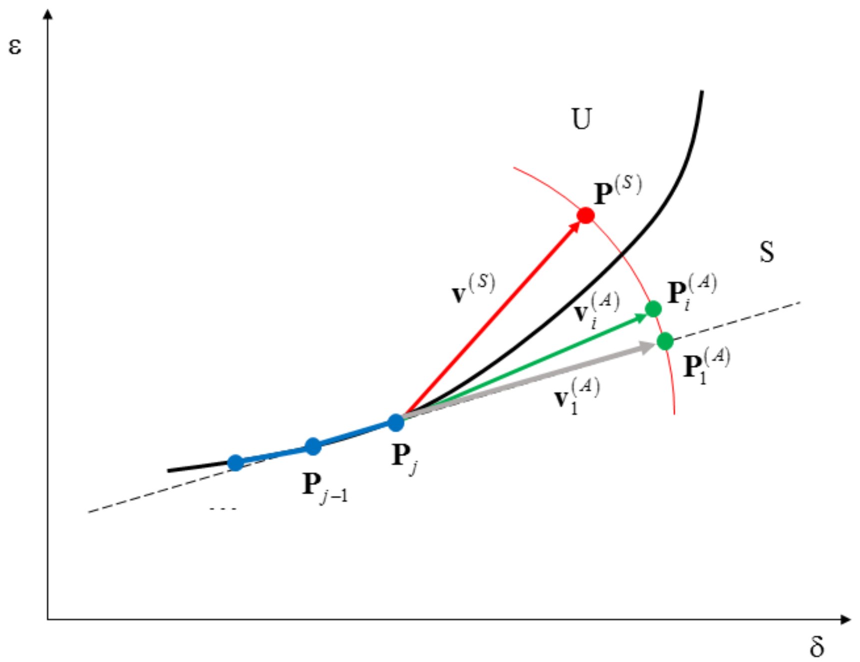

Figure 4.17: *Phase* 1 for stable $\mathbf{P}_1^{(A)}$. Black line: exact stability threshold

In Fig. 4.17, U and S stay for unstable and stable (regions) respectively, the black line is the exact stability threshold, while blue points represent the approximated critical points (discretized stability threshold, output of the previous steps). Green points represent stable point and the red point is the unstable point found by the sub-routine contained in *phase* 1. In Fig. 4.17, the norm V of the vectors **v** is exaggerated on purpose for the sake of clarity of representation. Notice that, by the definition of $\hat{\gamma}$, the searching sub-routine of *phase* 1 can span a maximum angle equal to π for a maximum of k_1 sub-steps, thus, it is able to handle even cusp points.

Phase 2. This phase takes as inputs two points: $\mathbf{P}^{(S)}$ and the last point of the sequence $\mathbf{P}_i^{(A)}$, say $\mathbf{P}^{(R)}$. These two points lie on different regions, *i.e.* if $\mathbf{P}^{(S)}$ is unstable then $\mathbf{P}^{(R)}$ is stable and vice versa. Since the global stability region is simply-connected, there exist a continuous path, passing through the two points, which intersects the stability threshold and, for sufficiently small $\hat{\gamma}$, this intersection is unique. Now consider the arc of the circle centered in $\mathbf{P}_j$ that has as extremal points $\mathbf{P}^{(R)}$ and $\mathbf{P}^{(S)}$, it is possible to collect information about the real parts of characteristic exponents for each point belonging to the arc. Consider a sequence of evenly spaced points $\mathbf{P}_z^{(M)}$ on the arc. Together with $\mathbf{P}^{(R)}$ and $\mathbf{P}^{(S)}$, they constitute a discretization of the arc (path):

$$\begin{cases} \mathbf{P}^{(R)} = \mathbf{P}_j + \mathbf{v}^{(R)} \\ \mathbf{P}_1^{(M)} = \mathbf{P}_j + \mathbf{v}_1^{(M)} \\ \mathbf{P}_2^{(M)} = \mathbf{P}_j + \mathbf{v}_2^{(M)} \\ \vdots \\ \mathbf{P}^{(S)} = \mathbf{P}_j + \mathbf{v}^{(S)} \end{cases} \tag{4.11.7}$$

As a consequence of *phase* 1, the module of the angle spanned by $\mathbf{P}^{(R)}$ and $\mathbf{P}^{(S)}$ is $|\hat{\gamma}|$. Consider once again the case in which $\mathbf{P}^{(S)}$ is unstable (hence $\mathbf{P}^{(R)}$ is stable), it follows that the vectors $\mathbf{v}_z^{(M)}$ can be computed starting from vector $\mathbf{v}^{(R)}$, which is known from *phase* 1, with a sequence of counterclockwise rotations. Hence:

$$\begin{cases} \mathbf{v}_z^{(M)} = \boldsymbol{\mathcal{R}}\left(z\hat{\beta}\right)\mathbf{v}^{(R)} \quad \Rightarrow \quad \mathbf{P}_z^{(M)} = \mathbf{P}_j + \boldsymbol{\mathcal{R}}\left(z\hat{\beta}\right)\mathbf{v}^{(R)}, \quad z = 1,2,\ldots,k_2 - 1 \\ \hat{\beta} = \dfrac{\hat{\gamma}}{k_2} \end{cases} \tag{4.11.8}$$

where k_2 is a positive integer. It is possible, now, to build a function, say $\Sigma\left(\hat{\alpha}\right)$, through interpolation of the values returned by the operator $\mathcal{M}(\cdot)$, evaluated in the $k_2 + 1$ points of the sequence $\mathbf{P}^{(R)}, \mathbf{P}_1^{(M)}, \ldots, \mathbf{P}_{k_2-1}^{(M)}, \mathbf{P}^{(S)}$:

$$\left\{0, \mathcal{M}(\mathbf{P}^{(R)})\right\}, \left\{\hat{\beta}, \mathcal{M}(\mathbf{P}_1^{(M)})\right\}, \ldots, \left\{(k_2 - 1)\hat{\beta}, \mathcal{M}(\mathbf{P}_{k_2-1}^{(M)})\right\}, \left\{\hat{\gamma}, \mathcal{M}(\mathbf{P}^{(S)})\right\} \quad \Rightarrow \quad \Sigma(\hat{\alpha}) \tag{4.11.9}$$

The function $\Sigma\left(\hat{\alpha}\right)$ has exactly one root on the interval $\left(0, \hat{\gamma}\right)$, say $\hat{\alpha}_R$. The latter procedure allows to compute a point for which the maximum real part of the characteristic exponents, returned by Eq. (4.4.11), is zero:

$$\mathbf{P}_{j+1} = \mathbf{P}_j + \boldsymbol{\mathcal{R}}\left(\hat{\alpha}_R\right)\mathbf{v}^{(R)} \tag{4.11.10}$$

In Fig. 4.18, *phase* 2 is schematized for $k_2 = 4$, in the case of unstable $\mathbf{P}^{(S)}$. The thick black line represents the exact stability threshold and, in this example $\mathbf{P}^{(R)}$ and $\mathbf{P}_1^{(M)}$ are stable (green dots), while $\mathbf{P}_2^{(M)}, \mathbf{P}_3^{(M)}$ and $\mathbf{P}^{(S)}$ are unstable (red dots). The cross represents the approximated critical point $\mathbf{P}_{j+1}$, which is the output of *phase* 2 (and of the whole generic step of the algorithm).

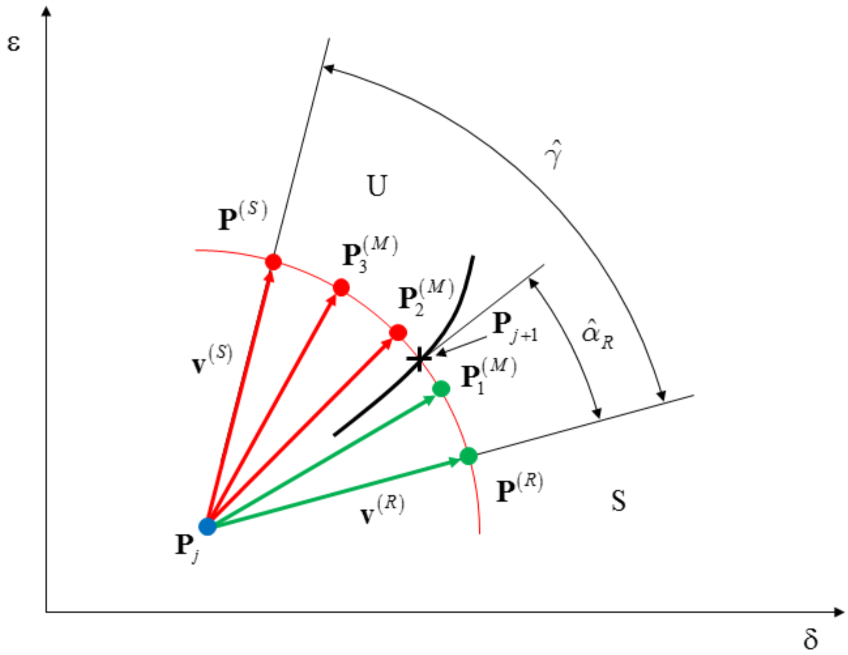

Figure 4.18: *Phase* 2 for unstable $\mathbf{P}^{(S)}$ and $k_2 = 4$. Thick black line: exact stability threshold

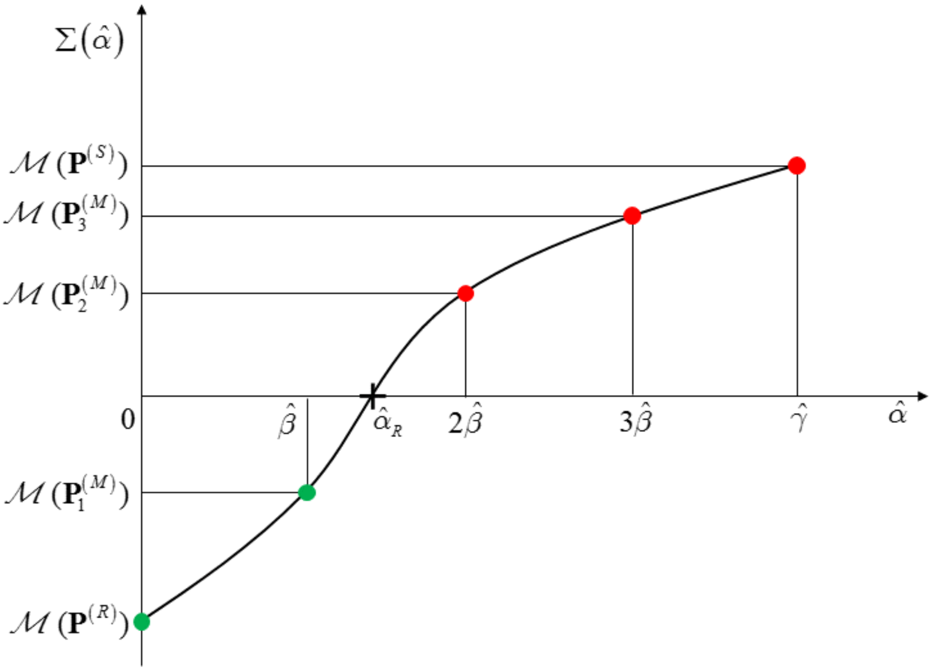

Figure 4.19: *Phase* 2 for unstable $\mathbf{P}^{(S)}$ and $k_2 = 4$. Interpolated curve: maximum real part of Λ

In Fig. 4.19, function $\Sigma(\hat{\alpha})$ is displayed for the case in Fig. 4.18 (unstable $\mathbf{P}^{(S)}$ and $k_2 = 4$). The root $\hat{\alpha}_R$ can be easily found through Newton-Raphson method. Once the algorithm has computed **P**$_{j+1}$, it restart from *phase* 1 with an updated list of approximated critical points. Notice that, if $\mathbf{P}^{(S)}$ is stable, the procedure related to *phase* 2 described above is still valid, but with $\mathbf{P}^{(S)}$ and $\mathbf{P}^{(R)}$ in inverted roles.

Initialization. This initialization phase provides two points, from which *phase* 1 and 2 can return a third point as output. Those two points can be computed as in the second part of *phase* 2 choosing two simple paths, *i.e.* two vertical lines, two horizontal lines or two operation lines $(\Delta L = const)$. Alternatively, the two points can be arbitrarily chosen (close to each other) near to the origin of the axes. The algorithm automatically change *V* in Eq. (4.11.1) until an intersection with the stability threshold is found.

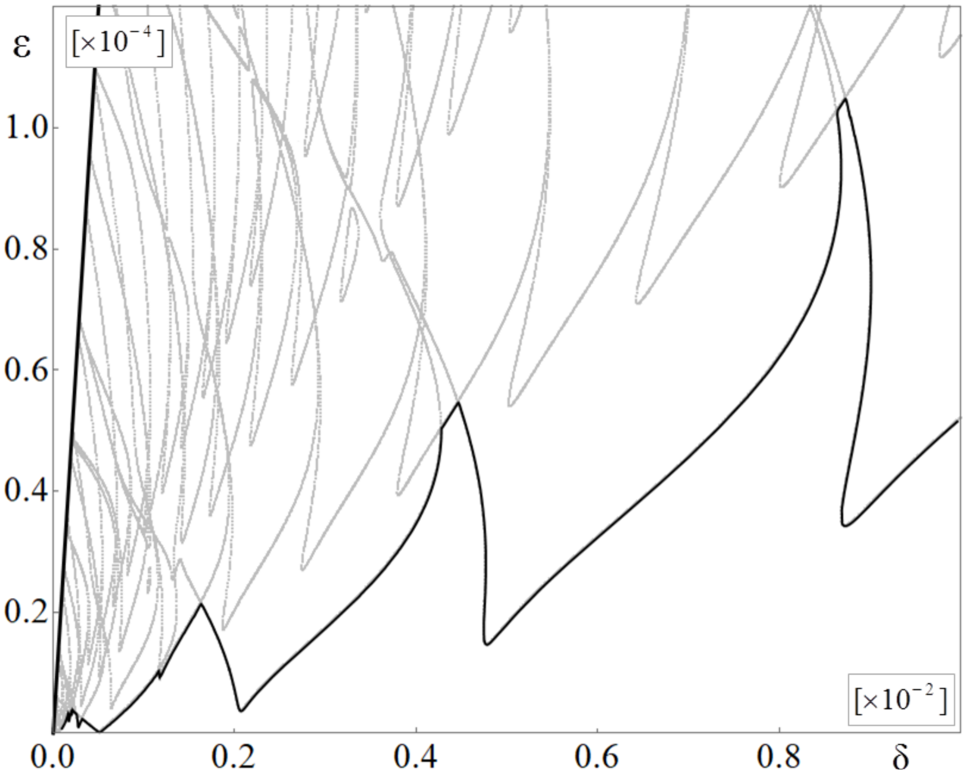

Figure 4.20: Ince-Strutt diagram for the *simplified case* 5 with $\zeta_0 = 0.01$. Black line: directly computed global stability threshold. Grey: modal sequences obtained through eigenvalue problem

In Fig. 4.20 an example of directly computed global stability threshold is displayed. The grey curves was obtained replacing critical values of Λ in Eq. (4.4.11) for the *simplified case* 5 with $\zeta_0 = 0.01$, then solving an eigenproblem for ε, (or δ), for every fixed δ (or ε). The black line is the stability threshold computed with the algorithm described in the present Section (see Fig. 4.13 for direct comparison).

In the case of very high chart resolution, the algorithm turns out to be a much faster method to trace the stability threshold, due to the lower amount of evaluation of the characteristic exponents. However, the algorithm struggles to compute the stability threshold if the global stability region is not of asymptotic kind (solutions are not asymptotically stable but only merely stable). In this case, every point belonging to the stability region returns only true (boolean) values in Eq. (4.11.4), thus *phase* 1 is not able to find $\mathbf{P}^{(S)}$ if $\mathbf{P}_1^{(A)}$ is stable. Conversely, if $\mathbf{P}_1^{(A)}$ is unstable, then *phase* 2 struggles to find a root $\hat{\alpha}_R$, because the maximum real part of Λ, inside the stability region, is null. The algorithm is meant to work with damped system and it is not negatively affected by the presence of gyroscopic effects, other types of non-self-adjointness and non-conservative force fields.

4.12 Simple shaft with gyroscopic effects and stabilizing damping distribution. The effects of slenderness ratio and preloads on the stability charts

With both gyroscopic and damping terms in the equations of motion, an expression of $\Lambda_{nk}^{crit}(\delta)$ as that in Eq. (4.8.13) no longer exists, and the procedure described in Section 4.8, based on superposition of sequences of instability regions, becomes impracticable. The reason why this happens is due to the heteroclinic behavior of multipliers under a perturbation. In order to shed light on the latter statement, consider the following system:

$$\begin{cases} \mathbf{I}\,\ddot{\mathbf{u}} + \bar{\bar{\mathbf{C}}}\,\dot{\mathbf{u}} + \left[\bar{\bar{\mathbf{K}}} + \Delta L\cos(\hat{\Omega}\tau)\,\bar{\bar{\mathbf{L}}}\right]\mathbf{u} = \mathbf{0} \\ \bar{\bar{\mathbf{C}}} \neq \bar{\bar{\mathbf{C}}}^{\mathrm{T}} \quad \wedge \quad \bar{\bar{\mathbf{C}}} \neq -\bar{\bar{\mathbf{C}}}^{\mathrm{T}} \end{cases} \tag{4.12.1}$$

Matrix $\bar{\bar{\mathbf{C}}}$ is neither diagonal nor symmetric (nor skew-symmetric, since it is the sum of a damping matrix and a gyroscopic matrix). It is always possible to find relaxed definitions of characteristic circles considering the unperturbed case in Eq. (4.4.11), *i.e.* imposing $\varepsilon = 0$ after the application of a standard harmonic balance method:

$$\begin{aligned} \mathbf{H}_{1,1}\mathbf{b}_0 = \mathbf{0} \quad &\Rightarrow \quad \frac{1}{2}\left(\Lambda^2\,\mathbf{I} + \Lambda\sqrt{\delta}\,\bar{\bar{\mathbf{C}}} + \delta\bar{\bar{\mathbf{K}}}\right)\mathbf{b}_0 = \mathbf{0} \quad \Rightarrow \\ &\Rightarrow \quad \det\left[\Lambda^2\,\mathbf{I} + \Lambda\sqrt{\delta}\,\bar{\bar{\mathbf{C}}} + \delta\,\bar{\bar{\mathbf{K}}}\right] = 0 \end{aligned} \tag{4.12.2}$$

The characteristic equation in Eq. (4.12.2) provides 8N values of Λ for every fixed δ, partitioned in forward and backward eigenvalues. Unlike the *simplified case* 2 (Section 4.8), in which the system can be cast in canonical (Hamiltonian) form, the real part of the eigenvalues Λ is not zero. Thus, when the system in Eq. (4.12.1) is stable, the Floquet multipliers do not lie on the unit circle. Indeed, the monodromy matrix is not symplectic: it is possible to obtain a system like Eq. (4.12.1) applying a perturbation that brings the Hamiltonian system, *i.e.* $\bar{\bar{\mathbf{C}}} = -\bar{\bar{\mathbf{C}}}^{\mathrm{T}}$, to a non-Hamiltonian system with $\bar{\bar{\mathbf{C}}}$ as in Eq. (4.12.1), continuously; Krein's theorem, Lyapunov-Poincaré theorem and the definition of strong stability do not apply if the perturbed system is non-Hamiltonian. Furthermore, forward and backward eigenvalues have different real parts (forward and backward modes are differently damped). Hence, while complex a quadruplet continue to exist, there is no circle with respect to which the quadruplet is symmetric (in the sense of the inversion). The latter deduction allows to draw an important conclusion: in the presence of both gyroscopic and damping effects, multipliers interact with each other without colliding and, consequently, their trajectories can intersect the unit circle only after having assumed a veering behavior. The latter conclusion remains valid even if $\bar{\bar{\mathbf{K}}}$ is symmetric and the damping distribution is of proportional type.

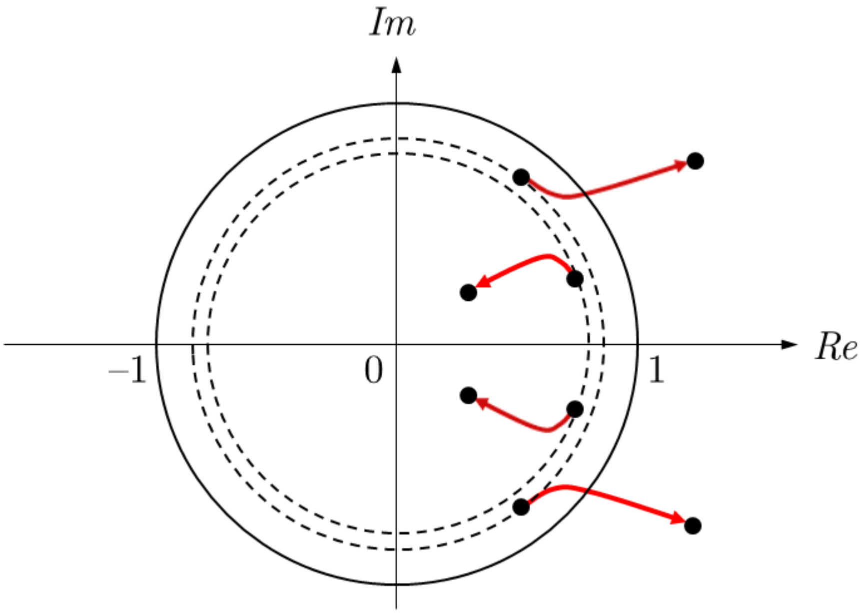

Figure 4.21: Multipliers exiting the unit circle without colliding

In Fig. 4.21 a complex quadruplet of multipliers, generated by a ε-dependent deformation (fixed δ), of a gyroscopic, damped system is schematized. The main difference with respect to the undamped case is that multipliers tend to remain distinct and repel each other without colliding. In the undamped case (Hamiltonian), complex quadruplets are generated by rotating pairs of multipliers with unitary moduli (moving in opposite directions). Since the monodromy matrix of that Hamiltonian system is symplectic, definite multipliers are forced to lie on the unit circle until they collide with multipliers of different kind, then they can leave the unit circle without breaking the symmetry. Notice that in Hamiltonian systems the unit circle is the only characteristic circle regardless the parameters (δ and ε) involved in the deformation of the Hamiltonian. In Fig. 4.21 dashed circles represent a weaker definition of characteristic circles. Thus, the veering phenomenon of multipliers makes it impossible to draw definite conclusions on critical solutions. This difficulty can be overcome by reconsidering the Λ eigenproblem associated to **H**, applied to the numerical algorithm introduced in Section 4.11. The developed numerical algorithm has been validated by comparison with the results obtained in the previous sections for less general cases. Combined gyroscopic and damping effects are highlighted in Fig. 4.22, obtained by means of the numerical algorithm applied to the study-case (without additional inertial elements), assuming $\zeta_0 = 0.01$ with damping distribution as in *simplified case* 5 (constant modal damping factors, Section 4.10). Clearly, without introducing additional inertial elements, differences with respect to the non-rotating case can be appreciated only by increasing the dimensionless angular speed up to unrealistic, exceedingly high values. In fact, even at $\hat{\omega} = 15$, *i.e.* at 23377 rpm (with $l = 400$ mm, $r = 0.01$ m, hence Ω = 163.2 rad/s in Eq. (3.7.1) and (3.7.2)) the global stability threshold displayed in Fig. 4.22 (black curve) cannot be practically distinguished from that at $\hat{\omega} = 0$ in Fig. 4.20 (black curve). At unrealistic values of angular speed, as in Fig. 4.22, however, a merging effect of adjacent instability regions can be noticed, enhanced by damping (red and grey curves).

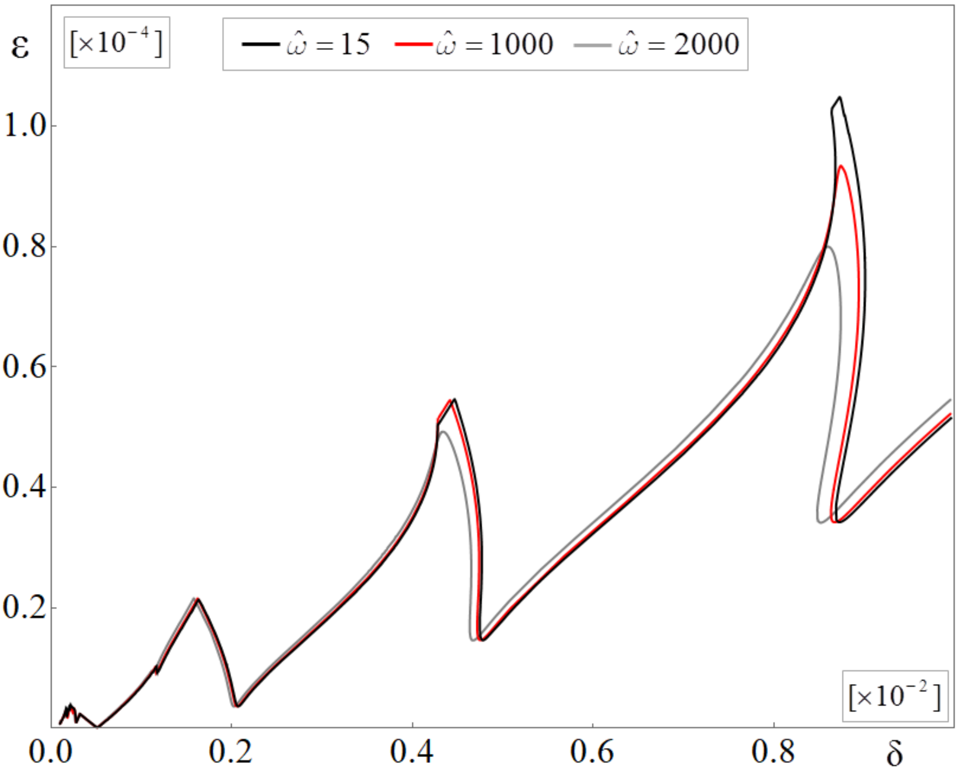

Figure 4.22: The effects of the angular speed on the stability threshold

Before switching to more realistic cases, the effects of slenderness ratio α and of preloads are investigated. Without introducing additional inertial elements, the effects of slenderness ratio are far larger than those of angular speed, as shown in Fig. 4.23: increasing α reduces almost everywhere the stability margin. As for the external load components, the effects of a twisting moment component $\hat{T}_0$ (torsional preload) does not produce noticeable changes in the stability charts (even for values of $\hat{T}_0$ far beyond the realistic upper bound). Also the effects of $\Delta\hat{T}$ are practically negligible in a broad range of values of $R_{T,N} = \Delta\hat{T} / \Delta\hat{N}$. The stability thresholds obtained setting $\Delta L = \Delta\hat{T}$ and $\Delta\hat{N} = 0$ in the equations of motion, would be scaled at far higher values of ε. Hence the contribution of oscillating components in the circulatory terms (due to $\hat{T}(\tau)$) in the equations of motion, Eq. (4.2.11), is usually negligible with respect to those of axial loads (due to $\hat{N}(\tau)$). As for the axial end thrust preload $\hat{N}_0$, an example of its influence on the stability threshold is shown in Fig. 4.24, in which a value equal to 15% of the first critical load (evaluated for $\hat{T}_0 = 0$, Section 3.13) was assumed for $\hat{N}_0$. Figure 4.24 shows that a compressive axial end thrust produce a shift of the entire global stability threshold to the right (red curve) with respect to the non-preloaded case (*simplified case* 5, black curve). This is imputable to the shift that $\hat{N}_0$ produces on the natural frequencies of the unperturbed system.

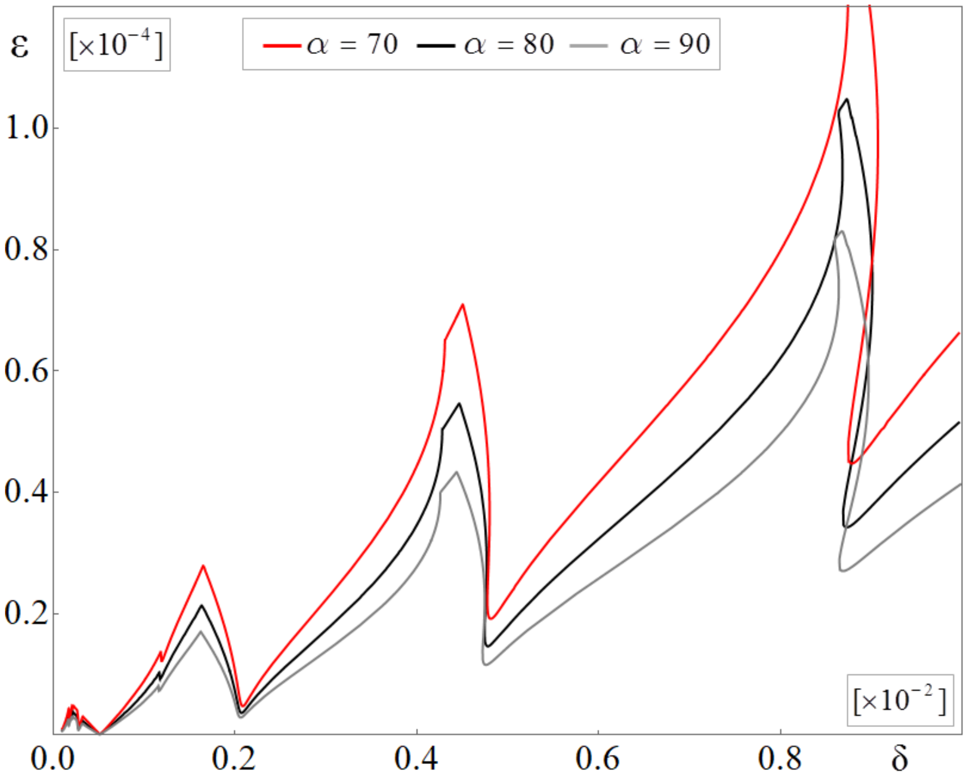

Figure 4.23: The effects of the slenderness ratio α on the stability threshold at null angular speed

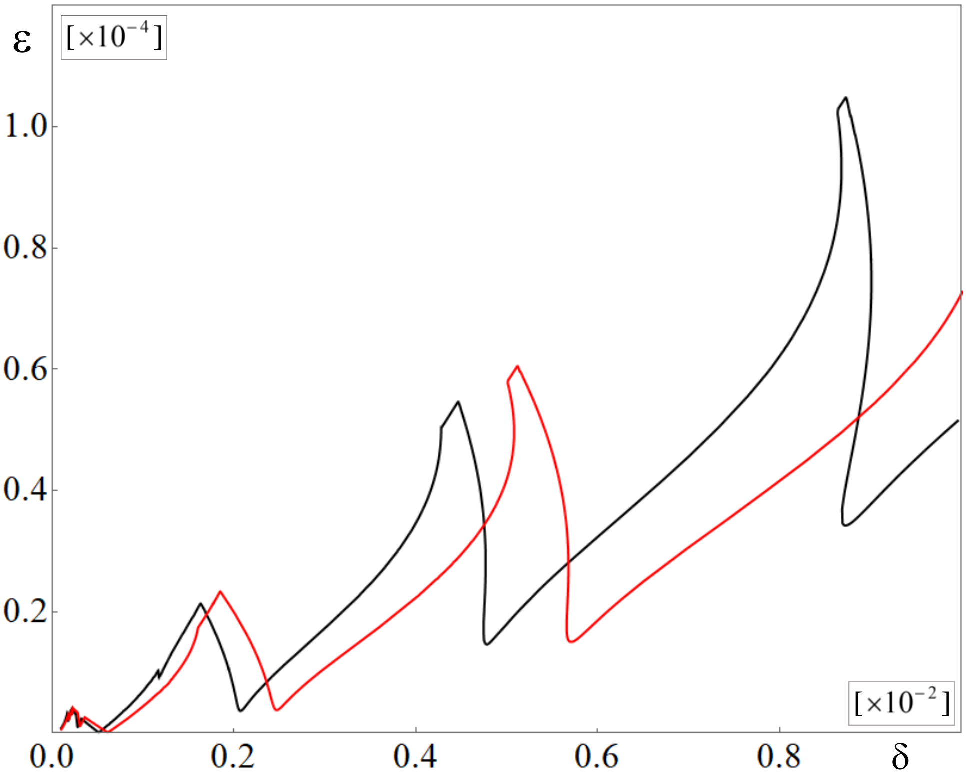

Figure 4.24: The effect of an axial preload $\hat{N}_0$ equal to 15% of the first critical load (red curve)

A compressive (negative) $\hat{N}_0$ returns lower natural frequencies with respect to the unloaded case, while the opposite happens for tractive $\hat{N}_0$ (Section 3.14). In the undamped case, critical values of δ (on the δ-axis) can be computed through Eq. (4.6.14) or Eq. (4.8.11). Lower natural angular frequencies means higher critical values of δ. The presence of damping terms does not interfere with the above shifting effect, *i.e.* the contracted instability tongues of the damped case are completely contained in those of the undamped one (due to the stabilizing effect of external damping distributions). This necessarily means that also the transition curves of the damped case are shifted to the right (compressive $\hat{N}_0$).
Both Fig 4.23 and Fig. 4.24 were obtained assuming $\zeta_0 = 0.01$ with damping distribution as in *simplified case* 5 (constant modal damping factors, Section 4.10) and null angular speed.
It can be concluded that, without considering additional inertial elements and in a realistic range of angular speeds, gyroscopic effects on the simple shaft are so small to be negligible, as are whose of $\hat{T}_0$ and $\Delta\hat{T}$. While the influence of the slenderness ratio α and of the axial end thrust preload $\hat{N}_0$ turned out to be dominant. As for damping, also in the presence gyroscopic effects, it produces substantial clearing of high-order mode contributions to the global stability region, with great advantage in terms of reduction of computational load.

4.13 Simple shaft with gyroscopic and internal (rotating) damping effects

It is well known that, contrary to external damping distributions, internal (or rotating) damping distributions may lead to instability even in the absence of parametric excitation of the rotor [2]. Introducing complex variables for displacements and rotations as in Eq. (3.2.2), the equations of motion, Eq. (4.2.1), in the case of undamped and unloaded rotating shaft ($N(t) = T(t) = 0$) without additional inertial element ($f_1 = f_2 = f_3 = 1$) can be written in the following form, similar to Eq. (3.6.2):

$$\begin{cases} \rho A \ddot{\mathrm{w}} - \kappa GA(\mathrm{w}^{\mathrm{II}} + i\theta^{\mathrm{I}}) = 0 \\ \rho J\ddot{\theta} - 2i\rho J\omega\dot{\theta} - \kappa GA(i\mathrm{w}^{\mathrm{I}} - \theta) - EJ\,\theta^{\mathrm{II}} = 0 \end{cases} \quad \text{with} \quad \begin{cases} \mathrm{w} = v + iw \\ \theta = \vartheta_y + i\vartheta_z \end{cases} \tag{4.13.1}$$

which can be rewritten in operator form:

$$\begin{cases} \mathbf{M}_c\mathbf{w} + \mathbf{G}_c\dot{\mathbf{w}} + [\mathcal{K}_c]\mathbf{w} = \mathbf{0} \\ \mathbf{w} = \{\mathrm{w}, \theta\}^{\mathrm{T}} \end{cases} \tag{4.13.2}$$

where:

$$\begin{cases} \mathbf{M}_c = \begin{bmatrix} \rho A & 0 \\ 0 & \rho J \end{bmatrix}, \quad \mathbf{G}_c = \begin{bmatrix} 0 & 0 \\ 0 & -2i\omega\rho J \end{bmatrix} \\ [\mathcal{K}_c(\cdot)] = \begin{bmatrix} -\kappa GA(\cdot)^{\mathrm{II}} & -i\kappa GA(\cdot)^{\mathrm{I}} \\ -i\kappa GA(\cdot)^{\mathrm{I}} & \kappa GA(\cdot) - EJ\,(\cdot)^{\mathrm{II}} \end{bmatrix} \end{cases} \tag{4.13.3}$$

A viscous-damping model is now adopted as simplest choice for an internal, rotating damping distribution, say $[\mathcal{D}_{rc}(\cdot)]$, in the complex variable space. Its introduction in the equations of motion, Eq. (4.13.2), according to the procedure described in [2], yields:

$$\mathbf{M}_c\ddot{\mathbf{w}} + \mathbf{G}_c\dot{\mathbf{w}} + [\mathcal{D}_{rc}]\dot{\mathbf{w}} + [\mathcal{K}_c]\mathbf{w} - i\omega[\mathcal{D}_{rc}]\mathbf{w} = \mathbf{0} \tag{4.13.4}$$

which, in case of stiffness-proportional distribution, takes the following particular form:

$$[\mathcal{D}_{rc}(\cdot)] = b[\mathcal{K}_c(\cdot)] \quad \Rightarrow \quad \mathbf{M}_c\ddot{\mathbf{w}} + \mathbf{G}_c\dot{\mathbf{w}} + b[\mathcal{K}_c]\dot{\mathbf{w}} + (1 - i\omega b)[\mathcal{K}_c]\mathbf{w} = \mathbf{0} \tag{4.13.5}$$

With $b \in \mathbb{R}$. Rewriting Eq. (4.13.5) back in the space of real displacements and rotations, the complex coefficient ($i\omega b$) generates an operator, say $[\mathcal{K}_r(\cdot)]$, which is different from $[\mathcal{K}(\cdot)]$. Cast in non-dimensional form for comparison with the expression of $[\mathcal{K}(\cdot)]$ reported in Eq. (4.6.2), (with $\psi(\tau) = 1$ and $\hat{T}(\tau) = 0$), it reads:

$$i[\mathcal{K}_c(\cdot)] = [\mathcal{K}_r(\cdot)] = \begin{bmatrix} 0 & \dfrac{\alpha^2}{\sigma}(\cdot)^{\mathrm{II}} & \dfrac{\alpha^2}{\sigma}(\cdot)^{\mathrm{I}} & 0 \\ -\dfrac{\alpha^2}{\sigma}(\cdot)^{\mathrm{II}} & 0 & 0 & \dfrac{\alpha^2}{\sigma}(\cdot)^{\mathrm{I}} \\ \dfrac{\alpha^2}{\sigma}(\cdot)^{\mathrm{I}} & 0 & 0 & (\cdot)^{\mathrm{II}} - \dfrac{\alpha^2}{\sigma}(\cdot) \\ 0 & \dfrac{\alpha^2}{\sigma}(\cdot)^{\mathrm{I}} & \dfrac{\alpha^2}{\sigma}(\cdot) - (\cdot)^{\mathrm{II}} & 0 \end{bmatrix} \tag{4.13.6}$$

After Galerkin discretization, however, the equations of motion of the parametrically excited shaft retain the same form of Eq. (4.3.14), the only difference given by the internal damping terms in matrix $\hat{\mathbf{C}}$ (in this case proportional to matrix $\hat{\mathbf{K}}_0$) and in matrix $\hat{\mathbf{K}}$ (in this case proportional to angular speed $\hat{\omega}$ and to matrix $\hat{\mathbf{K}}_r$, the latter obtained from operator $[\mathcal{K}_r(\cdot)]$):

$$\begin{cases} \hat{\mathbf{M}}\ddot{\mathbf{q}}_d + \hat{\mathbf{C}}\dot{\mathbf{q}}_d + \left[\hat{\mathbf{K}} + \Delta L\cos(\hat{\Omega}\tau)\hat{\mathbf{L}}\right]\mathbf{q}_d = \mathbf{0} \\ \hat{\mathbf{C}} = \hat{\mathbf{G}} + b\hat{\mathbf{K}}_0 \\ \hat{\mathbf{K}} = \hat{\mathbf{K}}_0 + \hat{\mathbf{L}}_0 - \hat{\omega}b\hat{\mathbf{K}}_r \\ \hat{\mathbf{K}}_r = \int_0^1 \mathbf{\Gamma}[\mathcal{K}_r]\mathbf{\Gamma}^{\mathrm{T}} d\xi \end{cases} \tag{4.13.7}$$

In which $\mathbf{\Gamma}$ is as in Eq. (4.3.7). Therefore stability analysis can be performed by adopting the same analytical and numerical tools developed in the previous sections. The effects of internal damping are highlighted considering a stiffness-proportional distribution with study-case parameters ($l = 400$ mm, $r = 0.01$ m, hence Ω = 163.2 rad/s, α = 80), setting b as previously done in the case of external damping ($\zeta_1 = \zeta_{0r}$, $b = 2\zeta_{0r}/\omega_1$). Ince-Strutt diagrams are shown in Fig. 4.25 and Fig. 4.26, displaying a comparison between stability thresholds at different values of angular speed $\hat{\omega}$ (Fig. 4.25) and damping factor ζ_{0r} (Fig. 4.26), in both cases with null external damping.

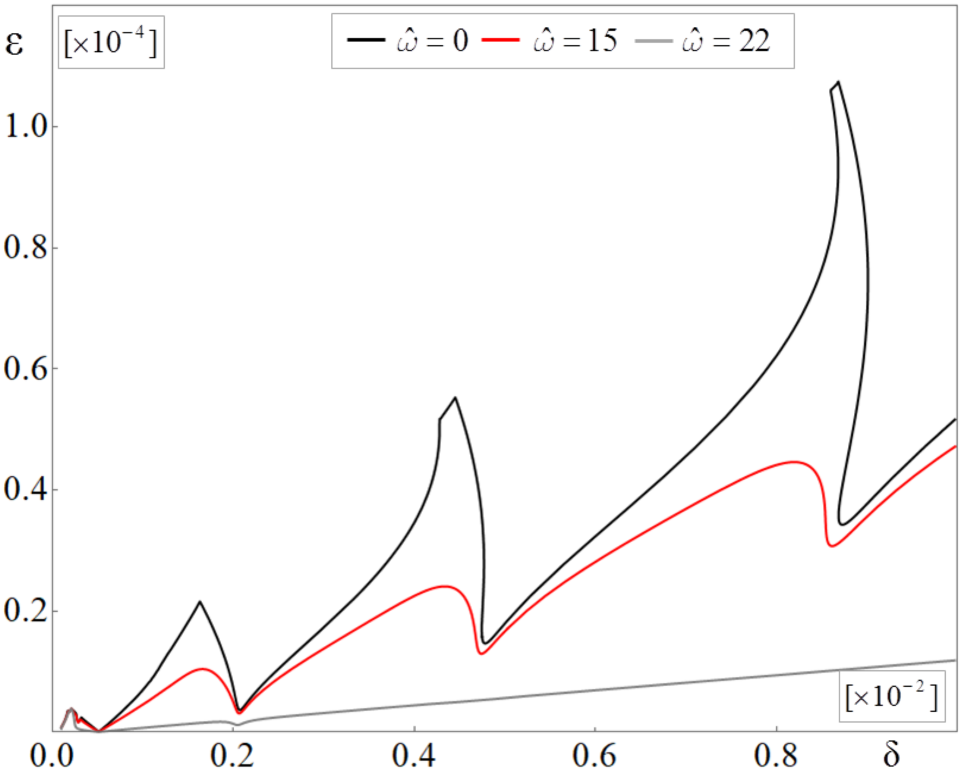

Figure 4.25: Internal (stiffness-proportional) damping:
effects different values of angular speed with $\zeta_{0r} = 0.01$

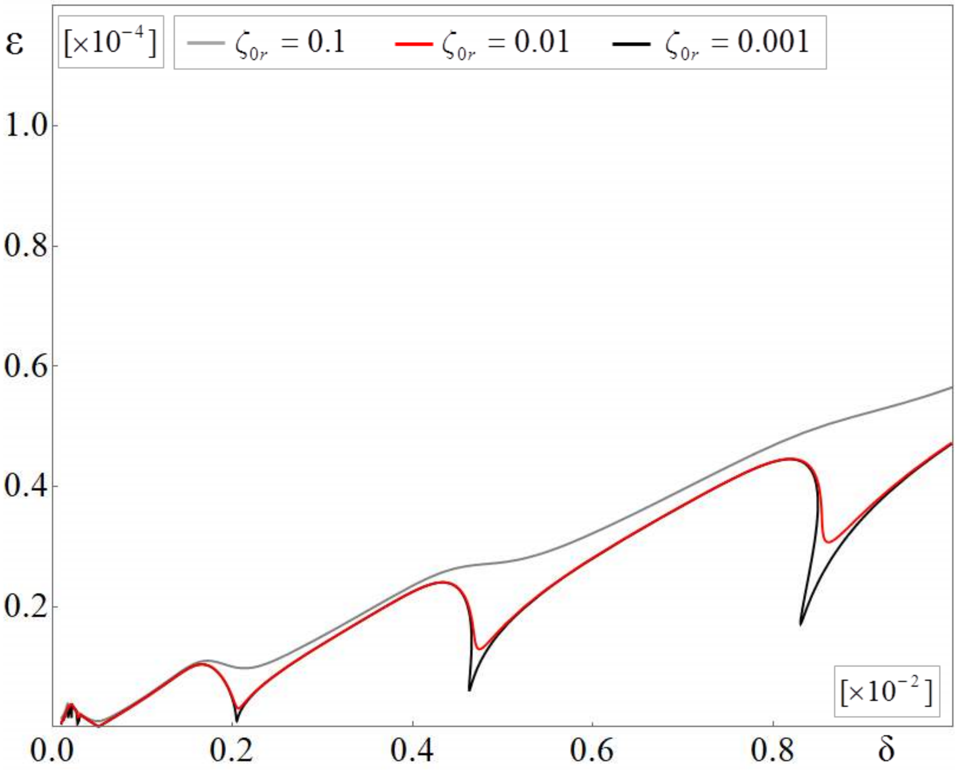

Figure 4.26: Internal (stiffness-proportional) damping:
effects of different levels of damping factor ζ_{0r} with $\hat{\omega} = 15$

In Fig. 4.25, differences between black ($\hat{\omega}=0$), red and grey curves ($\hat{\omega}\neq 0$) are almost totally due to the $\hat{\mathbf{K}}_r$ term in the equations of motion, since for the rotor under analysis even at $\hat{\omega}=15$ (about 23377 rpm) the gyroscopic $\hat{\mathbf{G}}$ term still plays a negligible role (as it results from Fig. 4.20 and Fig. 4.22). Dropping $\hat{\mathbf{K}}_r$ in Eq. (4.13.7) would therefore produce stability thresholds almost perfectly superimposed to the black ones. On the other hand, Fig. 4.26 shows the effects of different levels of damping factor ζ_{0r} at $\hat{\omega}=15$: it is evident that at high angular speed even small amounts of internal damping ($\zeta_{0r}=0.001$) can produce large modifications in the stability maps. Noticeably, external damping affects mainly the downward spikes of instability regions (producing smoothing and contractions, with stabilizing effects), while internal damping acts significantly also on their lateral borders (producing merging, with destabilizing effects induced by angular speed). Hence, increasing both components would result in a progressive flattening of the stability thresholds. The destabilizing effects of internal damping are directly proportional to angular speed: increasing the latter, reduces the residual stability region until it vanishes completely at the first critical speed of the shaft (Fig. 4.25). In fact, in the (unrealistic) case of no external damping, it is well known that a rotor becomes dynamically unstable due to internal damping when its angular speed passes its first critical value [2]. This is evident in complex Campbell diagrams as represented in Fig. 4.27 (real part, with $\zeta_{0r}=0.01$) for the first two eigenvalues of the unloaded simple shaft. The real part of the first forward eigenvalue becomes zero exactly at the first forward critical speed ($\hat{\omega}=22.18$, about 34560 rpm).

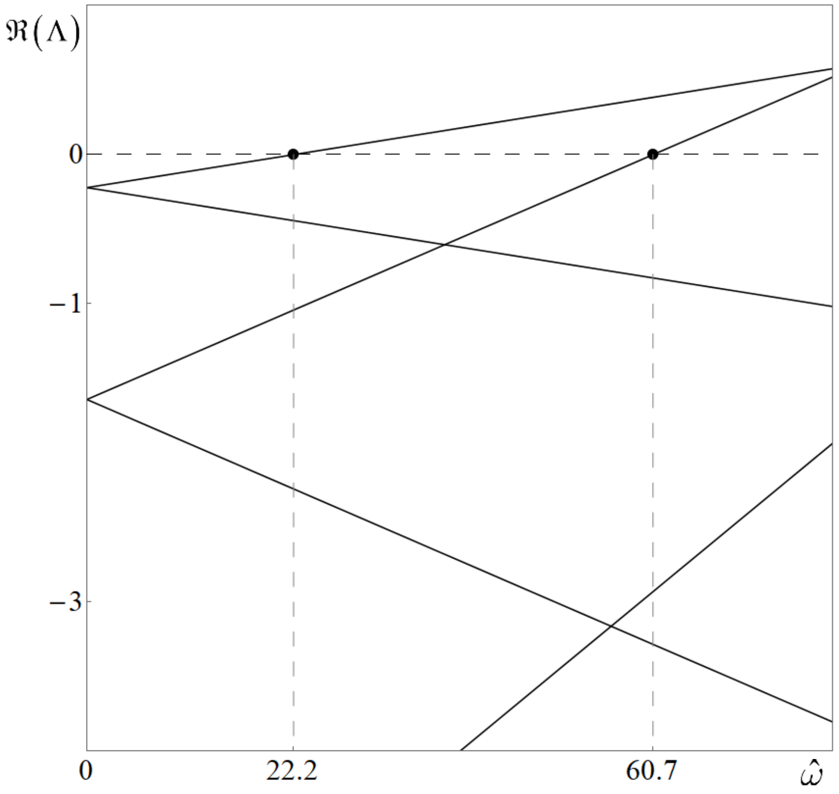

Figure 4.27: Campbell diagram (real part) of the first two eigenvalues of the unloaded shaft

More in general, it can be shown that in presence of internal damping without external damping, at each critical speed the real part of the related eigenvalue becomes zero. In fact, Laplace transforming with respect to time Eq. (4.13.4), and setting the critical condition $s = \Lambda = i\,\omega$, gives:

$$\begin{cases} s^2\,\mathbf{M}_c\mathbf{w} \ + s\,\mathbf{G}_c\mathbf{w} + (s - i\omega)[\mathcal{D}_{rc}]\mathbf{w} + [\mathcal{K}_c]\mathbf{w} = \mathbf{0} \\ s = i\omega \quad \Rightarrow \quad -\omega^2\,\mathbf{M}_c\mathbf{w} \ + i\omega\,\mathbf{G}_c\mathbf{w} + [\mathcal{K}_c]\mathbf{w} = \mathbf{0} \end{cases} \tag{4.13.8}$$

Therefore at the critical speeds the differential eigenproblem does not depend on the internal damping operator, yielding pure imaginary eigenvalues.

Finally, Fig. 4.28 shows the effects of hollow sections of the shaft, varying a dimensionless ratio defined as:

$$\mu_r = \frac{r_{internal}}{r_{external}} \tag{4.13.9}$$

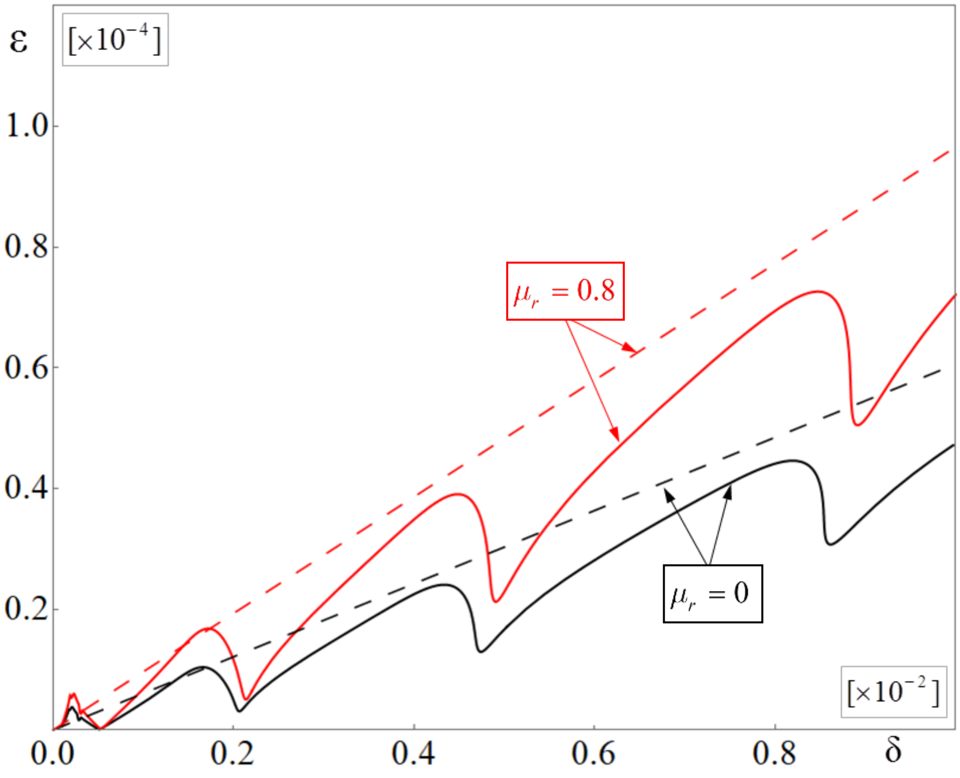

Figure 4.28: Effects of a hollow section of the shaft with internal damping

The study-case parameters values are adopted, with angular speed $\hat{\omega} = 15$ and a (high) internal damping factor ($\zeta_{0r} = 0.01$). The section with fixed $r_{external} = 0.01$ m is then modified varying μ_r from 0 (solid section) up to 0.8 (hollow section, which affects other parameters, so that the slenderness α varies from 80 to 62.47, the frequency parameter Ω from 163.2 to 209.0 rad s^{-1}, the angular speed ω from 23377 to 29936 rpm, and the dimensionless equivalent first Euler's critical load from 6.06×10^{-3} to 9.66×10^{-3}). Notice that the stabilizing effect due to $\mu_r > 0$, as well as the equivalent first Euler's critical load increase (dashed operation lines), are only apparent. In any case the operation lines related to equivalent first Euler's critical loads are well into the unstable regions, which clearly means that critical load analysis is not sufficient for assessing the stability of the parametrically excited rotor.

4.14 Shaft with additional inertial elements

An additional rigid disc is now considered (Fig. 4.1) with parameters:

$$\rho_d = 7700 \text{ Kg m}^{-3}, \quad R_e = 120 \text{ mm}, \quad R_i = 30 \text{ mm}, \quad h_e = 50 \text{ mm}, \quad h_i = 20 \text{ mm} \tag{4.14.1}$$

With shaft parameters given in Eq. (4.5.1), and assuming in this case $l = 400$ mm, $r = 0.01$ m and $\Delta\hat{T} = 0 \Rightarrow R_{T,\mathrm{N}} = 0,$ mounted on the study-case shaft at a coordinate $x_{01} = l/3$ to enhance the gyroscopic effects on stability charts, mainly due to the first eigenvalue contribution.

Varying $\hat{\omega}$ in presence of external damping only (stiffness-proportional distribution, $\zeta_0 = 0.01$) the gyroscopic induced modifications, consisting of shifts and merging of unstable regions, become very large, negligible only at low angular speed, as shown in Fig. 4.29 (at ω = 0, ω = 3896 rpm, ω = 7792 rpm, ω = 11669 rpm; the last value of angular speed still within the limits of resistance to centrifugal load). As already noticed, the magnitude of these modifications depends on separation of natural frequencies into pairs of forward and backward values, highlighted by the Campbell diagram (imaginary part) of the unloaded shaft with disc displayed in Fig. 4.31, where the grey vertical segments identify the differences ($\omega_{1f} - \omega_{1b}$) at the selected values of angular speed. Clearly, the average value ($\omega_{1f} + \omega_{1b}$) / 2 decreases with increasing angular speed, causing a shift of downward smoothened spikes to the right (towards higher δ).

The presence of internal damping, in addition to external damping, has the effect of further modifying the merging effect between adjacent instability regions. In Fig. 4.30 three stability thresholds are reported, computed with $\hat{\omega} = 7.5$, stiffness-proportional external damping with $\zeta_0 = 0.01$, and additional stiffness-proportional internal damping with $\zeta_{0r} = 0$, $\zeta_{0r} = 0.001$ and $\zeta_{0r} = 0.005$. In the passage from $\zeta_{0r} = 0$ to $\zeta_{0r} = 0.005$, a flattening effect can be observed on the stability threshold, as already noticed in Fig. 4.26; however, with a smaller amount of internal damping ($\zeta_{0r} = 0.001$), the effect is the opposite, with noteworthy reduction of the merging effect.

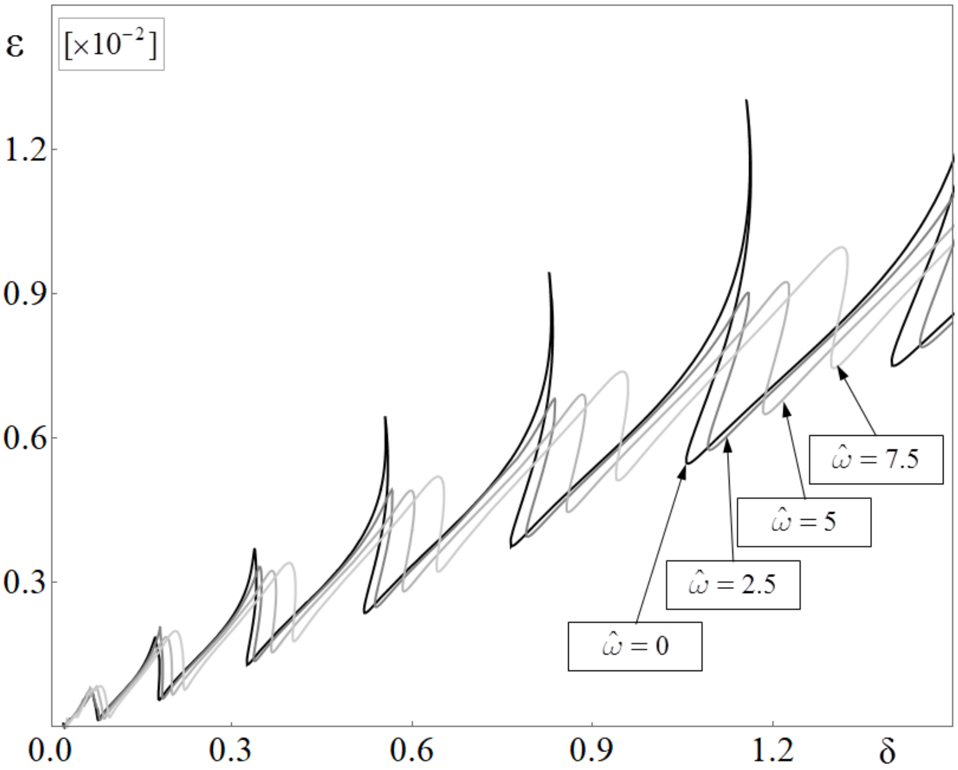

Figure 4.29: Effects of an additional inertial element:
varying $\hat{\omega}$ in presence of external damping only

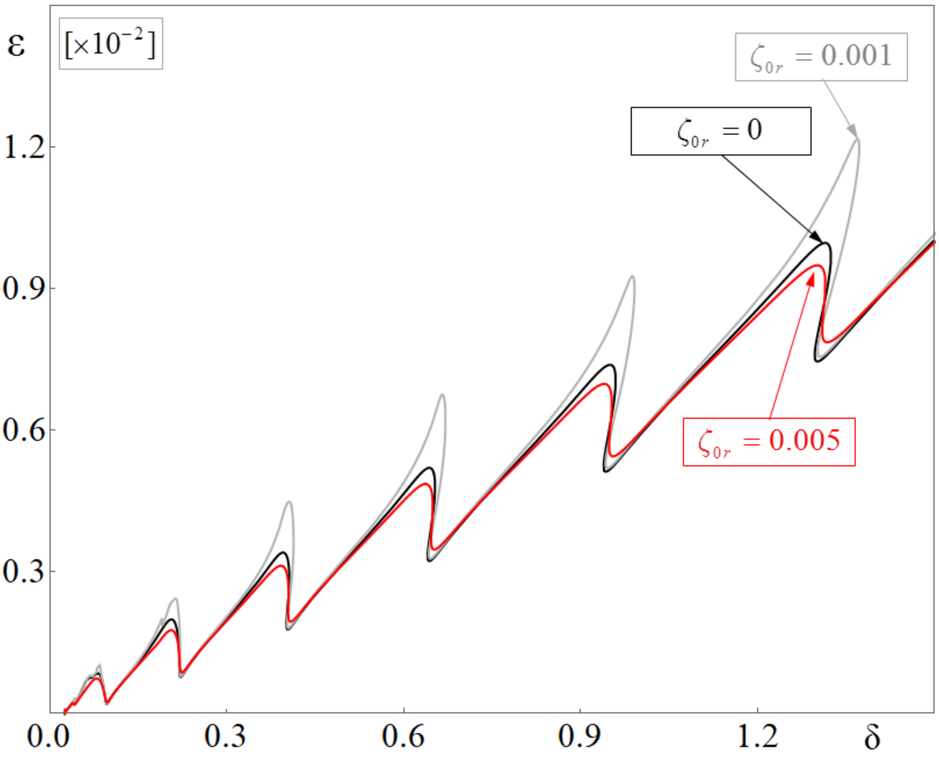

Figure 4.30: Effects of an additional inertial element:
varying ζ_{0r} in presence of both external and internal damping, at $\hat{\omega}=7.5$

For understanding this behaviour, the Campbell diagram (real part) of the unloaded shaft with disc displayed in Fig. 4.32 is considered. In the diagram, solid lines identify the real part of the first forward eigenvalue and dashed lines the real part of the first backward eigenvalue; at the first (forward) critical speed the internal damping does not work, yielding an invariance point for the real part of the first forward eigenvalue. Notice that with $\zeta_{0r} = 0$ the real part of the first forward eigenvalue in the diagram is monotonic decreasing with angular speed, while with $\zeta_{0r} = 0.005$ it is increasing towards positive values. With $\zeta_{0r} = 0.001$ its behavior is somewhat intermediate, and at a certain value of angular speed it equals the real part of the related backward eigenvalue. At this point the damping distribution would operate in the closest conditions with respect to the non-rotating case (coincident forward and backward eigenvalues), and therefore it would be the less effective in merging adjacent instability regions. At $\hat{\omega} = 7.5$, the difference between real parts of forward and backward first eigenvalues is the smallest with $\zeta_{0r} = 0.001$, yielding the reduction in merging effect observed in Fig. 4.30.

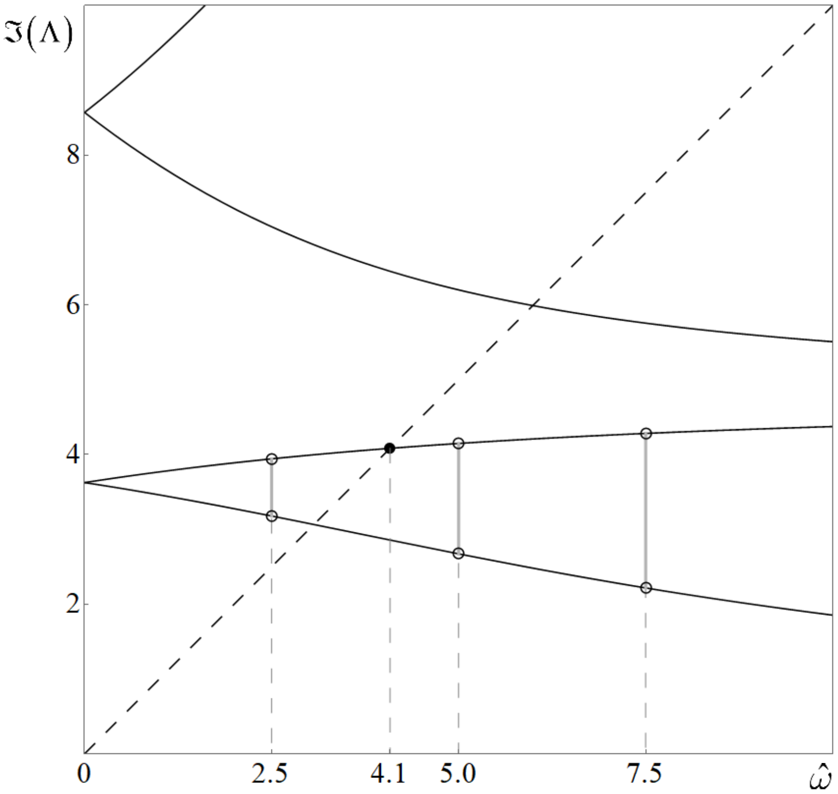

Figure 4.31: Campbell diagram of the unloaded shaft with disc: imaginary part related to the map in Fig. 4.29 (effect of angular speed)

It can be concluded that with additional inertial elements, enhancing separation of natural frequencies into pairs of forward and backward values, the gyroscopic induced modifications (shifts and merging of unstable regions) tend to become very large, negligible only at low angular speed. In addition, even very small variations of internal damping amount can produce large modifications in merging of adjacent instability regions.

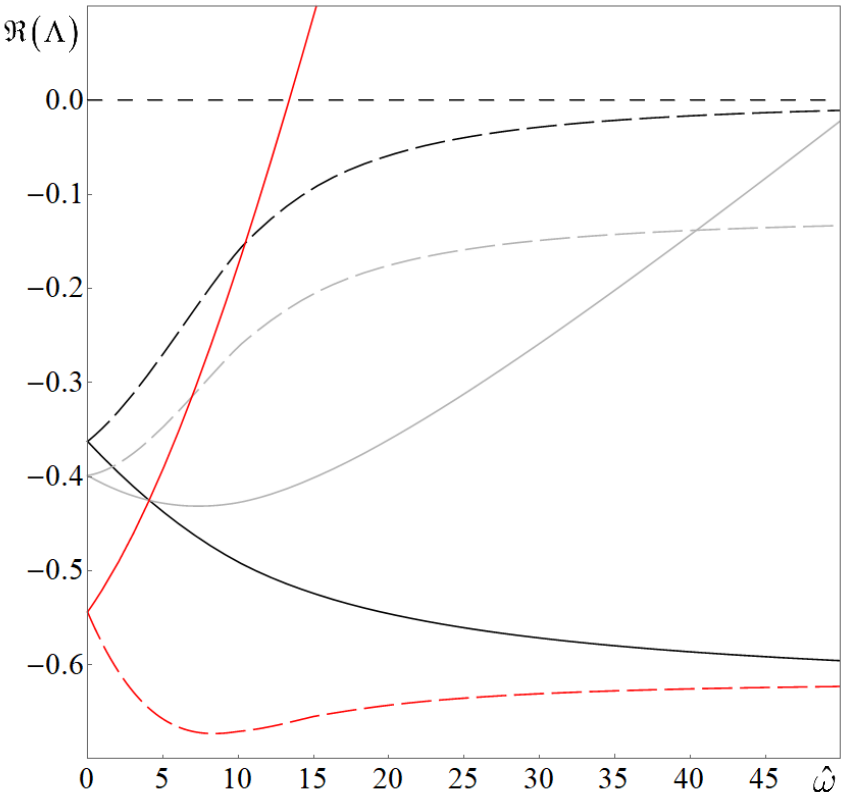

Figure 4.32: Campbell diagram of the unloaded shaft with disc: real part related to the map in Fig. 4.30 (addition of internal damping)

4.15 Practical use of the stability charts

Stability charts, as presented in the previous Sections, are a powerful tool for the analysis of parametrically excited rotor systems. But they are not without physiological inaccuracies that are difficult to avoid:

1 The natural angular frequencies of the unperturbed system are always approximated, due to the fact that they are estimated through Galerkin method.
2 The accuracy of transition curves depends on the number of terms included in the Fourier series (harmonic balance method).
3 Critical values of Λ are affected by numerical errors.
4 Realistic damping distributions are difficult to model.

The latter point is due to the difficulty of identifying realistic trends of modal damping factors with respect to natural frequencies. As discussed in the previous Sections, stability charts are highly sensitive with respect to damping variations. However, they can still be used as guideline, in order to identify regions in which the rotor can safely operate in stable conditions.
In the present Section, a graphical method aimed at establish conservative safety limits is presented.

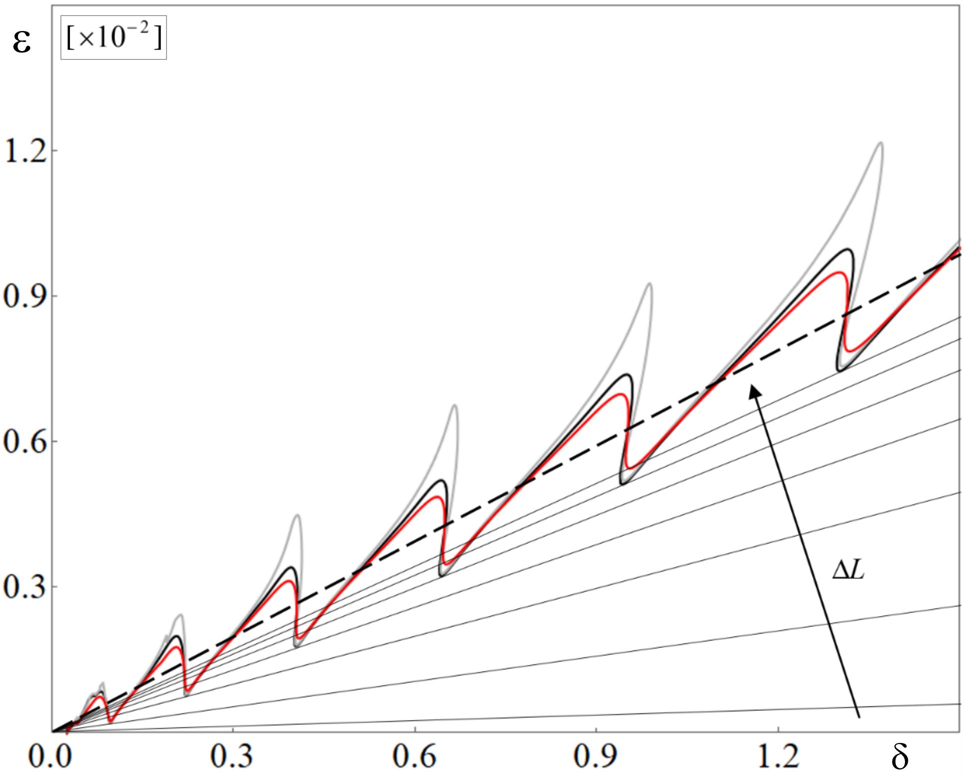

Figure 4.33: Operation lines tangent to the black stability threshold ($\zeta_{0r} = 0$)

Consider the stability chart in Fig. 4.30 (Section 4.14), obtained at $\hat{\omega} = 7.5$ varying ζ_{0r} for the study-case shaft with an additional inertial element mounted in $x_{01} = l/3$, in presence of both external and internal damping. Now consider a set of operation lines ($\Delta L = const$), tangent to the black stability threshold with $\zeta_{0r} = 0$, as in Fig. 4.33. Each operation line is tangent to the stability threshold near to a local minimum of the latter. Now consider two consecutive minimums and the operation line related to the first minimum (minima are numerated according to the direction of increasing δ). This operation line identifies a tangent point $\mathbf{P}_1$ and an angle such that:

$$\varphi_{\Delta L}^{(1)} = \arctan\left(\Delta L_1\right) \tag{4.15.1}$$

The point $\mathbf{P}_1$ identifies the value δ_1 on the δ-axis (as shown in Fig. 4.34). Uncertaities in the internal damping amount affect the upper part of the stability threshold (black, grey and red curves). Uncertaities in the external damping amount affect the position of the local minima of the stability threshold. In the unrealistic case of no external damping two critical values on the δ-axis can be computed through Eq. (4.8.11), say δ_1^{crit} and δ_2^{crit}. The second critical value δ_2^{crit} identifies a point $\mathbf{P}_2$ on the operation line related to ΔL_1 (see Fig. 4.34). The points $\mathbf{P}_1$ and $\mathbf{P}_2$, along with the values δ_1 and δ_2^{crit} on the δ-axis, identify a region (yellow convex quadrilateral in Fig. 4.34). This reduced stability region takes into account the uncertainties on the internal and external damping distributions (except for a neighborhood of point $\mathbf{P}_1$) in a conservative way. The red region, bounded above by the operation line related to the first equivalent Euler's critical load, is to be avoided due to the possible presence of instability tongues related to an higher sequence of transition curves (black dashed curves in Fig. 4.34, related to a higher-order sequence with very low damping).

Since the natural frequencies (forward and backward) of the unperturbed system are always approximated from above (Galerkin method), the critical values δ_1^{crit} and δ_2^{crit} have to be increased (point 1). In fact, lower frequencies means higher values of δ. A convergence test can easily quantify the shifts affecting δ_1^{crit} and δ_2^{crit}. While the shift of δ_2^{crit} is conservative with respect to stability, the opposite happens for that of δ_1^{crit}. Furthermore, a lack of accuracy in dynamic eigenvectors can affect significantly the shape of transition curves, which tend to vertical lines if taking into account a too small number of terms in the Fourier series (point 2). A convergence test can be performed also to evaluate the latter effect. Finally, it must be taken into consideration that the critical values of Λ are affected by numerical errors (point 3). Numerical errors in the computation of the eigenvalues Λ produce errors also on the multipliers of the system. The latter obvious consequence can be used to identify degraded values of Λ. Indeed, as was stated in Section 4.6, Eq. (4.4.11) returns $8N(2H+1)$ characteristic exponents Λ, of which only 8N correspond to independent multipliers. Thus an elimination criterion can be found: the values of Λ that returns isolated multipliers (non belonging to groups of overlapping multipliers) have to be discarded. Two values δ_2 and δ_3 are chosen in order to avoid areas in which instability regions (not foreseen by the algorithm in Section 4.11) can hide. The convergence tests allow to quantify the minimum shifts (of δ_1^{crit} and δ_2^{crit}) requested to identify δ_2 and δ_3. A further safety limit is obtained by slightly reducing the value ΔL_1. Thus, an angle $\varphi_{\Delta L}^{(2)} < \varphi_{\Delta L}^{(1)}$ is chosen and two points $\mathbf{P}_3$ and $\mathbf{P}_4$ are obtained as intersections between the operation line inclined by $\varphi_{\Delta L}^{(2)}$ and the vertical lines crossing δ_2 and δ_3. The green region in Fig. 4.34 represents the final output of the proposed graphical method. The parameters δ_2, δ_3 and $\varphi_{\Delta L}^{(2)}$ univocally determine dimensionless frequency range and maximum amplitude of the oscillating load, *i.e.*:

$$\begin{cases} \hat{\Omega}_1 = \dfrac{\omega_{L,1}}{\Omega} = \dfrac{\sqrt{\delta_3}}{\delta_3} \\ \hat{\Omega}_2 = \dfrac{\omega_{L,2}}{\Omega} = \dfrac{\sqrt{\delta_2}}{\delta_2} \quad \Rightarrow \quad \hat{\Omega}_1 < \hat{\Omega}_2 \\ \Delta L_2 = \tan\left(\varphi_{\Delta L}^{(2)}\right) \end{cases} \tag{4.15.2}$$

with $\Delta L_2 < \Delta L_1$.

The procedure above can be repeated for each pair of minima in order to cover a broader range of δ as shown in Fig. 4.35, in which spacing between safety stability regions (green) has been exaggerated for the sake of clarity.

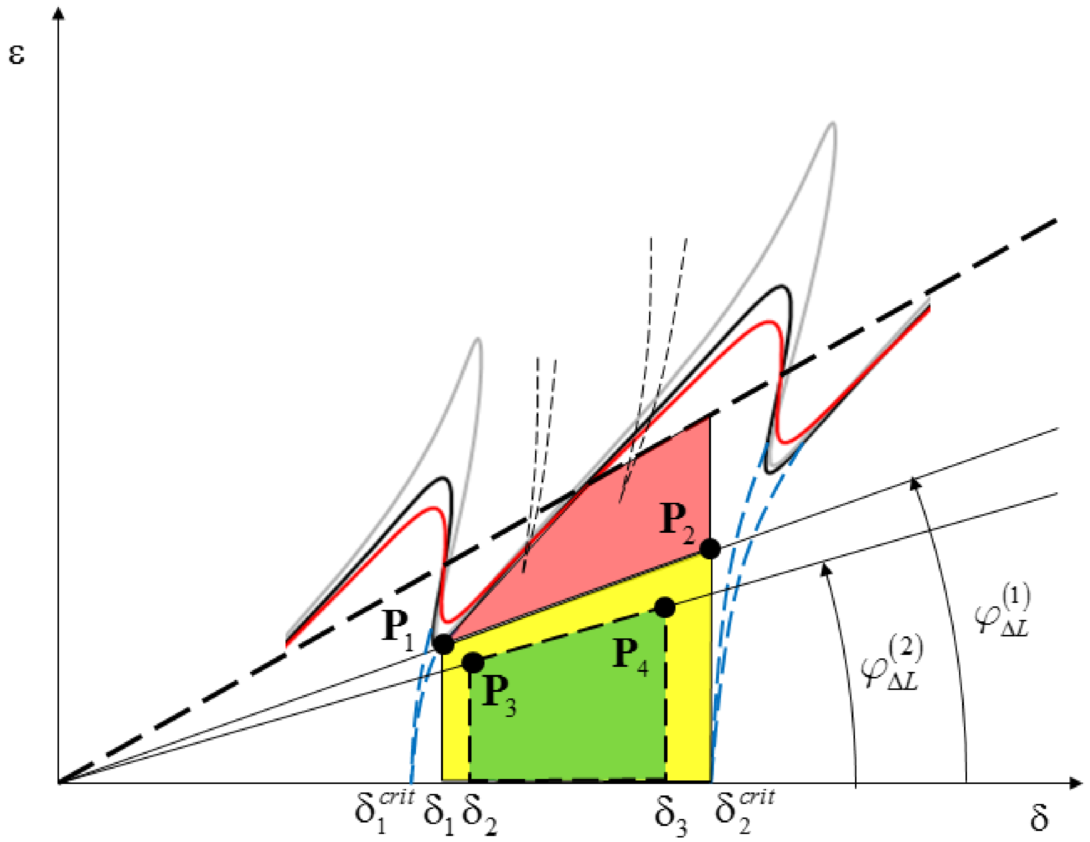

Figure 4.34: Graphical method for determining safety limits of frequency and amplitude of the load

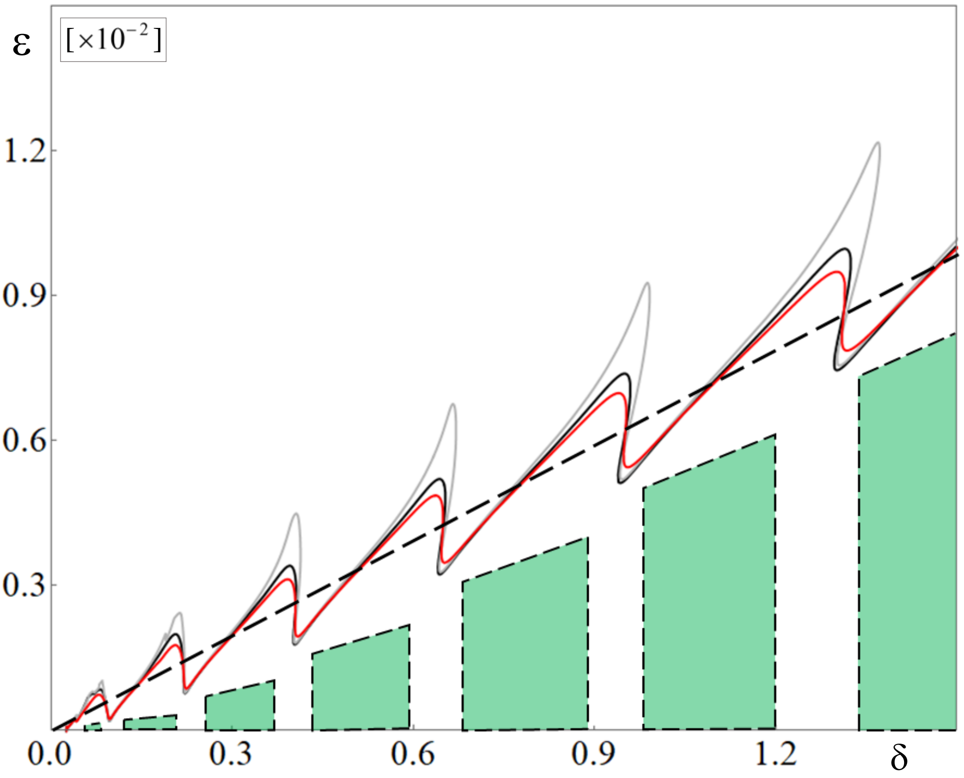

Figure 4.35: Sequence of safety stability regions (green) as output of the graphical method

5 CONCLUSIONS

The main novel contributions in this thesis regard modal analysis of continuous spinning shafts subjected to constant external loads and stability analysis of parametric excited rotors.

5.1 Final remarks and novel contributions concerning spinning Timoshenko beams subjected to constant external loads

A fast and easy to implement method has been proposed for the calculation of natural frequencies, modal shapes and critical speeds of a continuous spinning shaft, consisting of a homogeneous uniform Timoshenko straight beam, rotating at constant angular speed about its longitudinal axis and simultaneously subjected to axial end thrust and twisting moment.

The equations of motion have been derived in both Newtonian and Lagrangian formulations, correcting and clarifying some discrepancies existing in the literature. An alternative method to Taylor expansions of trigonometric terms due to selected (arbitrary) sequences of basic rotations (leading to non-univocal results, as discussed in [3]), is herein used in order to write the expression of the kinetic energy density: second-order approximation rotation matrix.

Modal analysis of the rotating shaft has then been developed for both complex and real displacement variables, presenting novel contributions in clarifying the relations between the two formulations, the structure of the algebraic and differential operators involved and the bi-orthogonality properties of the eigenfunctions in a state-space representation. The effects of varying the model main governing parameters, identified in slenderness ratio, angular speed, axial end thrust and twisting moment, have been studied on natural frequencies, modal shapes and critical speeds of the rotating shaft.

New evidence of existence of the second spectrum in the Timoshenko beam theory has been presented, together with a novel definition for its identification, only possible if considering gyroscopic effects. It has been found that the link between companion frequencies belonging to the first and second spectra is given by a peculiar asymptotic behavior at high rotating speed. Each non-zero horizontal asymptote in Campbell diagrams represents a link between two pairs of eigenvalues, one pair at lower frequencies, one pair at higher frequencies. The latter, at zero angular speed and in particular cases of boundary conditions in which the characteristic equation factorizes (as in the case of simply supported ends), can be identified with the Timoshenko second spectrum. However, when considering a rotating shaft, as $\omega \to \infty$ the existence of non-zero horizontal asymptotes for any boundary conditions suggests a new way for defining and identifying the natural frequencies of the Timoshenko first and second spectra. All first spectrum backward eigenfrequencies tend to 0; all second spectrum forward eigenfrequencies tend to infinity, while the absolute value of each first spectrum forward eigenfrequency converges to the backward companion one belonging to the second spectrum. As a result, it can be stated that the whole second spectrum gives no contribution to the forward critical speeds. In parallel, the role of the so-called cut-off frequencies has been investigated, extending their definition to include the effects of gyroscopic moments and external loads.

The presented model represents an ideal case-study including all features of interest for stability analysis of parametrically excited rotors.

5.2 Final remarks and novel contributions concerning spinning shafts subjected to parametric excitation

An in-depth stability analysis of a parametric excited rotor has been presented. A case-study rotor, modeled as a homogeneous uniform Timoshenko straight spinning beam with clamped ends and mounted inertial elements, subjected to time-periodic (of period T) external axial end thrust and twisting moment, was considered. The resulting coupled partial differential equations of motion were first cast in non-dimensional operator form, then discretized through Galerkin method giving rise to a system of coupled Mathieu-Hill differential equations. After adopting the Floquet-Lyapunov solution, an application of the harmonic balance method allowed to recast the equations in the form of an eigenproblem. The latter procedure allows to avoid direct computation of the monodromy matrix of the system since the resulting eigenproblem carries all the information regarding characteristic exponents and therefore Floquet multipliers.

Table 5.1 Summary of results relating to the five simplified cases

Case	Description	Critical multipliers	Transition solutions	Bifurcation
1	Hamiltonian, no damping, non-rotating shaft	Real, +1 or –1	T-periodic, 2T-periodic	Fold, period-doubling
2	Hamiltonian, no damping, rotating shaft	Complex	Generally non-periodic	Secondary Hopf
3	Non-Hamiltonian, mass-proportional damping, non-rotating shaft	Real, +1 or –1	T-periodic, 2T-periodic	Fold, period-doubling
4	Non-Hamiltonian, stiffness-proportional damping, non-rotating shaft	Real, +1 or –1	T-periodic, 2T-periodic	Fold, period-doubling
5	Non-Hamiltonian, constant modal damping factors, non-rotating shaft	Real, +1 or –1	T-periodic, 2T-periodic	Fold, period-doubling

Five simplified cases has been first analyzed. It was proven that, in these cases, conclusive information regarding critical characteristic exponents can be derived observing the algebraic operator resulting from the harmonic balance method. Thus, under certain simplifying hypothesis, critical conditions can be theoretically predicted. A summary of results relating to the five simplified cases is reported in Table 5.1.

It has been shown that if the spectrum of the unperturbed system is not partitioned in forward and backward values (non-rotating shaft) and if the damping distribution is of proportional type, then complex quadruplets of multipliers cannot exist and they occur in pairs of double multipliers of fixed kinds. Hence, critical collisions between multipliers can only happen on the real axis. On the other hand, if the shaft is spinning and no damping is considered (case 2) then collisions do not occur on the real axis. However, the position of Krein collisions (on the unit circle) in the case of spinning undamped shaft can be analytically predicted, thus, even in this case no direct computation of the monodromy matrix is required.

An accurate and numerically efficient algorithm has been proposed and validated for computing stability charts in the general case of coupled Mathieu–Hill equations with both gyroscopic and damping terms. The algorithm is aimed at directly tracing global stability thresholds and it is meant to work with any kind of gyroscopic, linear non-Hamiltonian system. Since it works directly with the eigenproblem resulting from the harmonic balance method, numerical integrations aimed at computing the monodromy matrix are, again, not required. Focusing only on the global stability threshold allows to avoid extensive evaluations over a wide parametric domain, restricting the search for transition points only in specific regions (accurately predicted through threshold-arc approximation). The resulting code is extremely fast compared to standard sampling-based algorithms (like Monte Carlo algorithms). Furthermore, it is possible to obtain higher chart resolutions with fewer evaluations of the real parts of the characteristic exponents.

If both gyroscopic and damping effects are considered, multipliers interact with each other without colliding and, consequently, their trajectories can intersect the unit circle only after having assumed a veering behavior (Fig. 4.21). This feature is due to a loss of symmetry in the dissipation mechanism, causing a distortion in the characteristic circles. Indeed, in the presence of damping, each pair of forward and backward eigenvalues (of the unperturbed system) have different non-zero real parts (forward and backward modes are differently damped). This conclusion suggests that even in absence of gyroscopic effects, but with generic non-proportional damping distribution (even if the damping matrix is symmetric and positive-definite), collisions between multipliers cannot occur. In fact, in a non-rotating beam system, non-proportional damping distributions induce a separation in terms of real parts of eigenvalues relating to companion modes (projections on two orthogonal planes). It can be concluded that the veering effect is always present in damped rotor systems (regardless the nature of the damping distribution) and in non-rotating systems in which a realistic non-proportional damping distribution is considered.

Gyroscopic effects on stability of parametrically excited rotor systems have been clarified with respect to incomplete and/or incorrect conclusions found in the literature, presenting novel theoretical developments and computational results. Summing up, these terms produce substantial qualitative differences in both critical solutions and stability thresholds. Critical solutions are (generally) non-periodic limited-amplitude functions (secondary Hopf bifurcation), and modifications induced on stability thresholds consist of shifts and merging of unstable regions, depending on the separation of eigenvalues of the unperturbed system into pairs of forward and backward values. When the magnitude of this separation is high (due for instance to inertial elements like discs), the gyroscopic-induced modifications tend to become very large, and negligible only at low angular speed.

Damping terms play an essential role in making stability charts readable for practical purposes, producing substantial clearing of high-order sequences of transition curves in global stability regions, with great advantage in terms of reduction of computational load, which would otherwise become prohibitive. On stability charts, external damping affects mainly the downward spikes of modal instability regions (producing smoothing and contractions, with stabilizing effects), while internal damping (even in very small amount) acts significantly on their lateral borders (producing merging, with potential destabilizing effects induced by angular speed).

The contribution of Timoshenko second spectrum on stability analysis of rotor systems is negligible for practical purposes. On stability charts the second spectrum always affects a small uninteresting sub-region of the whole parametric domain (very high load frequencies and amplitudes). The presented study on how the Timoshenko second spectrum affects critical speeds and stability charts, suggests that the use of higher order models is not justifiable in the face of a considerable increase in complexity. Hence, the spinning Timoshenko beam model has sufficient complexity and it includes all the features of interest for both critical speeds and stability analysis of parametrically excited rotors.

The effects of varying the model governing parameters, identified in slenderness ratio, angular speed, preloads and cross-section hollowness have been studied on stability charts.

Finally, a fast and practical graphical method aimed at identify safety stability regions on the obtained Ince-Strutt diagrams has been proposed. This method takes into account the physiological inaccuracies of stability charts, the latter used as guidelines.

5.3 Future developments

The above results can serve as a basis for future developments and improvements. The following summarizes the planned schedule of insights and additions.

1 Stability analysis of parametrically excited rotors modeled as Timoshenko beams carrying rigid discs subjected to arbitrary boundary conditions.
2 Theoretical insights concerning the behavior of multipliers of non-Hamiltonian systems in which spectra separation leads to veering effects.
3 Stability analysis of flexible shafts carrying flexible discs using known plate theories.
4 Extension to non-linear (linearizable) rotor systems.
5 FEM. The adopted formulation and numerical algorithm are suitable for application to a more general category of gyroscopic systems, including complex shape rotors in those cases in which properly condensed finite element models are available.
6 Experimental validation.

REFERENCE LIST

[1] Timoshenko S.P. (1922) On the transverse vibrations of bars of uniform cross-section. Philosophical Magazine 43: 125-131

[2] Dimentberg F.M. (1961) Flexural Vibrations of Rotating Shafts. Butterworth. London, 1961

[3] Raffa F.A., Vatta F. (1999) Gyroscopic effects analysis in the lagrangian formulation of rotating beams. Meccanica 34: 357–366

[4] Raffa F.A., Vatta F. (2001) Equations of motion of an asymmetric Timoshenko shaft. Meccanica 36: 201–211

[5] Filipich C.P., Rosales M.B. (1990) Free flexural–torsional vibrations of a uniform spinning beam. Journal of Sound and Vibration 141/3: 375–387

[6] Greenhill A.G. (1883) On the strength of shafting when exposed both to torsion and to end thrust. Proc. Inst. Mech. Eng., London 6: 182–209

[7] Southwell R.V., Gough B.S. (1921) On the stability of rotating shaft, subjected simultaneously to end thrust and twist. British Association for Advancement of Science 345

[8] Colomb M., Rosenberg R.M. (1951) Critical speeds of uniform shafts under axial torque. Proc. First U.S. National Congress of Applied Mechanics, New York, USA: 103-110

[9] Eshleman R.L., Eubanks R.A. (1969) On the critical speeds of a continuous rotor. Trans. Amer. Soc. Mech. Eng., Journal of Engineering for Industry 91/4: 1180–1188

[10] Yim K.B., Noah S.T., Vance J.M. (1986) Effect of tangential torque on the dynamics of flexible rotors. Trans. Amer. Soc. Mech. Eng., Journal of Applied Mechanics 53: 711–718

[11] Lee C.W. (1993) Vibration analysis of rotors. Dordrecht, Kluwer, 1993

[12] Choi S.H., Pierre C., Ulsoy A.G. (1992) Consistent modeling of rotating Timoshenko shafts subject to axial loads. ASME Journal of Vibration and Acoustics 114: 249–259

[13] Willems N., Holzer S. (1967) Critical speeds of rotating shafts subjected to axial loading and tangential torsion. Trans. Amer. Soc. Mech. Eng., Journal of Engineering for Industry 89: 259–264

[14] Dubigeon S., Michon J.C. (1975) Gyroscopic behaviour of stressed rotating shafts. Journal of Sound and Vibration 42/3: 281–293

[15] Lee C.W., Katz R., Ulsoy A.G., Scott R.A. (1988) Modal analysis of a distributed parameter rotating shaft. Journal of Sound and Vibration 122/1: 119–130

[16] Lacarbonara W., Antman S.S. (2008) What is a parametric excitation in structural dynamics? Sixth EUROMECH Nonlinear Oscillations Conference, Saint Petersburg, Russia, June 30-July 4 2008

[17] DaCunha J.J. (2005) Stability for time varying linear dynamic systems on time scales. Journal of Computational and Applied Mathematics 176/ 2: 381-410

[18] van der Kloet P., Neerhoff F.L. (2000) Diagonalization algorithms for linear time-varying dynamic systems. International Journal of Systems Science 31/8: 1053-1057

[19] Mathieu E. (1868) Mémoire sur le mouvement vibratoire d'une membrane de forme elliptique. Journal De Mathematiques Pures Et Appliquees 13: 137– 203

[20] Mathieu E. (1873) Cours de physique mathématique. Paris, Gauthier-Villars, Imprimeur-Libraire, 1873

[21] Floquet G. (1883) Sur les équations différentielles linéaires à coefficients périodiques. Ann. Ecole Norm., Ser. 2/12: 47-88

[22] Hill G.W. (1886) On the part of the motion of the lunar perigee which is a function of the mean motions of the sun and the moon. Acta Mathematica 8: 1-36

[23] Strutt J.W. Baron Rayleigh (1881-1887) Scientific Papers. London: C. J. Clay And Sons, Cambridge University Press Warehouse, Vol II, 1900

[24] Strutt J.W. Baron Rayleigh (1887-1892) Scientific Papers. London: C. J. Clay And Sons, Cambridge University Press Warehouse, Vol III, 1902

[25] Poincaré H. (1890) Sur le probléme des trois corps et les équations de la dynamique. Acta Mathematica 13: 5-270

[26] Lyapunov A.M. (1892) The General Problem of Stability of Motion. Khar'kov, republished in: Collected Works 2(1956): 7-263

[27] Meissner E. (1918) Ueber Schuettelschwingungen in Systemen mit Periodisch veraender-licher Elastizitaet. Schweizer Bauzeitung 72: 95-98

[28] Krein M.G. (1950) Generalization of some investigations of Lyapunov concerning linear differential equations with periodic coefficients. Dokl. Akad. Nauk SSSR 73/3: 445-448

[29] Krein M.G. (1951) On the application of an algebraic proposition in the theory of monodromy matrices. Uspekhi Mat. Nauk 6/1: 171-177

[30] Krein M.G. (1951) On the theory of the entire matrix-function of exponential type. Ukrain. Mat. 3/2: 164-173

[31] Krein M.G. (1951) On some maximum and minimum problems for characteristic numbers and Lyapunov stability zones. Prikl. Mat. Mekh. 15/3: 323-348

[32] Krein M.G. (1955) On criteria for stability and boundedness of solutions of periodic canonical systems. Prikl. Mat. Mekh. 19/6: 641-680

[33] Krein M.G. (1955) Fundamental aspects of the theory of λ-zones of stability for a canonical system of linear differential equations with periodic coefficients. In: Sb. Pamyati A.A. Androva, Moscow, Akad. Nauk SSSR: 413-498

[34] Krein M.G. (1957) On the characteristic function A(λ) of a linear canonical system of second-order differential equations with periodic coefficients. Prikl. Mat. Mekh. 21/3: 320-329

[35] Krein M.G. (1965) Introduction to the geometry of indefinite J-space and the theory of operators in these spaces. In: Vtoraya letnyaya mat. Shkola, Kiev, "Naukova Dumka": 15-92

[36] Krein M.G., Lyubarskii G. Y. (1961) On the theory of pass-bands of periodic waveguides. Prikl. Mat. Mekh. 25/1: 24-37

[37] Krein M.G., Lyubarskii G. Y. (1962) On analytical properties of multipliers of periodic canonical differential systems of positive type. Izv. Akad. Nauk SSSR, Ser. Mat. 26/4: 542-572

[38] Krein M.G., Yakubovich V.A. (1963) Hamiltonian systems of linear differential equations with periodic coefficients. Proceedings Intern. Symp. On Nonlinear Oscillations. Izv. Akad. Ukrain SSR 1: 277-305

[39] Yakubovich V.A., Starzhinskii V.M. (1975) Linear Differential Equations with Periodic Coefficients. Volume I, Wiley, 1975

[40] Yakubovich V.A., Starzhinskii V.M. (1975) Linear Differential Equations with Periodic Coefficients. Volume II, Wiley, 1975

[41] Ince E.L. (1953) Ordinary differential equations. New York, Dover, 1953

[42] Bolotin V.V. (1964) The dynamic stability of elastic systems. Holden–Day, San Francisco, 1964

[43] Ruzzene M. (2004) Dynamic buckling of periodically stiffened shells: application to supercavitating vehicles. International Journal of Solids and Structures 41/3–4: 1039-1059

[44] Ahsan Z., Sadath A., Uchida T.K. (2015) Galerkin–Arnoldi algorithm for stability analysis of time-periodic delay differential equations. Nonlinear Dynamics. 82/4: 1893-1904

[45] Nayfeh A.H., Sanchez N.E. (1989) Bifurcations in a forced softening duffing oscillator. International Journal of Non-Linear Mechanics 24/6: 483-497

[46] Ge Z.M., Chen H.H. (1997) Bifurcations and chaotic motions in a rate gyro with a sinusoidal velocity about the spin axis. Journal of Sound and Vibration 200/2: 121-137

[47] Lan L., Ni Y., Jiang Y., Li J. (2017) Motion of the Moonlet in the Binary System 243 Ida. Acta Mechanica Sinica 34/1: 214-224

[48] Sinha S.K. (1989) Stability of a viscoelastic rotor-disk system under dynamic axial loads. AIAA Journal 27 /11: 1653-1655

[49] Sinha S.K. (2004) Dynamic characteristics of a flexible bladed-rotor with Coulomb damping due to tip-rub. Journal of Sound and Vibration 273 /4–5: 875-919

[50] Sinha S.K. (2005) Non-linear dynamic response of a rotating radial Timoshenko beam with periodic pulse loading at the free-end. International Journal of Non-Linear Mechanics 40/1: 13-149

[51] Chen L.W., Ku D.M. (1990) Dynamic stability analysis of a rotating shaft by the finite element method. Journal of Sound and Vibration 143/1: 143-151

[52] Chen L.W., Ku D.M. (1991) Dynamic stability of a rotating shaft embedded in an isotropic Winkler-type foundation. Mechanism and Machine Theory 26 /7: 687-696

[53] Chen L.W., Ku D.M. (1992) Dynamic stability of a cantilever shaft-disk system. Transactions ASME Journal of Vibration and Acoustics 114/3: 326-329

[54] Ku D.M., Chen L.W. (1992) Dynamic stability of a shaft-disk system with flaws. Computers and Structures 43/2: 305-311

[55] Chen L.W., Peng W.K. (1998) Dynamic stability of rotating composite shafts under periodic axial compressive loads. Journal of Sound and Vibration 212/2: 215-230

[56] Sheu H.C., Chen L.W. (2000) Lumped mass model for parametric instability analysis of cantilever shaft-disk systems. Journal of Sound and Vibration 234/2: 331-348

[57] Lin C.Y., Chen L.W. (2005) Dynamic stability of spinning pre-twisted sandwich beams with a constrained damping layer subjected to periodic axial loads. Composite and Structures 70/3: 275-286

[58] Lee H.P. (1995) Dynamic stability of spinning pre-twisted beams subject to axial pulsating loads. Computer Methods in Applied Mechanics and Engineering 127 /1-4: 115-126

[59] Lee H.P. (1995) Effects of axial base excitations on the dynamic stability of spinning pre-twisted cantilever beams. Journal of Sound and Vibration 185/2: 265-278

[60] Ng T.Y., Lam K.Y., Reddy J.N. (1998) Parametric resonance of a rotating cylindrical shell subjected to periodic axial loads. Journal of Sound and Vibration 214/3: 513-529

[61] Liew K.M., Hu Y.G., Ng T.Y., Zhao X. (2006) Dynamic stability of rotating cylindrical shells subjected to periodic axial loads. International Journal of Solids and Structures 43/25–26: 7553-7570

[62] Yu S.D., Cleghorn W.L. (2002) Dynamic instability analysis of high-speed flexible four-bar Mechanisms. Mechanism and Machine Theory 37/11: 1261-1285

[63] Sinha S.K. (1992) On general conditions of rotordynamic stability under combined axial forces and torque. Transactions ASME Journal of Applied Mechanics 59/1: 225-228

[64] Yong-Chen P. (2008) Stability boundaries of a spinning rotor with parametrically excited gyroscopic system. European Journal of Mechanics A / Solids 28: 891–896

[65] Frulla G. (2000) Rigid rotor dynamic stability using Floquet theory. European Journal of Mechanics - A/Solids 19/1: 139-150

[66] Hussain J.I.I., Kanki H., Mureithi N.W. (2001) Stability and bifurcation of a rigid rotor in cavitated squeeze-film dampers without centering springs. Tribology International 34/10: 689-702

[67] Peletan L., Baguet S., Jacquet-Richardet G., Torkhani M. (2012) Use and Limitations of the Harmonic Balance Method for Rub-Impact Phenomena in Rotor-Stator Dynamics. Proceedings of the ASME Turbo Expo 2012: Turbine Technical Conference and Exposition. Volume 7: Structures and Dynamics, Parts A and B. Copenhagen, Denmark. June 11–15 2012: 647-655

[68] Varney P., Green I. (2017) Comparing the Floquet stability of open and breathing fatigue cracks in an overhung rotordynamic system. Journal of Sound and Vibration 408: 314-330

[69] Bartylla D. (2012) Stability investigation of rotors with periodic axial force. Mechanism and Machine Theory 58: 13-19

[70] Wettergren H.L., Olsson K.O. (1996) Dynamic instability of a rotating asymmetric shaft with internal viscous damping supported in anisotropic bearings. Journal of Sound and Vibration 195/1: 75-84

[71] Chinta M., Palazzolo A.B. (1998) Stability and bifurcation of rotor motion in a magnetic bearing. Journal of Sound and Vibration 214/5: 793-803

[72] Maldonado D.J.G., Karev A., Hagedorn P., Ritto T.G., Sampaio R. (2019) Analysis of a rotordynamic system with anisotropy and nonlinearity using the Floquet theory and the method of normal forms. Journal of Sound and Vibration 453: 201-213

[73] Ishida Y., Ikeda T., Yamamoto T., Esaka T. (1988) Parametrically excited oscillations of a rotating shaft under a period axial force. JSME International Journal, Series 3, Vibration, Control Engineering, Engineering for Industry 31/4: 698–704

[74] Coleman R.P. (1943) Theory of self-excited mechanical oscillations of hinged rotor blades. Technical Report NACA-WR-L-308, Langley Research Center, 1943

[75] Skjoldan P.F., Hansen M.H. (2009) On the similarity of the Coleman and Lyapunov–Floquet transformations for modal analysis of bladed rotor structures. Journal of Sound and Vibration 327/3-5: 424-439

[76] Stol K., Balas M., Bir G. (2002) Floquet modal analysis of a teetered-rotor wind turbine. ASME Journal of Solar Energy Engineering 124/4: 364–371

[77] Raffa F.A., Vatta F. (2007) Dynamic instability of axially loaded shafts in the Mathieu map. Meccanica 42: 347–553

[78] Sundararajan P., Noah S.T., (1998) An algorithm for response and stability of large order non-linear systems - application to rotor systems. Journal of Sound and Vibration 214/4: 695-723

[79] Al-Shudeifat M.A. (2015) Stability analysis and backward whirl investigation of cracked rotors with time-varying stiffness. Journal of Sound and Vibration 348: 365-380

[80] Kirchgäßner B. (2016) Finite Elements in Rotordynamics. Procedia Engineering 144: 736-750

[81] Arnoldi W.E. (1951) The principle of minimized iterations in the solution of the matrix eigenvalue problem. Quarterly of Applied Mathematics 9: 17-29

[82] Bauchau O.A., Nikishkov Y.G. (2001) An implicit Floquet analysis for rotorcraft stability evaluation. Journal of the American Helicopter Society 46: 200-209

[83] Friedman P. P. (1986) Numerical methods for determining the stability and response of periodic systems with applications to helicopter rotor dynamics and aeroelasticity. Computers and Mathematics with Applications 12A: 131-148

[84] Subramanian S., Gaonkar G. H., Nagabhushanam J., Nakad R. N. (1996) Parallel computing concepts and methods for Floquet analysis of helicopter trim and stability. Journal of the American Helicopter Society 41/4: 370-382

[85] Dugundji J., Wendell J. H. (1983) Some analysis methods for rotating systems with periodic coefficients. AIAA Journal 21/6: 890-897

[86] Mazzei A.J., Scott R.A. (2003) Effects of internal viscous damping on the stability of a rotating shaft driven through a universal joint. Journal of Sound and Vibration 265/4: 863-885

[87] Meirovitch L. (1997) Principles and Techniques of Vibrations. Prentice-Hall, Upper Saddle River, 1997

[88] Lancaster P. (2013) Stability of linear gyroscopic systems: a review. Linear Algebra and its Applications 439: 686-706

[89] De Felice A., Sorrentino S. (2019) On the dynamic behaviour of rotating shafts under combined axial and torsional loads. Meccanica 54/7: 1029-1055

[90] Traill-Nash R.W., Collar A.R. (1953) The effects of shear flexibility and rotatory inertia on the bending vibrations of beams. Quarterly Journal of Mechanics and Applied Mathematics 6/2: 186–222

[91] Levinson M., Cooke D.W. (1982) On the two frequency spectra of Timoshenko beams. Journal of Sound and Vibration 84/3: 319–326

[92] Stephen N.G. (2006) The second spectrum of Timoshenko beam theory-further assessment. Journal of Sound and Vibration 292: 372–389

[93] Stephen N.G., Puchegger S. (2006) On the valid frequency range of the Timoshenko beam theory. Journal of Sound and Vibration 297: 1082–1087

[94] Diaz-de-Anda A., Flores J., Gutierrez L., Mendez-Sanchez R.A., Monsivais G., Morales A. (2012) Experimental study of the Timoshenko beam theory predictions. Journal of Sound and Vibration 331: 5732–5744

[95] Manevich A.I. (2015) Dynamic of Timoshenko beam on linear and nonlinear foundation: Phase relations, significance of the second spectrum, stability. Journal of Sound and Vibration 344: 209–220

[96] De Felice A., Sorrentino S. (2017) Insights into the gyroscopic behaviour of axially and torsionally loaded rotating shafts. In Proc of 24th International Conference on Sound and Vibration (ICSV24), London United Kingdom: paper 879

[97] De Felice A., Sorrentino S. (2018) The second spectrum in Timoshenko beam theory: a new approach for its identification. In Proc of 25th International Conference on Sound and Vibration (ICSV25), Hiroshima, Japan: paper 780

[98] Faraday M. (1831) On a peculiar class of acoustical figure and on certain forms assumed by a group of particles upon vibrating elastic surfaces. Philosophical Transactions of the Royal Society, London, 121: 299-318

[99] Cowper G.R. (1966) The shear coefficient in Timoshenko’s beam theory. Journal of Applied Mechanics 33/2: 335–340

[100] Abramowitz M., Stegun L.A. (1964) Handbook of mathematical functions with formulas, graphs, and mathematical tables. New York, Dover, 1964

[101] Timoshenko S.P. (1936) Theory of elastic stability. New York-London, McGraw-Hill, 1936

[102] Blevins R.D. (1979) Formulas for natural frequency and mode shape. Van Nostrand, New York, 1979

[103] Takahashi K., Kawahara K. (1976) On a method of solution for the coupled Hill type equations and its application to the study of stability of nonlinear oscillation. Reports of the Faculty of Engineering, University of Nagasaki, 7: 43–52

[104] Barrios M.R, Collado J., Dohnal F. (2019) Coupled Mathieu Equations: γ-Hamiltonian and μ-Symplectic [Online First], IntechOpen, 2019

[105] Riesz F. (1907) Sur les systèmes orthogonaux de fonctions. Comptes rendus de l'Académie des sciences 144: 615–619

[106] Fischer E. (1907) Sur la convergence en moyenne. Comptes rendus de l'Académie des sciences 144: 1022–1024